

Semi-analytic modeling of stacked metasurfaces



**FRIEDRICH-SCHILLER-
UNIVERSITÄT
JENA**

Dissertation

zur Erlangung des akademischen Grades

doctor rerum naturalium (Dr. rer. nat.)

vorgelegt dem Rat der Physikalisch-Astronomischen Fakultät
der Friedrich-Schiller-Universität Jena

von Jan Sperrhake, Master of Science
geboren am 13.06.1989 in Gera

1. Gutachter: Prof. Dr. Thomas Pertsch
2. Gutachter: Prof. Dr. Carsten Rockstuhl, Karlsruhe
3. Gutachter: Prof. Dr. Niels Asger Mortensen, Odense (Dänemark)

Tag der Disputation: 03.11.2022

Contents

1	Introduction	3
2	Theoretical and computational concepts	12
2.1	Electrodynamics of continuous media	12
2.2	Boundary conditions and energy flux	17
2.3	Polarized light	20
2.4	Elements of the Fourier modal method	23
3	Fundamental mode approximation (FMA)	29
3.1	Principles of local field interaction	29
3.2	Wave propagation in periodic metamaterials	32
3.3	Fundamental mode interaction between metasurfaces	36
3.4	Coupling phases	41
4	Semi-analytic stacking algorithm	44
4.1	Fundamental mode scattering matrix formalism	44
4.2	Numerical validation	52
5	Experimental realization of complex stacks	60
5.1	Analysis of a fabricated chiral metasurface stack	60
5.2	Incommensurable period ratios and test of the FMA	68
6	Reflection paths in metasurface stacks	77
6.1	Equivalence of Feynman paths and reflection paths	78
6.2	Decomposition of Fabry-Pérot resonances	83
6.3	Reflection paths of a patch-wire metasurface stack	85
6.4	Chiral reflection paths	91
7	Summary and outlook	96

A	Supplementary material	I
A.1	Dispersion of gold and glass	I
A.2	Implementation of SASA	II
A.3	Comparison between layer rotation and unit cell rotation in twisted-wire-stack	X
A.4	Expressions of series coefficients and explicit calculations	XI
B	Bibliography	XVIII
C	Acknowledgments	XLIII
D	Zusammenfassung	XLV
E	Ehrenwörtliche Erklärung	XLIX

1 | Introduction

If we look through a telescope at the stars, we see their magnified ancient light. This magnification is one of the many technological achievements enabled by the lens – a piece of glass *shaped* so that it *refracts* light to do our bidding. Depending on their surface curvature, lenses can converge or diverge light and in combination create something like a Galilean telescope [1]. How does this happen? After all, glass is transparent – but not as transparent as air or vacuum. The molecules comprising glass interact with the electromagnetic waves which we *perceive* as visible light. They *respond* to it differently than the surrounding air molecules [2]. This gives rise to optical effects such as dispersion and refraction. Whereas dispersion is a result of frequency dependent propagation through a material, refraction arises from the discontinuity between two *different* materials [1]. Dispersion is the physical mechanism that “spreads” light into different colors or frequencies. Refraction enforces the continuity of electromagnetic fields at an interface depending on the angle of incidence, while changing the propagation direction in the adjacent medium according to Snell’s law [1]. It is extraordinary that we can manipulate these effects just by changing the type and geometry of the material in the path of light, like in the Galilean telescope, and thereby manipulate its properties to our advantage.

While optics is the physics of light as a whole, the mechanization of light for technological applications is called photonics [3]. This, clearly, necessitates a precise understanding of light-matter interaction [4]. For classical materials such as glasses or metals macroscopic models are sufficient. This relates to the macroscopic treatment of the electromagnetic fields interacting with a medium. While we can characterize solids by their electronic band structure and the presence of acoustic effects like phonons, treating the microscopic interaction of light with the vast ensemble of atoms and molecules would be rather unpractical [1, 4]. As long as we can model the macroscopic interaction of the ensemble homogeneously, the field interaction can be reduced to a scalar or tensorial factor, encompassing isotropic or anisotropic media, respectively [1, 5].

This thesis describes the propagation of light through stacked metasurfaces – layered, nano-structured media with generally microscopic field interactions. In order to treat these correctly, we need to adhere to strict physical principles, which are not immediately obvious [6].

Artificial optical materials Traditionally, chemistry grants us engineering access to material properties of optical media. Atomic or molecular orbitals vary the availability of bound and free electrons, therefore resulting in varied band structures [7,8]. Emerging frequency dependent charge displacements and induced currents produce polarization fields that respond to the presence of changing electromagnetic fields. This entire concept is contingent upon macroscopic field relations and averaged microscopic interactions [9–11]. Indeed, we can easily find frequency ranges where most solid materials become transparent and chemical attributes are of little consequence. Radar and radio waves, for example, can be several centimeters to kilometers long. Here, large scale charge distributions like the earths ionosphere or interstellar clouds possess the necessary scale for macroscopic field interaction to take effect [12,13]. On the other hand, artificial structures like antennas at about half-wavelength scale permit induced currents that produce a field response as well. Could we engineer an artificial radar or radio "material" based on an *arrangement* of antennas?

If we arrange several antennas in a periodic grid their combined dipolar response [14] mimics that of oscillating atomic or molecular dipoles in the Lorentz model of optical media [4,15]. As such, exciting the antenna array in its resonance band would make it highly reflective [16]. Similarly, we could imagine a sheet of metal with periodically arranged slots – inverted antennas. Whereas dipole-antennas would serve as a transmission band-stop filter in resonance, the slot array operates as a band-pass filter [14,17]. This concept of an artificial electromagnetic material is fittingly called *frequency selective surface* (FSS) [14]. In the past, FSS have been explored quite extensively [16–20] with research still ongoing [21–24].

Could we transfer the FSS concept to visible or infrared wavelengths as well? Certainly, there are limits to the classical approach of optical design that would benefit from artificial materials [25]. For instance, miniaturization and multifunctionalization [26–29] are prime targets in the continued development of photonics [30]. This idea of artificially enhanced optical materials was pioneered by JOHN PENDRY [31,32]. Inspired by the work of VIKTOR VESELAGO [33], PENDRY calculated the properties of a lens with *negative* refractive index. The resultant lens showed perfect imaging qualities [34]. PENDRY suggested the plasmonic behavior [35] of implanted metallic inclusions as the perpetrators of the necessary negative index of refraction. This launched an area of research into what is now known as *metamaterials* [36]. Very similar to the engineering of antennas and circuits for FSS [37], metamaterials are centered around the design of nanoscopic inclusions in a medium. By designing the multipolar microscopic response of micro- or nano-structures in a given arrangement, macroscopic field effects can be engineered [38–44].

But we are faced with a dilemma. Precise taxonomy is required in order to properly explain the physics of these artificial optical materials [36]. Here, our use of the word *material* is somewhat vague. Classically, *optical* material in photonics means a solid composed of bound

chemical elements, being anywhere between crystalline and amorphous [4, 45]. If we use the prefix *meta*, we imply some new type of material beyond what is naturally possible. However, as ARI SIHVOLA pointed out [36], this is not exactly true. All metamaterials are based on naturally occurring materials [28, 30, 46–50] and the physics governing classical field-matter interactions are always legislated by Maxwell’s equations [38–43].¹ Instead, metamaterial could emphasize *artificial* materials. Of course, this is problematic in its own right because most technically applied materials are human made and, thus, artificial.

Looking back at FSS the structured components are key. A simplistic definition of this was given by SERGEI TRETAKOV, defining a metamaterial as “[...] *an arrangement of artificial structural elements, designed to achieve advantageous and unusual electromagnetic properties [...]*” [51]. Similarly, TRETAKOV defined a *metasurface* as an “*optically thin layer [...] formed by engineered meta-atoms,*” [51] where the word *meta-atoms* is another terminology for artificial structural elements. In both cases an engineering goal is implied in the definition, circumventing the physical definition of a material. Why is that important? As motivated at the beginning, the use of optical materials is that of manipulating light, which necessitates control over certain physical parameters.

An understanding of metamaterials requires a sound physical concept of wave propagation inside a bulk metamaterial or through a metasurface. For optical physics this means finding a refractive index n for modes propagating in the medium. This in turn necessitates a permittivity ε that can be extracted from the medium. However, all metamaterials are composites of some arrangement of particles (or structures) that are embedded in a homogeneous material matrix [10, 28, 30, 50]. Naively, it could be argued that one could find an *effective* material parameter like ε_{eff} with a resulting effective refractive index n_{eff} leading, for instance, to the desired negative refractive index suggested by PENDRY [52–55]. This is, unfortunately, not always the case [56–60]

A historical perspective Historically, effective parameters in optical materials are connected to the concept of homogenization. The underlying question was first discussed at the beginning of the 20th century, asking whether a medium could be considered homogeneous despite thermal molecular motion within the medium [61]. Here, the term “homogeneous” implies that wave propagation through the medium is described by a homogeneous wave equation.

At that time, a long dispute was fought around the scattering of light and dissipation of energy in homogeneous media between MAX PLANCK [62] and LEONID MANDELSTAM [63]. It eventually led to the conclusion that light scattering in a homogeneous medium depends on the uniformity of the distribution of oscillators in it [5] - or as H. A. LORENTZ put it in 1910:

¹Here, we deliberately exclude quantum optical phenomena because this work deals with purely classical field theory.

“[...] scattering can only take place when the molecules are irregularly distributed, as they are in gases and liquids; in a body whose molecules have a regular geometrical arrangement, a beam of light is propagated without any diminution of its intensity.” [5]

Keeping LORENTZ’s quote in mind, we have to ask what homogeneity means for metamaterials. The structures of most metamaterials are regularly arranged [64,65], comprising periodic arrays [66], quasi-crystalline or disordered configurations [67–69], as well as patterns resembling lenses and holograms [70–75]. So, following LORENTZ’s argument, one could reason that these metamaterials should, on average, behave homogeneously. However, in the same manuscript LORENTZ also pointed out that “[...] a consideration of the resistances² will be incomplete if one does not keep in view the mutual action between the molecules.” [5].

If the distances between structures in a medium become small with respect to their individual size, it is easy to imagine that field interactions between the structures quickly become relevant. Indeed, LORD RAYLEIGH already identified the issue in 1892 [76], where he discussed the properties of media interspersed with cylinders or spheres in a rectangular lattice. By deriving approximations for the medium’s refractive index and conductivity (both heat and electric) he found a connection between the properties of the microscopic inclusions and the macroscopic medium. In essence, his treatise was one of the first approaches to finding *effective* parameters and thereby *homogenizing* a structured medium [9].

With the emergence of optical metamaterials about 100 years later, the treatment of homogeneity was, in a sense, reversed. Instead of starting from a microscopic level and deriving the macroscopic properties, like LORENTZ and RAYLEIGH did, material parameters were retrieved from macroscopic responses [58–60,77–79]. The basic procedure entailed measurement (numerical or experimental) of the Fresnel transmission and reflection coefficients (or S parameters) [77,77]. By inverting Fresnel equations the effective refractive index of the medium was retrieved and transformed into the material’s effective permittivity by virtue of the dispersion relation of an homogeneous medium [52–54].

However, KONSTANTIN SIMOVSKI formally showed that many of the retrieved parameters [52–55] were physically *meaningless* [80], although mathematically correct. Reflecting the discussion at the beginning of the 20th century and, especially, LORENTZ’s point on the importance of “*mutual action between the molecules*” [5], structural properties of the metamaterial as well as the frequency band operated in are key to unlocking meaning behind effective parameters. Otherwise metamaterials can not be treated as homogeneous media.

In summary, metamaterials only present effective physical materials if they are homogeneous. Recalling our previous perspective on taxonomy, we have to differentiate between *engineering* artificial structures for specific effects and designing materials with *targeted parameters*.

²Resistance in this context is equivalent to the impedance a field experiences when propagating through the medium. Scholars at the time sometimes even used the term “field friction” [61].

Properties and capabilities of metasurfaces In this work we follow TRET'YAKOV's definition of metasurfaces [51] and treat thin layers with laterally arranged nano-structures. These promise flat designer photonics for a large diversity of applications [81–87]. As motivated in the very first paragraph the main objective is that of light manipulation including phase, polarization, and amplitude as well as dispersion control [65, 88–91]. Furthermore, for applications in non-linear and quantum optics metasurfaces can achieve precisely engineered photon states [92–95]. Similarly, modern sensor development benefits from the miniaturization gained from nano-photonic multi- and hyperspectral filters [71, 96–102]. Arranging meta-atoms concentrically produces a phase profile comparative to that of a lens [70, 74, 75]. Here, the modern paradigm shifted from designing material parameters for a perfect lens to engineered wavefronts [103–105].

There are even cases where structural design and the right assortment of materials expand the boundary of known optical effects. A quite prominent and recent example are so-called bound states in the continuum [106–109]. They are non-radiative modes, i.e. eigen-solutions of the material, that exist in a continuum of radiative modes. They are a direct result of structurally engineered dispersion that creates the right interference conditions so that a small subset of the radiative modes vanishes [109, 110].

Of particular interest is the design of anisotropy. Classical anisotropic media are crystalline materials such as sapphire, diamond or lithium niobate [111, 112], leading to the well-known effect of birefringence or double-refraction [1, 4]. Anisotropy also creates changes in the orientation and oscillation direction of the electromagnetic field vector, known as polarization. Similarly, the structural symmetry of metasurfaces can be broken to achieve different kinds of polarization [113–115]. The symmetry class and orientation of meta-atoms produce tensorial field interactions that can lead to effects such as dichroism [116, 117] and in combination with strong near-field effects optical activity [118, 119]. Dichroism of linearly or circularly polarized light describes a different response for different incident polarization. Optical activity, on the other hand, rotates the input polarization.

A very special case of asymmetry is that of *chirality*. Originating from ancient greek, chiral means *handed*, which refers to the mirror-asymmetry of the human hand. It is impossible to map one hand onto to the other by any rotation, although both hands look very much alike. The same asymmetry can be created in meta-atoms [120]. First and foremost, all meta-atoms of a chiral metasurface have to be mirror asymmetric. If that is the case, they will exhibit both polarization rotation and *magneto-electric coupling* [120]. The latter describes an interdependence of the electric and magnetic field, created by the anisotropy. Materials with this property are also called bi-anisotropic.³ Many examples of bi-anisotropic and chiral metasurfaces involve three-dimensional meta-atoms [121–124], which are laterally arranged on a thin sheet and intrinsically,

³There are also bi-isotropic materials [36] but we will exclude them here for brevity.

geometrically chiral [125]. A prominent example of an intrinsically chiral structure is the helix [85,126]. Concerning fabrication, it seems obvious that such intricate structures are much more challenging to realize than, say, planar structures with only a two-dimensional in-plane asymmetry [127]. One alternative are asymmetric split ring resonators [114, 128, 129], which extrinsically create chiral effects through symmetry broken near-field interactions [130–132]. Nevertheless, the small gaps required for the *split* rings make them, still, rather unpractical to fabricate at the scale of optical wavelengths. Recently, it was demonstrated that optical chirality can be accomplished with planar nano-structures by using multiple types of meta-atoms in one unit cell [133].

We can find yet another route towards bi-anisotropy by using planar nano-structures sandwiched as strongly coupled bi-layers [115, 134–136]. Here, one uses simple geometries such as wires (i.e. antennas) or crosses which are then rotated with respect to each other in two very close layers [137–139]. This creates the conditions for the polarization of an incident field to be broken by the enhancement of the geometrical asymmetry through near-field coupling [140,141]. This, however, requires perfect alignment of the individual meta-atoms of each layer.

Layer alignment is an easily underestimated fabrication challenge that could be avoided by increasing the distance between layers, albeit weakening the near-field coupling. Interestingly, as ZHAO et al. showed [142,143], one can achieve a chiral polarization response in the absence of near-field coupling by combining multiple layers of successively rotated nano-wires. Whereas each individual layer is achiral, the concert of repeated rotations twists light just like a helix would. We call this process of combining multiple *individual* metasurfaces *stacking*.

Stacked metasurfaces Although few, there are other examples of stacked metasurfaces beside ZHAO’s twisted metasurfaces [142] in the literature [144]. Recent studies demonstrated how stacking can combine properties of individual metasurfaces and retain their separate characteristics [145–151], rather than merging them into a complex amalgamation [140,141]. Here, the lack of strong near-field effects is compensated for by simplified design in a multiplicative fashion, while benefiting from less demanding fabrication. An exceptional example of this is the multi-wavelength meta-lens design proposed by ZHOU et al. [74]. Taking three meta-lenses comprised of concentric rings of dielectric cylinders, each was designed to process the light of the one before. Because they avoided near-field coupling, the meta-lenses could be constructed as individual elements based solely on the input provided by incident far-fields.

Meta-lensing is an example of complex stack configurations. In principle, the category of stacked metasurfaces also includes combinations with homogeneous dielectric layers, such as nano-structures embedded in Fabry-Pérot cavities. Here, Fabry-Pérot resonances [152] are enhanced by the presence of a metasurface sandwiched between two mirrors, e.g. Bragg-reflectors [153].

The scheme of stacking individual metasurfaces relies on an understanding of inter-layer interactions, which are controlled by the thickness of the spacer layer separating the metasurfaces. Rigorous simulations of the fields surrounding the involved structures can show which type of coupling occurs [74, 147, 154]. However, the results are always case-dependent and full numerical treatment is needed for each stacked metasurface design. If we look at periodic metasurfaces, there is a possible generalization regarding homogeneity. Basically, we can categorize inter-layer coupling into three mechanisms: evanescent coupling, diffractive coupling and far-field coupling. Evanescent fields resemble what we previously called near-fields [155]. In periodic arrays of meta-atoms they incorporate non-propagating diffraction orders. These will start to propagate if the propagation constant of the respective modes becomes real-valued [145, 156], transitioning to diffractive coupling. To avoid this, periods have to be kept smaller than the wavelength of incident light, which also limits the size of nano-structures comprising the unit cells [11, 145]. If higher diffraction orders are non-existent and evanescent coupling is negligible, far-field coupling dominates. Then, each individual metasurface operates like a homogeneous interface for all modes in the far-field regime [58, 156–158]. Borrowing from the terminology of photonic crystals these modes are called *fundamental* modes [159–162]. Assuming the sufficient decay of evanescent fields the reduction to only the fundamental mode is fittingly called the *fundamental mode approximation* (FMA) [145, 156].

Parametric blind spots As a prerequisite and touchstone for *semi*-analytic modeling, simulations of individual metasurfaces can be computationally demanding tasks. Parameterization of the geometries, materials, and scale of metasurfaces creates parameter spaces that grow quickly in dimension and combinatoric possibility [163–165]. This can be beneficial as it increases the chances of finding a parameter combination that would suit a targeted application [166–169]. Application driven metasurfaces for color filtering [83, 101, 170] and polarization manipulation [142, 171, 172] are immediate examples of this. Weighing the achievable degrees of freedom against parameter space complexity [165], we can reach limits where searches for optimal parameter combinations lead to non-intuitive solutions [164, 173, 174]. For very high-dimensional problems it becomes necessary to employ optimization algorithms [164, 165, 168] or train suitable neural networks [105, 175–178].

Each approach has its place in nano-photonics research. Regardless of the method, we can identify a utilitarian simplification in the concept of stacking. Indeed, stacking multiple metasurfaces naturally increases the degrees of freedom with each added layer [74, 147, 179–181]. Then, parameter spaces of individual layers could be optimized independently with the target functionality of the stack as a boundary condition. Considering periodic metasurfaces, physical limits are presented by the FMA [146, 148, 151]. On the other hand, *computational* bounds arise from the period ratios of metasurfaces’ lattices. Unequal periods will necessitate super-

cell simulations that incorporate the smallest common period multiple of each layer [145]. The most extreme case of this are *incommensurable* period ratios, i.e. non-rational ratios. These produce infinitely large super-cells, making rigorous simulations impossible. Obviously, large rational ratios and those close to incommensurability present computational challenges as well. This presents a so far unresolved parametric blind spot in stacked metasurfaces design.

Scope of this thesis This thesis expands upon the body of work on stacked metasurfaces by offering a thus far unexplored but highly promising approach to semi-analytic modeling of such systems. It is centered around the FMA as its theoretical foundation. Therefore, the FMA's validity for stacked metasurfaces is a prime target of our investigation. Moreover, it is not entirely certain at what spacer thickness two metasurfaces will sufficiently transition to the far-field regime necessary for the FMA. Consequently, it is a task of this thesis to derive a *critical* stacking distance at which the FMA holds true for different stacks [145]. Awareness of these validity conditions will allow us to judge the homogeneity of metasurfaces and formally distinguish stacked metasurfaces from bulk metamaterials. This conceptual divide will provide precise taxonomy, leading to methodical physical interpretations beyond brute force numerics. Resting on this framework is the main objective of this thesis: to develop, verify, and experimentally apply a semi-analytic model of stacked metasurfaces, based on the principles of the FMA, while expanding on its applicability.

If we look at chiral metasurface stacks like the one demonstrated by ZHAO et al. [142,143], we can identify subtle questions concerning anisotropy and stacking. How is it, that chiral asymmetry emerges from achiral components in the absence of near-field coupling? If the layers are independent of each other, does their relative distance influence the total asymmetry? Potentially, these questions could be answered using semi-analytic models based on the FMA. However, we need to investigate how and to what extent such models can provide sufficient information to produce reliable answers. This entails describing the relation between stacking and the symmetry of electromagnetic fields [146]. More generally, we ought to consider the period of metasurfaces and their combined ratios in stacks. It is particularly important to inquire about ratios that present boundaries to the semi-analytic treatment. This includes the question whether *incommensurable* ratios in metasurface stacks can be realized numerically or experimentally [151].

For a full grasp of transmitted and reflected fundamental modes, including their polarization, we aim to employ a scattering matrix (S-matrix) formalism [145,182]. S-matrices can be considered a class of matrix methods in optics, that treats the propagation of light through various media algebraically [152,179,183–186]. Comparable methods include the adapted transfer matrix formalism by BERKHOUT and KOENDERINK [149,150]. Furthermore, rigorous Jones calculus [187,188] was shown to be equivalent to the S-matrix formalism [189–191], albeit less mathematically compact. Particularly, the PhD thesis by XAVIER ROMAIN [192] theoreti-

cally demonstrated an extended Jones matrix calculus that regarded the presence of evanescent fields. Here, we aim to incorporate FMA principles into an S-matrix formalism to develop a semi-analytic modeling approach that is applicable to a variety of periodic metasurfaces and is transferable to experimental results. Finally, we aim to expand upon the model's analytical potential by investigating inter-layer interaction processes which are unresolvable in rigorous numerical simulations [148].

Thesis structure We will introduce the reader to theoretical concepts most necessary for this thesis in chapter 2. Here, we emphasize on fundamental physical ideas and derive conventions and notation used throughout this work. Additionally, we will briefly introduce the Fourier modal method (FMM) in sec. 2.4 as our simulation method of choice.

The first half of chapter 3 presents an extension to theory chapter 2 and will derive the FMA based on plane wave and Bloch mode expansions, which ties directly into the ideas behind the FMM. Furthermore, the second half of chapter 3, starting with sec. 3.3, is committed to the proper conceptualization of metasurface stacks and validity conditions for the FMA. These will be applied directly in chapter 4, where we derive an FMA-based scattering matrix formalism which leads to a semi-analytic stacking algorithm (SASA) for arbitrary stacks of periodic metasurfaces. Then, sec. 4.2 will put SASA through a series of rigorous numerical tests, comparing to full FMM-simulations as well as to a unique finite difference time domain (FDTD) calculation.

With SASA established, we apply it to design and analyze experimentally realized stacks in chapter 5. First, we will employ SASA to explain the polarization response of a chiral metasurface stack (sec. 5.1). Then, we demonstrate the realization of a *pseudo*-incommensurable metasurface stack, while analyzing FMA-validity in a sequence of comparable stacks, transitioning between different coupling regimes (5.2). In the final research chapter 6 we draw a comparison between mesoscopic electron transport and nano-optics, transferring the concept of Feynman paths to stacked metasurfaces. Applying this to a specifically designed sample as well as the previously realized stacks from chapter 5, we present a series expansion of interferometric layer interactions.

2 | Theoretical and computational concepts

This chapter establishes necessary elements of electromagnetic theory underlying the theoretical and numerical concepts in this thesis. It aims to give the reader a summary of basic equations, notation schemes, and physical concepts on which later chapters are built upon. First, we will introduce Maxwell's equations in the frequency domain, which is the operational domain of all models derived in this thesis. Then, we will describe light-matter interaction based on the DRUDE-LORENTZ model of optical materials. Furthermore, we will establish plane waves as the basis of all our simulations. This includes a short discussion on the classical boundary problem between two homogeneous media and an introduction of the Fresnel equations.

Being of great importance for later chapters, starting with chapter 4, we take a closer look at vector field symmetry represented by different states of polarization. The main method of describing the change of polarization will be Jones calculus, which ties in perfectly with this thesis' main algebraic tool: the scattering matrix (S-matrix). We will introduce the S-matrix as a result of compact notation from the Fourier modal method (FMM). The FMM is a numerical method for simulating nano-optical phenomena in periodic materials. Here, we introduce the core concepts of the FMM as it will later be used mainly as a rigorous solver.

All concepts introduced in this chapter present a point of reference for derivations of the semi-analytic approach presented in chapters 3 and 4.

2.1 Electrodynamics of continuous media

2.1.1 Electromagnetic fields in homogeneous media

The propagation of light in optical media involves the interaction of electromagnetic waves with matter in a given frequency range. The relation between the charges and currents in a medium and electromagnetic fields is governed by a set of field equations known as macroscopic Maxwell equations [193, 194]. As both the fields and their electronic response are time dependent, the rate at which interactions occur is determined by the angular frequency ω of the fields which are present in a medium [4, 35]. For the coupled electric and magnetic fields at a point in space \mathbf{r} ,

$\mathbf{E}(\mathbf{r}, \omega)$ and $\mathbf{H}(\mathbf{r}, \omega)$, we can write the macroscopic Maxwell equations in the *frequency* domain,

$$\nabla \times \mathbf{E}(\mathbf{r}, \omega) = i\omega \mathbf{B}(\mathbf{r}, \omega), \quad (2.1)$$

$$\nabla \times \mathbf{H}(\mathbf{r}, \omega) = \mathbf{j}(\mathbf{r}, \omega) - i\omega \mathbf{D}(\mathbf{r}, \omega), \quad (2.2)$$

$$\nabla \cdot \mathbf{D}(\mathbf{r}, \omega) = 0, \quad (2.3)$$

$$\nabla \cdot \mathbf{B}(\mathbf{r}, \omega) = 0. \quad (2.4)$$

They are a set of eight coupled partial differential equations that form a relation between $\mathbf{E}(\mathbf{r}, \omega)$ and $\mathbf{H}(\mathbf{r}, \omega)$ in the presence of the current density $\mathbf{j}(\mathbf{r}, \omega)$. Importantly, using *macroscopic* Maxwell's equations implies an *absence* of external charges and, thus, a charge density $\rho(\mathbf{r}, \omega) = 0$. The field equations can be interpreted as the current density influencing the propagation of electromagnetic fields, while the fields themselves shape the current density during the interaction. The effect of this mutual interaction inside a material is described by two auxiliary fields, the electric flux density or displacement $\mathbf{D}(\mathbf{r}, \omega)$ and the magnetic flux density or induction $\mathbf{B}(\mathbf{r}, \omega)$. They are related to $\mathbf{E}(\mathbf{r}, \omega)$ and $\mathbf{H}(\mathbf{r}, \omega)$ via the material equations,

$$\mathbf{D}(\mathbf{r}, \omega) = \varepsilon_0 \mathbf{E}(\mathbf{r}, \omega) + \mathbf{P}(\mathbf{r}, \omega), \quad (2.5)$$

$$\mathbf{B}(\mathbf{r}, \omega) = \mu_0 \mathbf{H}(\mathbf{r}, \omega) + \mathbf{M}(\mathbf{r}, \omega), \quad (2.6)$$

where the constants ε_0 and μ_0 are called the vacuum permittivity and permeability, respectively. When an electric field is present in matter, it perturbs the distribution of charges within and produces a dipole polarization $\mathbf{P}(\mathbf{r}, \omega)$. Similarly, the presence of a magnetic field induces a magnetization $\mathbf{M}(\mathbf{r}, \omega)$ [155]. However, for macroscopic optics, i.e. for continuous homogeneous media in optical frequency ranges, $\mathbf{M}(\mathbf{r}, \omega)$ can be neglected. In this work, we consider light in the visible (VIS), near-infrared (NIR), and up to the short wavelength infrared (SWIR) regime, with wavelengths $\lambda_{\text{light}} \in [400 \text{ nm}, 1800 \text{ nm}]$. For the corresponding frequencies $\nu_{\text{light}} \in [167 \text{ THz}, 750 \text{ THz}]$ the displacement of electrons with an approximate velocity in the order of $v_e \approx \mathcal{O}(10^6 \text{ m/s})$ [7] has a magnitude of $v_e/\omega = v_e/(2\pi\nu_{\text{light}}) \approx \mathcal{O}(10^{-10} m)$. This is three orders of magnitude smaller than the atomic scale $\sim \mathcal{O}(10^{-7} m)$. We can conclude that the induced magnetic polarization $\mathbf{M}(\mathbf{r}, \omega)$ can be considered to be negligible with respect to the external electromagnetic fields and, therefore, $\mathbf{B}(\mathbf{r}, \omega) = \mu_0 \mathbf{H}(\mathbf{r}, \omega)$ [155, 195].¹

2.1.2 Description of optical materials

Above, we have only estimated the displacement of bound electrons in an arbitrary material to gauge the scale of field-matter interactions. However, in order to properly calculate the

¹At the moment of writing this thesis a very recent publication showed, for the first time, a naturally occurring magnetic polarization in a multi-layered, crystalline semi-conductor [196].

optical properties of a material we have to model its macroscopic electronic behavior. As a preliminary step we need to categorically introduce the types of optical materials we could encounter. These are, glasses, metals, semiconductors, crystalline insulators, molecular materials and doped glasses or insulators [4]. Relevant for this thesis are glass (fused silica) and metals, i.e. the noble metal gold. Whereas metals possess both bound and free electrons, glasses are *dielectric* and, thus, characterized by bound electrons only. The former are shiny and absorptive in the VIS, contrasting the latter which are transparent and without significant losses. These properties can be influenced by different physical aspects, which include electronic bands, vibrational bands, and the density of states [4].

For glasses and metals at optical wavelengths it is sufficient to model both bound and free electrons as an ensemble of oscillating dipoles and current densities, respectively. Other effects, emerging from the specific solid state physics of the medium, such as intraband transitions, can be included in phenomenological constants [4]. Free electrons, which characterize many metals, adhere to the DRUDE model [197], which describes the displacement $\mathbf{s}(\mathbf{r}, \omega)$ of electrons with an effective mass m_e and elementary charge e using the (frequency domain) oscillator equation

$$\omega^2 \mathbf{s}_f(\mathbf{r}, \omega) + i\gamma_f \omega \mathbf{s}_f(\mathbf{r}, \omega) = \frac{e}{m_{f,e}} \mathbf{E}(\mathbf{r}, \omega), \quad (2.7)$$

where γ denotes the dampening rate and the subscript f the specific properties of free electrons. Bound electrons, on the other hand, are characteristic to dielectrics and are described by the LORENTZ model [15], given by a driven harmonic oscillator with an additional restoring force term,

$$\omega^2 \mathbf{s}_b(\mathbf{r}, \omega) + i\gamma_b \omega \mathbf{s}_b(\mathbf{r}, \omega) - \omega_0^2 \mathbf{s}_b(\mathbf{r}, \omega) = \frac{e}{m_{b,e}} \mathbf{E}(\mathbf{r}, \omega), \quad (2.8)$$

where the subscript b denotes bound electrons. The restoring force is characterized by the resonance frequency ω_0 . The characteristic of the free electron gas in the DRUDE model does not require a restoring force and so there $\omega_0 = 0$ [4]. In both models the displacement is driven by the external electric field $\mathbf{E}(\mathbf{r}, \omega)$.

The displacement of bound charges induces a dipole moment $\mathbf{p}_b(\mathbf{r}, \omega) = -e\mathbf{s}_b(\mathbf{r}, \omega)$. For N_b bound electrons per unit volume it produces the electric polarization density $\mathbf{P}_b(\mathbf{r}, \omega) = -N_b e \mathbf{s}_b(\mathbf{r}, \omega)$. In contrast, a displacement of free charges produces, a *conductive* current density $\mathbf{j}_{\text{cond}}(\mathbf{r}, \omega) = i\omega N_f e \mathbf{s}_f(\mathbf{r}, \omega)$, for N_f free electrons per unit cell. Solving eqs. (2.7) and (2.8) for the displacement and inserting $\mathbf{P}_b(\mathbf{r}, \omega)$ and \mathbf{j}_{cond} gives us

$$\mathbf{j}_{\text{cond}}(\mathbf{r}, \omega) = i \frac{N_f e^2}{m_{f,e}} \frac{\omega}{\omega^2 + i\gamma_f \omega} \mathbf{E}(\mathbf{r}, \omega) \quad \text{and} \quad \mathbf{P}_b(\mathbf{r}, \omega) = \frac{\varepsilon_0 f}{\omega_0^2 - \omega^2 - i\gamma_b \omega} \mathbf{E}(\mathbf{r}, \omega). \quad (2.9)$$

Here, we introduced the oscillator strength $f = \frac{N_b e^2}{\varepsilon_0 m_{b,e}}$. Phenomenologically, there can be multiple oscillators in a material, each with a different strength, emerging from the specific

solid state physics of the medium. The resulting polarization density is, thus, best described by a sum of oscillators,

$$\mathbf{P}_b(\mathbf{r}, \omega) = \sum_j \frac{f_j}{(\omega_{0,j}^2 - \omega^2 - i\gamma_j\omega)} \mathbf{E}(\mathbf{r}, \omega) = \chi(\omega) \mathbf{E}(\mathbf{r}, \omega), \quad (2.10)$$

where each f_j is a phenomenological constant. We can interpret eq. (2.10) as the *susceptibility* of the medium $\chi(\omega)$ producing the polarization field $\mathbf{P}_b(\mathbf{r}, \omega)$.

Likewise, the conduction current density $\mathbf{j}_{\text{cond}}(\mathbf{r}, \omega)$ can be interpreted to emerge from the surface *conductivity* σ , defined as

$$\sigma(\omega) = i \frac{\varepsilon_0 \omega \omega_p^2}{\omega^2 + i\gamma_f \omega}, \quad \text{with} \quad \mathbf{j}_{\text{cond}}(\mathbf{r}, \omega) = \sigma(\omega) \mathbf{E}(\mathbf{r}, \omega), \quad (2.11)$$

introducing the *plasma frequency* $\omega_p^2 := \frac{Ne^2}{\varepsilon_0 m_{f,e}}$, representing the eigenfrequency of the free electron gas charge density. As the conduction current density is representative of a temporal variation of the polarization density of the free electron gas, we can substitute in the frequency domain $\mathbf{j}_{\text{cond}}(\mathbf{r}, \omega) = -i\omega \mathbf{P}_f(\mathbf{r}, \omega)$ in eq. (2.9) to get $\mathbf{P}_f(\mathbf{r}, \omega) = i\sigma(\omega)\omega^{-1} \mathbf{E}(\mathbf{r}, \omega)$.

If we assume that optical materials are generally characterized by the combined properties of both bound and free electrons, their optical response is described by the joint DRUDE-LORENTZ model. This enables us to substitute the polarization density in the material equation (2.5) with $\mathbf{P}(\mathbf{r}, \omega) = \mathbf{P}_b(\mathbf{r}, \omega) + i\omega^{-1} \mathbf{j}_{\text{cond}}(\mathbf{r}, \omega)$, which results in

$$\begin{aligned} \mathbf{D}(\mathbf{r}, \omega) &= \left(\varepsilon_0 + \sum_j \frac{f_j}{(\omega_{0,j}^2 - \omega^2 - i\gamma_j\omega)} - \frac{\varepsilon_0 \omega_p^2}{\omega^2 + i\gamma_f\omega} \right) \mathbf{E}(\mathbf{r}, \omega) \\ &= \varepsilon_0 \left(1 + \chi(\omega) + i \frac{\sigma(\omega)}{\omega} \right) \mathbf{E}(\mathbf{r}, \omega) := \varepsilon_0 \varepsilon(\omega) \mathbf{E}(\mathbf{r}, \omega). \end{aligned} \quad (2.12)$$

The overall material property that produces the displacement $\mathbf{D}(\mathbf{r}, \omega)$ in the presence of $\mathbf{E}(\mathbf{r}, \omega)$ is described by the complex valued *relative permittivity* $\varepsilon(\omega)$, as defined above. Examples for gold and also glass are shown in appendix A.1. Any linear, homogeneous medium can be fully characterized, at optical frequencies, by $\varepsilon(\omega)$. Hence, any discussion on optical material properties needs to be lead by a well defined $\varepsilon(\omega)$. This will become important in the discussion of effective material parameters in sec. 3.1.

Lastly, we can use the complex permittivity to define a complex refractive index for fields propagating in the medium,

$$n(\omega) = n'(\omega) + in''(\omega) = \sqrt{\varepsilon'(\omega) + i\varepsilon''(\omega)}. \quad (2.13)$$

Here, the imaginary part of the refractive index n'' characterizes the field dampening due to the dampening force of the material parameter $\varepsilon(\omega)$. Using the Poynting theorem it can be shown that the imaginary part of $\varepsilon(\omega)$ relates to energy loss inside the medium [4, 155].

2.1.3 Plane waves

For the purpose of this thesis it is necessary to find propagating solutions of Maxwell's equations. Adhering to the material model described in the previous section, we use the constitutive relations eqs. (2.11) and (2.12). Upon inserting Maxwell equation (2.2) into (2.1), we arrive at a homogeneous wave equation for the electric field,

$$\nabla \times \nabla \times \mathbf{E}(\mathbf{r}, \omega) - \frac{\omega^2}{c^2} \varepsilon(\omega) \mathbf{E}(\mathbf{r}, \omega) = 0, \quad (2.14)$$

where $c = (\varepsilon_0 \mu_0)^{-1/2}$ defines the vacuum speed of light.

For brevity we will restrict ourselves to the electric field from now on, as the magnetic field follows from Maxwell's equations. Using the identity $\nabla \times \nabla \times = -\nabla^2 + \nabla \cdot \nabla \cdot$ and recalling the absence of external charges, we can further simplify for homogeneous materials with $\nabla \cdot \nabla \cdot \mathbf{E}(\mathbf{r}, \omega) = 0$. A transformation to the spatial frequency domain, i.e. k -space, yields the eigenvalue equation

$$\left(-\mathbf{k}^2 + \frac{\omega^2}{c^2} \varepsilon(\omega) \right) \mathbf{E}(\mathbf{k}, \omega) = 0. \quad (2.15)$$

It relates the k -vector with the permittivity via the dispersion relation,

$$\mathbf{k}^2 = \frac{\omega^2}{c^2} \varepsilon(\omega). \quad (2.16)$$

With this, a solution to the wave equation (2.14) is presented to us in the form of so-called plane waves,

$$\mathbf{E}(\mathbf{k}, \omega) = |\mathbf{E}(\mathbf{k}, \omega)| e^{i(\mathbf{k}\mathbf{r} - \omega t)} = |\mathbf{E}(\mathbf{k}, \omega)| e^{i(\phi - \omega t)}, \quad (2.17)$$

where planes of equal (temporal) phase are perpendicular to the k -vector. The propagation direction is given by \mathbf{k} with $\mathbf{E}(\mathbf{k}, \omega) \cdot \mathbf{k} = 0$. We will remain in k -space and the frequency domain throughout this thesis. Therefore, we omit the dependencies of the field, $\mathbf{E}(\mathbf{k}, \omega) \rightarrow \mathbf{E}$. Furthermore, we will always assume a harmonic time dependence $\exp(-i\omega t)$ and quietly omit it as well from now on.

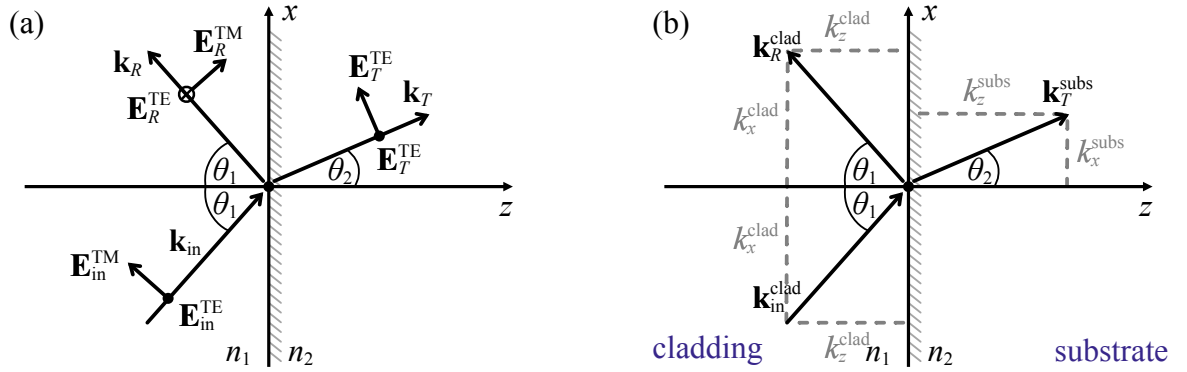


Figure 2.1: (a) Illustration of reflection and refraction (transmission) at an interface between two media with refractive indices n_1 and n_2 . The electric field is split into transverse electric and transverse magnetic components, perpendicular and parallel to the plane of incidence. (b) Definition of the medium of incident fields as the cladding and the medium of transmitted fields as the substrate and their respective k -vectors.

2.2 Boundary conditions and energy flux

2.2.1 Plane waves at interfaces

So far, we have described the propagation of electromagnetic waves in a continuous homogeneous medium. If light passes from one medium to another, the field is presented with a discontinuity at the interface between the media (fig. 2.1). Although the material parameters may change abruptly, Maxwell's equations demand continuity relations for fields at the boundary. This is a well known problem in the classical theory of electrodynamics [198] that can be solved using the integral representation of Maxwell's equations.

Constructing a cylinder with faces parallel to the boundary surface between medium 1 and 2, we can apply the Gauss divergence theorem to the integral form of (2.3) and (2.4). As the cylinder height approaches zero the integral reduces to the cylinder's end surfaces, leading to

$$\mathbf{n} \cdot (\mathbf{D}_2 - \mathbf{D}_1) = \tilde{\rho}, \quad \text{and} \quad \mathbf{n} \cdot (\mathbf{B}_2 - \mathbf{B}_1) = 0, \quad (2.18)$$

where the surface charge density $\tilde{\rho}$ vanishes in absence of surface charges, as is the usual case in optics [155]. The vector \mathbf{n} denotes the surface normal of the interface. In similar fashion we can draw a rectangular contour with its long sides parallel to the boundary and apply Stokes theorem to the integral form of eqs. (2.1) and (2.2) [198]. As the width of the rectangle approaches zero the integral reduces to its long sides, leading to

$$\mathbf{n} \times (\mathbf{E}_2 - \mathbf{E}_1) = 0, \quad \text{and} \quad \mathbf{n} \times (\mathbf{H}_2 - \mathbf{H}_1) = \tilde{\mathbf{j}}, \quad (2.19)$$

where the surface current density $\tilde{\mathbf{j}}$ vanishes in the absence of sources.

In summary, at the boundary the longitudinal components of the \mathbf{D} and \mathbf{B} fields are continuous, whereas for the \mathbf{E} and \mathbf{H} fields the tangential components are continuous.

If a plane wave propagates at an arbitrary angle θ_1 through an interface (fig. 2.1), parts of it will be refracted at angle θ_2 and other parts reflected by θ_1 , according to Snell' law [152]. The parts that are reflected or transmitted (refracted) follow from applying the boundary conditions to the incident plane wave, which yields the well known Fresnel formulas [1]. If we define the plane of incidence as the x-z-plane (fig. 2.1.a), the transversal components of the electric and magnetic field become E_x , E_y and H_x , H_y . Placing the interface in the x-y-plane ($z = 0$) then fixes the tangential components.

It is convenient to split the field vectors into components parallel and perpendicular to the plane of incidence. The ones *perpendicular* to the plane of incidence, $\mathbf{E}_{\text{TE}} = E_y \mathbf{e}_y$, we call the transverse electric (TE) field vector, with the magnetic component $\mathbf{H}_{\text{TE}} = H_x \mathbf{e}_x + H_z \mathbf{e}_z$.² Similarly, the vector $\mathbf{E}_{\text{TM}} = E_x \mathbf{e}_x + E_z \mathbf{e}_z$ lies *parallel* to the plane of incidence, while $\mathbf{H}_{\text{TM}} = H_y \mathbf{e}_y$ is perpendicular. This component is thus called transverse magnetic (TM). The tangential component of the electric field in TE and TM are then E_y and E_x .

Consider a plane wave incident from medium 1 with refractive index n_1 and transmitted into medium 2 with n_2 (fig. 2.1.a). Demanding continuity at the interface the respective transmitted and reflected components are related to the incident field by transmission and reflection coefficients such that,

$$T_{\text{TE}} = \frac{E_{y,T}}{E_{y,\text{in}}}, \quad T_{\text{TM}} = \frac{E_{x,T}}{E_{x,\text{in}}} \quad \text{and} \quad R_{\text{TE}} = \frac{E_{y,R}}{E_{y,\text{in}}}, \quad R_{\text{TM}} = \frac{E_{x,R}}{E_{x,\text{in}}}. \quad (2.20)$$

Following textbook derivations, these lead to the Fresnel formulas [1, 152],

$$T_{\text{TM}} = \frac{2n_1 \cos \theta_1}{n_1 \cos \theta_2 + n_2 \cos \theta_1} \quad R_{\text{TM}} = \frac{n_1 \cos \theta_2 - n_2 \cos \theta_1}{n_1 \cos \theta_2 + n_2 \cos \theta_1} \quad (2.21)$$

$$T_{\text{TE}} = \frac{2n_1 \cos \theta_1}{n_1 \cos \theta_1 + n_2 \cos \theta_2} \quad R_{\text{TE}} = \frac{n_1 \cos \theta_1 - n_2 \cos \theta_2}{n_1 \cos \theta_1 + n_2 \cos \theta_2}. \quad (2.22)$$

For normal incidence the difference between TE and TM vanishes and we simply get

$$T = \frac{2n_1}{n_1 + n_2} \quad \text{and} \quad R = \frac{n_1 - n_2}{n_1 + n_2}. \quad (2.23)$$

Throughout this thesis we use a strictly Cartesian coordinate system and always propagate *forward* in positive z-direction. Regarding eq. (2.20), we will use a Cartesian nomenclature, thus $T_{\text{TE}} \rightarrow T_y$, $T_{\text{TM}} \rightarrow T_x$, $R_{\text{TE}} \rightarrow R_y$, and $R_{\text{TM}} \rightarrow R_x$.

The medium from which a plane wave impinges at an interface will consistently be called

²Here, \mathbf{e}_x , \mathbf{e}_y , \mathbf{e}_z and are the Cartesian unit vectors

the *cladding* and the medium in which it transmits the *substrate*. The k -vectors in these are named accordingly, as defined in fig. 2.1.b).

2.2.2 Reflectance and transmittance

While we can describe how the electric field and the k -vector of a plane wave behave at an interface, the question remains how much energy is transported from the incident field into reflection and transmission. The direction of energy flux of an electromagnetic wave is given by the Poynting vector $\mathbf{S} = \mathbf{E} \times \mathbf{H}$, orthogonal to the electromagnetic vector field [198]. As optical frequencies are comparatively large (between 10^{14} and 10^{15} Hz) rapidly oscillating quantities cannot be observed and measurements will always produce time averaged results. It is, therefore, sensible to use the time average of the Poynting vector in the frequency domain [1],

$$\langle \mathbf{S} \rangle = \frac{1}{2} \text{Re}(\mathbf{E} \times \mathbf{H}^*), \quad \text{with} \quad \mathbf{H}^* = \frac{1}{2\omega\mu_0} (\mathbf{k}^* \times \mathbf{E}^*). \quad (2.24)$$

For a plane of incidence in the x-z-plane, as defined in fig. 2.1.b), the energy flux transmitted through the interface at $z = 0$ and into the substrate follows as

$$\langle \mathbf{S}_{\text{subs}} \rangle \mathbf{e}_z = \frac{1}{2\omega\mu_0} \text{Re}(k_z^{\text{subs}}) |\mathbf{E}_T|^2. \quad (2.25)$$

Similarly, the energy flux in *backward* direction, i.e. negative z , *into* the cladding is given by

$$\langle \mathbf{S}_{\text{clad}} \rangle \mathbf{e}_z = \frac{1}{2\omega\mu_0} k_z^{\text{clad}} (|\mathbf{E}_{\text{in}}|^2 - |\mathbf{E}_R|^2). \quad (2.26)$$

Here, we assume k_z^{clad} to be real-valued because the plane wave, originating from infinity, impinges within the cladding and would, otherwise, be completely absorbed. The total flux is restrained by the law of energy conservation and, hence, bounded by the input flux. Thus, eqs. (2.25) and (2.26) lead to

$$|\mathbf{E}_{\text{in}}|^2 = |\mathbf{E}_R|^2 + \frac{\text{Re}(k_z^{\text{subs}})}{k_z^{\text{clad}}} |\mathbf{E}_T|^2. \quad (2.27)$$

For perpendicular incidence, using $k_z^{\text{subs}} = k_0 n_{\text{subs}}$ and $k_z^{\text{clad}} = k_0 n_{\text{clad}}$, we define

$$\tau := \frac{\text{Re}(n_{\text{subs}})}{n_{\text{clad}}} \frac{|\mathbf{E}_T|^2}{|\mathbf{E}_{\text{in}}|^2} \quad \text{and} \quad \rho := \frac{|\mathbf{E}_R|^2}{|\mathbf{E}_{\text{in}}|^2} \quad (2.28)$$

as the transmittance and reflectance, respectively.³ These represent the transmitted and reflected intensities that would be measured by a detector. The case of oblique incidence involves the continuity of the tangential k -vector components at the interface, which produces different

³Alternatively, these quantities are called transmissivity and reflectivity.

energy flux in TE and TM. In Cartesian notation this leads to

$$\tau_{x,y} = \frac{\operatorname{Re} \left(\sqrt{n_{\text{subs}}^2 - n_{\text{clad}}^2 \sin^2 \theta_1} \right)}{n_{\text{clad}} \cos \theta_1} |\mathbf{E}_{T;x,y}|^2 \quad \text{and} \quad \rho_{x,y} = |\mathbf{E}_{R;x,y}|^2 \quad (2.29)$$

If the interface represents itself a medium that is absorptive we can define the absorbtance $\alpha_{x,y}$ as the total intensity absorbed in the medium. Normalizing the input energy, the total energy balance at the interface reads

$$1 = \tau_x \sin^2 \psi + \tau_y \cos^2 \psi + \rho_x \sin^2 \psi + \rho_y \cos^2 \psi + \alpha_x \sin^2 \psi + \alpha_y \cos^2 \psi, \quad (2.30)$$

where ψ is the *polarization* angle of the field vector with respect to the TE component, i.e. E_y .

2.3 Polarized light

2.3.1 Polarization ellipse

If we define the propagation direction of light parallel to the z-axis, the plane waves' property $\mathbf{E} \cdot \mathbf{k} = 0$ demands that the z-component of the electric field \mathbf{E} vanishes. This leaves two complex field components *transversal* to the propagation direction,

$$\mathbf{E} = \begin{pmatrix} E_x e^{i\phi_x} \\ E_y e^{i\phi_y} \\ 0 \end{pmatrix}. \quad (2.31)$$

Each component has an amplitude $E_{x,y}$ and a phase $\phi_{x,y}$. They are complex values who's real parts, $E'_{x,y} := \operatorname{Re}(E_{x,y}) = E_{x,y} \cos \phi_{x,y}$ describe an ellipse based on their relative phase shifts and amplitudes [199],

$$\left(\frac{E'_x}{E_x} \right)^2 + \left(\frac{E'_y}{E_y} \right)^2 - 2 \frac{E'_x}{E_x} \frac{E'_y}{E_y} \cos \delta = \sin^2 \delta, \quad (2.32)$$

where $\delta = \phi_x - \phi_y$ is the relative phase shift. As the field propagates, E'_x and E'_y produce a resultant vector that describes the evolution of the optical field at any instant of time. This behavior is known as *polarization*. The corresponding ellipse is thus called *polarization ellipse* and its shape and orientation define the state of polarization of the optical field.

Generally, light is *elliptically* polarized. Certain parameter combinations produce special kinds of polarization. If either $E'_x = 0$ or $E'_y = 0$ the ellipse reduces to a line parallel to the x- or y-axis along which the field then oscillates. This we call *linear* x- or y-polarization. Linearly

polarized light is also created for phase shifts $\delta = 0$ and $\delta = \pi$. In that case

$$\left(\frac{E'_x}{E_x} \pm \frac{E'_y}{E_y}\right)^2 = 0, \quad (2.33)$$

where the sign depends on δ . This represents a line rotated about the coordinate center depending on the ratio of E_x and E_y .

Another extreme of the ellipse is the circle. For equal amplitudes $E_x = E_y$ a phase shift of $\delta = \pm\pi/2$ produce what is called left or right *circularly* polarized light.⁴ In this case, the field vector draws a circle as it propagates rotating in one or the other direction. Interestingly, this implies a *handedness* of the symmetry of electric field. Borrowing from the Greek language this property is called *chirality*. The word suggest a broken symmetry, such as for the human hand, which cannot be mapped back onto itself by a mirror operation in any plane [120]. Henceforth, light with this symmetry property will be called chiral light. In that regard, also elliptically polarized light fulfills the criteria for chirality.

2.3.2 Jones matrix calculus and symmetry

Based on our understanding of the polarization ellipse we can formalize the treatment of polarized light using Jones calculus [187]. For propagation in z -direction we reduce the three-dimensional electric field to only its transversal components, which we call the Jones vector,

$$\mathbf{E} = \begin{pmatrix} T_x \\ T_y \end{pmatrix} = \begin{pmatrix} E_x e^{i\phi_x} \\ E_y e^{i\phi_y} \end{pmatrix}. \quad (2.34)$$

In some cases the Jones vector is denoted by the symbol \mathbf{J} . In our case it will be more convenient to simply redefine \mathbf{E} as the Jones vector, as it will be used frequently throughout this thesis. The complex coefficients $T_{x,y}$ are composed of the real-valued amplitudes $E_{x,y}$ and complex phases $\exp(i\phi_{x,y})$ of the transversal electric field components.⁵ The norm of the Jones vector,

$$|\mathbf{E}| = \mathbf{E}^\dagger \cdot \mathbf{E} = (T_x^*, T_y^*) \cdot \begin{pmatrix} T_x \\ T_y \end{pmatrix}, \quad (2.35)$$

gives the total intensity of the electric field and is by definition set to $|\mathbf{E}| = 1$ [199], where superscripts \dagger and $*$ denote the complex transpose and complex conjugate. To give a few

⁴Other naming conventions are clockwise or counterclockwise and plus or minus circularly polarized light

⁵Note that we stay consistent in our notation regarding Fresnel equations. At the interface of an isotropic medium T_x and T_y take the form of Fresnel equation.

examples, the Jones vectors for linearly and circularly polarized light read as

$$\mathbf{E}_{\text{lin},x} = \begin{pmatrix} 1 \\ 0 \end{pmatrix}, \quad \mathbf{E}_{\text{lin},y} = \begin{pmatrix} 0 \\ 1 \end{pmatrix}, \quad \text{and} \quad \mathbf{E}_{\text{circ},R} = \frac{1}{\sqrt{2}} \begin{pmatrix} 1 \\ i \end{pmatrix}, \quad \mathbf{E}_{\text{circ},L} = \frac{1}{\sqrt{2}} \begin{pmatrix} 1 \\ -i \end{pmatrix}, \quad (2.36)$$

which are precisely the (complex) field components resulting from the parameterization of the polarization ellipse (2.32).

The norm is, furthermore, motivated by the fact that \mathbf{E} is usually taken as an input field vector interacting with a polarizing medium. Such is the case for anisotropic materials with tensorial material parameters. Generally, this would entail solving the wave equation (2.15) with a permittivity *tensor*. Nevertheless, if we assume a plane wave emerging from an anisotropic, polarizing medium the Cartesian field components will, to some degree, mingle,

$$\mathbf{E} = \begin{pmatrix} T_{xx}T_{x,0} + T_{xy}T_{y,0} \\ T_{yx}T_{x,0} + T_{yy}T_{y,0} \end{pmatrix} = \begin{pmatrix} T_{xx} & T_{xy} \\ T_{yx} & T_{yy} \end{pmatrix} \begin{pmatrix} T_{x,0} \\ T_{y,0} \end{pmatrix} = \hat{T}\mathbf{E}_0, \quad (2.37)$$

where \mathbf{E}_0 is the input Jones vector. The 2×2 matrix \hat{T} is called the Jones matrix and its complex coefficients T_{ij} , with $i, j = x, y$ describe the coupling between the Cartesian components.⁶ For instance, the contributing factor of $T_{y,0}$ to the new T_x is given by T_{xy} . This we call *cross-polarization*. The coupling in the same coordinate T_{xx} we call *co-polarization*.

To give two examples, the Jones matrix of a linear y-polarizer and a circular polarizer read

$$\hat{T}_{\text{lin},y} = \begin{pmatrix} 0 & 0 \\ 0 & 1 \end{pmatrix}, \quad \text{and} \quad \hat{T}_{\text{circ},L} = \begin{pmatrix} 1 & 1 \\ i & -i \end{pmatrix}. \quad (2.38)$$

The latter transforms x- or y-polarized light into right- and left-handed circularly polarized light [200]. Generally speaking, a Jones matrix describes the effect of transmission through a polarizing medium and can, therefore, be called a transmission matrix, which will be common place throughout this thesis. Note that from here on we will always assume linearly polarized light to be impinging in a medium.

We can discern polarization *symmetry* of a material by looking at it from positive and negative z -direction, which we call *front* and *back* and the light incident from one of these sides *forward* or *backward* propagating, respectively. Taking the complex norm of \mathbf{E} in forward direction and subtracting it from its backward counterpart leads to

$$\Delta_x = |T_{xx}^f|^2 + |T_{xy}^f|^2 - |T_{xx}^b|^2 - |T_{xy}^b|^2, \quad (2.39)$$

where superscripts f and b denote forward and backward direction. Since optical materials

⁶In this work all quantities with hat denote 2×2 matrices.

are usually reciprocal [201], the forward and backward co-polarization Jones matrix coefficients have to be identical. Thus, (2.39) reduces to [200]

$$\Delta_x = |T_{xy}^f|^2 - |T_{xy}^b|^2 = |T_{xy}^f|^2 - |T_{yx}^f|^2. \quad (2.40)$$

The quantity $\Delta_x = \Delta_y$ is called *asymmetric transmission* [89]. A non-zero Δ_x means there is an unequal transfer between x- and y-polarization that hints at a distortion from a linear polarization ellipse to elliptical or circular states. As we mentioned before, this is an indicator for chirality. Therefore, an anisotropic material described by such a Jones matrix must have, at least partially, a chiral asymmetry [89, 146].

To characterize *how* the state of polarization changes after propagation through the medium we can analyze the shape of the polarization ellipse via its ellipticity ϵ . For incident x -polarization (analogously for y -polarization) ϵ_x is defined as the ratio of the major and minor half axis of the polarization ellipse produced by multiplication with the Jones matrix,

$$\epsilon_x = \frac{2|T_{xx}^f||T_{yx}^f|}{|T_{xx}^f|^2 + |T_{yx}^f|^2} \sin \delta_x, \quad (2.41)$$

where $\delta_x = \arg(T_{xx}) - \arg(T_{yx})$ is the phase difference between the elements of the outgoing field. If ϵ is equal to ± 1 we have circular polarization and if it goes to 0 we get linear polarization.

2.4 Elements of the Fourier modal method

Thus far, we have derived plane waves in a continuously homogeneous medium and established boundary conditions at an interface to a different homogeneous medium. Now, we confront the case of a distribution of discontinuities. This could mean a multilayered system with a series of consecutive interfaces [152, 202, 203]. Moreover, what if an interface itself is discontinuous in the transversal plane? Facing these questions is paramount if we wish to successfully simulate the optical properties of *structured* media, such as nano-scale metasurfaces [204–206]. To limit the range of possibilities, we will concentrate on transversely periodic structures of limited height, where the periodically repeating discontinuities are themselves homogeneous materials. Our task is to describe the interaction of an incident plane wave with a periodically structured interface and derive the resulting reflected and transmitted fields. Such periodic, computational problems are ideally solved with the well established Fourier modal method (FMM) [182, 207–211, 211–217].

The theoretical foundation of the FMM is essentially based on the works by EERO NOPONEN and JARI TURUNEN [218] and LIFENG LI [182, 207–210]. To attempt a full derivation of the method would require a chapter in its own right. A comprehensive description of the

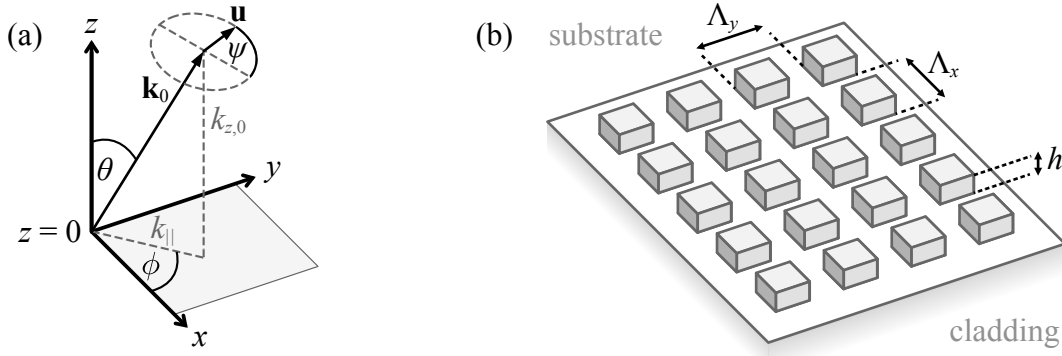


Figure 2.2: (a) Coordinate system of the FMM defining the azimuthal angle θ , polar angle ϕ , and polarization angle ψ of the incident field vector \mathbf{k}_0 , with $k_{\parallel} = \sqrt{k_{x,0}^2 + k_{y,0}^2}$. (b) Sketch of a periodic layer with periods Λ_x and Λ_y and height h .

FMM can be found in the book *Fourier Modal Method and Its Applications in Computational Nanophotonics* by KIM, PARK, and LEE [219]. Here, we are going to introduce only the essential ideas and equations necessary to understand the simulations presented in later chapters.

2.4.1 Fourier modal expansion

The FMM transforms the differential problem of Maxwell's equations to an eigenvalue problem and applies modal expansions to all fields involved. Previously, we restricted the plane of incidence for convenience to the x-z-plane. Now, the plane of incidence and the direction of propagation are variable, while assuming a linear polarization basis. Then, the field vector of an incident electric field is written [218]

$$\mathbf{E}_{\text{in}}(\mathbf{r}) = \mathbf{u}e^{i\mathbf{k}_0\mathbf{r}}, \quad \text{with} \quad \mathbf{k}_0 = k_{x,0}\mathbf{e}_x + k_{y,0}\mathbf{e}_y + k_{z,0}\mathbf{e}_z. \quad (2.42)$$

The k -vector components $k_{x,0} = n_1k_0 \sin \theta \cos \phi$, $k_{y,0} = n_1k_0 \sin \theta \sin \phi$, and $k_{z,0} = n_1k_0 \cos \theta$ are projections from spherical coordinates onto the Cartesian axes, depending on the azimuthal angle of incidence θ and the polar angle ϕ . Here, $k_0 = 2\pi/\lambda$ is the vacuum propagation constant. The unit amplitude vector \mathbf{u} also depends on the polarization angle ψ , as shown in fig. 2.2a). Involving all three angles, \mathbf{u} reads as

$$\mathbf{u} = (\cos \psi \cos \theta \cos \phi - \sin \psi \sin \phi)\mathbf{e}_x + (\cos \psi \cos \theta \sin \phi + \sin \psi \cos \phi)\mathbf{e}_y - \cos \psi \sin \theta \mathbf{e}_z. \quad (2.43)$$

Assuming periodic discontinuities in the x-y-plane at $z = 0$ and with a z-height h (fig. 2.2.b), the fields in the substrate and the cladding can be expanded in a Rayleigh series [220], i.e. a

plane wave expansion [218],

$$\mathbf{E}_T(\mathbf{r}) = \sum_{m,n} \mathcal{E}_T^{mn} \exp(i\mathbf{k}_T^{mn}(\mathbf{r} - h\mathbf{e}_z)), \quad (2.44a)$$

$$\mathbf{E}_R(\mathbf{r}) = \sum_{m,n} \mathcal{E}_R^{mn} \exp(i\mathbf{k}_R^{mn}\mathbf{r}), \quad (2.44b)$$

where \mathcal{E}_T^{mn} and \mathcal{E}_R^{mn} are the complex vectorial transmission and reflection amplitudes of each order m, n . Similarly, \mathbf{k}_T^{mn} and \mathbf{k}_R^{mn} are their respective k -vectors, giving the direction of each constituent plane wave,

$$\mathbf{k}_T^{mn} = k_{x,m}\mathbf{e}_x + k_{y,n}\mathbf{e}_y + k_{T,mn}\mathbf{e}_z, \quad (2.45a)$$

$$\mathbf{k}_R^{mn} = k_{x,m}\mathbf{e}_x + k_{y,n}\mathbf{e}_y - k_{R,mn}\mathbf{e}_z, \quad (2.45b)$$

with $k_{x,m} = k_{x,0} + 2\pi m/\Lambda_x$ and $k_{y,n} = k_{y,0} + 2\pi n/\Lambda_y$. Λ_x and Λ_y are the grating periods in x - and y -direction. As the periodic layer is invariant in z -direction, the z -components of the k -vector can be written

$$k_{T,mn} = \sqrt{(n_1k)^2 - (k_{x,m})^2 - (k_{y,n})^2} \quad (2.46a)$$

$$k_{R,mn} = \sqrt{(n_2k)^2 - (k_{x,m})^2 - (k_{y,n})^2}. \quad (2.46b)$$

For now, we assume the square roots to be real.⁷ Together eqs. (2.42) – (2.46) fully describe the electric field in the half-spaces surrounding the structured layer. The magnetic field follows from Maxwell's equations.

Inside the periodic layer the fields are pseudo-periodic Bloch vectors [221].⁸ Because of that we can expand the fields in the doubly periodic medium in pseudo Fourier series [80, 218, 222],

$$\mathbf{E}(\mathbf{r}) = \sum_{m,n} \mathcal{E}_{mn} \exp(i(k_{x,m}x + k_{y,n}y + \gamma_{mn}z)), \quad (2.47)$$

where γ_{mn} is the propagation constant inside the periodic layer. Furthermore, the permittivity $\varepsilon(x, y)$ is now a periodic function of the transversal coordinates. It can be written as the Fourier series

$$\varepsilon(x, y) = \varepsilon_0 \sum_{m,n} \varepsilon_{mn} \exp\left(i2\pi\left(\frac{m}{\Lambda_x}x + \frac{n}{\Lambda_y}y\right)\right), \quad (2.48)$$

with the Fourier coefficients of the permittivity ε_{mn} . By applying Maxwell's equations to the \mathbf{E} field to get the \mathbf{H} field we introduce coefficients of the inverse permittivity and, therefore,

⁷Later, in chapter 3 we will look at the emergence of evanescent modes when the square root becomes imaginary.

⁸The corresponding Bloch theorem will be applied and explained in greater detail in sec. 2.1.1.

another Fourier expansion [218]. Here, we mathematical caution is in order. An ad hoc insertion of the Fourier expanded ε and its inverse into Maxwell's equations will result in computational issues [208]. As LALANNE showed numerically [211] and LI proved mathematically with his Fourier factorization rule [208, 209], the problem can be circumvented by writing the *inverse* coefficients of a Toeplitz matrix of the Fourier coefficients ε_{mn} .⁹

If we reduce, for a moment, the problem to a one-dimensional grating, the coupled field equations of the Bloch coefficients in the Fourier domain take the form [208, 218]

$$\omega\mu_0\gamma H_{y,n} = -k_0^2 \sum_{m=-M}^M \left[\left[\frac{1}{\varepsilon} \right]_{mn} \right]^{-1} E_{x,m} \quad (2.49a)$$

$$\omega\varepsilon_0\gamma E_{x,n} = k_0^2 H_{y,n} - k_{x,n} \sum_{m=-M}^M [\varepsilon]_{mn}^{-1} k_{x,m} H_{y,m}, \quad (2.49b)$$

with $E_{x,n}$ denoting the y-component of \mathcal{E}_n from eq. (2.47) in the one-dimensional case and analogously $H_{y,n}$. Here, we used LI's notation denoting a Toeplitz matrix coefficient $[.]$ [208]. For numerical calculation the series have to be truncated at some order M , which also determines the truncation of the Rayleigh expansion (2.44). Including the full two-dimensional periodicity, we get the full double sums as in eq. (2.47) and a second truncation order N . Lastly, we must also obey the boundary conditions at the interfaces to substrate and cladding [218]. This relates the Rayleigh transmission and reflection coefficients with the Bloch coefficients of the internal fields. Together, they present an algebraic eigenvalue problem whose solution gives us the interaction of plane waves with a periodically structured interface [219]. This is the core concept of the FMM.

Its precision depends on the number of Fourier orders M, N taken into account. This affects the accuracy of the Fourier expansion of the permittivity, given as a distribution in a unit cell of size $\Lambda_x \times \Lambda_y$. Once the eigenvalue problem is solved the total energy flux through the structured layer is the sum of all modal energy fluxes in forward and backward direction.

2.4.2 Scattering matrix formalism

Once the eigenvalue problem is solved and the fields are obtained it would be practical to express the interface problem in a compact mathematical form. Whereas we used Fresnel equations to express the transmission and reflection at the interface, our task is now to connect the multitude of modes of the periodic layer with adjacent layers. Similar to the idea of Jones matrices we can map the fields from both sides of the periodic layer using a scattering matrix (S-matrix) [182]. We distinguish between *forward* and *backward* propagating fields, \mathbf{E}^f and \mathbf{E}^b ,

⁹A Toeplitz matrix has equal entries along each of its diagonals. If A is a Toeplitz matrix, then its coefficients are $A_{i,j} = A_{i+1,j+1} = a_{i-j}$, where a_j are its unique entries.

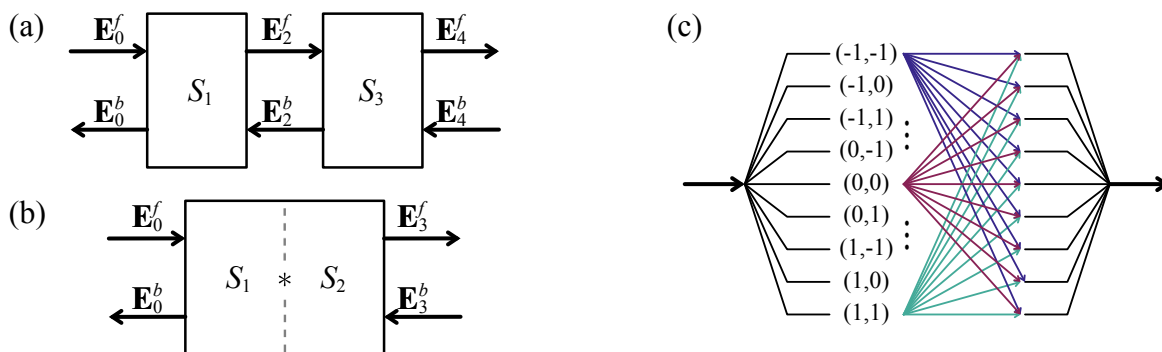


Figure 2.3: (a) Illustration of the four-port structure of the S-matrix. The output port in forward direction of S_1 produces the block vector in layer 2 \mathbf{E}_2^f which is incident on the forward input port of S_3 . The opposite in backward direction: the output of S_3 is input to S_1 . (b) Two S-matrices connected as a single layer by the star product. (c) Graphical representation of mapping of input diffraction orders onto output orders. The numbers in parentheses denote coefficient indices (m, n) for $N = M = 1$ orders.

in positive and negative z -direction, respectively. If S_p is the S-matrix of the p th layer in some multi-layered system, the fields in the adjacent layer are connected by

$$\begin{bmatrix} \mathbf{E}_{p+1}^f \\ \mathbf{E}_{p+1}^b \end{bmatrix} = S_p \begin{bmatrix} \mathbf{E}_{p-1}^f \\ \mathbf{E}_{p-1}^b \end{bmatrix} = \begin{bmatrix} T_p^f & R_p^b \\ R_p^f & T_p^b \end{bmatrix} \begin{bmatrix} \mathbf{E}_{p-1}^f \\ \mathbf{E}_{p-1}^b \end{bmatrix}. \quad (2.50)$$

There are several things to unwrap. First, the expanded fields are written as block vectors, denoted by square brackets $[\cdot]$, distinguishing forward and backward propagating fields \mathbf{E}^f and \mathbf{E}^b . On the left-hand side of the equation are the output fields and on the right-hand side the input fields (fig. 2.3.a). Notice that the layer indices reflect the respective layer of incidence. Accordingly, the S-matrix S is a 2×2 block matrix constituting reflection and transmission matrices for each direction. The block vectors \mathbf{E}_{p-1}^f and \mathbf{E}_{p+1}^b each include $2(2M+1) \cdot 2(2N+1)$ Rayleigh coefficients, indicating an equal number of diffraction orders (fig. 2.3.c).¹⁰ The factor 2 represents the x- and y-polarization in a linear polarization basis. Correspondingly the sub-matrices of the S-matrix are of size $2(2M+1)(2N+1) \times 2(2M+1)(2N+1)$. So, the total number of elements of a 2×2 S-matrix is $16(2M+1)^2(2N+1)^2$. For example, for $M = N = 11$ orders we get approximately $4.5 \cdot 10^6$ complex coefficients, requiring about 72 MB of computer memory. This means that FMM simulations can require large amounts of memory.

Looking at the transmission and reflection matrices it becomes apparent that they encode polarization in similar fashion as Jones matrices, albeit including higher orders. Indeed, each sub-matrix reverts to a 2×2 Jones matrix at zeroth order. More abstractly speaking, the S-matrix represents a four-terminal network [182] with each block-element symbolizing a scat-

¹⁰Whether a diffraction order is propagating or evanescent depends on the propagation constant $k_{z,mn}$. This is discussed in detail in sec. 3.3.1

tering port (fig. 2.3.a). Here, each port also handles the coupling between different orders (fig. 2.3.c). This is a very practical concept because we can use these ports to connect multiple layers to get their common response as a whole (fig. 2.3.b).

Furthermore, we can stack any number of S-matrices using a binary operation $*$ called the star product [182]. Let S_1 and S_2 be arbitrary S-matrices of equal Fourier order and with sub-matrices a_{ij} and b_{ij} . Then, the combined S-matrix results from the star product

$$\begin{aligned} S_1 * S_2 &= \begin{pmatrix} a_{11} & a_{12} \\ a_{21} & a_{22} \end{pmatrix} * \begin{pmatrix} b_{11} & b_{12} \\ b_{21} & b_{22} \end{pmatrix} \\ &= \begin{pmatrix} b_{11} (\mathbb{I} - a_{12} b_{21})^{-1} a_{11} & b_{12} + b_{11} a_{12} (\mathbb{I} - b_{21} a_{12})^{-1} b_{22} \\ a_{21} + a_{22} b_{21} (\mathbb{I} - a_{12} b_{21})^{-1} a_{11} & a_{22} (\mathbb{I} - b_{21} a_{12})^{-1} b_{22} \end{pmatrix}, \end{aligned} \quad (2.51)$$

where \mathbb{I} is an appropriately sized identity matrix. This can be applied to accommodate a full system of N layers, condensed to a single S-matrix,

$$S = S_1 * S_2 * S_3 * \cdots * S_{k-1} * S_k * S_{k+1} * \cdots * S_N. \quad (2.52)$$

Furthermore, it can be shown that the star product is associative [182],

$$S_1 * (S_2 * S_3) = (S_1 * S_2) * S_3, \quad (2.53)$$

which is of great utility for numerical applications and is exploited in chapter 4.

As a final remark, the star product was formally introduced by RAYMOND REDHEFFER to show a linear fractional transformation of a quadrupel of linear operators [223]. The thus called *Redheffer* star product is a map of two quadrupels onto a single quadrupel. In that regard, the S-matrix formalism treats transmission and reflection matrices as operators on incident fields, mapping complex coefficients of diffraction orders, including their polarization symmetry. The latter will be of great importance for the semi-analytic analysis presented in chapters 4–6.

3 | Fundamental mode approximation (FMA)

In this chapter we will derive the theoretical foundation which is at the core of this thesis. In order to minimize the necessity for rigorous numerical simulations it is essential to correctly simplify or refine physical models of metasurfaces. For that purpose, this chapter introduces the fundamental mode approximation (FMA) - a reduction of a metasurface's far-field interaction and next-neighbor-coupling to only fundamental modes. We will properly define the meaning of *fundamental* in the context of Bloch modes in periodic metasurfaces. This is a prerequisite because the physical interpretation of the FMA ties into the important question of homogeneity in describing metamaterials, generally.

3.1 Principles of local field interaction

A first step in the direction of introducing effective parameters for periodic metamaterials is a limit on the size of the inclusions (independent on their geometry). According to Maxwell-Garnett theory [224], if a represents the size of the unit cell or the diameter of a particle then the incident wavelength λ should be much larger, so $a \ll \lambda$. Additionally, the average volume fraction of the inclusions has to be small with respect to the enclosing volume [9]. However, in metamaterials structure sizes are usually in the order of the wavelength [36, 225], although still smaller, typically $a/\lambda < 0.5$.

It is especially important to note that λ inside the medium has an effective length $\lambda_{\text{eff}} = \lambda/n$, where, generally, the refractive index n is dispersive (see sec. 2.1.2). Furthermore, for resonant frequencies the introduced additional phase shift changes the optical path length [35, 155]. Roughly speaking, this can be incorporated into an effective (dispersive) refractive index $n_{\text{eff}}(\lambda)$, and thus $\lambda_{\text{eff}} = \lambda/n_{\text{eff}}(\lambda)$. This leads to an adapted size limit of

$$\frac{an_{\text{eff}}(\lambda)}{\lambda} < 0.5. \quad (3.1)$$

Relation 3.1 is a rough estimate that ignores complex field interactions with neighboring structures and relies on the existence of effective parameters. Yet, simple mixing theories [9, 226] are not suitable at this point since they are only valid for size ratios up to $a/\lambda = 0.01$ [226].

We have to identify under which conditions effective parameters can have any physical

Condition	Definition
I. Passivity	A harmonic time dependence $e^{-i\omega t}$ implies $\text{Im}(\varepsilon_{\text{loc}}) > 0$ and $\text{Im}(\mu_{\text{loc}}) > 0$.
II. Causality	$\partial(\omega\varepsilon_{\text{loc}})/\partial\omega > 1$, $\partial(\omega\mu_{\text{loc}})/\partial\omega > 1$ if losses are negligible and $\partial \text{Re}(\varepsilon_{\text{loc}})/\partial\omega > 0$, $\partial \text{Re}(\mu_{\text{loc}})/\partial\omega > 0$ outside of the resonant band of inclusions.
III. Absence of radiation losses	The medium is in thermodynamic equilibrium in the absence of incident fields [195] and scattering losses are small or non-existent [5, 61].
IV. Independence from wave propagation direction	Material parameters are independent from the angle of incidence for a given frequency.

Table 3.1: Conditions for local material parameters [80, 157]

meaning and how else to describe the optical properties of a metamaterial [10, 157]. Fundamentally, the question of effective material parameters boils down to that of *locality* [195]. Local material parameters ε_{loc} and μ_{loc} relate the field vectors \mathbf{D} and \mathbf{B} with the *averaged* macroscopic fields $\langle \mathbf{E} \rangle$ and $\langle \mathbf{H} \rangle$ [80], such that

$$\mathbf{P} = \mathbf{D} - \varepsilon_0 \langle \mathbf{E} \rangle = \varepsilon_0(\varepsilon_{\text{loc}} - 1) \langle \mathbf{E} \rangle \quad (3.2)$$

$$\mathbf{M} = \mathbf{B} - \mu_0 \langle \mathbf{H} \rangle = \mu_0(\mu_{\text{loc}} - 1) \langle \mathbf{H} \rangle, \quad (3.3)$$

defining the bulk electric and material polarizabilities \mathbf{P} and \mathbf{M} . As per standard Maxwell theory the averaged macroscopic fields at the center, \mathbf{r} , of a unit cell are calculated by integrating over the unit cell volume V ,

$$\langle \mathbf{E} \rangle(\mathbf{r}) := \frac{1}{V} \int_V \mathbf{E}(\mathbf{r} + \mathbf{r}') d^3 \mathbf{r}' \quad (3.4)$$

$$\langle \mathbf{H} \rangle(\mathbf{r}) := \frac{1}{V} \int_V \mathbf{H}(\mathbf{r} + \mathbf{r}') d^3 \mathbf{r}'. \quad (3.5)$$

This presents us with a very simple definition of locality in Maxwell theory: the *relationship* of the fields \mathbf{D} , \mathbf{B} and \mathbf{E} , \mathbf{H} can be expressed *at any point* \mathbf{r} of a lattice [195]. However, there are strict physical conditions for material parameters ε_{loc} and μ_{loc} to be considered local.

As summarized in table 3.1, local parameters have to be passive, meaning there is no optical activity [157, 195]. Furthermore, the condition of causality implies that their response is retarded. In addition, radiation losses from non-equilibrium thermodynamics and scattering cross-sections need to be negligible. These would imply field interactions not purely determined

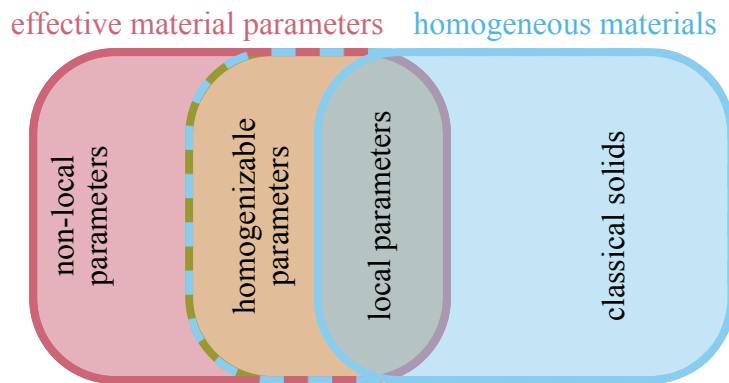


Figure 3.1: Conceptual map of physical interpretations of optical material parameters.

by the average field of a unit cell and thus be non-local. Lastly, material parameters only have physical meaning if they are independent on the direction of propagation and are invariant with respect to the angle of incidence.

From this we can deduce that there are two general classes of effective parameters: either local or non-local, fig. 3.1. While the former implies a genuinely homogeneous medium, the latter has to be interpreted carefully. The regime of non-local parameters can be divided into those which are homogenizable via suitable retrieval models and those that have no meaningful interpretation at all [57]. Each subset of effective parameters depends on the frequency regime (see table 3.1). A metamaterial can transition between regimes across different frequency intervals [6, 79, 227]. The idea of transitioning between conceptual regimes will be taken up again in sec. 3.4.

At its core, the entire discussion around the meaning of optical material parameters aims at a concise description of wave propagation in structured media. If a metamaterial can be homogenized, wave propagation through it follows the classical theory of electrodynamics in homogeneous media [1, 195]. If, however, a metamaterial would be completely non-local, rigorous numerical simulations are the only way of determining its optical behavior [6, 227].

Analytic solutions allow us to grasp the metamaterial intuitively in terms of refractive indices and concepts such as Snell’s law, Fresnel formulas or Jones calculus. In contrast, rigorous simulations always require detailed consideration of field-field and field-matter interactions in order to understand their outcome. Both approaches are of course perfectly valid when it comes to determining optical behavior. While numerical simulations are always possible¹, the necessity for effective parameters comes into play when an application demands specific macroscopic properties. Beyond that, homogeneity and locality are physical attributes that can be employed as conceptual foundations to derive and simplify theoretical methods.

In the following, we will describe the propagation of waves in periodic metamaterials and

¹Within their mathematical bounds and physical applicability.

show how the ideas discussed above lead to a simplified understanding of such metamaterials.

3.2 Wave propagation in periodic metamaterials

Assuming periodicity in all three spatial dimensions we can borrow from the theory of photonic crystals [159–162] and describe the propagation of light inside the metamaterial using a Bloch mode formalism [80, 222]. Let us take a moment and introduce the concept of Bloch modes, which we only briefly mentioned in the introduction to the FMM (sec. 2.4).

In a periodic medium the inhomogeneous permittivity (and similarly the permeability) is a periodic function with respect to the lattice periodicity $\mathbf{a} = (\Lambda_x, \Lambda_y, \Lambda_z)^T$

$$\varepsilon(\mathbf{r}, \omega) = \varepsilon(\mathbf{r} + D_{\mathbf{n}}\mathbf{a}, \omega), \quad (3.6)$$

where $D_{\mathbf{n}}$ is a diagonal matrix corresponding to a vector of integers $\mathbf{n} = (n_x, n_y, n_z)^T$. According to the Bloch theorem [221] the electromagnetic fields $\mathbf{E}(\mathbf{r})$ and $\mathbf{H}(\mathbf{r})$ become quasi-periodic functions that are separated into a periodic Bloch mode $\mathcal{E}(\mathbf{r})$ and $\mathcal{H}(\mathbf{r})$ and a phase term describing spatial evolution², yielding

$$\mathbf{E}(\mathbf{r}) = e^{i\mathbf{k}\cdot\mathbf{r}}\mathcal{E}(\mathbf{r}), \quad \text{with} \quad \mathcal{E}(\mathbf{r}) = \mathcal{E}(\mathbf{r} + D_{\mathbf{n}}\mathbf{a}), \quad (3.7)$$

$$\mathbf{H}(\mathbf{r}) = e^{i\mathbf{k}\cdot\mathbf{r}}\mathcal{H}(\mathbf{r}), \quad \text{with} \quad \mathcal{H}(\mathbf{r}) = \mathcal{H}(\mathbf{r} + D_{\mathbf{n}}\mathbf{a}). \quad (3.8)$$

Inserted in Maxwell's equations, Bloch-wave propagation (of the $\mathbf{H}(\mathbf{r})$ -field) is then described by the eigenvalue equation

$$\mathbf{k} \times \left[\frac{1}{\varepsilon(\mathbf{r})} \mathbf{k} \times \mathcal{H}(\mathbf{r}) \right] - \frac{\omega^2}{c^2} \mathcal{H}(\mathbf{r}) = 0. \quad (3.9)$$

Together with the longitudinal Bloch k -vector component

$$k_z(k_x, k_y, \omega) = k_z(\Omega), \quad \text{with} \quad \Omega := \{k_x, k_y, \omega\}, \quad (3.10)$$

we can describe the electric field inside the metamaterial as a superposition of Bloch modes,

²Reminder: throughout this thesis we assume monochromatic fields with a time dependence $\exp(-i\omega t)$.

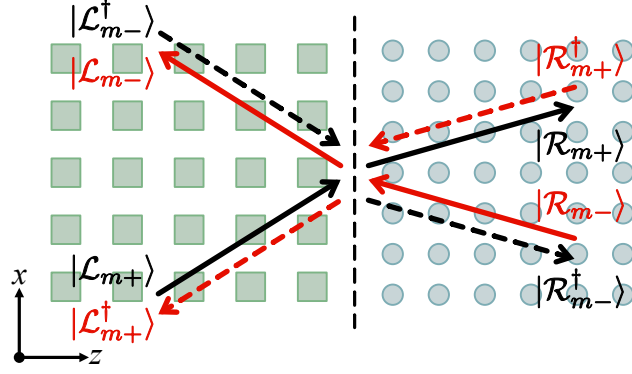


Figure 3.2: Illustration of an interface between two periodic metamaterials. Black arrows represent Bloch modes with energy flux in positive z -direction and red ones in negative z -direction. Dashed arrows indicate adjoint fields (marked by the symbol \dagger). Figure adapted from fig. 1 in [156].

where

$$\begin{aligned} \mathbf{E}(\mathbf{r}; \Omega) &= \sum_p \mathcal{E}_p(\mathbf{r}; \Omega) e^{ik_{p,z}(\Omega)z} \\ &= \sum_p \left[\sum_{l,m,n} \mathcal{E}_p^{l,m,n}(\mathbf{r}; \Omega) \exp \left\{ i \left[\left(k_x + \frac{2\pi}{\Lambda_x} l \right) x + \left(k_y + \frac{2\pi}{\Lambda_y} m \right) y + \left(\frac{2\pi}{\Lambda_z} n \right) z \right] \right\} \right] e^{ik_{p,z}(\Omega)z}, \end{aligned} \quad (3.11)$$

where $k_{p,z}$ is the longitudinal wave vector of the Bloch mode p . The triple sum in the second part of the equations constitutes a plane wave expansion of each mode.³ Hence, light propagation in periodic media, including metamaterials, can be described using a generally infinite set of Bloch modes [229–231].

Naturally, one might ask how we could describe the interface between two metamaterials. Suppose we have two (semi-infinite) periodic metamaterials left and right of an interface (fig. 3.2). Following the notation style introduced by PAUL et al. in [156], we can describe the interaction at the interface with two sets of modes on each side of the interface.

Using Dirac notation, we define a Bloch vector $|\mathcal{B}_p\rangle$ that includes all tangential field components, i.e. $|\mathcal{B}_p\rangle := (E_{p,x}, E_{p,y}, H_{p,x}, H_{p,y})^T$. Accordingly, we define $|\mathcal{L}_{m+}\rangle$ and $|\mathcal{L}_{m-}\rangle$ as the two sets of modes of the *left* metamaterial, propagating in positive (+) and negative (–) z -direction. Similarly, the *right* metamaterial is populated by the modes $|\mathcal{R}_{m+}\rangle$ and $|\mathcal{R}_{m-}\rangle$. For each set of modes there is an adjoint set, ($|\mathcal{L}_{m+}^\dagger\rangle$, $|\mathcal{L}_{m-}^\dagger\rangle$ and $|\mathcal{R}_{m+}^\dagger\rangle$, $|\mathcal{R}_{m-}^\dagger\rangle$), for which the tangential wave vector components $\mathbf{k}_\parallel = (k_x, k_y)^T$ are reversed ($-\mathbf{k}_\parallel$) [232]. Additionally, the energy flow of the adjoint fields is reversed (see dashed arrows in fig. 3.2). Whereas $|\mathcal{L}_{m+}\rangle$

³It is no coincidence that this expansion is analogous to the mathematical approach used to describe fields of a modulated region in the FMM. Compare, for instance, to eq. (19) in [228].

fulfills $\text{Im}(k_{i,z}) > 0$ the energy of the adjoint fields $|\mathcal{L}_{m+}^\dagger\rangle$ flows in negative z-direction⁴.

Each set of Bloch modes in a metamaterial fulfills orthogonality relations [156] based on the generalized inner product [233]

$$\langle \mathcal{B}_m^\dagger | \mathcal{B}_n \rangle := \int \int_{\text{cross section}} (\mathbf{E}_n \times \mathbf{E}_m^\dagger - \mathbf{E}_m^\dagger \times \mathbf{E}_n) \mathbf{e}_z \, dx \, dy, \quad (3.12)$$

while integrating over the cross section of a unit cell. Because we propagate along the z-axis we consider tangential cross sections. Hence, the integrand solely depends on the tangential field components. With this, the orthogonality relations for the Bloch modes of the left medium read as

$$\langle \mathcal{L}_{m+}^\dagger | \mathcal{L}_{n+} \rangle = L_m^+ \delta_{mn}, \quad (3.13a)$$

$$\langle \mathcal{L}_{m-}^\dagger | \mathcal{L}_{n-} \rangle = -L_m^- \delta_{mn}, \quad (3.13b)$$

$$\langle \mathcal{L}_{m+}^\dagger | \mathcal{L}_{n-} \rangle = 0, \quad (3.13c)$$

$$\langle \mathcal{L}_{m-}^\dagger | \mathcal{L}_{n+} \rangle = 0, \quad (3.13d)$$

and analogously for the right medium. Here, δ_{mn} is the Kronecker symbol and L_m^\pm are the normalization constants of the left side modes. Similarly, the right side modes will have the normalization constants R_m^\pm . With these we have the orthogonality relations within each set of Bloch modes. At the interface we have to obey boundary conditions in order to apply the orthogonality relations (3.13a) - (3.13d).

Assuming light propagation in *positive* z-direction, light impinges from the left to the right at the interface. Intuitively, both reflected ($|\mathcal{L}_{m-}\rangle$) and transmitted ($|\mathcal{R}_{m+}\rangle$) modes will be excited. Using the continuity of the tangential field components at the interface we can find a relation similar to the energy conservation introduced in sec. 2.2,

$$\sum_m I_m |\mathcal{L}_{m+}\rangle + \sum_m R_m |\mathcal{L}_{m-}\rangle = \sum_m T_m |\mathcal{R}_{m+}\rangle. \quad (3.14)$$

In conjunction with the decomposition in the FMM (sec. 2.4), T_n and R_n are transmission and reflection coefficients, with I_n representing amplitude and phase of an impinging field. We can then calculate the transmission and reflection coefficients by projecting $\langle \mathcal{R}_{n-}^\dagger |$ and $\langle \mathcal{L}_{n+}^\dagger |$ onto eq. 3.14. Furthermore applying orthogonality relations 3.13a through 3.13d creates two

⁴In an absorbing material.

separate equations [156],

$$\sum_m \langle \mathcal{R}_{n-}^\dagger | \mathcal{L}_{m+} \rangle I_m = - \sum_m \langle \mathcal{R}_{n-}^\dagger | \mathcal{L}_{m-} \rangle R_m, \quad (3.15)$$

$$\sum_m L_m^+ \delta_{mn} I_m = \sum_m \langle \mathcal{L}_{n+}^\dagger | \mathcal{R}_{m+} \rangle T_m. \quad (3.16)$$

Using the matrix coefficients

$$O_{nm} := \langle \mathcal{R}_{n-}^\dagger | \mathcal{L}_{m-} \rangle, \quad (3.17a)$$

$$P_{nm} := \langle \mathcal{R}_{n-}^\dagger | \mathcal{L}_{m+} \rangle, \quad (3.17b)$$

$$Q_{nm} := \langle \mathcal{L}_{n+}^\dagger | \mathcal{R}_{m+} \rangle, \quad (3.17c)$$

$$L_{nm} := L_n^+ \delta_{nm} \quad (3.17d)$$

we can rewrite eqs. 3.15 and 3.16 into matrix form and invert them to solve for the transmission and reflection coefficients of the Bloch modes,

$$\hat{\mathbf{O}}\mathbf{R} = \hat{\mathbf{P}}\mathbf{I} \implies \mathbf{R} = \hat{\mathbf{O}}^{-1}\hat{\mathbf{P}}\mathbf{I}, \quad (3.18)$$

$$\hat{\mathbf{Q}}\mathbf{T} = -\hat{\mathbf{L}}\mathbf{I} \implies \mathbf{T} = -\hat{\mathbf{Q}}^{-1}\hat{\mathbf{L}}\mathbf{I}. \quad (3.19)$$

The coupling matrices $\hat{\mathbf{O}}$, $\hat{\mathbf{P}}$, $\hat{\mathbf{Q}}$, and $\hat{\mathbf{L}}$ are populated by the respective elements 3.17a–3.17d. \mathbf{T} and \mathbf{R} are vectors of the transmission and reflection coefficients T_n and R_n , representing the interface interaction of the complete set of Bloch modes. Since we assume that an arbitrary field $|\mathcal{I}\rangle$ impinges from left to right, the coefficients I_m are given simply by projection with $\langle \mathcal{L}_{m+}^\dagger |$, resulting in $I_m = \langle \mathcal{L}_{m+}^\dagger | \mathcal{I} \rangle / L_m^+$.

If both media were identical, the matrix elements 3.17a–3.17d would simplify to eqs. 3.13a–3.13d. Consequently, for very similar metamaterials the Bloch modes at the interface will match to great extent. As a result the matrices $\hat{\mathbf{O}}$, $\hat{\mathbf{P}}$, and $\hat{\mathbf{Q}}$ will become sparse. With this, we can move towards formulating homogeneity conditions of these metamaterials.

If the metamaterials behaved like genuine homogeneous media, the coupling between modes at their interface would be Fresnel-like. Just determined by one reflected and one transmitted mode on the left and right. In the present case this can be achieved if only one of the impinging left-side modes dominates the interaction at the interface and, furthermore, only one Bloch mode of the right-side set is excited. Returning to eq. 3.11 we can sort the series with increasing imaginary part of the propagation constant $k_{p,z}(\Omega)$. Then, the 0th order mode with $\mathcal{E}_0(\mathbf{r}) \exp(ik_{0,z}(\Omega)z)$ will dominate if all higher orders ($p > 0$) decay at a faster rate or are only weakly excited. With respect to the projected left and right propagating modes 3.15 and 3.16

we can directly determine the 0th order reflection and transmission coefficients

$$R_0 = -\frac{\langle \mathcal{R}_{0-}^\dagger | \mathcal{L}_{0+} \rangle}{\langle \mathcal{R}_{0-}^\dagger | \mathcal{L}_{0-} \rangle}, \quad (3.20)$$

$$T_0 = \frac{\mathcal{L}_0^+}{\langle L_{0+}^\dagger | \mathcal{R}_{0+} \rangle}. \quad (3.21)$$

We will call the 0th order modes *fundamental modes*. Under the assumption that the off-diagonal elements of the (sparse) coupling matrices $\hat{\mathbf{O}}$, $\hat{\mathbf{P}}$, and $\hat{\mathbf{Q}}$ are negligible and that the amplitude of all higher orders (left or right) is sufficiently small while decaying faster,

$$|\langle \mathcal{B}_0^\dagger | \mathcal{B}_0 \rangle| \gg |\langle \mathcal{B}_{p>0}^\dagger | \mathcal{B}_{p>0} \rangle|, \quad (3.22)$$

R_0 and T_0 can sufficiently describe wave propagation. This defines the *fundamental mode approximation* (FMA).

3.3 Fundamental mode interaction between metasurfaces

3.3.1 Defining metasurfaces via fundamental modes

We now look at the case where the right-hand-side medium of fig. 3.2 is not a metamaterial but a homogeneous dielectric medium⁵. Assuming the fundamental Bloch mode, $\mathcal{E}_0 \exp(ik_{0,z}(\Omega)z)$, to be dominant in the periodic medium, we can write the transmitted field $\mathbf{E}_T \equiv \mathbf{E}^f$ in the adjacent homogeneous dielectric as a Rayleigh expansion [145, 220, 228],

$$\mathbf{E}_T(\mathbf{r}) = \sum_{l,m} \mathbf{t}^{lm} \exp \left\{ i \left[\frac{2\pi l}{\Lambda_x} x + \frac{2\pi m}{\Lambda_y} y \right] \right\} \exp(ik_z^{lm} z), \quad (3.23)$$

where \mathbf{t}^{lm} are the transmitted diffraction orders of the electric field. The propagation constant in the homogeneous medium k_z^{lm} is defined as

$$k_z^{lm} = \sqrt{k_0^2 n^2 - \left(\frac{2\pi l}{\Lambda_x} \right)^2 - \left(\frac{2\pi m}{\Lambda_y} \right)^2}, \quad (3.24)$$

with the refractive index n and the vacuum wavenumber k_0 . Within the FMA, the boundary conditions (3.14) simply relate the fundamental mode of the metamaterial with diffracted fields (3.23) in the adjacent medium. Vice versa, this also applies to the *excitation* of a fundamental mode when impinging onto the metamaterial.

⁵Infinitely extended in positive z-direction.

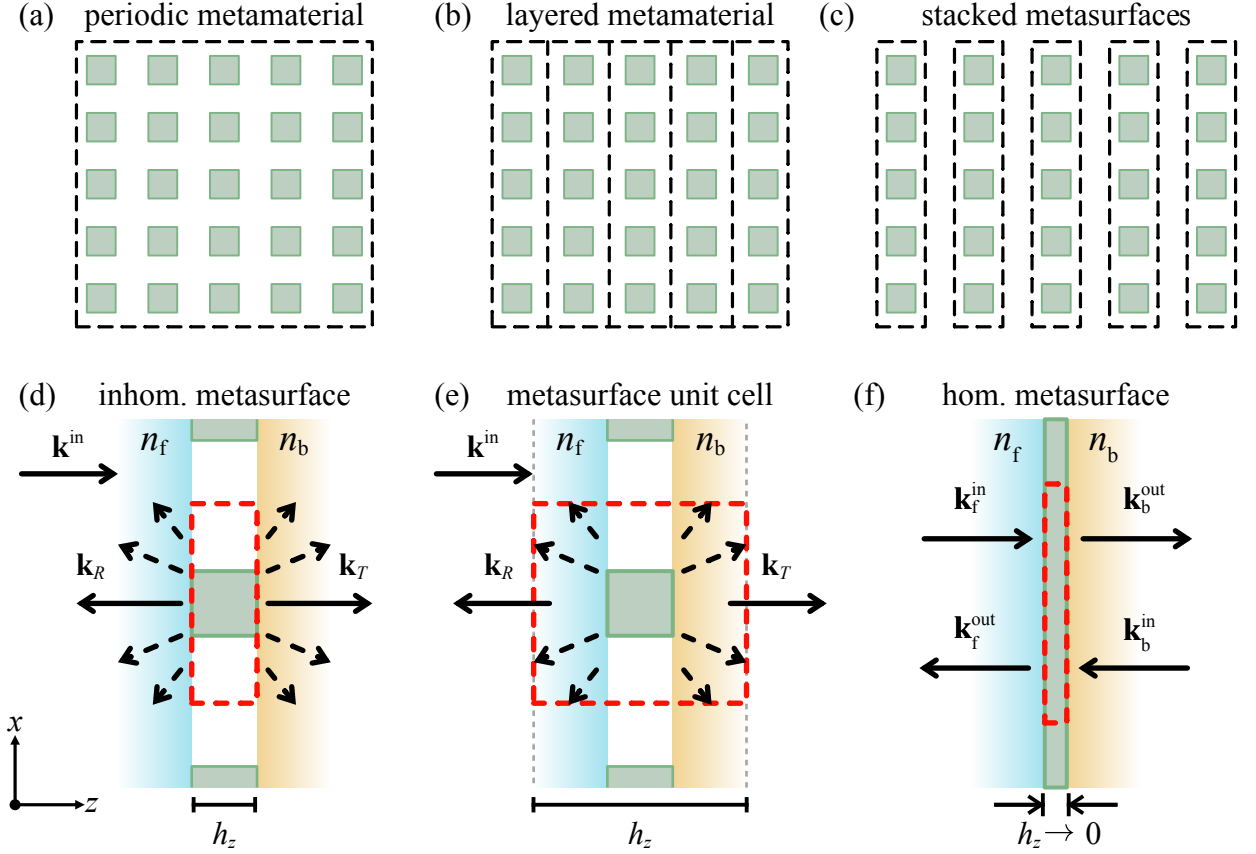


Figure 3.3: Conceptual transition from bulk metamaterial (a) to stacked metasurfaces (c). The intermediate step (b) considers the z -periodicity as a layered system of individual metamaterials with x - y -periodicity. To consider each layer as an individual metasurface, the inhomogeneity due to higher order modes (d) has to be contained in the metamaterial’s unit cell (e) by including spacer layers for sufficient decay of evanescent fields. A homogeneous metasurface emerges if the considered layer thickness h_z conceptually approaches 0, transforming the metasurface into a 4-port interface or gate of fundamental modes. Figures (d)–(f) adapted from fig. 1 in [145].

Here, we can start a conceptual transition from a bulk metamaterial to multiple layers of *stacked* metasurfaces. We can imagine a 3D-periodic metamaterial (fig. 3.3.a) to be comprised of repeating layers in propagation direction (fig. 3.3.b). If we interpret each layer as an individual metamaterial that is periodic only in the x - y plane and unchanging in z -direction, eq. (3.11) reduces to

$$\mathbf{E}(\mathbf{r}; \Omega) = \sum_p \left[\sum_{l,m} \mathcal{E}_p^{lm}(\mathbf{r}; \Omega) \exp \left\{ i \left[\left(k_x + \frac{2\pi}{\Lambda_x} l \right) x + \left(k_y + \frac{2\pi}{\Lambda_y} m \right) y \right] \right\} \right] e^{ik_{p,z}(\Omega)z}, \quad (3.25)$$

dropping the z -periodicity.⁶ Then the interaction between the fundamental mode with $p = 0$

⁶In principle $\Lambda_z \rightarrow \infty$.

and surrounding fields yields the excitation of both transmitted and reflected plane waves (fig. 3.3.d),

$$\begin{aligned}
& \sum_{l,m} \mathcal{E}_0^{lm}(\mathbf{r}; \Omega) \exp \left\{ i \left[\left(k_x + \frac{2\pi}{\Lambda_x} l \right) x + \left(k_y + \frac{2\pi}{\Lambda_y} m \right) y \right] \right\} e^{ik_{0,z}(\Omega)z} \\
& + \sum_{l,m} \mathbf{r}^{lm} \exp \left\{ i \left[\frac{2\pi l}{\Lambda_x} x + \frac{2\pi m}{\Lambda_y} y \right] \right\} \exp(-ik_z^{lm} z) \\
& = \sum_{l,m} \mathbf{t}^{lm} \exp \left\{ i \left[\frac{2\pi l}{\Lambda_x} x + \frac{2\pi m}{\Lambda_y} y \right] \right\} \exp(ik_z^{lm} z), \tag{3.26}
\end{aligned}$$

where \mathbf{r}^{lm} are the reflected diffraction orders of the electric field. The first sum of the equation above represents the incident field in a metamaterial layer. This is equivalent to the structure of eq. (3.14) if we demand $p = m = 0$,

$$\frac{\langle \mathcal{L}_{0+}^\dagger | \mathcal{I} \rangle | \mathcal{L}_{0+} \rangle}{L_0^+} + R_0 | \mathcal{L}_{0-} \rangle = T_0 | \mathcal{R}_{0+} \rangle. \tag{3.27}$$

Obviously, this shows the self-consistency of our formulation of the boundary condition. As the FMA demands, only a zeroth order Bloch mode is excited in each metamaterial layer (fig. 3.3.b), which in turn is converted into a superposition of plane waves at the interface. (fig. 3.3.d). Vice versa, eqs. (3.26) and (3.27) also suggest that the incident field should only carry a zeroth order mode when in-coupling at the interface.

Under this condition each layer of the metamaterial can be conceptualized as an individual metasurface. On a microscopic level, we now define the dimensions of a metasurface's unit cell such that its evanescent fields are enclosed in it (fig. 3.3.e) [145]. Consequently, from a macroscopic field perspective, each metasurface becomes a *homogeneous* and conceptually infinitely thin interface (fig. 3.3.f). In other words: if we exclude near-fields from coupling between layers, only the far-field interaction matters. That is the FMA.

3.3.2 Conditions for exclusive fundamental mode interaction

Based on the discussion above, it seems reasonable to demand that all higher diffraction orders of the incident field are evanescent. Consequently, the propagation constant of higher order modes k_z^{lm} (eq. (3.24)) has to be imaginary. Generally, we need to differentiate three cases

$$(i) \quad k_0^2 n^2 < \left(\frac{2\pi l}{\Lambda_x}\right)^2 + \left(\frac{2\pi m}{\Lambda_y}\right)^2 \implies k_z^{lm} \in \mathbb{C} : \text{evanescent modes} \quad (3.28a)$$

$$(ii) \quad k_0^2 n^2 = \left(\frac{2\pi l}{\Lambda_x}\right)^2 + \left(\frac{2\pi m}{\Lambda_y}\right)^2 \implies k_z^{lm} = 0 : \text{Wood anomaly} \quad (3.28b)$$

$$(iii) \quad k_0^2 n^2 > \left(\frac{2\pi l}{\Lambda_x}\right)^2 + \left(\frac{2\pi m}{\Lambda_y}\right)^2 \implies k_z^{lm} \in \mathbb{R} : \text{propagating modes.} \quad (3.28c)$$

Case (i) is a necessary condition for FMA validity. If we reach (ii), the Wood anomaly of order (l, m) will mark the emergence of propagating diffracted modes of that order [234, 235]. All modes that fulfill (iii) propagate to the far-field and can interact with adjacent metamaterial layers.

Even though evanescent modes are non-propagating their interaction as near-fields is significant. As suggested in fig. 3.3.e) near-fields can be contained by including spacer layers around a metasurface. So, even if condition (i) is fulfilled, there exists a *critical distance* d_{crit} , a minimal layer separation, at which evanescent fields have decayed sufficiently. Below this d_{crit} higher order modes will start to couple [145], disrupting homogeneity [77, 222].

We can estimate d_{crit} by looking at the decay rate of the first diffraction order. Without loss of generality we restrict ourselves to x-polarization in the absence of cross-polarization (isotropic case), so $\mathbf{t}^{lm} \rightarrow T_{xx}^{lm}$ ⁷. Assuming that the decay rate increases with each consecutive order, we choose $l = 1$ and $m = 0$. For an upper estimate we approximate the amplitude as $|T_{xx}^{1,0}| \approx 1$, ignoring its imaginary part as it will benefit the decay through absorption. For a metasurface with a physical interface in positive z-direction at $z = 0$ we are looking for the distance $z = d$ at which the first order has decayed below an upper estimate σ . Inserting our assumptions into eq. (3.23) and using eq. (3.24)⁸ we can deduce the following inequality,x

$$\exp\left(-d\sqrt{\left(\frac{2\pi}{\Lambda_x}\right)^2 - \left(\frac{2\pi n}{\lambda}\right)^2}\right) \leq \sigma \implies d\sqrt{\left(\frac{2\pi}{\Lambda_x}\right)^2 - \left(\frac{2\pi n}{\lambda}\right)^2} \geq \ln\left(\frac{1}{\sigma}\right). \quad (3.29)$$

For an arbitrary polarization we can omit the subscript and define the critical distance d_{crit}

⁷The first element of the Jones matrix.

⁸Obeying the condition for evanescent modes (3.28a).

based on the estimate σ as

$$d_{\text{crit}} = \tilde{\sigma}\Lambda \left/ \sqrt{1 - \frac{n^2\Lambda^2}{\lambda^2}} \right., \quad \text{with} \quad \tilde{\sigma} := \frac{\ln(1/\sigma)}{2\pi}. \quad (3.30)$$

The factor $\tilde{\sigma}$ can be considered as an attenuation coefficient to the critical distance. Note that the necessary precision of σ is contingent upon the accuracy of either measured or simulated data the estimate might be compared to [146,151]. Hence, appropriate values of σ can be chosen that fit the circumstances. For instance, we can control the order of magnitude by choosing $\sigma = e^{-2\pi} \approx 2\%$ with $\tilde{\sigma} = 1$, $\sigma = 1\%$ with $\tilde{\sigma} = \ln(10)/\pi$, or $\sigma = 10\%$ with $\tilde{\sigma} = \ln(10)/2\pi$.

Regardless of the chosen precision we can make an observation similar to eqs. (3.28a) - (3.28c). For given period Λ , the wavelength λ can be divided in three cases for the physical behavior of higher diffraction orders,

$$\lambda > n\Lambda \implies d_{\text{crit}} \in \mathbb{R} : \text{evanescent higher orders} \quad (3.31a)$$

$$\lambda = n\Lambda \implies d_{\text{crit}} \rightarrow \infty : \text{Wood anomaly} \quad (3.31b)$$

$$\lambda < n\Lambda \implies d_{\text{crit}} \in \mathbb{C} : \text{propagating higher orders.} \quad (3.31c)$$

Thus, the validity of the FMA depends on both λ and d_{crit} for a given metasurface. Obviously, for two adjacent metasurfaces, the larger period Λ determines the necessary critical distance. The argument on the scale of λ ties in nicely with the discussion of effective media in sec. 3.1 and eq. (3.1). Finally, we can collect a set of necessary conditions for the validity of the FMA and, thus, the homogeneity of a metamaterial comprised of multiple layers of stacked metasurfaces:

- (i) Structure or particle sizes a are of subwavelength scale, $a \cdot n/\lambda \lesssim 0.5$.
- (ii) Higher diffraction orders are evanescent, $\lambda > n\Lambda$ or $k_0 n < 2\pi/\Lambda$.
- (iii) Adjacent metasurfaces have to be separated by at least a critical distance d_{crit} at which higher orders have decayed below an upper limit σ .

3.3.3 Oblique fundamental modes

In many experimental scenarios the considerations for perpendicular incidence suffice. However, for the sake of completeness it is important to consider conditions of fundamental modes for oblique angles. Indeed, the same principles as before apply. The difference now is the projection of the k -vector onto the metasurface lattice that determines the tangential components. Regarding that, FMA condition (i) is unchanged but (ii) and (iii) need to be adapted.

Using the same spherical coordinate system the FMM employs (sec. 2.4) we get for the propagation constant in transmission

$$k_z^{lm} = \sqrt{k_0^2 n^2 - \left(k_0 n \sin \theta \cos \phi + \frac{2\pi l}{\Lambda_x}\right)^2 - \left(k_0 n \sin \theta \sin \phi + \frac{2\pi m}{\Lambda_y}\right)^2}, \quad (3.32)$$

with the polar angle $\phi \in [0, 2\pi)$ and azimuth angle $\theta \in [0, \pi/2]$. To derive d_{crit} the same scheme as in eq. (3.29) can be used. However, in this instance we ought to distinguish positive and negative diffraction orders. Thus, d_{crit} becomes an angular dependent matrix with entries⁹

$$d_{\text{crit}}^{lm}(\theta, \phi) = \tilde{\sigma} \Lambda \left/ \sqrt{l^2 + m^2 + 2 \frac{n\Lambda}{\lambda} \Gamma^{lm}(\theta, \phi) - \frac{n^2 \Lambda^2}{\lambda^2} \cos^2 \theta} \right., \quad (3.33)$$

$$\text{with } \Gamma^{lm}(\theta, \phi) = \sin \theta (l \cos \phi + m \sin \phi).$$

The limit $\theta, \phi \rightarrow 0$ with $l = 1$ and $m = 0$ reverts eq. (3.33) to the perpendicular incidence d_{crit} . On the other hand, $d_{\text{crit}}^{lm}(\theta, \phi)$ can reach a maximum if light impinges in the x-z or y-z-plane, i.e. $\phi = 0$ or $\phi = \pi/2$, respectively. Then the sign of $\Gamma^{lm}(\theta, \phi)$ reveals that, among all possible tuples (l, m) , the negative first diffraction order requires the largest critical distance. So, for $\phi = 0$ and $(l, m) = (-1, 0)$ or $\phi = \pi/2$ and $(l, m) = (0, -1)$ the upper estimate for oblique incidence is given by

$$d_{\text{crit}}(\theta) = \tilde{\sigma} \Lambda \left/ \sqrt{1 - 2 \frac{n\Lambda}{\lambda} \sin \theta - \frac{n^2 \Lambda^2}{\lambda^2} \cos^2 \theta} \right. . \quad (3.34)$$

Thus, the generalizations of the FMA conditions (ii) and (iii) are

- (ii*) Higher diffraction orders are evanescent for $\lambda > (1 + \sin \theta)n\Lambda$.
- (iii*) Adjacent metasurfaces have to be separated by at least an *angular dependent* critical distance $d_{\text{crit}}(\theta)$.

3.4 Coupling phases

To conclude this chapter we will give an interpretation of the FMA in the context of homogenization and locality discussed in sec. 3.1. If the FMA is valid the far-field of a metasurface is comparable to that of any other (natural) homogeneous medium. Within the bounds of eqs. (3.30) and (3.34) the FMA replicates locality condition IV. in table 3.1. Furthermore, by

⁹For simplicity we assume $\Lambda_x = \Lambda_y = \Lambda$. In the case of dissimilar periods an additional degree of freedom has to be taken into account for $d_{\text{crit}}(\theta)$.

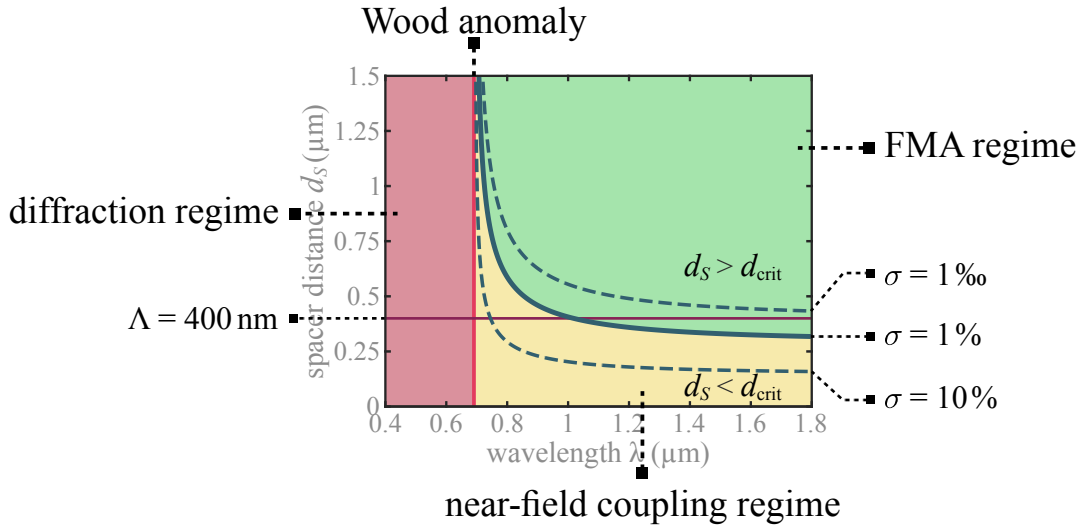


Figure 3.4: Coupling phase diagram (CPD): plot of the critical distance d_{crit} . The blue solid line represents d_{crit} with an accuracy $\sigma = 1\%$. The dashed blue lines show d_{crit} with alternative choices of σ . The thin red line marks $d_s = \Lambda = 400 \text{ nm}$, to which d_{crit} with $\sigma = 1\%$ asymptotically converges. The colored areas identify different regimes of coupling to adjacent layers, annotated in the figure. The Wood anomaly marked by a vertical red line marks an asymptotic limit to which d_{crit} converges for small λ regardless of σ .

restricting the periodicity Λ the FMA implicitly limits the size of structures or particles comprising a metasurface. Assuming a general state of thermodynamic equilibrium, this translates to fulfilling locality condition III (absence of radiation losses). Passivity and causality depend on the chosen particle materials and are assured by a suitable retrieval procedure for μ_{loc} and ε_{loc} [58, 77].

Interestingly, the FMA allows us to interpret a metasurface as a homogeneous medium without considering μ_{loc} and ε_{loc} . Wave propagation as such can be described by the transmission and reflection coefficients of an infinitely thin interface conceptually representing the metasurface (sec. 3.3.1) [145]. Then, FMA conditions (i), (ii*), and (iii*) suffice to consider the metasurface as a homogeneous *interface*-medium. Moreover, if material and wave parameters are peripheral, conditions I and II in table 3.1 can be neglected.¹⁰

Finally, we can describe the different validity regimes of the FMA similarly to the conceptual map discussed in fig. 3.1, sec. 3.1. Instead of distinguishing different types of effective parameters we switch to coupling regimes defined by FMA conditions (i), (ii*), and (iii*) and the critical distance d_{crit} . For simplicity we assume perpendicular incidence in the following.¹¹

If we plot (3.30) versus the wavelength λ for a given period Λ , the inverse square root

¹⁰It can be argued phenomenologically that they are fulfilled automatically in the FMA as long as the material comprising particles does not itself produce extraordinary effects such as optical activity.

¹¹The oblique case follows the same scheme.

of d_{crit} separates the parameter space in three distinct areas. Fig. 3.4 shows a plot for an arbitrary metasurface with period $\Lambda = 400$ nm surrounded by glass with dispersive refractive index $n(\lambda)$.¹² Moving along the horizontal axis, the critical distance becomes imaginary for wavelengths $\lambda < \Lambda n$ and produces a visible singularity that marks the Wood anomaly [234,235]. On the left side of that singularity (where the root would become imaginary; red area of the plot) the metasurface behaves like a grating with propagating diffraction modes. In contrast, on the right side of the singularity an individual metasurface can in principle behave like an effective medium.

Moving vertically, we change the distance from the metasurface d_S , which we call spacer or stacking distance with regard to possible adjacent layers. In a stacked configuration the coupling to adjacent layers depends on the presence of evanescent fields. This is represented by the area below the critical distance ($d_S < d_{\text{crit}}$). Here, the FMA is *invalid* and coupling includes evanescent diffraction orders. Above the critical distance ($d_S > d_{\text{crit}}$) the FMA is *valid* and the metasurface behaves like an effective medium even with respect to adjacent layers.

Because d_{crit} is an upper estimate that represents a soft boundary and the change between coupling regimes is akin to a phase transition, we term this type of plot *coupling phase diagram* (CPD). A CPD maps the FMA conditions for a given metasurface geometry. As we will show in the following chapters, it can be used to both design and analyze different stacks of metasurfaces. Meanwhile, the CPD also tells us what mathematical formalism to use. In the fully FMA-valid case simplifications can be made that lead to a semi-analytic formalism which will be derived in the next chapter.

¹²Calculated using the Sellmeier equation (A.2) in the appendix.

4 | Semi-analytic stacking algorithm

This chapter establishes a framework for modeling and simulating metasurface stacks semi-analytically. The underlying model is based on the fundamental mode approximation (FMA). We will derive the necessary calculus for our semi-analytic approach and formulate an algorithm with which to semi-analytically simulate arbitrary stacks that are within the FMA coupling regime. An important hallmark of semi-analytic modeling is the capability to reduce computational cost by only performing numerical calculations of certain *individual* layers of a stack. Furthermore, the mathematical structure of S-matrices can be manipulated and analyzed for closer insight into symmetries and polarization. Necessarily, we will check the numerical accuracy of the FMA, while demonstrating the use of our semi-analytic stacking algorithm (SASA), compared to rigorous simulations. This is based on our publication “*Efficient treatment of stacked metasurfaces for optimizing and enhancing the range of accessible optical functionalities*” [145].

4.1 Fundamental mode scattering matrix formalism

4.1.1 Zeroth order scattering matrices

The FMA as derived in chapter 3 reduces the diffraction coefficients used in the FMM, sec. 2.4. The S-matrices, as defined by Li’s [236], then reduce from a total size of $4 \cdot (2M+1)^2 \times 4 \cdot (2N+1)^2$, for $M \times N$ Fourier orders in an FMM, to 4×4 matrices for zeroth order output. Concerning the propagation of modes, a zeroth order S-matrix is now, conceptually, a Jones-vector-port with Jones matrices for reflection $\hat{R}^{f,b}$ and transmission $\hat{T}^{f,b}$ in forward and backward direction. Thus, the 2×2 block matrix form is preserved and we can write for electric fields of two adjacent layers, p and $p + 1$,

$$\begin{bmatrix} \mathbf{E}_{p+1}^f \\ \mathbf{E}_p^b \end{bmatrix} = S \begin{bmatrix} \mathbf{E}_p^f \\ \mathbf{E}_{p+1}^b \end{bmatrix} = \begin{pmatrix} \hat{T}^f & \hat{R}^b \\ \hat{R}^f & \hat{T}^b \end{pmatrix} \begin{bmatrix} \mathbf{E}_p^f \\ \mathbf{E}_{p+1}^b \end{bmatrix}. \quad (4.1)$$

Here, the S-matrix maps fundamental modes from the front to the back of the interface, layer or stack it represents, depending on the propagation direction. These modes can constitute

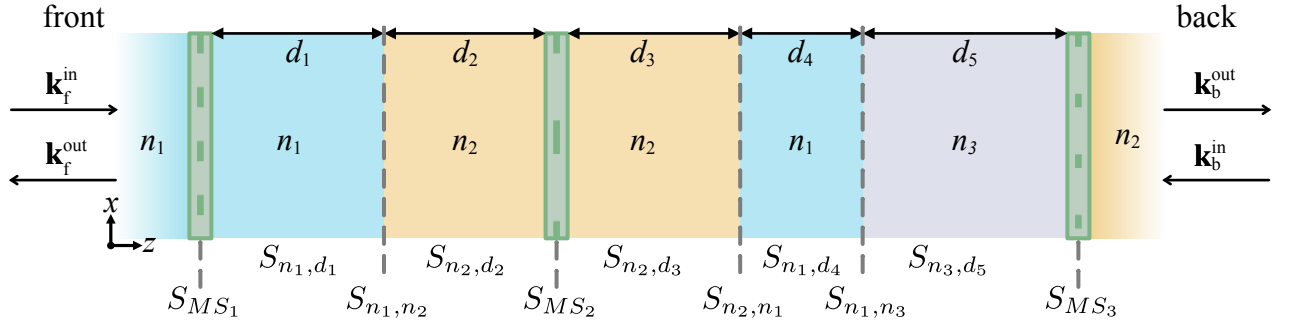


Figure 4.1: Schematic of a stack with arbitrary layers.

incident fields as well as transmitted or reflected fields from other layers. Based on the general form eq. (2.51), the FMA star product for two arbitrary layers S_1 and S_2 reads [145]

$$S_1 * S_2 = \begin{pmatrix} \hat{T}_2^f \left(\hat{\mathbb{I}} - \hat{R}_1^b \hat{R}_2^f \right)^{-1} \hat{T}_1^f & \hat{R}_2^b + \hat{T}_2^f \hat{R}_1^b \left(\hat{\mathbb{I}} - \hat{R}_2^f \hat{R}_1^b \right)^{-1} \hat{T}_2^b \\ \hat{R}_1^f + \hat{T}_1^b \hat{R}_2^f \left(\hat{\mathbb{I}} - \hat{R}_1^b \hat{R}_2^f \right)^{-1} \hat{T}_1^f & \hat{T}_1^b \left(\hat{\mathbb{I}} - \hat{R}_2^f \hat{R}_1^b \right)^{-1} \hat{T}_2^b \end{pmatrix}, \quad (4.2)$$

where $x*$ denotes the star product and $\hat{\mathbb{I}}$ the 2-by-2 identity.¹ Any number of FMA-valid layers can be expressed as a cascade of S-matrices using the star product. S-matrices of metasurface layers can be constructed from measured phase and intensity values or calculated numerically. For any type of homogeneous layer, such as spacers between the metasurfaces, the S-matrices follow from analytical equations. In our S-matrix formalism homogeneous layers are a combination of interface S-matrices $S_{n_p, n_{p+1}}$ and propagation S-matrices S_{n_p, d_p} . For instance, a glass plate of thickness d_{glass} between two half spaces of air has the S-matrix representation

$$S_{\text{slab}} = S_{n_{\text{air}}, n_{\text{glass}}} * S_{n_{\text{glass}}, d_{\text{glass}}} * S_{n_{\text{glass}}, n_{\text{air}}}. \quad (4.3)$$

Here, the $S_{n_{\text{air}}, n_{\text{glass}}}$ reads as: interface when propagating from air to glass in forward direction and vice versa in backward direction. This way we can stack any number of metasurfaces together with arbitrary combinations of homogeneous layers. If we define S_{MS} as the S-matrix of an arbitrary periodic metasurface, we could construct a stack as shown in fig. 4.1 that is constructed by

$$S_{\text{stack}} = S_{\text{MS}_1} * S_{n_1, d_1} * S_{n_1, n_2} * (S_{n_2, d_2} * S_{\text{MS}_2} * S_{n_2, d_3}) * S_{n_1, d_4} * S_{n_1, n_3} * S_{n_3, d_5} * S_{\text{MS}_3} \quad (4.4)$$

Notice that no interface S-matrices are needed for the metasurfaces S_{MS} , as they are themselves conceptual interfaces. However, this means that simulations of these layers need to incorpo-

¹Recall that all quantities with a hat are 2×2 matrices.

rate the correct embedding. Otherwise, additional spacer layers are needed in order to add FMA-valid extra interfaces. In eq. (4.4) such a case is indicated by the parenthesis around S_{MS_2} , incorporating the surrounding spacers with $d_{2,3} > d_{\text{crit}}(\Lambda_{\text{MS}_2})$, as previously indicated in fig. 3.3.e). If the FMA is valid for each individual layer, the entire stack can be considered homogeneous.

4.1.2 Analytical scattering matrices

Interfaces and propagators

Interface and propagation S-matrices of homogeneous layers, both isotropic and anisotropic, follow analytical expressions. The propagation S-matrix $S_{n,d}$ manages phase evolution over distance d . For an isotropic, homogeneous layer with index n it is defined as

$$S_{n,d} = \mathcal{P}_{n,d} \cdot \text{diag}(1, 1, 1, 1), \quad (4.5)$$

with $\mathcal{P}_{n,d} = \exp(ik_0nd)$ and $k_0 = 2\pi/\lambda_0$ [145]. Correspondingly, the S-matrix S_{n_1,n_2} of an interface between isotropic, homogeneous media, n_1 and n_2 , is populated by Fresnel equations (2.23),

$$S_{n_1,n_2} = \begin{pmatrix} \frac{2n_1}{n_1+n_2} & 0 & \frac{n_1-n_2}{n_1+n_2} & 0 \\ 0 & \frac{2n_1}{n_1+n_2} & 0 & \frac{n_1-n_2}{n_1+n_2} \\ -\frac{n_1-n_2}{n_1+n_2} & 0 & \frac{2n_2}{n_1+n_2} & 0 \\ 0 & -\frac{n_1-n_2}{n_1+n_2} & 0 & \frac{2n_2}{n_1+n_2} \end{pmatrix}. \quad (4.6)$$

Anisotropic media with $n \rightarrow \mathbf{n} = (n_x, n_y)$ break the symmetry of eq. (4.6) and introduce polarization effects. This includes, for instance, uniaxial crystals with their principal axes aligned to the Cartesian coordinate system of the fields' Jones vectors² while propagating, per definition, in z-direction. Hence, for linear polarization parallel to the principal axes (x and y) the S-matrix phase propagator splits,

$$S_{\mathbf{n},d} = \text{diag}(\mathcal{P}_{n_x,d}, \mathcal{P}_{n_y,d}, \mathcal{P}_{n_x,d}, \mathcal{P}_{n_y,d}). \quad (4.7)$$

Similarly, the interface between two anisotropic media additionally handles polarization,

$$S_{\mathbf{n}_1,\mathbf{n}_2} = \begin{pmatrix} \frac{2n_{x1}}{n_{x1}+n_{x2}} & 0 & \frac{n_{x1}-n_{x2}}{n_{x1}+n_{x2}} & 0 \\ 0 & \frac{2n_{y1}}{n_{y1}+n_{y2}} & 0 & \frac{n_{y1}-n_{y2}}{n_{y1}+n_{y2}} \\ -\frac{n_{x1}-n_{x2}}{n_{x1}+n_{x2}} & 0 & \frac{2n_{x2}}{n_{x1}+n_{x2}} & 0 \\ 0 & -\frac{n_{y1}-n_{y2}}{n_{y1}+n_{y2}} & 0 & \frac{2n_{y2}}{n_{y1}+n_{y2}} \end{pmatrix}. \quad (4.8)$$

²And, thus, the S-matrix's coordinate system.

To give a quick example, a Fabry-Pérot cavity with a crystal layer characterized by \mathbf{n}_2 and sandwiched between two different isotropic layers n_1 and n_3 can be written as

$$S = S_{n_{\text{air}},n_1} * S_{n_1,d_1} * S_{n_1,\mathbf{n}_2} * S_{\mathbf{n}_2} * S_{\mathbf{n}_2,n_3} * S_{n_3,d_3} * S_{n_3,n_{\text{air}}}. \quad (4.9)$$

The interface between isotropic and anisotropic layers $S_{n_i,\mathbf{n}_{i+1}}$ can be constructed as a hybrid of eqs. (4.6) and (4.8).

Propagating a scattering matrix

We can propagate any S-matrix S by star-product-multiplication of a propagator $S_{\mathbf{n},d}$. Given the correct boundary conditions, i.e. propagating with the same refractive index as the substrate or cladding of this specific S-matrix, we can propagate in *front* of S by

$$S_{\mathbf{n},d} * S = \begin{pmatrix} \mathcal{P}_x T_{xx}^f & \mathcal{P}_x T_{xy}^f & R_{xx}^b & R_{xy}^b \\ \mathcal{P}_y T_{yx}^f & \mathcal{P}_y T_{yy}^f & R_{yx}^b & R_{yy}^b \\ \mathcal{P}_x^2 R_{xx}^f & \mathcal{P}_x \mathcal{P}_y R_{xy}^f & \mathcal{P}_x T_{xx}^b & \mathcal{P}_x T_{xy}^b \\ \mathcal{P}_y \mathcal{P}_x R_{yx}^f & \mathcal{P}_y^2 R_{yy}^f & \mathcal{P}_y T_{yx}^b & \mathcal{P}_y T_{yy}^b \end{pmatrix}, \quad (4.10)$$

where we simplified the notation of the scalar factors $\mathcal{P}_{n_{x,y},d} \rightarrow \mathcal{P}_{x,y}$ for readability. As we can see, the structure of S and, thus, its symmetry are preserved. The front reflection matrix \hat{R}^f adds twice the phase because light takes a full round trip through the extra layer. If we propagate S from the *back* with $S * S_{\mathcal{P}_{\mathbf{n},d}}$ the squared factors are applied to \hat{R}^b .

4.1.3 Transformation rules for scattering matrices

Another important tool of our S-matrix formalism are transformations of S-matrices and their block elements. In effect we can transform the constituent Jones matrices to any polarization base. Additionally, there are transformations that map directly to the metasurfaces as geometrical or symmetry operations. We will begin by introducing the general 2×2 block matrix transformation.

Block matrix transformation

In order for our formalism to be self-consistent, transformations have to be applied to both the fields and the S-matrix handling the ports of a given layer. We investigate the interaction of incident fields $\mathbf{E}_{p,p+1}^{f,b}$ with an arbitrary S-matrix S of layer $p+1$. Let $\hat{\Omega}$ be an arbitrary, well defined 2×2 transformation matrix, such that

$$\mathbf{E}_{p,p+1}^{f,b} = \hat{\Omega} \bar{\mathbf{E}}_{p,p+1}^{f,b}. \quad (4.11)$$

Using the vector form of eq. (4.1) we get a basis transformation of the Jones matrices,

$$\bar{\mathbf{E}}_{p+1}^f = \hat{\Omega}^{-1} \hat{T}^f \hat{\Omega} \bar{\mathbf{E}}_p^f + \hat{\Omega}^{-1} \hat{R}^b \hat{\Omega} \bar{\mathbf{E}}_{p+1}^b, \quad (4.12)$$

$$\bar{\mathbf{E}}_p^b = \hat{\Omega}^{-1} \hat{R}^f \hat{\Omega} \bar{\mathbf{E}}_p^f + \hat{\Omega}^{-1} \hat{T}^b \hat{\Omega} \bar{\mathbf{E}}_{p+1}^b. \quad (4.13)$$

Thus, the corresponding transformed S-matrix can be written as

$$\bar{S} = \begin{pmatrix} \hat{T}^f & \hat{R}^b \\ \hat{R}^f & \hat{T}^b \end{pmatrix} := \begin{pmatrix} \hat{\Omega}^{-1} \hat{T}^f \hat{\Omega} & \hat{\Omega}^{-1} \hat{R}^b \hat{\Omega} \\ \hat{\Omega}^{-1} \hat{R}^f \hat{\Omega} & \hat{\Omega}^{-1} \hat{T}^b \hat{\Omega} \end{pmatrix} =: \Omega^{-1} S \Omega, \quad \text{with} \quad \Omega := \begin{pmatrix} \hat{\Omega} & \hat{0} \\ \hat{0} & \hat{\Omega} \end{pmatrix}, \quad (4.14)$$

where $\hat{0}$ is a 2×2 matrix of zeros. As defined above, Ω is a transformation block matrix that can be applied to any 4×4 S-matrix. Inverting a block matrix such as Ω is the same as inverting its comprising matrices. Note that Ω is defined within the forward coordinate system of the S-matrix. Thus, all backward modes are generally seen in the forward coordinate system. Allowing the backward Jones matrices to preserve their laboratory coordinate system would translate to a flip (see below) of the entire stack and *its* coordinate system. Hence, the Cartesian basis would transform as

$$\begin{pmatrix} x^b \\ y^b \\ z^b \end{pmatrix} = \begin{pmatrix} x^f \\ -y^f \\ -z^f \end{pmatrix}. \quad (4.15)$$

For consistency and without loss of generality, all calculations will be performed in the forward coordinate system.

Basis transformation: Cartesian to circular

As a first example we will demonstrate a transformation from a linear to a circular polarization basis. In our formulation of the S-matrix formalism the standard basis is linear. To transform to a circular basis we need to construct $\hat{\Omega}$ from circular eigenvectors [200],

$$\hat{\Omega}_{\text{circ}} = \frac{1}{\sqrt{2}} \begin{pmatrix} 1 & 1 \\ i & -i \end{pmatrix}. \quad (4.16)$$

Plugging eq. (4.16) into (4.14) we get the S-matrix in a circular basis,

$$S_{\text{circ}} = \Omega_{\text{circ}}^{-1} S \Omega_{\text{circ}} = \begin{pmatrix} \hat{T}_{\text{circ}}^f & \hat{R}_{\text{circ}}^b \\ \hat{R}_{\text{circ}}^f & \hat{T}_{\text{circ}}^b \end{pmatrix} = \begin{pmatrix} \hat{S}_{\text{circ}}^{11} & \hat{S}_{\text{circ}}^{12} \\ \hat{S}_{\text{circ}}^{21} & \hat{S}_{\text{circ}}^{22} \end{pmatrix}, \quad (4.17)$$

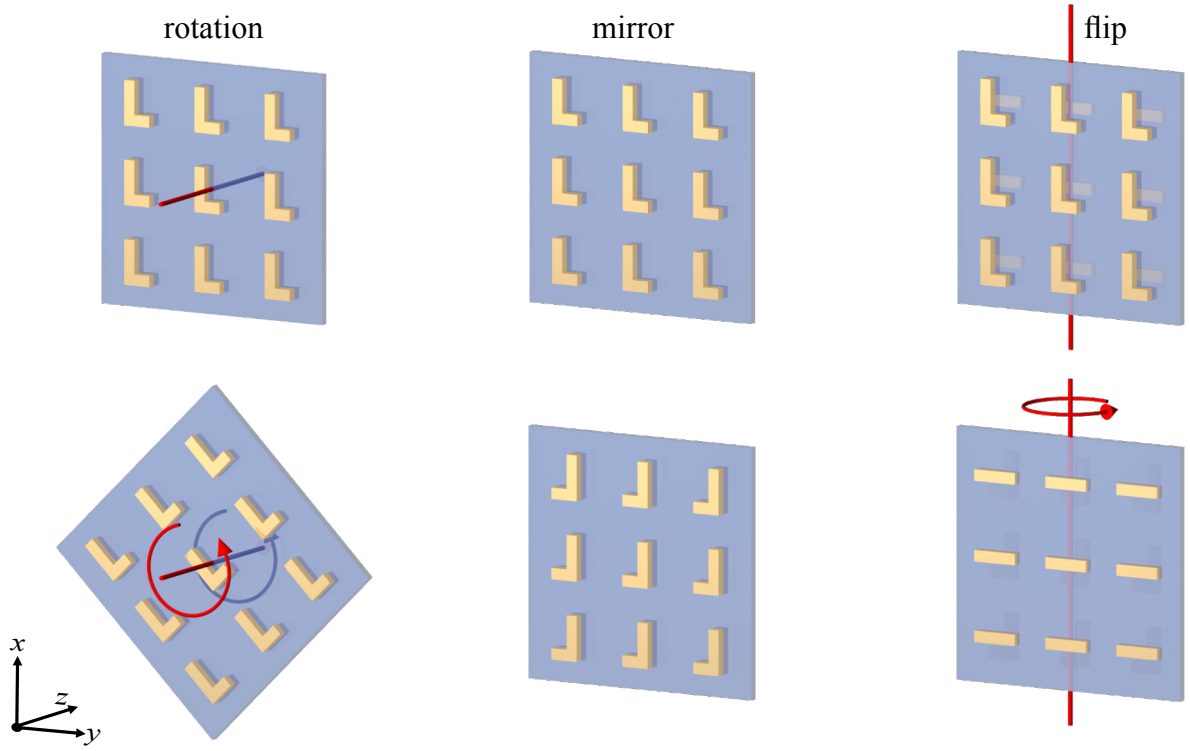


Figure 4.2: Illustration of the effect of symmetry operations on a metasurface. Each column shows a different operation: rotation, mirror, and flip. For the latter, the exemplary metasurface comprises Ls on one side and wires on the other to showcase the effect of the flip.

where each S-matrix $\hat{S}_{\text{circ}}^{ij}$ element follows from

$$\hat{S}_{\text{circ}}^{ij} = \frac{1}{2} \begin{pmatrix} S_{xx}^{ij} + S_{yy}^{ij} + i(S_{xy}^{ij} - S_{yx}^{ij}) & S_{xx}^{ij} - S_{yy}^{ij} - i(S_{xy}^{ij} + S_{yx}^{ij}) \\ S_{xx}^{ij} - S_{yy}^{ij} + i(S_{xy}^{ij} + S_{yx}^{ij}) & S_{xx}^{ij} + S_{yy}^{ij} - i(S_{xy}^{ij} - S_{yx}^{ij}) \end{pmatrix}, \quad (4.18)$$

with $i, j \in \{1, 2\}$. Staying in the forward coordinate system, all transformations of the Jones matrices have the same structure.

Symmetry operations

Similar to the basis transformation demonstrated above, we can perform symmetry operations on an S-matrix. These include: mirroring, rotation about the propagation (z) axis, and a flip around the x - or y -axis. Each of these operations mimics a *physical* operation on the metasurface represented by the S-matrix. Fig. 4.2 gives a visual reference of the following.

Rotating an S-matrix in the transversal plane maps the counterclockwise rotation matrix $\hat{\mathcal{R}}_{\varphi}$ onto each Jones matrix, while preserving the forward coordinate system. For mathematical

rotation around φ of an arbitrary 2D matrix \hat{A} , $\hat{\mathcal{R}}_\varphi$ is defined by

$$\hat{A}_\varphi = \hat{\mathcal{R}}_\varphi^{-1} \hat{A} \hat{\mathcal{R}}_\varphi, \quad \text{with} \quad \hat{\mathcal{R}}_\varphi = \begin{pmatrix} \cos \varphi & -\sin \varphi \\ \sin \varphi & \cos \varphi \end{pmatrix}. \quad (4.19)$$

Using eq. (4.14) with $\hat{\Omega}_\varphi := \hat{\mathcal{R}}_\varphi$ the rotation of the S-matrix follows immediately,

$$S_\varphi = \Omega_\varphi^{-1} S \Omega_\varphi = \begin{pmatrix} \hat{\mathcal{R}}_\varphi^{-1} \hat{T}^f \hat{\mathcal{R}}_\varphi & \hat{\mathcal{R}}_\varphi^{-1} i \hat{R}^b \hat{\mathcal{R}}_\varphi \\ \hat{\mathcal{R}}_\varphi^{-1} \hat{R}^f \hat{\mathcal{R}}_\varphi & \hat{\mathcal{R}}_\varphi^{-1} \hat{T}^b \hat{\mathcal{R}}_\varphi \end{pmatrix}. \quad (4.20)$$

Rotation is a symmetry operation on the *relative* coordinate system of the fields, represented by the transformed Jones matrices or a rotation of the metasurface (fig. 4.2.a,b). Rotating either has the same effect on the symmetry of the S-matrix and, thus, the polarization of the fields. This will be important in the discussion of chiral metasurface stacks in sec. 5.1.

Mirroring an S-matrix applies the two-dimensional mirror matrix \hat{M} . For an arbitrary 2D matrix \hat{A} the mirror operation with respect to a transversal coordinate axis is defined by

$$\hat{A}_M := \hat{M}_\pm^{-1} \hat{A} \hat{M}_\pm, \quad \text{with} \quad \hat{M}_\pm := \begin{pmatrix} \mp 1 & 0 \\ 0 & \pm 1 \end{pmatrix}. \quad (4.21)$$

The upper sign in \hat{M}_\pm denotes the operation with respect to the y-z-plane whereas the lower one is with respect to the x-z-plane. For brevity we will use the latter as our standard mirror plane. Since $M = M^T = M^{-1}$ the block transformation simply reads

$$S_M = \Omega_M S \Omega_M = \begin{pmatrix} \hat{M} \hat{T}^f \hat{M} & \hat{M} \hat{R}^b \hat{M} \\ \hat{M} \hat{R}^f \hat{M} & \hat{M} \hat{T}^b \hat{M} \end{pmatrix}. \quad (4.22)$$

The physical effect of mirroring the S-matrix is shown in figs. 4.2.c,d).

Flipping of an S-matrix means rotating it 180° about a transversal axis. This effectively flips the front and back side of the metasurface (fig. 4.2.e,f). The operation on the S-matrix is, therefore, slightly more complex as it entails swapping front and back Jones matrices. Additionally, the 180° longitudinal rotation mirrors the structures about the orthogonal axis of the rotation axis. The flipped S-matrix is a combination of a point reflection of its block elements and the mirror operation,

$$S_F = \Omega_M \Omega_I S \Omega_I \Omega_M = \Omega_F S \Omega_F = \begin{pmatrix} \hat{M} \hat{T}^b \hat{M} & \hat{M} \hat{R}^f \hat{M} \\ \hat{M} \hat{R}^b \hat{M} & \hat{M} \hat{T}^f \hat{M} \end{pmatrix}, \quad \text{with} \quad \Omega_I := \begin{pmatrix} \hat{0} & \hat{\mathbb{I}} \\ \hat{\mathbb{I}} & \hat{0} \end{pmatrix}, \quad \Omega_F := \begin{pmatrix} \hat{0} & \hat{M} \\ \hat{M} & \hat{0} \end{pmatrix}. \quad (4.23)$$

In the following we will summarize the effect of symmetry operations on isotropic and anisotropic metasurfaces.

4.1.4 Symmetry operations on propagators and interfaces

It is obvious that symmetry operations will have varying effects on different types of S-matrices. A structural overview of this would be helpful both for the understanding of asymmetric field interaction and efficient computation later on. First, we apply the transformation block matrices Ω_φ , Ω_M , and Ω_F to the analytical S-matrices for propagation (eqs. (4.5), (4.7)) and interfaces (eqs. (4.6), (4.8)), both isotropic and anisotropic. The result shows us if a symmetry operation has an effect or not, summarized in table 4.1.

The results are intuitive and map directly to metasurfaces of the same symmetry class (i.e. C_4 and C_2). Anisotropy is needed for rotations to have any effect. Flipping a propagator is meaningless. Flipping interfaces, however, reverses the order of refractive indices, $\Omega_F S_{n_1, n_2} \Omega_F = S_{n_2, n_1}$ in either case. Interestingly though, mirroring has no effect on neither S_{n_1, n_2} nor $S_{n, d}$. Looking at the illustration in fig. 4.2 it becomes clear, that an additional break in symmetry is necessary for effective mirroring. At the very least the transmission matrices of the S-matrix need cross polarization components to populate their off-diagonals [200]. Such a case is discussed later in sec. 5.1.

The question remains what happens when an isotropic or anisotropic layer is adjacent to an anisotropic layer that is rotated. This could be the case for a crystal rotated about the propagation axis. Then, it would be a mistake to rotate the interface S-matrix of the two layers because that would effectively apply the operation to both. In order to perform the transformation with Ω_φ separately we can employ a trick. It is possible to insert a dummy layer with refractive index n_0 between the two layers. Then, by trait of the star product, the interface can be split such that,

$$S_{n_1, n_2} \equiv S_{n_1, n_0} * S_{n_0, n_2}. \quad (4.24)$$

Operation	Propagator $S_{n, d}$		Interface S_{n_1, n_2}	
	isotropic	anisotropic	isotropic	anisotropic
Ω_φ	×	✓	×	✓
Ω_M	×	×	×	×
Ω_F	×	×	✓	✓

Table 4.1: Summary of the effect of symmetry operations on propagation and interface S-matrices of homogeneous layers. Check marks and crosses indicate the presence or absence of resulting effects, respectively.

ani $_{\varphi}$ -iso	iso-ani $_{\varphi}$	ani $_{\varphi}$ -ani	ani-ani $_{\varphi}$	ani $_{\varphi}$ -ani $_{\varphi}$
$S_{\mathbf{n}_1, n_0}^{\varphi} * S_{n_0, n_2}$	$S_{n_1, n_0} * S_{n_0, \mathbf{n}_2}^{\varphi}$	$S_{\mathbf{n}_1, n_0}^{\varphi} * S_{n_0, \mathbf{n}_2}$	$S_{\mathbf{n}_1, n_0} * S_{n_0, \mathbf{n}_2}^{\varphi}$	$S_{\mathbf{n}_1, n_0}^{\varphi} * S_{n_0, \mathbf{n}_2}^{\varphi}$

Table 4.2: Overview of anisotropic interface rotations. The header defines the type of interfaces, abbreviating *iso* for isotropic and *ani* for anisotropic.

In that regard eq. (4.24) is something like an identity of the star product of interfaces. We can exploit it to correctly apply the rotation on just one half of the interface matrix. Table 4.2 summarizes all possible interface combinations in our formalism.

4.1.5 Implementation of SASA

The FMA-based S-matrix formalism described in section 4.1 is an analytical framework for calculating stacks of arbitrary layers in all possible combinations. S-matrices of metasurfaces can be simulated numerically and combined with analytical S-matrices with the same options for transformations. Hence, in combination it forms the starting point of a semi-analytic stacking algorithm (SASA). A full description of SASA for MATLAB can be found in appendix A.2. At a later stage SASA was also transferred to Python. Furthermore, all analytical elements of the S-matrix formalism were implemented in Wolfram Mathematica. To a large part, Mathematica was used to simplify and structure the calculus for MATLAB and Python. Lastly, SASA for MATLAB (or Python) is fully *vectorized*, so that all operations can be performed over the complete discretized wavelength interval as *array*-operations. In that regard, the star product was numerically optimized for an efficient calculation of vectorized block matrix elements.

4.2 Numerical validation

In the previous section 4.1 we have introduced an FMA version of the classical S-matrix formalism used in the FMM [208, 210]. While the simplification is physically meaningful within the realm of homogenization, it is also utilitarian. The resulting algorithm SASA is applicable to a broad range of metasurface stacks and very efficient at handling large parameters spaces³. This is a result of the analytical component of SASA. The numerical component, i.e. the combination with pre-calculated metasurfaces, relies on the accuracy of the FMA. In other words, does a zeroth order S-matrix calculation compare well to a rigorous, higher order simulation?

In the following we will test the numerical accuracy of the FMA and, hence, SASA for different metasurface stacks of varying complexity. All simulations are carried out over the same

³Especially, wavelengths and layer heights.

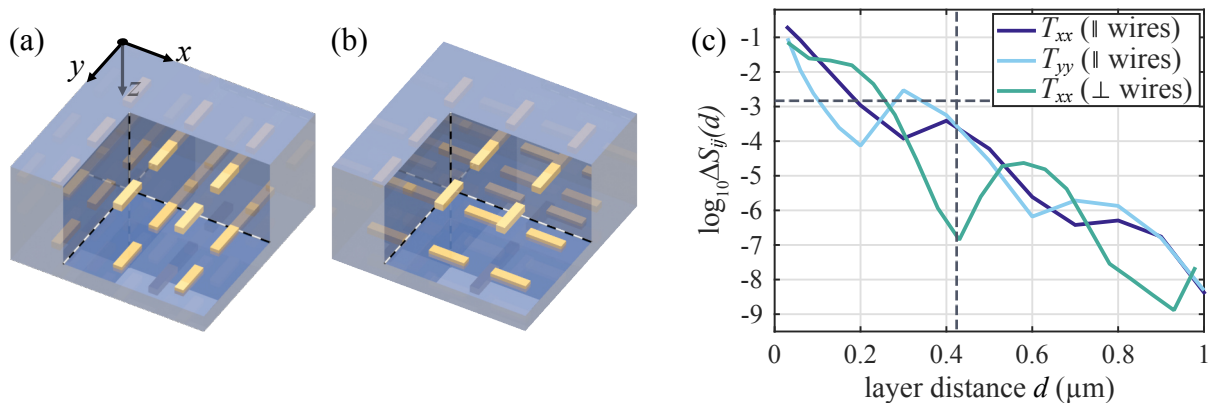


Figure 4.3: a) Rendering of a stack of two identical nano-wire metasurfaces. b) The same stack as a) but with the lower layer rotated by 90° . c) Plot of the maximal difference $\Delta S_{ij}(d)$ between the FMM and SASA simulation of the corresponding stack. The horizontal and vertical dashed lines show the set accuracy σ and corresponding critical distance d_{crit} , respectively.

frequency range⁴ $\nu \in [100 \text{ THz}, 500 \text{ THz}]$, equivalent to the approximate vacuum wavelength interval $\lambda \in [0.6 \mu\text{m}, 3 \mu\text{m}]$. For quantifying the difference between rigorous and semi-analytic simulations we will use the maximal difference between S-matrix components [145]

$$\Delta S_{ij}(d) := \max_{\omega} \left| |S_{ij}^{\text{rig}}(\omega, d)|^2 - |S_{ij}^{\text{SASA}}(\omega, d)|^2 \right|. \quad (4.25)$$

The analysis of numerical results is based on our publication [145].

4.2.1 Stacks of parallel and orthogonal nano-wires

We start with a stack two identical nano-wire metasurfaces with period $\Lambda = 300 \text{ nm}$, embedded symmetrically in glass and separated by a glass spacer. The wires are comprised of gold with length $l = 240 \text{ nm}$, width $w = 60 \text{ nm}$, and height (in z-direction) $h = 30 \text{ nm}$. We investigate two versions of this stack: parallel wires (the same metasurface twice, fig. 4.3.a) and orthogonal wires (the bottom metasurface rotated by 90° , fig. 4.3.b). The first stack is, in total, C_2 symmetric and second C_4 . Hence, the orthogonal wires behave isotropically and have only one unique coefficient in transmission, T_{xx} . In case of the parallel wires a second component, T_{yy} , has to be considered additionally, accounting for linear co-polarization.

In the given wavelength range and for $\Lambda = 300 \text{ nm}$ the Wood anomaly is safely excluded and the critical distance d_{crit} , eq. (3.30), shows flat behavior. Thus, choosing a high accuracy $\sigma = e^{-2\pi} \approx 2\%$, the strictest measure of d_{crit} is found by inserting the smallest wavelength $\lambda = 600 \text{ nm}$ which gives $d_{\text{crit}} = 423 \text{ nm}$. Testing the exponential behavior of d_{crit} as well as the numerical validity of the FMA we scanned the spacer distance d from 30 nm to 1000 nm .

⁴Here we use frequency instead of wavelength, because it reflects the harmonic dependence of the Drude-Lorentz oscillator model. When comparing to experimental data, later on, we will switch to wavelengths.

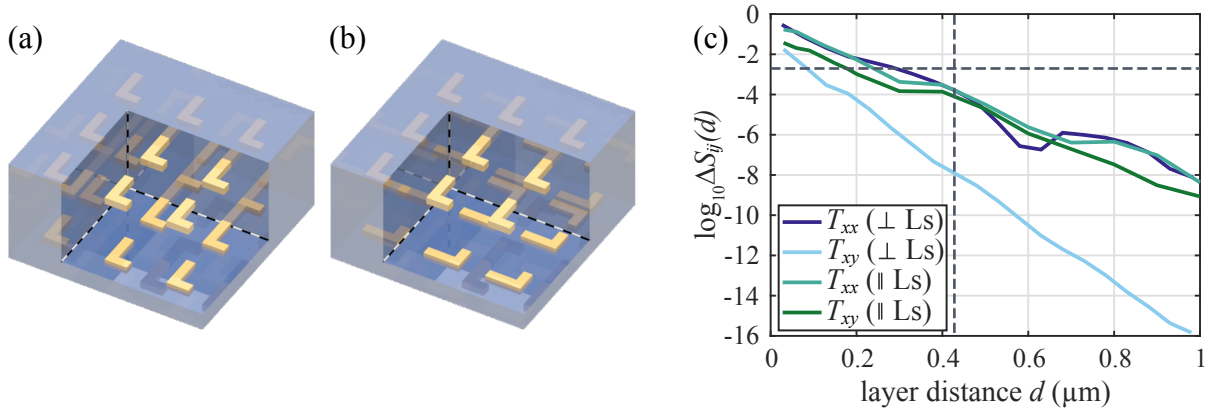


Figure 4.4: a) Rendering of a stack of two identical nano-L metasurfaces. b) the same stack as a) but with the lower layer rotated by 90° . c) Plot of the maximal difference $\Delta S_{ij}(d)$ between the FMM and SASA simulation of the corresponding stack. The horizontal and vertical dashed lines show the set accuracy σ and the corresponding critical distance d_{crit} , respectively.

First, we simulated the stack rigorously using the FMM [209, 218]⁵. The wires' gold was modeled using a gold Drude-Lorentz model and glass was defined as $n = 1.41$ (see appendix A.1). Then, we simulated an individual nano-wire metasurface, using FMM, and plugged it into SASA's framework. Here, we calculated the rotated metasurface using the rotation operation $\Omega_{\pi/2}$, eq. (4.20). The difference between the resulting S-matrix components $\Delta S_{ij}(d)$ is plotted for transmission in fig. 4.3.c) for both stacks.

We can clearly observe an exponential decay as expected from our derivation in eq. (3.29), similar for all components. The non-monotonic fluctuations of their decay are due to oscillations from occurring Fabry-Pérot resonances. Nevertheless, the difference $\Delta S_{ij}(d)$ drops below the limit set by σ when crossing the threshold of d_{crit} towards larger distances.

4.2.2 Stacks of parallel and orthogonal nano-Ls

For our next test we increase the complexity of the stack by breaking the symmetry of the metasurfaces, using Ls instead of wires. Using the same period as before, $\Lambda = 300$ nm, their arm lengths measure $l_x = 160$ nm and $l_y = 240$ nm, with a width $w = 60$ nm and height $h = 30$ nm. Once again, we consider two cases with parallel and orthogonal Ls, fig. 4.4.a) and b), respectively.

A single L particle has no in-plane symmetry and produces elliptically polarized light [200]. In addition to T_{xx} and T_{yy} it is therefore necessary to consider the cross-polarization component $T_{xy} = T_{yx}$. Intuitively, the same is true for stacked parallel Ls. The combination of orthogonal Ls, on the other hand, increases the symmetry of the stack, eliminating all cross-polarization components.

⁵see sec. 2.4

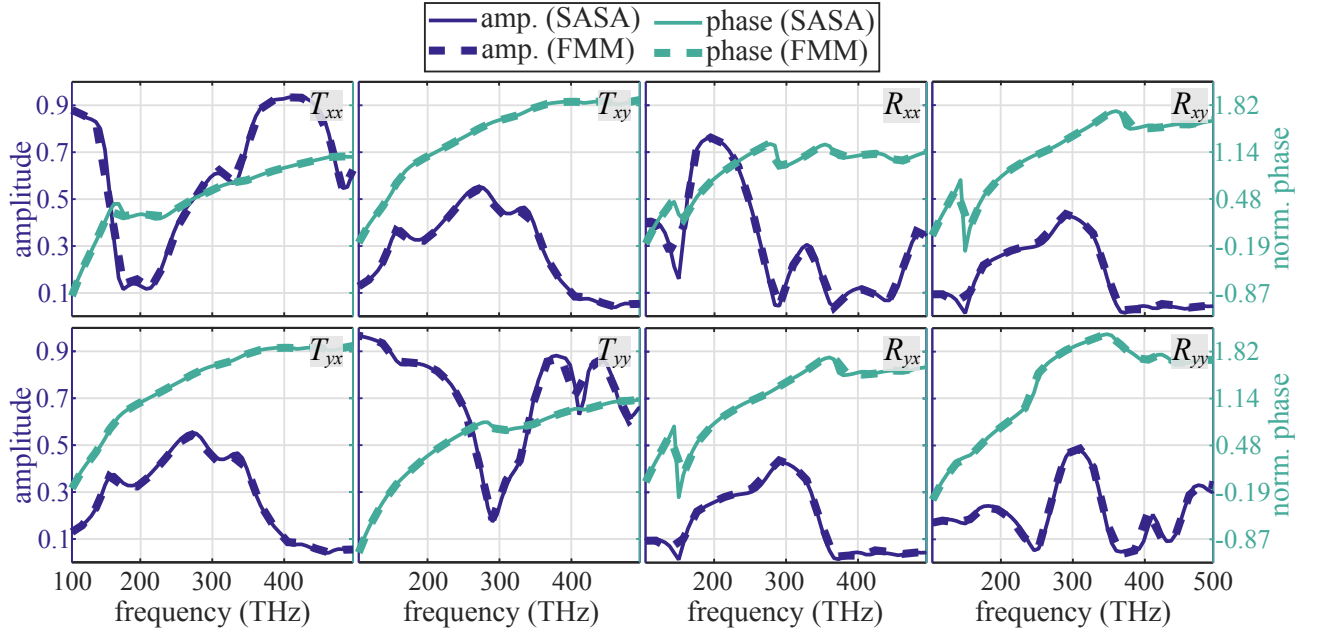


Figure 4.5: Plotted amplitudes (indigo lines) and phases (teal lines) of a stack of parallel Ls with a spacer distance $d = 150$ nm. The first and second column show the Jones matrix in forward transmission \hat{T}^f (components annotated in the corners). The third and fourth column show the Jones matrix in forward reflection \hat{R}^f .

Using the same methods and materials as in the previous section we simulated both stack variants rigorously with the FMM and semi-analytically with SASA. The rotation of the lower metasurfaces in SASA was performed once more using $\Omega_{\pi/2}$. The comparison of both approaches is plotted in fig. 4.4.c) for excitation with x-polarized light.

Very similar to the wire-metasurfaces we see an exponential decay of the error for increasing layer distances modulated by Fabry-Pérot oscillations. With the same accuracy level $\sigma = e^{-2\pi}$ and identical periods, d_{crit} is the same. Again, the error drops below σ when passing the threshold of d_{crit} . Interestingly, the difference of T_{xy} (cyan line) from the orthogonal Ls is not constantly zero. For distances $d < d_{\text{crit}}$ we see it grow until it crosses the σ threshold shortly after $d = 150$ nm. Although symmetry forbids cross-polarization it does appear in the near-field coupling regime of the stack. Hence, bi-anisotropic coupling might occur for very small spacer distances [120, 122, 181].

In the FMA regime ($d > d_{\text{crit}}$) symmetry fully determines polarization [146]. For closer insight we plotted amplitude and phase for forward transmission and reflection of both stacks at a distance of $d = 150$ nm. Fig. 4.5 shows the results for parallel Ls and fig. 4.6 for orthogonal wires. In all instances the phase was normalized by k_0 . At the scale of the plots FMM and SASA match very well, even for a spacer distance smaller than d_{crit} .

The symmetry of the stack of parallel Ls is clearly visible in fig. 4.5, with $T_{xx} \neq T_{yy}$, $T_{xy} = T_{yx}$ and $R_{xx} \neq R_{yy}$, $R_{xy} = R_{yx}$. The orthogonal counterpart shown in fig. 4.6 is C_4

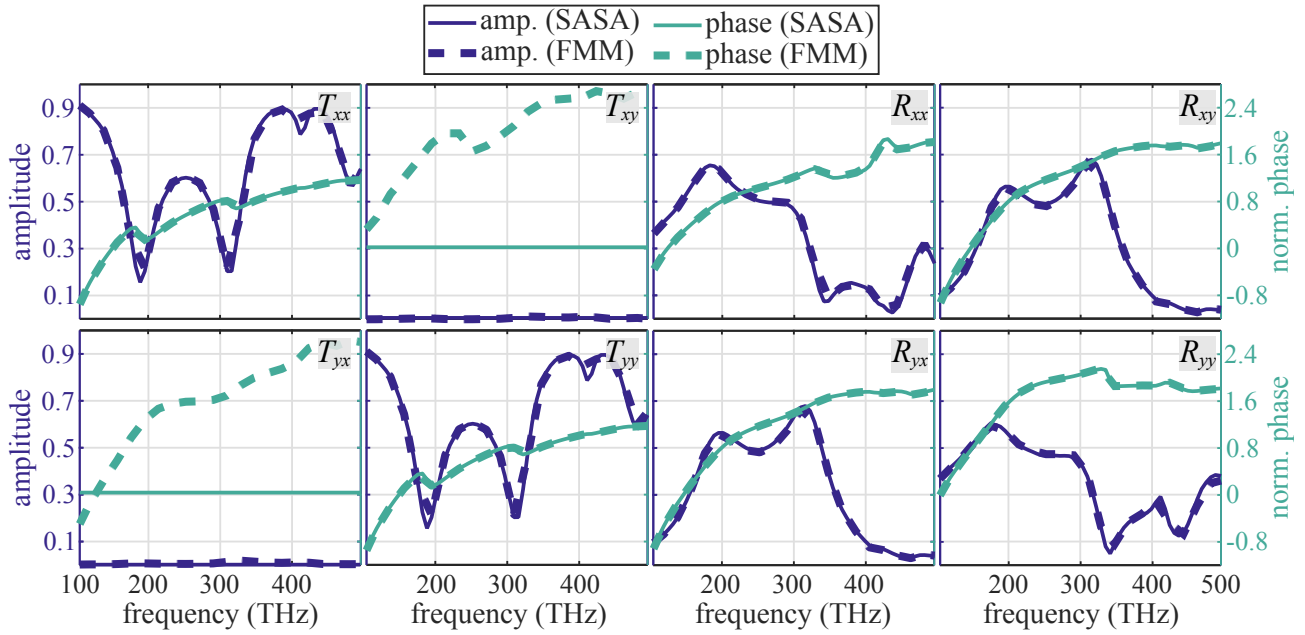


Figure 4.6: Plotted amplitudes (indigo lines) and phases (teal lines) of a stack of orthogonal Ls with a spacer distance $d = 150$ nm. The first and second column show the Jones matrix in forward transmission \hat{T}^f (components annotated in the corners). The third and fourth column show the Jones matrix in forward reflection \hat{R}^f . The cross-polarization of forward transmission resulting from SASA, both amplitude and phase, is *exactly* zero, due to symmetry. The FMM result is *numerically* zero in amplitude and, thus, shows an arbitrary phase.

symmetric in transmission, with $T_{xx} = T_{yy}$, $T_{xy} = T_{yx} = 0$, but has the same symmetry as the parallel version in reflection. This is due to the number of passes light travels through the stack. Reflected light sees the upper layer twice: when entering the stack and flipped when exiting the stack. These kinds of propagation related symmetry effects are discussed again in secs. 5.1 and 6.3.

4.2.3 Super-periodic stack of Ls and wires

One of the major advantages of stacking semi-analytically is the separate simulation of complex layers. This allows SASA to stack metasurfaces of unequal periods without the need for *super-cell* computations [151]. If the periods of two layers are different, their ratio will determine the necessary computational domain of a rigorous simulation. Then, the smallest commensurate number of periods from each layer defines their super-cell with a *super-period*. With ratios tending towards incommensurability the domain can get impractically large⁶. SASA completely circumvents this issue.

To check SASA's capability we simulated a stack of two metasurfaces with different periods

⁶In sec. 5.2 we will demonstrate the experimental realization of a pseudo-incommensurable stack.

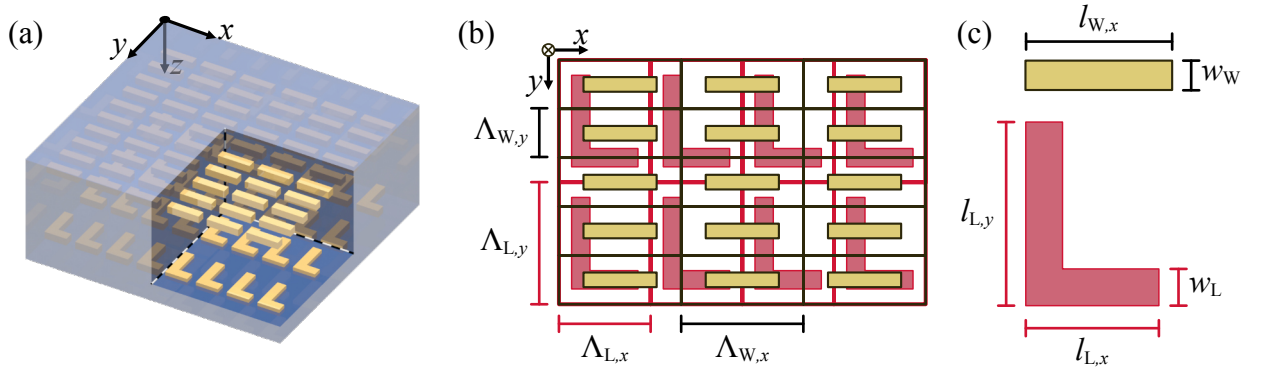


Figure 4.7: a) Rendering of a stack of a wire- and an L-metasurface. b) Illustration of the stack super-cell, comprised of the smallest commensurate number of periods from each layer. The lower layer of Ls is colored red and the upper layer of wires yellow. Each layer's unit cell is asymmetric with a different period in x- and y-direction. c) Sketch of each particle with annotations of parameter definitions.

and particles. The upper metasurface is comprised of gold wires and the lower of gold Ls (fig. 4.7.a,b). Both layers have the same height $h = 30$ nm. The array of wires has a period of $\Lambda_{W,x} = 333.3$ nm and $\Lambda_{W,y} = 133.3$ nm, a length of $l_{W,x} = 200$ nm and a width $w_W = 50$ nm. The array of Ls has a period of $\Lambda_{L,x} = 250$ nm and $\Lambda_{L,y} = 333.3$ nm, arm lengths of $l_{L,x} = 180$ nm and $l_{L,y} = 250$ nm, and a width $w_L = 60$ nm. The geometrical parameters are referenced in fig. 4.7.c). The super-period of both layers is $\Lambda_x = 1000$ nm and $\Lambda_y = 666.6$ nm. Embedding and spacer are again comprised of $n = 1.41$ glass.

Because a full FMM is impractical for this kind of super-cell we employed instead the Finite Difference Time Domain (FDTD)⁷ method. Using the FDTD software package *MIT Electromagnetic Equation Propagation* (MEEP) [237] we chose a spatial resolution of 2 nm for computing the S-matrices. This was necessary to run the super-cell calculation in parallel mode. The S-matrices were then constructed manually by calculating the x- and y-polarized zeroth order transmitted T_{ij} and the reflected R_{ij} complex fields, which resulted from x- and x-polarized normally incident plane wave excitation. Here, the reflected and transmitted fields are defined with respect to planes 20 nm in front and behind the metasurfaces, respectively.

For the individual arrays of wires and L's a single period was used in the FDTD, drastically decreasing the numerical efforts compared to the super-cell calculation necessary for the stacked system. Furthermore, due to the mirror symmetry with respect to the x-y-plane and the reciprocity [201] of the system the S-matrices of each individual layer could be constructed

⁷This is the only time in this thesis an FDTD is used.

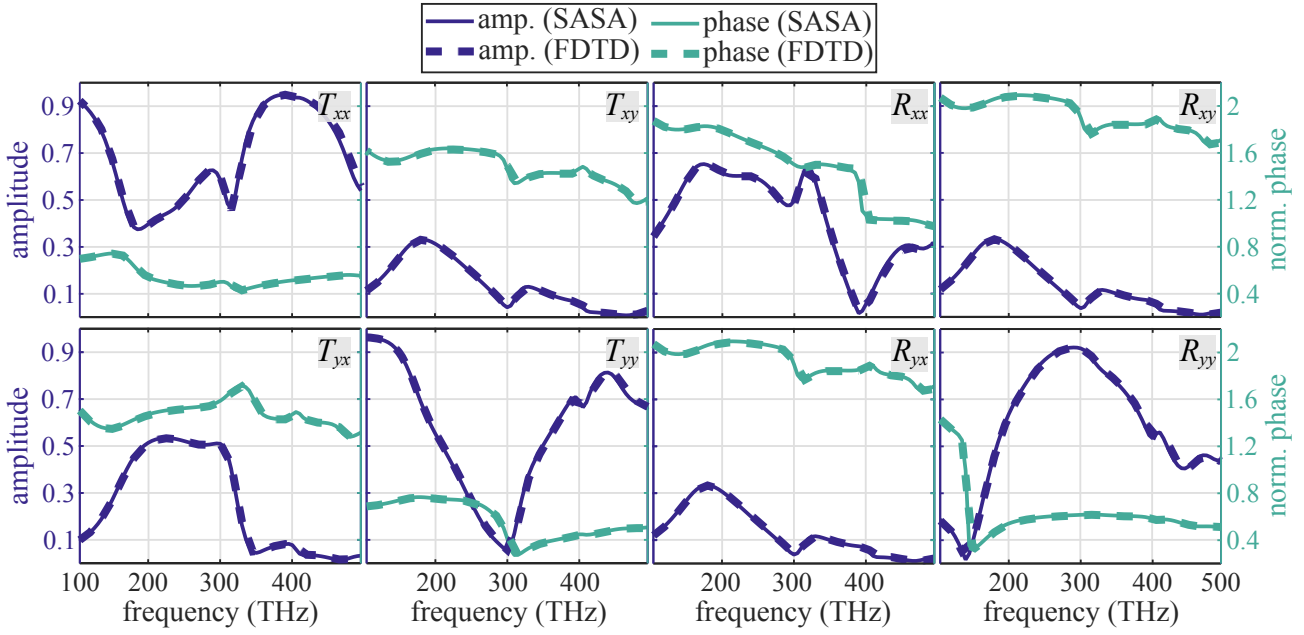


Figure 4.8: Plotted amplitudes (indigo lines) and phases (teal lines) of a stack of wires and Ls with a spacer distance $d = 250$ nm. The first and second column show the Jones matrix in forward transmission \hat{T}^f (components annotated in the corners). The third and fourth column show the Jones matrix in forward reflection \hat{R}^f .

based on the transmission and reflection coefficients for illumination in forward direction,

$$S_W = \begin{pmatrix} [T_{xx}^f] & 0 & R_{xx}^b & 0 \\ 0 & [T_{yy}^f] & 0 & R_{yy}^b \\ [R_{xx}^f] & 0 & T_{xx}^b & 0 \\ 0 & [R_{yy}^f] & 0 & T_{yy}^b \end{pmatrix}, \quad S_L = \begin{pmatrix} [T_{xx}^f] & [T_{xy}^f] & R_{xx}^b & R_{xy}^b \\ T_{xy}^f & [T_{yy}^f] & R_{xy}^b & R_{yy}^b \\ [R_{xx}^f] & [R_{xy}^f] & T_{xx}^b & T_{xy}^b \\ R_{xy}^f & [R_{yy}^f] & T_{xy}^b & T_{yy}^b \end{pmatrix}. \quad (4.26)$$

Only the coefficients in brackets had to be determined to get the full S-matrices. The highest estimate of the critical distance for this stack is determined by the largest period, i.e. $\Lambda_{W,x} = \Lambda_{L,y} = 333.3$ nm. With the other parameters set identical to the ones of the preceding sections the critical distance becomes $d_{\text{crit}} = 536.1$ nm. Furthermore, as we learned from the stacks prior, a high accuracy $\sigma = e^{-2\pi}$ is not strictly necessary, we chose for the L-wire stack $d = 250$ nm $< d_{\text{crit}}/2$.

The results in fig. 4.8 clearly show a good fit between the full FDTD and FDTD-based SASA. As a conclusion, for future stack designs we can choose σ one or two magnitudes higher, especially when considering experimental accuracy [146, 148, 151]. Concerning the polarization symmetry there is, again, a difference between transmission and reflection. In transmission, the symmetry is completely broken, whereas in reflection the symmetry of the Ls prevails. Strangely, both wires and Ls have at least one symmetry and it is counter-intuitive that the transmission Jones matrix is completely asymmetric. The reason behind this will be discussed

in sec. 5.1.

To conclude, we could show that SASA is numerically accurate within the FMA and works with data supplied by different methods. Furthermore, the S-matrix structure together with symmetry considerations make a good tandem in designing and analyzing the polarization of stacks.

5 | Experimental realization of complex stacks

In this chapter we apply the semi-analytic stacking algorithm (SASA) to two experimentally realized metasurfaces stacks. We will begin by analyzing the polarization response of a chiral metasurface stack comprised of twisted nano-wires. By taking advantage of the mathematical structure of S-matrices we will show how anisotropy can be designed from symmetry considerations. Based on measurements of a fabricated chiral metasurface stack we formulate a SASA model which we utilize to show the spacer height dependence of the stack’s polarization behavior. This is based on our publication “*Analyzing the polarization response of a chiral metasurface stack by semi-analytic modeling*” [238].

In the second half of this chapter we compose an isotropic metasurface stack with a pseudo-incommensurable period ratio. This ratio is as close as we can get to actual incommensurability within fabrication precision, but still creates a super-period that is orders of magnitude larger than that of the unit cells comprising each metasurface layer. Moreover, while experimentally demonstrating SASA’s capability, we test the validity of the FMA beyond its breaking point. We will analyze 23 versions of the pseudo-incommensurable stack, each varying in spacer height such that we can observe the transition between the coupling regimes discussed in sec. 3.4. This was published in our paper “*Experimental validation of the fundamental mode approximation for stacked metasurfaces and its application to the treatment of arbitrary period ratios*” [151].

5.1 Analysis of a fabricated chiral metasurface stack

Anisotropic metasurfaces can be engineered to manipulate polarization generating effects such as asymmetric transmission [114, 115, 239], dichroism [116, 117] or optical activity [118, 119]. If the geometry of the structures used is such that they cannot be superposed with their mirror, image they become chiral and can produce a chiral polarization response in turn [85]. To be intrinsically chiral, structures have to be three-dimensional or volumetric [121–124]. Nevertheless, two-dimensional structure designs have been demonstrated which also achieve a chiral polarization response through engineered near-fields [127, 132]. A prominent example are resonant particles such as asymmetric split ring resonators [131, 132]. Other approaches use *b*ianisotropically coupled bilayers of metasurfaces. Here, bianisotropy is induced through

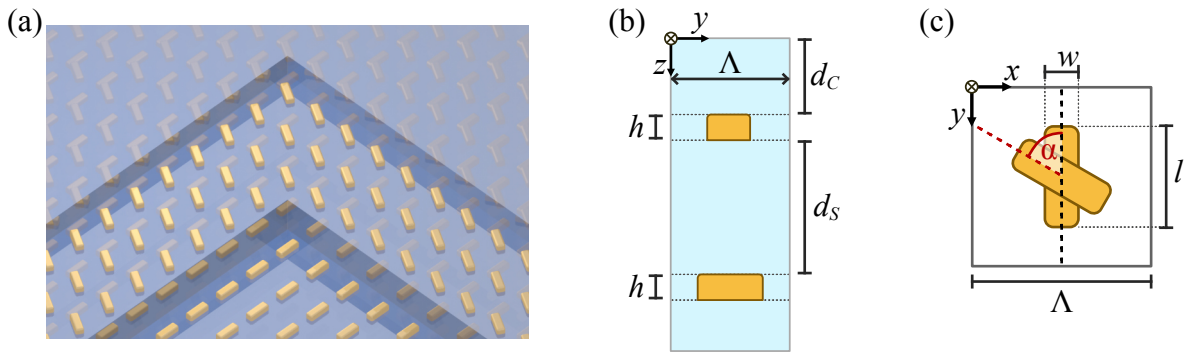


Figure 5.1: a) Rendering of a chiral metasurface stack comprised of twisted nano-wires. b) Sketch of a cut through the y - z -plane of the chiral stack showing its vertical structure. From top to bottom: cover layer of height d_C , twisted wire-metasurface of height h , spacer layer of thickness d_S , and wire-metasurface of same height h on a glass substrate. c) Sketch of the stacked unit cells of each metasurface layer. The wires in each layer are of identical size.

near-field coupling between the layers and can create or enhance chiral polarization effects [115,134–136]. Following this approach achiral particles like wires [137,143] or crosses [138,139] can be rotated with respect to each other to achieve chiral polarization effects [140].

Here, we consider two layers of wire-metasurfaces. To establish our model of the chiral stack we begin by considering two metasurfaces that are separated by a spacer of thickness d_S , a half space of glass as a substrate and air as the cladding. For the experimental realization we add a cover layer of thickness d_C at the top of the stack (fig. 5.1.a,b).

The lower metasurface is comprised of parallel nano-wires, measuring $w \times l \times h$, aligned to the y -axis, and arranged in a square lattice. The upper metasurface is of the same type as the lower one but its wires are rotated counterclockwise by angle α (fig. 5.1.c).

5.1.1 Deducing polarization from scattering matrix structure

In the following, we will use SASA to analyze the polarization behavior of the stack qualitatively from the structure of its S-matrices using only symbolic representations of their coefficients¹. Here, only the S-matrices of the metasurfaces are relevant. The homogeneous and isotropic layers only propagate the phase and do not affect the symmetry, as shown in eq. (4.10).

The S-matrices of two wire-based metasurfaces from fig. 5.1a,c) can be constructed analytically. We make the following assumptions: the particle geometry is identical in both metasurfaces, one has wires aligned to the y -axis, the other wires rotated by an angle α about the z -axis, and both are symmetrically embedded. Similar to the connection of unit cell symmetries and the corresponding Jones matrix symmetries [145,188] we can derive each of our S-matrices

¹Calculated using a Mathematica implementation of SASA.

by considering the polarization properties of nano-wires². A nano-wire will have a different polarization response depending along which axis it is excited. Furthermore, its response is reciprocal [201] making its S-matrix C_2 -symmetric [240]. Correspondingly, the S-matrix of a wire-metasurface S_W is written as

$$S_W = \begin{pmatrix} T_x & 0 & R_x & 0 \\ 0 & T_y & 0 & R_y \\ R_x & 0 & T_x & 0 \\ 0 & R_y & 0 & T_y \end{pmatrix}, \quad (5.1)$$

where the single-letter subscript of the coefficients gives credit to the cross-polarization free response. For the twisted wires we can approximate the rotation by an angle α of the wires in the unit cell by applying a rotation to S_W [145, 241]. However, this implies a rotation of the entire metasurface. The complex coefficients of the S-matrix will differ slightly to the unit cell rotated case. This is due to different alignment of the wires towards each other in the lattice [241]. Nevertheless, if no near-field coupling occurs between the two metasurfaces, the same polarization characteristic is achieved as in the unit cell rotated case. This is sufficient for our main objective, which is the structure of the S-matrix. Thus, using eq. (4.20) the S-matrix of rotated wires is *generally* given by

$$S_W^\alpha = \Omega_\alpha^{-1} S_W \Omega_\alpha = \begin{pmatrix} T_{xx}^\alpha & T_{xy}^\alpha & R_{xx}^\alpha & R_{xy}^\alpha \\ T_{xy}^\alpha & T_{yy}^\alpha & R_{xy}^\alpha & R_{yy}^\alpha \\ R_{xx}^\alpha & R_{xy}^\alpha & T_{xx}^\alpha & T_{xy}^\alpha \\ R_{xy}^\alpha & R_{yy}^\alpha & T_{xy}^\alpha & T_{yy}^\alpha \end{pmatrix}, \quad (5.2)$$

where the angular dependent coefficients read: $T_{xx}^\alpha = T_x \cos^2 \alpha + T_y \sin^2 \alpha$, $T_{yy}^\alpha = T_y \cos^2 \alpha + T_x \sin^2 \alpha$, $T_{xy}^\alpha = (T_y - T_x) \cos \alpha \sin \alpha$, $R_{xx}^\alpha = R_x \cos^2 \alpha + R_y \sin^2 \alpha$, $R_{yy}^\alpha = R_y \cos^2 \alpha + R_x \sin^2 \alpha$, and $R_{xy}^\alpha = (R_y - R_x) \cos \alpha \sin \alpha$. Notice that all cross-polarization components are identical. Hence, although S_W^α may produce cross-polarization it is unable to produce asymmetric transmission $\Delta_{x,y}$ (eq. (2.40) in sec. 2.3)³.

²See also the discussion on wire metasurfaces in sec. 4.2.1.

³The asymmetric transmission $\Delta_{x,y}$ vanishes for equal cross-polarization.

To judge the symmetry of the full stack we combine S_W and S_W^α with a spacer $S_{d_S,n}$ (eq. (4.5)).⁴ Performing the star product on the three S-matrices results in [151]

$$S_{\text{stack}} = S_W^\alpha * S_{d_S,n} * S_W = \begin{pmatrix} \bar{T}_{xx} & \bar{T}_{xy} & \bar{R}_{xx}^b & \bar{R}_{xy}^b \\ \bar{T}_{yx} & \bar{T}_{yy} & \bar{R}_{xy}^b & \bar{R}_{yy}^b \\ \bar{R}_{xx}^f & \bar{R}_{xy}^f & \bar{T}_{xx} & \bar{T}_{yx} \\ \bar{R}_{xy}^f & \bar{R}_{yy}^f & \bar{T}_{xy} & \bar{T}_{yy} \end{pmatrix}. \quad (5.3)$$

The explicit expressions of the resulting coefficients can be found in appendix A.4.1. Now asymmetric transmission Δ_x clearly emerges with $\bar{T}_{xy} \neq \bar{T}_{yx}$ and, thus, potentially produces chiral light.⁵ This is somewhat surprising because each individual layer is evidently achiral. The answer lies in the consecutive interactions with each layer. As discussed in sec. 4.1.3 whether the electromagnetic fields are transformed or S-matrices (i.e. layers) is relative. Hence, each interaction of a field with an S-matrix can be understood as a transformation that maps the S-matrices' symmetry onto the field symmetry. Each asymmetry accumulates in an increasingly more broken symmetry of the fields. If we imagine x- or y-polarized light interacting with S_W^α , both will experience the same symmetry operation. However, because of the C_2 symmetry of S_W the already symmetry-broken fields will interact differently, depending on their initial polarization.⁶ This presents us with an avenue towards asymmetric transmission, and in that regard chirality, based on (multi-) layered symmetry. This is conceptually different to choosing intrinsically chiral meta-atoms [114, 115, 239, 242] or designing bianisotropic coupling in metamaterials [120, 243–246].

In the following section we will test whether the predictions using purely symbolic expressions hold true for a fabricated version of the stack discussed above.⁷

5.1.2 Analysis of a fabricated stack by semi-analytic modeling

It was shown experimentally by Zhao et.al. [142] that multiple layers of successively rotated nano-wires can form a so called twisted metamaterial with a chiral polarization response in the absence of near-field coupling. In addition, their work demonstrated that lateral layer alignment during fabrication could be ignored in this type of stacked metasurface [143]. Both cases are, in essence, demonstrations of the FMA. Layer alignment is irrelevant because fundamental mode coupling homogenizes each metasurface.⁸

⁴While the spacer is physically necessary for the validity of the FMA we can ignore the cover layer on top.

⁵That is, light with a handedness, such as circularly or elliptically polarized light.

⁶The interaction can be understood as a coupling between dipoles of the wires and the incident fields [38, 39]. Depending on polarization and orientation of the wires there will be a different "preferred" direction.

⁷A comparison between a twisted-wire-stack modeled with unit cell rotation versus the analytic layer rotation can be found in appendix A.3.

⁸This reflects the conceptual transition shown in fig. 3.3.

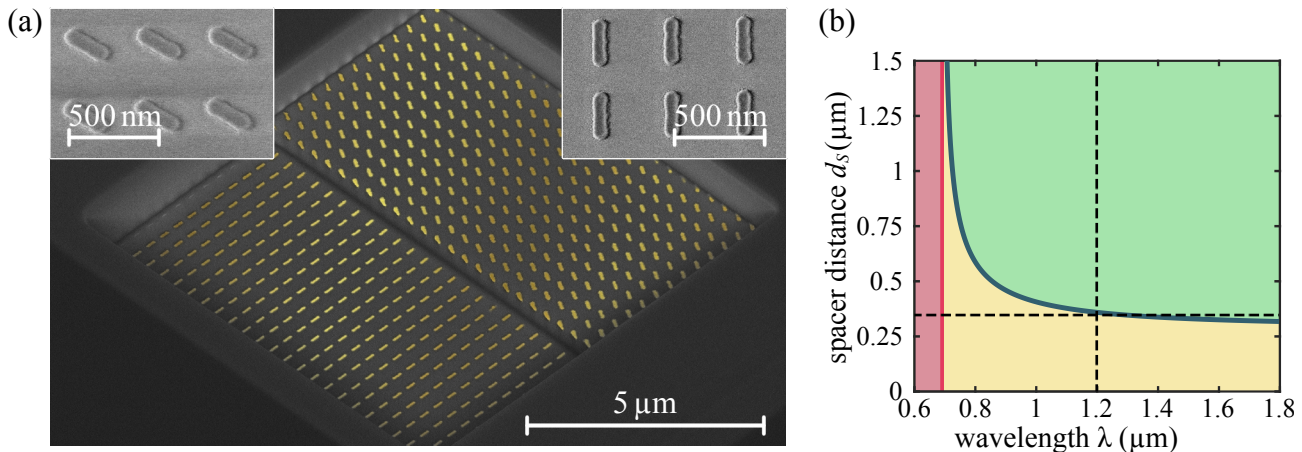


Figure 5.2: a) Scanning electron microscope (SEM) image of the fabricated twisted-wire stack. The two insets in the upper corners show SEM images of the upper (left) and lower (right) metasurface layer. The main SEM image shows a focused ion beam (FIB) cut, revealing the complete stack. Nano-wires were colored golden for better visibility. b) Coupling phase diagram (CPD) of the fabricated stack with period $\Lambda = 400$ nm and d_{crit} -accuracy $\sigma = 1\%$. The horizontal dashed line shows the spacer height $d_s = 345$ nm. The vertical dashed line shows the corresponding wavelength cut-off for FMA validity.

Here, we will analyze a stack of only two twisted wire-metasurfaces in order to understand, precisely, how the chiral response depends on the layer separation. For this, we fabricated a stack resembling the one shown in fig. 5.1.a) and analyzed it both experimentally, rigorously with an FMM, and approximately using SASA.

We chose equal periods with $\Lambda = 400$ nm and aligned unit cells for both metasurfaces. The rotation angle of the upper layer metasurface's wires was set to $\alpha = 60^\circ$. During fabrication of each metasurface we applied a two-step electron beam lithography process.⁹ They were structured by exposure of a two layer electron beam resist (150 nm Allresist ARP617.08 and on top of that 100 nm Allresist ARP6200.4) with a variably shaped electron beam (Vistec, SB 350). This was followed by chemical development and coating by gold evaporation. Finally, we applied a lift-off process to remove the resist. During this process we produced two fields of the same metasurface as the lower layer of the stack. The spacer layer was spin-coated (Futurrex IC1-200) on top of both fields, tempered at 200 °C for half an hour and etched to the desired spacer height using Argon ion beam etching. We produced two versions of the stack: spacer thickness $d_s = 40$ nm on one field and $d_s = 345$ nm on the other.

Then, the top-layer metasurface was fabricated with the same processes as the lower one. In this way, we made sure that both versions were comparable with nearly identical structures. Finally, a cover layer was spin-coated to $d_C = 900$ nm. In total the field size of each fabricated sample was 2×2 mm².

⁹Sample fabrication was performed by Stefan Fasold at facilities of the Institute of Applied Physics in Jena.

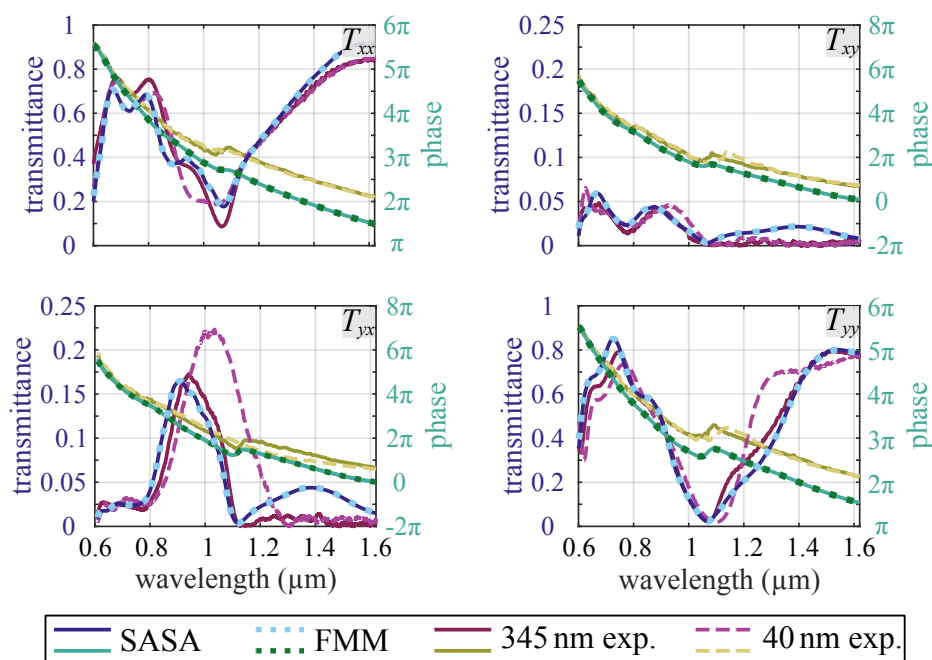


Figure 5.3: Transmittance (right axes) and phase (left axes) of the fabricated stack with $d_S = 345$ nm based on SASA (indigo and teal solid lines), FMM (cyan and green dotted lines) and experiment (wine and olive solid lines). For comparison, the stack version with $d_S = 40$ nm is plotted as dashed lines (rose and yellow). Blue-tinted and red-tinted line colors refer to transmission. Green and yellow tints refer to phase. The annotation in the top right corner of each plot denotes the corresponding Jones matrix coefficient.

A scanning electron microscope (SEM) image of the resulting stack with $d_S = 345$ nm is shown in fig. 5.2.a), where parts of the layers were removed with a focused ion beam (FIB) to reveal the structures underneath. The average dimensions of the nano-wires of both layers, acquired by evaluation of the SEM images, are almost identical, with: $l_L = 235$ nm, $w_L = 75$ nm, $h_L = 50$ nm, $l_U = 225$ nm, $w_U = 75$ nm, and $h_U = 75$ nm, with l , w , and h defined in fig. 5.1.b,c). The subscripts L and U denote the lower and upper layer, respectively.

With a common period of $\Lambda = 400$ nm the CPD of the stack (fig. 5.2.b) tells us, that the spacer version $d_S = 40$ nm is definitely near-field coupled. The larger spacer, however, lies with $d_S = 345$ nm at the asymptotic boundary of d_{crit} . As we saw in sec. 4.2, $d_S = d_{\text{crit}}/2$ could still be tolerable. Whether this and the presence of the diffraction regime for $\lambda < 700$ nm disrupts our SASA model is an open question.

We characterized the stack in our target wavelength range from 600 nm to 1620 nm using an interferometric setup¹⁰ which measures both the transmitted intensity (transmittance) and phase in a linear polarization basis.¹¹ The diameter of the characterization beam on the sample

¹⁰Further details on the setup can be found in [122, 247].

¹¹The measurement was performed by Matthias Falkner at the Abbe Center of Photonics, Jena.

was 2 mm, making sure that it was fully illuminated and no finite-size effects occurred. The results for both variants of the stack are plotted in fig. 5.3, showing the fully reconstructed Jones matrix in forward propagation. The plots show the transmittance as defined in sec. 2.2.2 because measurements detect *intensities* instead of the amplitudes [146].

For comparison, we developed a model of the $d_S = 345$ nm version of the stack as a sequence of layers. Since the sample was fabricated and characterized on a glass wafer, the substrate was assumed to be a glass half-space. Both the spacer and the cover layer on top of the stack were modeled analytically using equation (4.5). Likewise, the interfaces were calculated using the interface S-matrix S_i (4.6). The stack's S-matrix S_{stack} is therefore composed by the cascaded star product

$$S_{\text{stack}} = S_{n_{\text{air}},n_{\text{SiO}_2}} * S_{d_C,n_{\text{SiO}_2}} * S_U * S_{d_S,n_{\text{SiO}_2}} * S_L, \quad (5.4)$$

where $S_{d_C,n_{\text{SiO}_2}}$ and $S_{d_S,n_{\text{SiO}_2}}$ denote the S-matrices of cladding and spacer and $S_{n_{\text{air}},n_{\text{SiO}_2}}$ the cladding interface to air. The metasurfaces' S-matrices are represented by S_L and S_U , referring to the lower and upper metasurface, respectively.

The S-matrix coefficients of both metasurfaces S_L and S_U were calculated numerically as single layers, using a self-implemented Fourier-Modal-Method (FMM) [218,248] and the geometric parameters from SEM measurement. Based on a convergence test the FMM was truncated at 15 Fourier orders (in x- and y-direction). In case of the upper metasurface the nano-wires were rotated individually in their unit cell in adaption to the fabricated sample. To account for the corner rounding of the fabricated structures a curvature radius of 25 nm was assumed for the corners of our model particles. As material parameters we used measured ellipsometric data of evaporated gold and spin-on glass as they result from our fabrication process [249].

In addition to SASA a rigorous FMM of the full stack was performed to determine the accuracy of the semi-analytical model. A rigorous FMM takes all evanescent and propagating orders into account up to a set truncation limit (here: 15 Fourier orders) [218,236]. Hence, a direct comparison to SASA will help to indicate the validity of the FMA. As a side note, the computation times of the rigorous FMM and SASA are compared in the appendix A.2.4.

The resulting transmittance and phase plots of both methods are shown together with the experimental results in fig. 5.3 [146]. SASA and FMM results coincide perfectly, with respect to the scale of the plot, both in transmittance and phase, indicating the validity of the FMA. Notably, all the main features of the measured curves were reproduced. The difference to the measured co-polarization components T_{xx} and T_{yy} is comparatively small in transmittance and almost identical in phase. The difference to the measured cross-polarization components T_{xy} and T_{yx} is more noticeable pertaining to their relatively low transmittance. The results confirm the predicted asymmetric polarization behavior. Moreover, SASA holds in the experimental test to both FMM and actual measurement data. The FMA coupling condition imposed by d_{crit} seems to hold also for shorter wavelengths. Furthermore, since the Wood anomaly has no

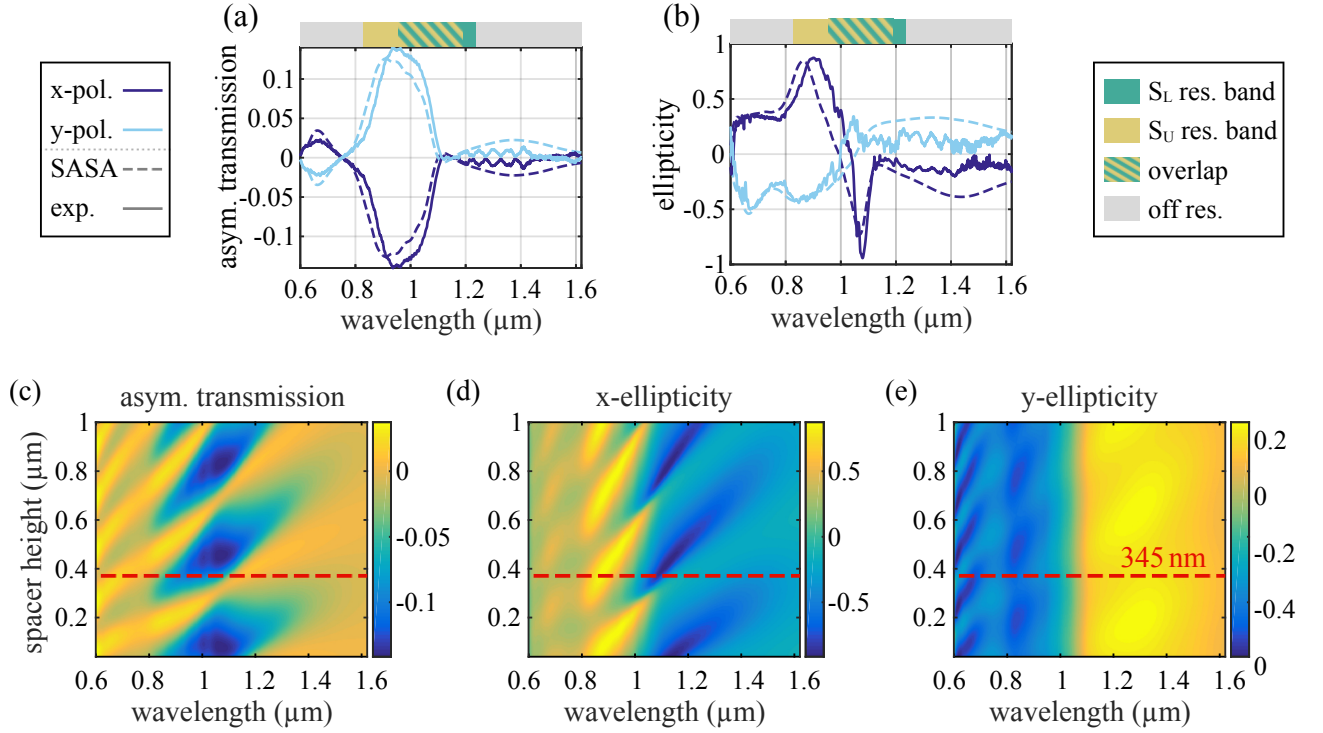


Figure 5.4: Linear asymmetric transmission (a) and ellipticity (b) derived from measurement (solid lines) and SASA results (dashed lines). Indigo indicates x -polarized and cyan y -polarized incident light. The colorbar on top of each plot shows the resonant bands determined by the FWHM for $\min(T_{xx})$ and $\min(T_{yy})$ of the upper and lower metasurfaces. (c)-(e): Asymmetric transmission and ellipticity scanned over the spacer thickness from 40 nm to 1000 nm. (c) Asymmetric transmission scanned for x -polarization. (d) and (e) display ellipticity for x - and y -polarization. The red dashed line in each surface plot marks a spacer thickness of $d_S = 345$ nm.

noticeable effect in either experimental or simulated results, the first diffraction order of this particular stack appears to be negligible.

Compared to the $d_S = 40$ nm version of the stack we can identify noticeable differences in the measured spectra. In particular, the peak in T_{yx} exhibits a redshift of 150 nm for the thin spacer stack. This indicates near-field coupling between the metasurfaces of the $d_S = 40$ nm stack.

In order to analyze the polarization behavior of the stack we derived its asymmetric transmission $\Delta_{x,y}$, eq. (2.40), and ellipticity $\epsilon_{x,y}$, eq. (2.41), in forward transmission. In fig. 5.4.a) we see that asymmetric transmission is strongest in the resonants bands of both layers, with an extremum at $\lambda_0 = 950$ nm reaching up to $\pm 12\%$. In the same spectral region, we see a strong conversion from x -polarized to elliptically polarized light that is almost circular (fig. 5.4.b). The ellipticity for incident y -polarized light is more shallow and does not go beyond ± 0.5 . This is explained by the cross-polarization, in combination with the C_2 symmetric lower metasurface, giving light a different twist depending on the incident polarization.

It is necessary to clarify the role of the spacer for the polarization behavior. Although it does not possess any S-matrix symmetry its height and dispersion affect the phase of light. Therefore, we varied thickness d_S from 40 nm to 1000 nm in 1 nm steps using SASA. As discussed in sec. A.2.3, we applied the associativity of the star product [236] for greater efficiency,

$$S_{\text{stack}}(d_S) = ((S_{n_{\text{air}}, n_{\text{SiO}_2}} * S_{d_C, n_{\text{SiO}_2}} * S_U) * S_{d_S, n_{\text{SiO}_2}}) * S_L. \quad (5.5)$$

Based on this we calculated Δ_x and $\epsilon_{x/y}$ as a function of d_S , (fig. 5.4.c-e). The resulting Fabry-Pérot type patterns show that the polarization characteristic of this stack is highly sensitive with respect to the spacer thickness. Both the emerging polarization states and the dispersion of the asymmetric transmission change as the Fabry-Pérot condition changes with the spacer thickness. Moreover, the SASA result reveals that the ellipticity in y -polarization retains its flat characteristic from 1000 nm to longer wavelengths for different spacer thicknesses. Evidently, y -polarized light is converted to a slightly elliptical state mostly determined by the geometry of the stack.¹² At the short wavelength edge of the overlap resonant band the ellipticity switches its sign due to the phase change between the resonance bands (fig. 5.4.b).

Figs. 5.4.c) shows that the asymmetric transmission $\Delta_x = -\Delta_y$ is sensitive to the chosen spacer thickness d_S . Indeed, a different choice of d_S could almost result in Δ_x vanishing [146]. Thus, when designing chiral stacks of this type it is insufficient to define the geometry of the structure, and it is necessary to also optimize the separation between the metasurfaces.

In conclusion, the spacer thickness of complex metasurface stacks represents another degree of freedom in the design of sophisticated layered media. While controlling the presence of Fabry-Pérot resonances it can also be utilized to enhance otherwise negligible polarization effects.

5.2 Incommensurable period ratios and experimental test of the FMA

In the larger context of this thesis we will experimentally explore the conceptual transition discussed in sec. 3.3.1 (fig. 3.3). Comparing our semi-analytic data with experimental results we show the limits of the FMA and demonstrate its use as an analytic tool even beyond its validity. Although there are works that thoroughly discuss the modal theory behind the FMA [77, 157, 158, 222] or test its accuracy as a numerical and homogenization method [145, 222, 250] there seems to be a lack of experimental studies on its validity.

The specific stack example in this section addresses a parametric blind spot when designing

¹²It should be noted that in this particular region both cross-polarization components of the stack almost vanish.

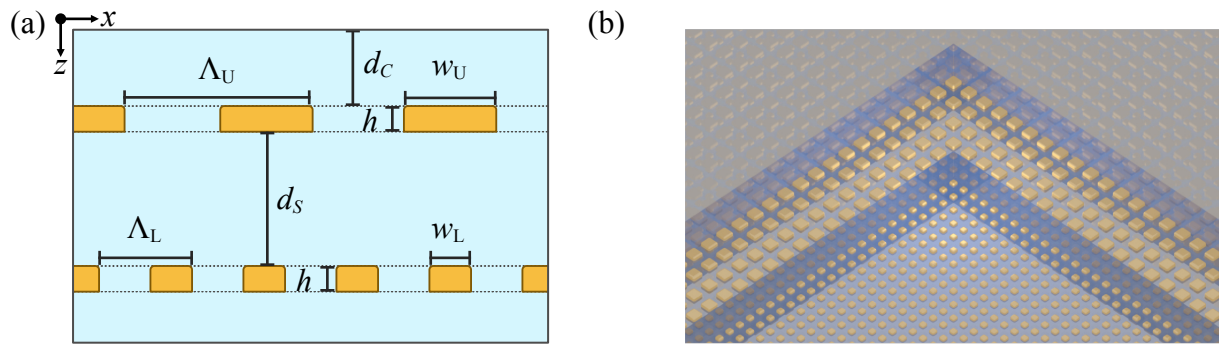


Figure 5.5: a) Vertical cut through the x - z -plane of the stack. The annotations define all necessary geometric parameters. b) Rendering of the stack design showing two layers of gold-patch-metasurfaces embedded in glass. Substrate and cladding are glass and air, respectively.

periodic metasurface stacks. As mentioned before in sec. 4.2.3, computational issues arise when stacking metasurfaces whose periods have an *incommensurable*, i.e. non-rational, period ratio. As a result a super cell across the entire stack is no longer properly defined as it tends to infinity. The computational domain would have to be extremely large, making rigorous simulations of the stack impractical. Moreover, the computational challenge is not only restricted to exact incommensurable ratios. Rather, there is a range of ratios close to incommensurability that still demand vast super-cell dimensions.

Using SASA we demonstrate both the design and analysis of incommensurable metasurface stacks, applicable to arbitrary period ratios.

5.2.1 Constructing a pseudo-incommensurable stack

As the main subject of our argument we concentrate on a four-layer stack comprised of two different isotropic periodic metasurfaces. As before, they are separated by a spacer layer of thickness d_S and have a cover layer of thickness d_C on top (fig. 5.5). Each metasurface is a periodic array comprising square nano-patches made of gold. This creates an overall isotropic stack allowing us to ignore polarization in this particular case [188, 238, 251]. Nevertheless, everything that follows can be adapted to the anisotropic case as well.

Square nano-patches present three degrees of freedom for the geometric design of each metasurface: height h , particle width w , and period Λ . For our model system we chose an equal height $h = 30$ nm for both metasurfaces. Aiming for plasmonic resonances at the boundary between VIS and NIR we selected the widths of the upper and lower metasurface to be $w_U = 160$ nm and $w_L = 70$ nm, respectively (fig. 5.5.a). With $h \ll w_{U,L}$ the lateral dimensions $w_{U,L}$ will predominantly determine the resulting dispersion.

Our geometrical design targets the metasurfaces' periods ratio Λ_U/Λ_L . If it becomes incommensurable the super-period grows to infinity and loses its meaning [151]. Then, a physically

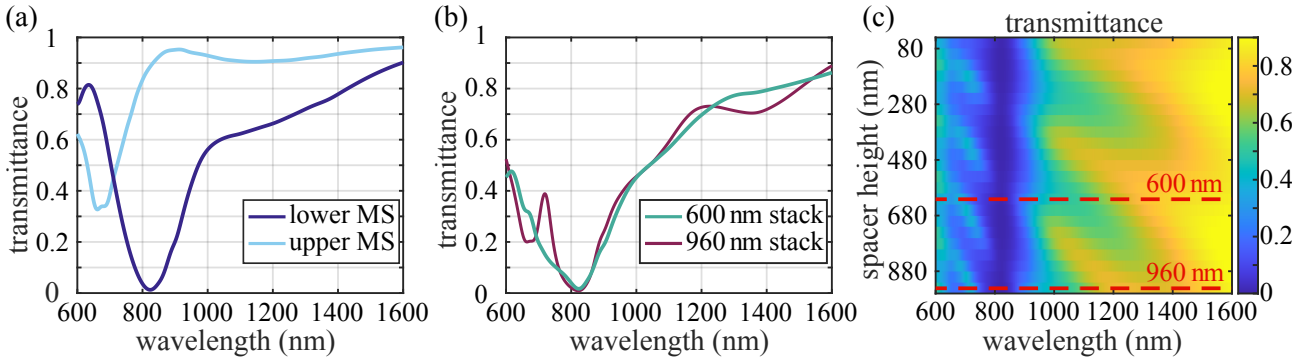


Figure 5.6: Simulation results of the stack: a) Upper (red line) and lower metasurface (blue line) as single layers. b) SASA result of the full stack with $d_S = 600$ nm and $d_S = 960$ nm. c) SASA result scanning the spacer height d_S from 80 nm to 960 nm in 40 nm steps. The red dashed lines reference the results of b).

accurate simulation of such a stack becomes nearly impossible using rigorous numerical methods. Here, we chose the periods of the lower and upper metasurface to be $\Lambda_U = 341$ nm and $\Lambda_L = 200$ nm. This value of Λ_U resembles the closest we can get to $\pi \times 100$ nm with 1 nm precision (limited by fabrication). The respective ratio of $\Lambda_U/\Lambda_L = 1.705$ produces a super-period of $68.2 \mu\text{m}$. The resulting computational domain is two orders of magnitude larger than the individual periods $\Lambda_{U,L}$, making it practically infinite with respect to the wavelength. Thus, we term this type of period ratio *pseudo* incommensurable [151]. We used the FMM [228, 236] to simulate the individual metasurfaces embedded in glass. In all simulations we used the Sellmeier equation for dispersive fused silica [252] and the permittivity of gold as produced by our fabrication machines [249].¹³

To be comparable to actual samples we added a glass cover layer of thickness $d_C = 500$ nm with an interface to air on top of each metasurface, using SASA. As shown in fig. 5.6.a) the resonances of both metasurfaces are positioned close to one-another (at approximately 820 nm and 660 nm) with overlapping flanks. Combined in the stack this creates a noticeable peak between the two single layer resonances (fig. 5.5.b). The prominence of the peak then largely depends on Fabry-Pérot resonances determined by the separation distance of the layers (fig. 5.6.b,c).

Employing SASA we assembled the full stack based on fig. 5.6.a), using the single layer S-matrices and the parameters listed above. The full stack S_{stack} is a combination of: the cover interface $S_{n_{\text{air}}, n_{\text{SiO}_2}}$, the cover layer $S_{d_C, n_{\text{SiO}_2}}$, the upper metasurface S_U , the separating spacer layer $S_{d_S, n_{\text{SiO}_2}}$, and the lower metasurface S_L

$$S_{\text{stack}} = S_{n_{\text{air}}, n_{\text{SiO}_2}} * S_{d_C, n_{\text{SiO}_2}} * S_U * S_{d_S, n_{\text{SiO}_2}} * S_L. \quad (5.6)$$

¹³That is, from the gold evaporation of the facilities at the Institute of Applied Physics, Jena.

Varying d_S from 80 nm to 960 nm, the resulting Fabry-Pérot fringe pattern variably subdues or enhances the overlap peak in the resonance region (fig. 5.6.c) [151].

5.2.2 Experimental results

Based on our design parameters we fabricated the metasurfaces stack on a fused silica wafer, characterized it using SEM, and measured its transmittance interferometrically¹⁴. From the results of the SEM evaluation of the sample we derived updated model parameters and performed SASA simulations once more in order to compare them to the experimental findings.

Fabrication

The main goal of our fabrication effort was the realization of 23 metasurface stacks with identical layers and varying spacer thickness from 80 nm to 960 nm in 40 nm steps. For comparison we produce reference fields of the individual metasurfaces comprising the stack, in order to confirm the predicted structural and optical properties.

Starting with a standard 4 inch circular fused silica wafer, we divided our fabrication design into 24 equal sections around the polar grid of the wafer. This was comprised of 23 individual stack sections and a 24th section intended for reference fields. The lower metasurface layer was fabricated in parallel, processing all sections at once. This way, we can assume these metasurfaces to be structurally identical. The reference field then viably represents this metasurface layer for all stack variants [151].

Our fabrication technique of each metasurface employed electron beam lithography. Each metasurface started as a $2\text{ mm} \times 2\text{ mm}$ field comprised of a two layer electron beam resist (150 nm Allresist ARP617.08 and 100 nm Allresist ARP6200.4). The desired periodic patch-geometry was then written onto each field by exposing the resist with a variably shaped electron beam (Vistec, SB 350). After chemical development of the resist we coated the sample with 30 nm gold by evaporation and removed the resist by applying a lift-off process [151].

Next, a uniform layer of SiO_2 was deposited on the wafer to a height of $1\ \mu\text{m}$, using chemical vapor deposition (CVD). In order to achieve the desired spacer heights we first covered one half the wafer and removed 480 nm SiO_2 on the other half via ion beam etching (Oxford Ionfab 300 using 400 eV Ar-ions). We then rotated the cover by 15° etched 40 nm and repeated this step 10 more times, resulting in a height distribution from 80 nm to 960 nm in 40 nm steps. By performing the etching steps 11 times in total the reference section (the 24th) was left at the original SiO_2 height of $1\ \mu\text{m}$ [151].

Similarly, we fabricated the upper metasurface on top of the spacer layer of the 23 stack

¹⁴Fabrication and optical measurement were again performed by Stefan Fasold and Matthias Falkner, respectively. SEM images were obtained with support by Michael Steinert at the Abbe Center of Photonics.

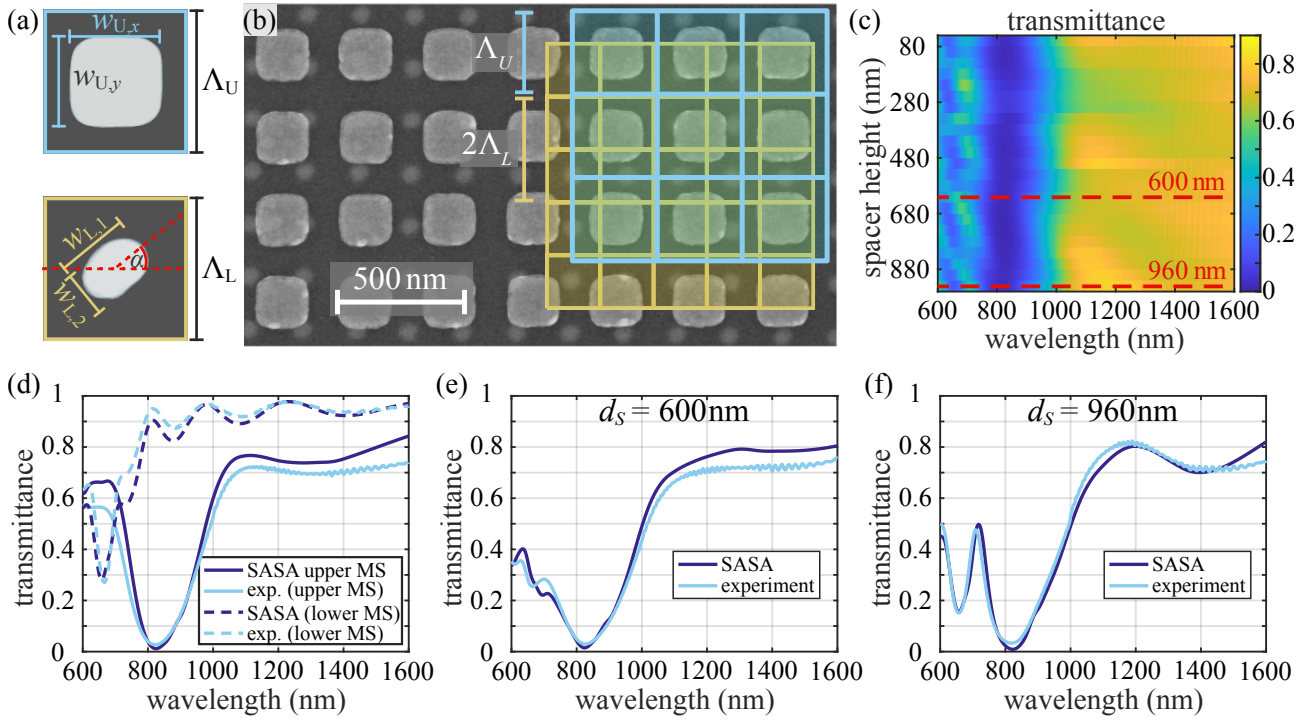


Figure 5.7: Experimental results and comparison to the adapted SASA model. a) Unit cells extracted from averaging the particles in SEM images. b) SEM image of a stack with spacer height ($d_S = 120$ nm) before the cladding layer was added. The blue and the yellow grid represent the lattices of the upper and lower metasurface, respectively. c) Surface plot of the measured transmittances of all 23 stack variants with spacer heights d_S from 80 nm to 960 nm in 40 nm steps. The red dashed lines reference the results in e) and f) at $d_S = 600$ nm and 960 nm. d) - f) Direct comparison between measurement (cyan) and SASA (indigo) results: d) Individual single layer results for the lower (dashed line) and upper (solid line) metasurface. e) Stack with $d_S = 600$ nm. f) Stack with $d_S = 960$ nm.

sections, directly above the lower fields. The reference field of that metasurface was placed on the 24th section with a large displacement to the other reference metasurface. We employed the same fabrication process as before. Finally, we added a 500 nm SiO_2 cladding layer covering the entire sample using CVD [151].

In summary, we fabricated 23 stacks in total, each varying in spacer height. A 24th sample was fabricated to provide reference fields of the two metasurfaces comprising each of the 23 stacks. An SEM image depicting a top view of one exemplary stack with spacer height of $d_S = 120$ nm is shown fig. 5.7.b) with the extracted average particles in 5.7.a).

Measurement and comparison

By averaging over the particles in SEM images we measured their respective widths, $w_L = 70$ nm for the lower metasurface and $w_U = 180$ nm for the upper metasurface. While the particle size

can be affected by many fabrication parameters, deviations in the periods are defined by the calibration of the electron beam lithography system only. Since this error is well below the error of the SEM calibration, the periods will be considered to be exact. As indicated by the illustration of the blue and yellow grid in fig. 5.7.a) we achieved pseudo incommensurability. Therefore, there is no possibility to superposition both lattices so that their boundaries form a common frame within less than $68.2\ \mu\text{m}$ edge length [151].

Using a home-built interferometric characterization setup we measured the normalized transmittance of each field of the sample in a spectral interval from 600 nm to 1600 nm.¹⁵ The results for all 23 stack variants sorted by height are summarized in fig. 5.7.c). The surface plot clearly reproduces the Fabry-Pérot fringe pattern predicted by our initial design (fig. 5.6.c). There are some visible discontinuities, likely due to fabrication variances.

The lobes on the right side of the surface plot (from 1000 nm to 1600 nm) modulate the monotonic off-resonance dispersion. On the left of the surface plot (from 600 nm to 800 nm) the lobes alternately subdue and enhance the overlap peak between the two metasurface resonances.

We compared measurement results of the individual metasurfaces layers' transmittances from the reference section of the wafer to our single layer FMM simulations (fig. 5.7.d). Our original model only needed to be adapted with regard to the cladding height. The cladding deviated by approximately 70 nm of optical path length. All other parameters were comparable to our experimental results. Thus, using the same single layer FMM simulations we added the updated cladding using SASA. Note that the lower reference metasurface is covered by an additional $1\ \mu\text{m}$ of glass due to the fabrication steps explained in the previous section.

Judging from fig. 5.7.d-f), the fit between experiment and SASA is very good. We can identify the plasmonic metasurface resonances at 660 nm and 820 nm of the lower and upper metasurface, respectively. Moreover, the sinusoidal modulation on the right of each plasmonic resonance are the expected Fabry-Pérot resonances. They are more frequent for the lower metasurface since it is covered by a total of 1570 nm of glass in contrast to the upper one with only 570 nm [151].

Similarly, SASA and the experiment match very closely for the full stacks (figs. 5.7.e) and fs). Each plot shows a slice from 5.7.c), one at $d_s = 600\ \text{nm}$ and the other at 960 nm. First, this proves the validity of our model. Second, it confirms the assumption of similarity between the reference metasurfaces and their counterparts in the stacks. Furthermore, this demonstrates that we can predict and realize the optical behavior of pseudo-incommensurable stack super cells using a SASA [151].

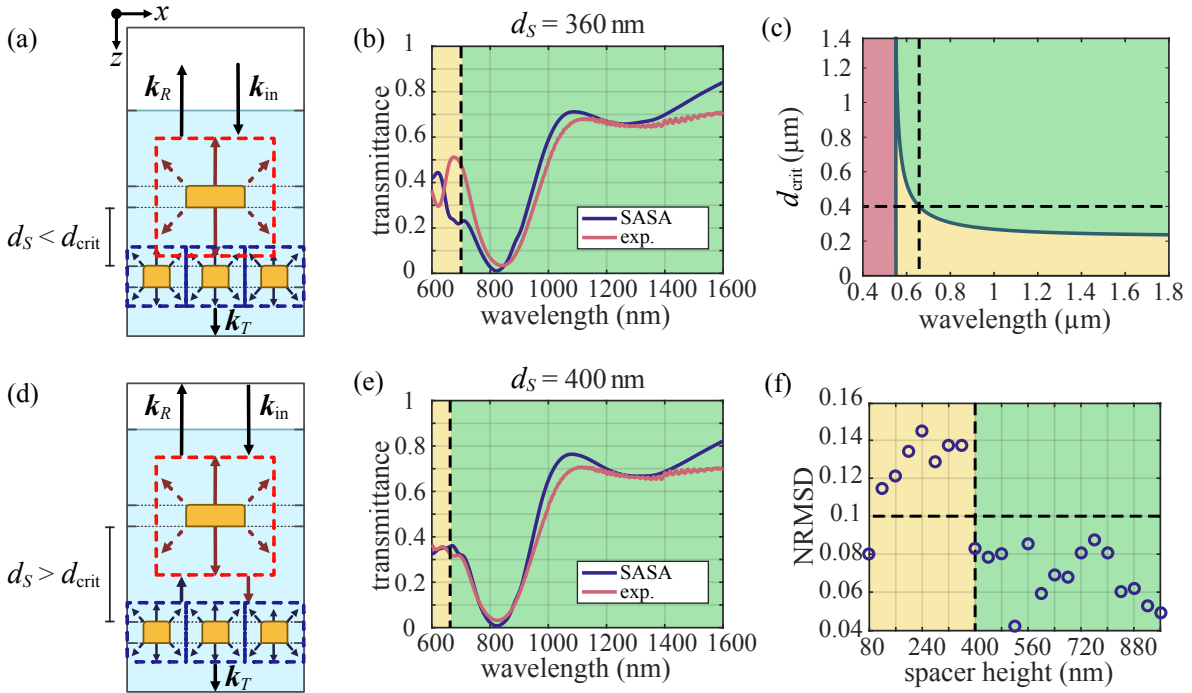


Figure 5.8: Transition between coupling regimes: Illustration of the coupling of evanescent diffraction orders for $d_S < d_{\text{crit}}$ (a) and $d_S > d_{\text{crit}}$ (d). The dashed boxes indicate the reach of evanescent fields. Correspondingly, (b) and (e) show plots comparing SASA and measurement for different coupling cases. The colored areas correspond to the coupling regimes in the CPD (c). The blue line in (c) marks d_{crit} with accuracy $\sigma = 1\%$. The horizontal and vertical dashed lines denote the spacer thickness limit and wavelength cut-off for the SASA model. The cut-off is also marked by dashed lines in (b) and (e). f) Normalized root mean square deviation (NRMSD) between SASA and measurement results calculated for all 23 stack heights. The change between the two coupling phases is indicated by dashed lines and colored areas.

5.2.3 Experimental validation of the FMA

By comparing the measurement results with the SASA model we can experimentally track the transition between coupling regimes defined by the CPD (sec. 3.4). Furthermore, this allows us to observe the conceptual transition between stacked metasurfaces and a layered metamaterial discussed in sec. 3.3.1.

As a reminder, the physical concept behind the transition is illustrated in fig. 5.8.a),d), showing coupling or decoupling of evanescent diffraction orders. The transition occurs between a spacer thickness of $d_S = 360$ nm and $d_S = 400$ nm (fig. 5.8.b,e). Larger differences between SASA and measurement are visible in fig. 5.8.b) than e). The expected spacer limit is, thus, approximately 400 nm. In concert with the critical distance d_{crit} (eq. (3.30)) we can confirm that, for an accuracy $\sigma = 1\%$, this fulfills the FMA condition down to a cut-off wavelength

¹⁵Further details on the setup can be found in [122, 247].

shown as a dashed line in the corresponding CPD (fig. 5.8.c)¹⁶. It indicates the change between coupling phases. As in fig. 5.8.c) the green and yellow areas in 5.8.b),e) mark spectral regimes where the FMA is valid or invalid.

Interestingly, fig. 5.8.b) shows a clear deviation between SASA and experiment right at the cut-off wavelength. Whereas the SASA model predicts a suppression of the overlap peak the experimental data exhibits an enhancement. We can conclude that this is likely an effect of near-field coupling of higher evanescent diffraction orders [151].

In contrast, fig. 5.8.e) shows only a weak deviation between SASA and experiment for the $d_S = 400$ nm stack. So, the deviation from the FMA condition in the small cut-off interval could be considered negligible in the larger scheme. From this we can extrapolate that, for a fixed wavelength interval, the *overall* validity of the FMA remains stable with regard to small deviations close to the short wavelength boundary [151].

To properly quantify the overall accuracy of SASA with respect to the experimental result we employ the normalized root mean square deviation (NRMSD). First, we calculate the root mean square deviation (RMSD) of the transmittances from experiment (τ_e) and SASA (τ_s) as a function of d_S over the wavelength interval

$$\text{RMSD}(d_S) = \sqrt{\frac{\sum_{k=1}^{N_\lambda} (\tau_e(\lambda_k, d_S) - \tau_s(\lambda_k, d_S))^2}{N_\lambda}}, \quad (5.7)$$

where we sum over all discrete wavelengths $\lambda_k \in [600 \text{ nm}, 1600 \text{ nm}]$ with $k \in \{1, \dots, N_\lambda\} \subseteq \mathbb{N}$ for a total of $N_\lambda = 512$ wavelength points. Next, we normalize $\text{RMSD}(d_S)$ by the mean range of the measured transmittance

$$\text{NRMSD}(d_S) = \frac{\text{RMSD}(d_S)}{\max_\lambda (\tau_e(\lambda, d_S)) - \min_\lambda (\tau_e(\lambda, d_S))}. \quad (5.8)$$

We calculated $\text{NRMSD}(d_S)$ for all 23 stacks and plotted the result in fig. 5.8.f). The plot clearly shows the two regimes with NRMSD dropping below 10 % at the predicted cut-off wavelength $\lambda = 400$ nm. With the exception of $\text{NRMSD}(d_S = 80 \text{ nm})$ all other, FMA-invalid, results are scattered well above the 10 % line. We interpret the runaway result as a coincidentally correct match. Regardless, the predicted behavior of the FMA and SASA solidifies with all results beyond $d_S > 400$ nm [151].

Regarding the exponential decay of the error observed in sec. 4.2 the results here are inconclusive. Since we deal with experimental data, other error sources have to be taken into account to properly explain the NRMSD. These include, but certainly are not limited to, the accuracy of the FMM simulations of individual metasurfaces as well as experimental deviations

¹⁶To broaden the view we increased the spectral interval by 200 nm on each boundary to $\lambda \in (400 \text{ nm}, \dots, 1800 \text{ nm})$.

not taken into account by our model (e.g. deviations from the assumed refractive indices of gold and glass). However, because the single layer results of the reference samples in fig. 5.7.d) compare reasonably well we can assume the magnitude of these errors to be relatively small.

In conclusion our results demonstrate that the stacking condition imposed by an estimate of d_{crit} gives an accurate limit for the FMA. Vice versa, this implies that models breaking the FMA limit can indirectly identify certain aspects in experimental data. Knowing that far-field interactions are fully and easily covered within the FMA and SASA, any significant deviations will likely be the results of near-field interactions.

6 | Reflection paths in metasurface stacks

In the previous chapters we developed and tested SASA both as a design tool and analytical method. In conjunction with the FMA, SASA has proven to be accurate for a variety of metasurface stacks. In this chapter we will venture beyond SASA’s ability to simulate stacks and show what physical insights can be found within its mathematical framework. The following is based on our publication ”*Equivalence of reflection paths of light and Feynman paths in stacked metasurfaces*” [148].

The idea behind this chapter originates from the concept of electron scattering paths in mesoscopic¹ solid state physics [253, 254]. The aim is to compare and partially transfer this concept to the physics of nano-optics in the specific case of metasurface stacks. Our point of contact is the study of conduction in mesoscopic systems. It uses descriptive concepts equivalent to the modal coupling of fundamental modes in metasurface stacks [255–257]. In particular, the process of electron scattering at junctions in mesoscopic structures can be considered analogously to the scattering of light at nano-structures or metasurfaces [257–259].

As we discussed in secs. 2.4 and 4.1 the interaction between light and (homogeneous) metasurfaces can be described by scattering processes. More abstractly, their interaction is determined by a set of connected ports in or out of which particles or waves can be transmitted or reflected [236, 255]. In the case of mesoscopic electron transport this is the interaction of electrons from different leads at a given junction. Whether an electron is transmitted or reflected into a specific port is given by a certain probability [255, 260, 261]. Thus, for each combination of ports and whether the interaction results in transmission or reflection there exists a certain combined probability. When a scattering process is completed, the final path an electron took can be described as a sum of all its possible paths, weighted by their probability for a given initial port [254]. Therefore, these paths give a picture of the interaction during the scattering process. In electron scattering theory they represent what is sometimes called the ”Feynman paths” of the system [253, 254].

Here, Feynman path literally means all possible paths an electron, or a photon for that matter, can take in a physical system. A rigorous quantum mechanical treatment of these would entail the use of path integrals and possibly Feynman diagrams [262, 263]. This poses a

¹The physical realm between the microscopic and the macroscopic.

unique challenge for the interaction of electromagnetic fields with periodically arranged nano-structures. Fortunately, S-matrices are representations of the overlap integral between the incident fields and their local interaction with the nano-structures, as they can be expressed as Greens functions [253]. This allows us to seize the concept of Feynman paths as an effective model. In the following we will show how this translates into the S-matrix formalism of SASA and which physical interpretations it allows.

6.1 Equivalence of Feynman paths and reflection paths

6.1.1 Geometric expansion of stacked scattering matrices

The star product eq. (4.2) gives an overlap of the transmission functions of adjacent metasurfaces and includes all contributions of reflections between them. Mathematically, these are represented by a reflection kernel of the form

$$(\hat{\mathbb{I}} - \hat{R}_i^b \hat{R}_{i+1}^f)^{-1}. \quad (6.1)$$

The reflection kernels contain exactly the Fabry-Pérot type interactions of far-field coupled metasurfaces we saw before in secs. 5.1.2 (fig. 5.4) and 5.2 (figs. 5.6, 5.7). Finding the nano-optical equivalent of Feynman paths then means accessing the back and forth reflected components of light propagating through adjacent metasurfaces [148].

We can expand the reflection kernel of the star product of two S-matrices ($N = 2$) into a geometric matrix series ², such that

$$\left(\hat{\mathbb{I}} - \hat{R}_1^b \hat{R}_2^f\right)^{-1} = \hat{\mathbb{I}} + \sum_{\alpha=1}^{\infty} \left(\hat{R}_1^b \hat{R}_2^f\right)^{\alpha}. \quad (6.2)$$

Then, each block matrix element \hat{S}^{ij} of a stacked S-matrix can be written as a matrix series

$$\hat{S}^{ij} = \hat{S}_0^{ij} + \hat{S}_1^{ij} + \hat{S}_2^{ij} + \dots, \quad (6.3)$$

where $i, j \in \{1, 2\}$ are the S-matrix's block indices or Jone matrices.

In optics of stratified media such an expansion is known as a Bremmer series [264, 265]. It represents the optical Wentzel-Kramers-Brillouin (WKB) approximation of the Helmholtz equation for one-dimensionally inhomogeneous media [264]. Even in the much more complex case of stacked metasurfaces we can separate the response of the stack into a leading order term

²If it is invertible and its block-matrix elements do not take values > 1 . This is usually the case for physical systems including absorption.

(i.e. the WKB term) and a series of consecutive interferometric terms. For two adjacent layers and front to back propagation this takes the form of

$$\hat{T}^f = \underbrace{\hat{T}_2^f \hat{T}_1^f}_{\text{leading transmissive term}} + \hat{T}_2^f \underbrace{\left(\sum_{\alpha=1}^{\infty} \left(\hat{R}_1^b \hat{R}_2^f \right)^\alpha \right)}_{\text{interferometric term}} \hat{T}_1^f \quad (6.4)$$

for transmission and

$$\hat{R}^f = \hat{R}_1^f + \hat{T}_1^b \hat{R}_2^f \hat{T}_1^f + \hat{T}_1^b \hat{R}_2^f \left(\sum_{\alpha=1}^{\infty} \left(\hat{R}_1^b \hat{R}_2^f \right)^\alpha \right) \hat{T}_1^f. \quad (6.5)$$

for reflection. The infinite power series of reflection matrices describes the interactions of all possible paths light can take between layers after consecutive reflections. For coherent excitation these paths will interfere, including the leading transmissive term. However, separating the pure transmission from inter-layer reflections allows us to analyze how the latter influence the final result [148].

6.1.2 Transmission and reflection for N layers as a geometric series

It is convenient for this discussion to restrict ourselves to either front or back direction since the mathematical structure will be similar. We start by considering the 0th order of transmission in front direction. This is straightforward Jones matrix calculus and we can immediately write,

$$\begin{aligned} \hat{T}_{1,2,\dots,N}^{f(0)} &= \hat{T}_N^f \left[\hat{T}_{N-1}^f \dots \left(\hat{T}_2^f \hat{T}_1^f \right) \right] \\ &= \prod_{k=0}^{N-1} \hat{T}_{N-k}^f, \end{aligned} \quad (6.6)$$

where the superscript (0) denotes the leading order term. To include higher orders, we start with a three layer stack. Plugging eq. (6.4) into itself, while using the associativity of the star product, we get

$$\begin{aligned} \hat{T}_{(1,2),3}^f &= \hat{T}_3^f \hat{T}_{1,2}^f + \hat{T}_3^f \left(\sum_{k=1}^{\infty} \left(\hat{R}_{1,2}^b \hat{R}_3^f \right)^k \right) \hat{T}_{1,2}^f \\ &= \hat{T}_3^f \hat{T}_2^f \hat{T}_1^f + \hat{T}_3^f \hat{T}_2^f \sum_{k=1}^{\infty} \left(\hat{R}_1^b \hat{R}_2^f \right)^k \hat{T}_1^f + \hat{T}_3^f \sum_{k=1}^{\infty} \left(\hat{R}_{1,2}^b \hat{R}_3^f \right)^k \hat{T}_2^f \hat{T}_1^f \end{aligned}$$

$$+ \hat{T}_3^f \sum_{k=1}^{\infty} \left[\underbrace{\left(\hat{R}_2^b + \hat{T}_2^f \hat{R}_2^b \hat{T}_2^b + \hat{T}_2^f \hat{R}_1^b \sum_{j=1}^{\infty} \left(\hat{R}_2^f \hat{R}_1^b \right)^j \hat{T}_2^b \right) \hat{R}_3^f}_{\hat{R}_{1,2}^b} \right]^k \hat{T}_2^f \sum_{k=1}^{\infty} \left(\hat{R}_1^b \hat{R}_2^f \right)^k \hat{T}_1^f, \quad (6.7)$$

where we used eq. (6.5) in backward direction for $\hat{R}_{1,2}^b$. Matrices with multi-indices separated by a comma, $\hat{T}_{m,n}$, collectively describe transmission or reflection from layer m to n . Multi-index notation is helpful when increasing the number of layers. For $N = 4$ layers we can write the transmission in a form that represents the structure of the stack,

$$\hat{T}_{((1,2),3),4}^f = \hat{T}_4^f \left(\hat{\mathbb{I}} + \sum_{k=1}^{\infty} \left(\hat{R}_{(1,2),3}^b \hat{R}_4^f \right)^k \right) \hat{T}_3^f \left(\hat{\mathbb{I}} + \sum_{k=1}^{\infty} \left(\hat{R}_{1,2}^b \hat{R}_3^f \right)^k \right) \hat{T}_2^f \left(\hat{\mathbb{I}} + \sum_{k=1}^{\infty} \left(\hat{R}_1^b \hat{R}_2^f \right)^k \right) \hat{T}_1^f. \quad (6.8)$$

From eqs. (6.7) and (6.8) we can identify a pattern to generalize to N layers. Using the associativity of the star product, eqs. (6.4) and (6.5) can be generalized to N layers by applying each new layer to all the previous ones combined. For this, we introduce the multi-index $M_k := 1, \dots, (N - k)$, denoting all modal contributions from the 1st to the $(N - k)$ th layer. Then, the transmission through an N -layer stack can be written as [148]

$$\hat{T}_{M_k}^f = \hat{T}_{N-k}^f \prod_{p=1}^{N-k-1} \left(\hat{\mathbb{I}} + \sum_{\alpha=1}^{\infty} \left(\hat{R}_{M_p}^b \hat{R}_{n_{p-1}}^f \right)^{\alpha} \right) \hat{T}_{n_p}^f, \quad (6.9)$$

using the index abbreviation $n_p := N - k - p$. The occurring reflection matrices can be written recursively,

$$\begin{aligned} \hat{R}_{M_k}^f &= \hat{R}_{M_{k+1}}^f + \hat{T}_{M_{k+1}}^b \hat{R}_{N-k}^f \hat{T}_{M_{k+1}}^f \\ &\quad + \hat{T}_{M_{k+1}}^b \hat{R}_{N-k}^f \sum_{\alpha=1}^{\infty} \left(\hat{R}_{M_{k+1}}^b \hat{R}_{N-k}^f \right)^{\alpha} \hat{T}_{M_{k+1}}^f. \end{aligned} \quad (6.10)$$

If $M_k = 1$, only the first layer matrices are applied. The case $k = 0$ gives the transmission or reflection of the full stack. Note that the order of indices results from applying the matrices right to left. Changing from forward to backward direction simply results in interchanging the superscripts f and b as well as reversing the index order. The geometric expansion of the star product was added to our implementation of SASA in MATLAB and Mathematica.

6.1.3 Interpreting reflection path coefficients

The expansion of S-matrix kernels yields the sum of all interactions within a stack. These represent an interaction picture of Feynman paths of fundamental modes between metasurfaces. Because they originate from a series of consecutive reflections, we will call them *reflection paths*.

For more insight on individual reflection paths we can subtract series that are truncated at different orders Ψ . For brevity, we choose an arbitrary, scalar transmission coefficient T of a stack described by eq. (6.9). Introducing the subscript notation $\{\Psi\}$ for a series *up to* order Ψ , we define

$$T_{\{\Psi\}} := \sum_{\alpha=0}^{\Psi} T_{\alpha}. \quad (6.11)$$

With this, the Ψ th order contribution is given by

$$T_{\Psi} = T_{\{\Psi\}} - T_{\{\Psi-1\}}. \quad (6.12)$$

We call these coefficients *virtual* as they influence the final response of the stack indirectly through interference. This becomes clear when deriving the transmittance of a truncated coefficient $T_{\{\Psi\}}$, which yields

$$\begin{aligned} |T_{\{\Psi\}}|^2 &= \left(\sum_{\alpha=0}^{\Psi} T_{\alpha} \right) \left(\sum_{\beta=0}^{\Psi} T_{\beta}^* \right) = \sum_{\alpha=0}^{\Psi} |T_{\alpha}|^2 + \sum_{\alpha=1}^{\Psi} \sum_{\beta=0}^{\Psi-\alpha} (T_{\beta} T_{\beta+\alpha}^* + T_{\beta}^* T_{\beta+\alpha}) \\ &= \sum_{\alpha=0}^{\Psi} |T_{\alpha}|^2 + 2 \sum_{\alpha=1}^{\Psi} \sum_{\beta=0}^{\Psi-\alpha} |T_{\beta}| |T_{\beta+\alpha}| \cos(\delta_{\alpha\beta}). \end{aligned} \quad (6.13)$$

Higher order paths interfere depending on the phase difference $\delta_{\alpha\beta} := \phi_{\beta} - \phi_{\beta+\alpha}$ between their respective phases ϕ_{α} .

6.1.4 Physical formulation for a four layer stack

The experimentally realized stacks we discussed previously (secs. 5.1 and 5.2) are comprised of four layers, cover, upper metasurface, spacer, and lower metasurface. Therefore, the transmission and reflection matrices of the geometric series describe interfaces, propagators, and complex layers. We will now add these to our formulation of reflection paths and derive their general reflection paths. Assuming symmetrically embedded metasurfaces there are $N = 5$

distinct layer S-matrices. Using eqs. (6.9) and 6.10 we get

$$\begin{aligned}
\hat{T}_{M_0}^f &= \hat{T}_5^f \prod_{p=1}^4 \left(\hat{\mathbb{I}} + \sum_{\alpha=1}^{\Psi} \left(\hat{R}_{M_p}^b \hat{R}_{n_{p-1}}^f \right)^\alpha \right) \hat{T}_{n_p}^f \\
&= \hat{T}_5^f \left(\hat{\mathbb{I}} + \sum_{\alpha=1}^{\Psi} \left(\hat{R}_{M_1}^b \hat{R}_5^f \right)^\alpha \right) \hat{T}_4^f \left(\hat{\mathbb{I}} + \sum_{\alpha=1}^{\Psi} \left(\hat{R}_{M_2}^b \hat{R}_4^f \right)^\alpha \right) \hat{T}_3^f \\
&\quad \times \left(\hat{\mathbb{I}} + \sum_{\alpha=1}^{\Psi} \left(\hat{R}_{M_3}^b \hat{R}_3^f \right)^\alpha \right) \hat{T}_2^f \left(\hat{\mathbb{I}} + \sum_{\alpha=1}^{\Psi} \left(\hat{R}_{M_4}^b \hat{R}_2^f \right)^\alpha \right) \hat{T}_1^f.
\end{aligned} \tag{6.14}$$

Numbering from top to bottom (forward direction), layers 2 and 4 are propagators and do not reflect, thus $\hat{R}_2^b, \hat{R}_4^b \rightarrow \hat{0}$. Furthermore, transmission matrices of propagators can be rewritten as scalars, using eq. (4.5), $\hat{T}_2^f \rightarrow \mathcal{P}_2$ and $\hat{T}_4^f \rightarrow \mathcal{P}_4$. With this equation (6.14) becomes

$$\hat{T}_{M_0}^f = \hat{T}_5^f \left(\hat{\mathbb{I}} + \sum_{\alpha=1}^{\Psi} \left(\hat{R}_{M_1}^b \hat{R}_5^f \right)^\alpha \right) \mathcal{P}_4 \hat{T}_3^f \left(\hat{\mathbb{I}} + \sum_{\beta=1}^{\Psi} \left(\hat{R}_{M_3}^b \hat{R}_3^f \right)^\beta \right) \mathcal{P}_2 \hat{T}_1^f. \tag{6.15}$$

The multi-index reflection matrices $\hat{R}_{M_1}^b$ and $\hat{R}_{M_3}^b$ are each a group of reflection paths in backward direction. They have to be calculated recursively starting from the back of the stack, where each recursion step adds a bundle of paths up to a certain layer. This yields³

$$\hat{R}_{M_3}^b = \mathcal{P}_2 \hat{R}_1^b \mathcal{P}_2, \tag{6.16}$$

$$\hat{R}_{M_1}^b = \mathcal{P}_4 \hat{R}_3^b \mathcal{P}_4 + \mathcal{P}_4 \hat{T}_3^f \mathcal{P}_2 \hat{R}_1^b \left(\hat{\mathbb{I}} + \sum_{\gamma=1}^{\Psi} \left(\mathcal{P}_2 \hat{R}_3^f \mathcal{P}_2 \hat{R}_1^b \right)^\gamma \right) \mathcal{P}_2 \hat{T}_3^b \mathcal{P}_4. \tag{6.17}$$

Inserted into eq. (6.15) we arrive at the geometric series of the entire stack,

$$\begin{aligned}
\hat{T}_{M_0}^f &= \hat{T}_5^f \left[\hat{\mathbb{I}} + \sum_{\alpha=1}^{\Psi} \left(\left(\mathcal{P}_4 \hat{R}_3^b \mathcal{P}_4 + \mathcal{P}_4 \hat{T}_3^f \mathcal{P}_2 \hat{R}_1^b \left(\hat{\mathbb{I}} + \sum_{\gamma=1}^{\Psi} \left(\mathcal{P}_2 \hat{R}_3^f \mathcal{P}_2 \hat{R}_1^b \right)^\gamma \right) \mathcal{P}_2 \hat{T}_3^b \mathcal{P}_4 \right) \hat{R}_5^f \right)^\alpha \right] \mathcal{P}_4 \hat{T}_3^f \\
&\quad \times \left[\hat{\mathbb{I}} + \sum_{\beta=1}^{\Psi} \left(\mathcal{P}_2 \hat{R}_1^b \mathcal{P}_2 \hat{R}_3^f \right)^\beta \right] \mathcal{P}_2 \hat{T}_1^f.
\end{aligned} \tag{6.18}$$

The cascaded sums in eq. 6.18 allow us to identify each possible path in the multi-layer system. For instance, truncating the series at $\Psi = 1$ gives us all reflection paths occurring at first order. An illustration of these is shown in fig. 6.1. In total, there are seven unique paths contained in the first order. Each has a different amount through the metasurfaces and recurring reflections. Together they accumulate slightly different transmission profiles that add interferometrically

³The explicit calculations can be found in appendix A.4.2.

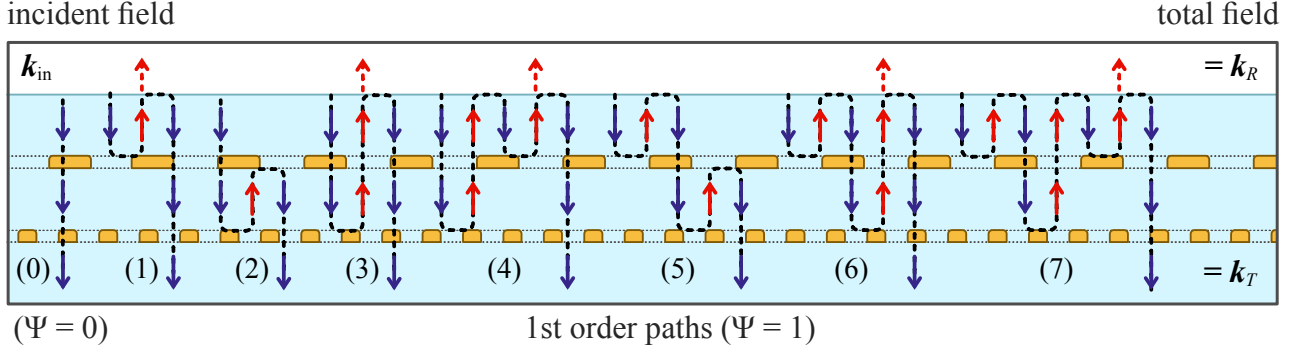


Figure 6.1: Illustration of all reflection paths included up to 1st order ($\Psi = 1$). Red and blue arrows represent reflected and transmitted k -vectors. Each occurrence of a bend in the black dashed line of a path corresponds to a reflection at an interface or metasurface. The first order paths (1) – (7) combine (interfere) with the leading order path (0) to the total transmitted field (\mathbf{k}_T). Correspondingly, red *dashed* arrows represent branches of reflection paths back into air. Together, these combine to the total reflected field (\mathbf{k}_R).

to the overall response of the stack.

Before we look at an example of a real stack, there remains the question of truncation. Above, we truncated all partial sums at Ψ . When we say first order it implies the first order of all sums. Yet, it would be equally feasible to truncate each sum differently. Then, however, we would need some foundation on how to choose the truncation. As this appears to be arbitrary we can circumvent the issue mathematically. Using the multinomial theorem it is possible sort the series by the combinatorial occurrence of each path. The comparatively long result can be found in appendix A.4.3. We note that the combinatorics of reflection paths could be potentially interesting for analyzing which type of path influences a particular stack the most.

6.2 Decomposition of Fabry-Pérot resonances

In this section we revisit the pseudo-incommensurable metasurface stack discussed in sec. 5.2. An important spectral feature of this stack were the Fabry-Pérot resonances subduing or enhancing the overlap peak between the main metasurface resonances (fig. 5.7.c,e,f). Now, we will analyze to which order reflection paths influence that result.

Based on the star product of the incommensurable stack, eq. (5.6), and using eqs. (6.18) and (6.16) the geometric series reads

$$\hat{T}_{\text{stack}}^f = \hat{T}_L^f \left(\hat{\mathbb{I}} + \sum_{\alpha=1}^{\Psi} \left(\hat{R}_{L,S}^b \hat{R}_L^f \right)^\alpha \right) \mathcal{P}_S \hat{T}_U^f \left(\hat{\mathbb{I}} + \sum_{\beta=1}^{\Psi} \left(\hat{R}_{L,C}^b \hat{R}_U^f \right)^\beta \right) \mathcal{P}_C \hat{T}_I^f, \quad (6.19)$$

with

$$\hat{R}_{I,C}^b = \mathcal{P}_C \hat{R}_I^b \mathcal{P}_C, \quad (6.20)$$

and

$$\hat{R}_{I,S}^b = \mathcal{P}_S \hat{R}_U^b \mathcal{P}_S + \mathcal{P}_S \hat{T}_U^f \mathcal{P}_C \hat{R}_I^b \left(\hat{\mathbb{I}} + \sum_{\gamma=1}^{\Psi} \left(\mathcal{P}_C \hat{R}_U^f \mathcal{P}_C \hat{R}_I^b \right)^\gamma \right) \mathcal{P}_C \hat{T}_U^b \mathcal{P}_S. \quad (6.21)$$

For brevity we abbreviate: lower metasurface L , upper metasurface U , spacer layer S , cladding layer C , and interface to air I . The scalar propagators $\mathcal{P}_C = \exp\{i(nk_0d_C)\}$ and $\mathcal{P}_S = \exp\{i(nk_0d_S)\}$ describe the phase propagation within the cladding and spacer layer.

Together with fig. 6.1 we can interpret eqs. (6.19), (6.20), and (6.21). First, light enters into the stack through the air interface (\hat{T}_I^f). It then propagates through the cover (\mathcal{P}_C) and interacts with the upper metasurface (\hat{R}_U^f and \hat{T}_U^f). The first geometric series over β describes recurring reflection processes in the cladding, which can give rise to Fabry-Pérot resonances. After propagating through the upper metasurface (\hat{T}_U^f) light travels through the spacer layer (\mathcal{P}_S) to interact with the lower metasurface (\hat{R}_L^f and \hat{T}_L^f). Again, recurring reflections are created as represented by the geometric series over α . After completing all internal paths light exits through the lower metasurface (\hat{T}_L^f) into the underlying glass wafer [151].

Even though eq. (6.19) considers propagation in *forward* direction, *backward* propagating reflection paths have to be considered as a part of the interaction process inside the stack [266]. These are created by reflections of forward propagating light (\hat{R}^f) that flip the propagation direction. The resulting backward paths will create a cascade of reflection and transmission processes depending on their point of origin in the layer system of the stack [151]. Reflection from the upper metasurface creates paths that take a round trip through the cover as represented by eq. (6.20) (paths (1) and (4) to (7) in fig. 6.1).

In contrast, backward paths originating from reflection at the lower metasurface (eq. (6.21)) create a complex combination of reflection paths that can reach back to the top interface. These can include further reflections in the cover. For instance, comparing paths (3) and (4) both have the same amount of interaction with the lower metasurface. The latter, however, shows an additional reflection off of the upper metasurface, likely resulting in stronger damping [151].

As we discussed in sec. 6.1.3 all individual paths are considered to be virtual phenomena. To discern their combined impact as an interferometric perturbation we can employ a geometrically expanded version of SASA. Using the numerical data from our experimentally validated model of the stack, we calculated the Fabry-Pérot decomposition for a spacer distance $d_S = 960$ nm up to second order ($\Psi = 2$). The results are shown in fig. 6.2.

The full series up to second order, $T_{xx\{\Psi\}}^f$, is plotted in fig. 6.2.a). At leading order the stack's

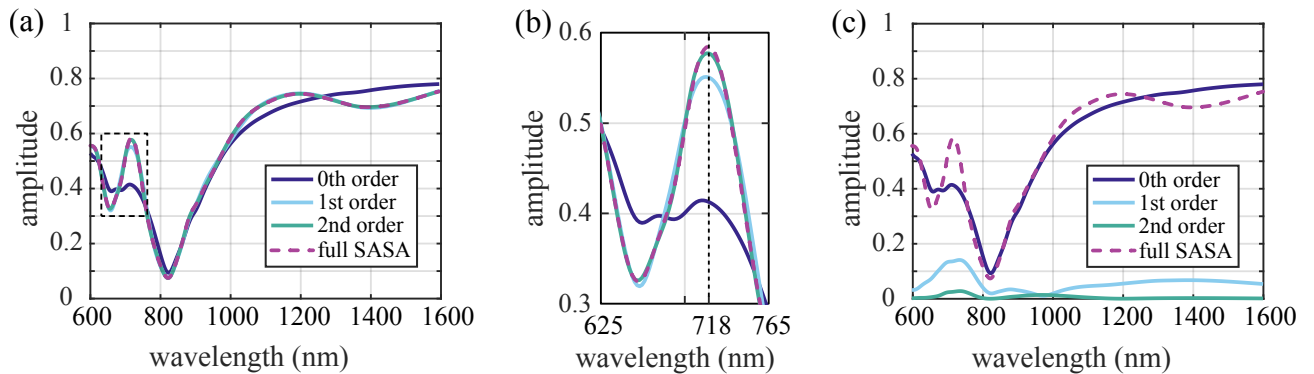


Figure 6.2: Plots of the geometric expansion a pseudo-incommensurable stack with $d_S = 960$ nm. a) Computed amplitude of the full stack compared to the geometric expansion from 0th order up to 2nd order. b) Enlarged plot interval of a) showing the differences between different orders close to the Fabry-Pérot resonance. c) Computed amplitude of the virtual path coefficients of 1st and 2nd order compared to the full stack and 0th order expansion.

transmittance is purely determined by transmission through all layers. This fully neglects the overlap peak as shown by the indigo solid line. We already reach a good approximation of the full stack’s transmittance by adding the first order to the series. Zooming in on the overlap peak at 718 nm we see that the series up to second order sufficiently matches the full SASA result (fig. 6.2.c). This convergence is probably due to the added plasmonic dampening of the metasurface for each higher order path.

Each individual order T_Ψ has its own amplitude profile. Looking at these profiles separately tells us about their relative contribution with respect to the zeroth order (fig. 6.2.d). They clearly reproduce features of the individual metasurfaces like the resonance at 820 nm. As assumed before, dampening is strongly increased with each order.

We can conclude that both the Fabry-Pérot fringe pattern and the overlap peak between the individual plasmonic resonances are mainly created by first order reflection paths and a modest modulation by second order paths. From our analytical investigation we can ascertain that the paths contributing to first order comprise the ones summarized in fig. 6.1.

6.3 Reflection paths of a patch-wire metasurface stack

As we have seen, reflection paths present us with a perspective into small features of a stack’s optical response. In that regard, virtual reflection paths give a glimpse into the hidden interactions that shape these features. This immediately leads to the question what further insights can be found in considering the phase and polarization of different paths. To satisfy our curiosity we designed and fabricated a stack that combines an isotropic metasurface with a C_2 symmetric one. This allows us to analyze individual contributions to the ellipticity.

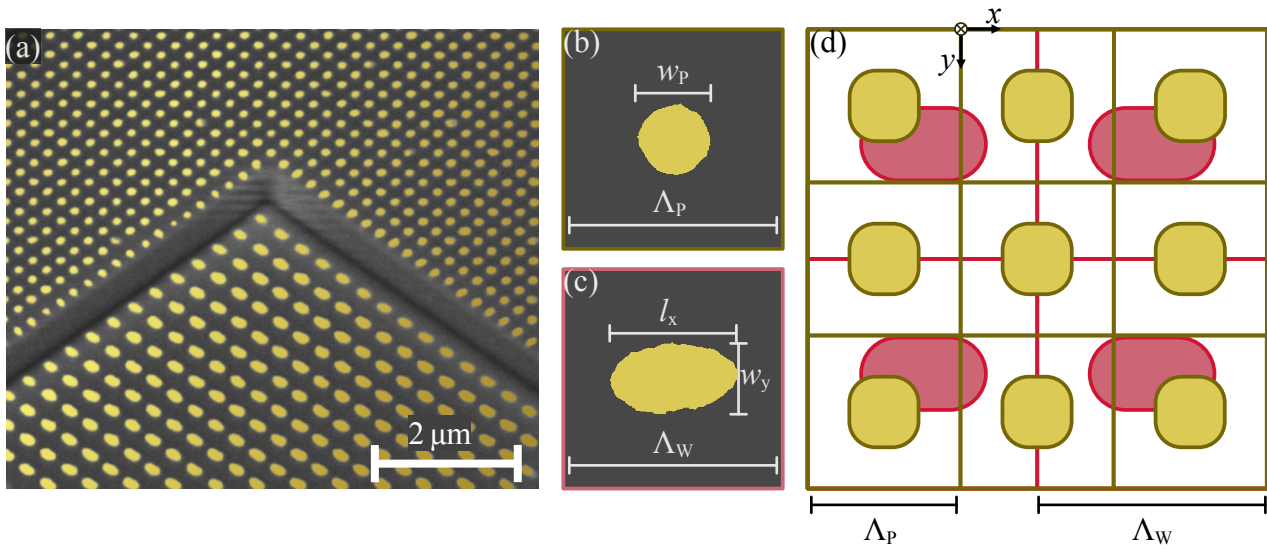


Figure 6.3: (a) SEM image of a FIB cut revealing the fabricated patch-wire stack. Particles are colored golden for better visibility. (b), (c) Average particles extracted from SEM images. (d) Sketch of superimposed unit cells of the metasurfaces, forming a super-cell of period 600 nm. The red grid and particles designate the lower metasurface and yellow ones the upper metasurface.

6.3.1 Design and fabrication

Based on our previous experimental experience (chapter 5) we chose a four layer design. From top to bottom this stack is comprised of: a cover layer, a patch-metasurface (S_P), a spacer layer, and a wire-metasurface (S_W). As with the previous samples, the nano-particles were comprised of gold and the dielectric embedding of fused silica. We fabricated everything on top of a fused silica wafer, which defined the lower half-space of the stack. The patches of the upper metasurface are isotropic with a C_4 symmetry. With the C_2 of the wires in the lower metasurface the stack is in total C_2 . The full stack is represented by the star product

$$S_{\text{stack}} = S_{n_{\text{air}}, n_{\text{SiO}_2}} * S_{d_C, n_{\text{SiO}_2}} * S_P * S_{d_S, n_{\text{spin-on}}} * S_W, \quad (6.22)$$

where $n_{\text{spin-on}}$ is the refractive index of spin-on glass supplied by Futurrex IC1-200.

Like in our previous fabrication runs, we employed electron beam lithography, gold evaporation, and a chemical lift-off process to fabricate the nano-structures.⁴ To obtain reference fields of each metasurface layer in the stack, we fabricated each on two separate fields: the stack itself (fig. 6.3.a) and a single layer of the respective metasurfaces, resulting in a total of three samples. After fabricating the first metasurface, we added a spacer layer using spin-on glass (Futurrex IC1-200) and etched it to the desired thickness of $d_S = 450$ nm. We then fabricated

⁴The fabrication was performed by Stefan Fasold.

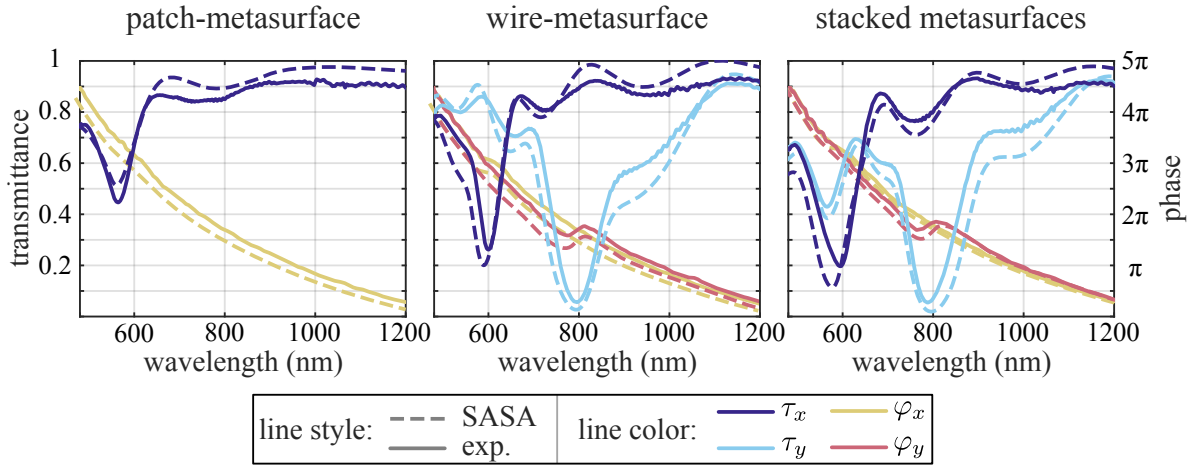


Figure 6.4: Comparison of measurement and SASA model. Left to right: measured (solid lines) and simulated (dashed lines) data of the single layer reference fields of the upper and lower metasurface, and of the full stack at the right, respectively. Each plot shows both transmittance and phase, color coded by the legend. Only x-polarization is plotted for the patch-metasurface as it is isotropic.

the upper metasurface. Finally, we added an SiO_2 cover layer of thickness $d_C = 585$ nm by chemical vapor deposition [148].

Testing the limits of our fabrication machines we attempted to make the nano-particles as small as possible to operate, at least partially, in the visible wavelength range. The minimum gold particle diameter we can control is 80 nm before their geometry loses shape and disintegrates for very small sizes. A minimum lateral distance between two adjacent particles should be larger than 50 nm to prevent them from fusing together.⁵

After fabrication the average particle sizes were extracted from SEM images (fig. 6.3.a–c). The nano-patches have a period of $\Lambda_P = 200$ nm, average diameter $w_P = 68$ nm, and height $h_P = 55$ nm. The nano-wires have a period $\Lambda_W = 300$ nm, average lateral dimensions $w_y = 108$ nm and $l_x = 176$ nm, and height $h_W = 45$ nm. The periods were chosen so that each particle is contained with just enough next-neighbor separation. Incidentally, they have a ratio of $\Lambda_W/\Lambda_P = 3/2$, creating a super-period of 600 nm (fig. 6.3.d).

6.3.2 Measurement results compared to SASA

The stack was simulated using the established combination of single layer FMM calculations and SASA (fig. 6.4). Ellipsometric measurements of the materials produced by our fabrication processes supplied refractive index data [116]. The wavelength interval was defined by our interferometric measurement [122,247] setup, ranging from 470 nm to 1200 nm. We performed interferometric measurements of both the single layer fields and the full stack, simultaneously

⁵The numbers depend of the height of the gold layer and the fabrication process.

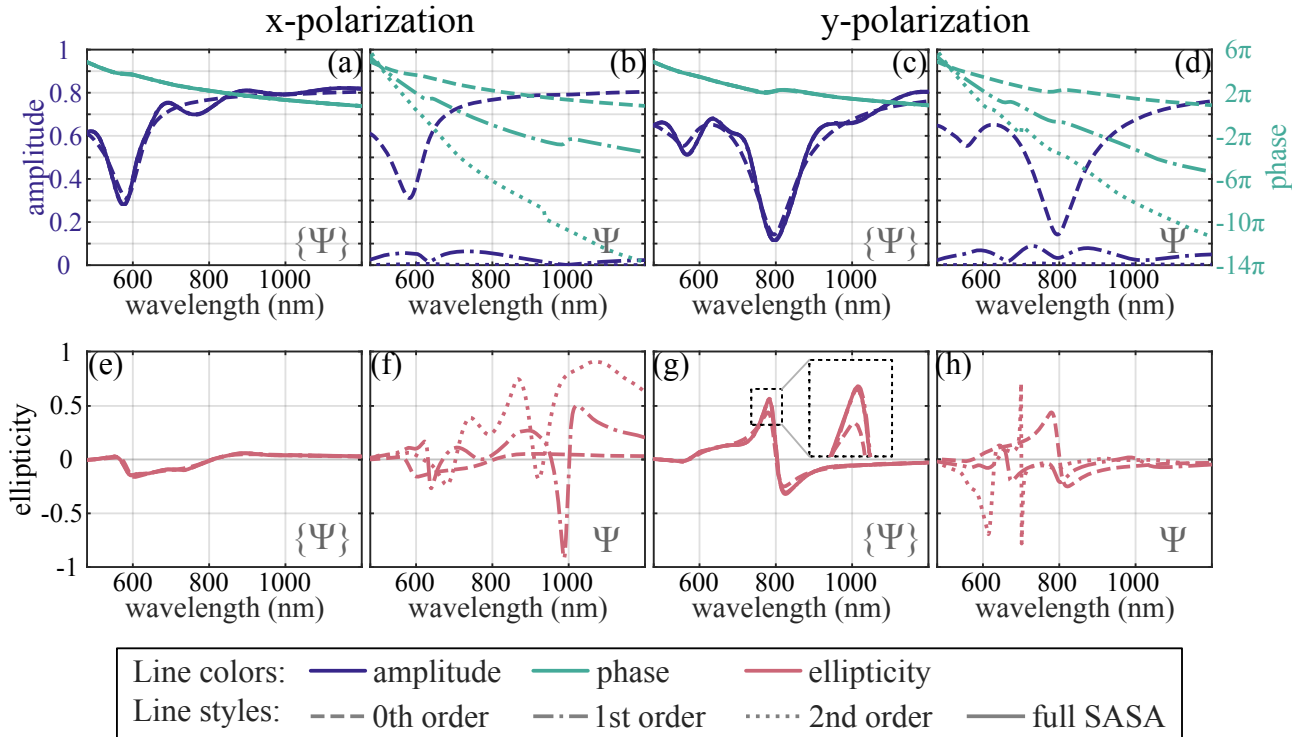


Figure 6.5: Upper row (a)–(d): amplitudes (indigo) and phases (teal) resulting from the geometric expansion of the SASA model. The two columns on the left and the right show for different input polarization. Plots annotated with $\{\Psi\}$ show the truncated series compared to the full SASA result and those marked by Ψ the corresponding coefficients. Lower row (e)–(f): ellipticity corresponding to the input polarization and series or coefficients above. The inset in (g) shows an enlarged view of the maximum ellipticity.

measuring transmittance and phase in x- and y-polarization.⁶ As shown in fig. 6.4 there is very good agreement between the SASA model and the measurement, both for transmittance and phase.

The isotropic patch-metasurface of the upper layer exhibits a single resonance at approximately 580 nm. On the other hand, the C_2 symmetric wire-metasurface of the lower layer shows two distinct resonances for different polarization at approximately 600 nm and 800 nm. The isotropic resonance overlaps with polarization sensitive resonances in the stacked configuration. For x-polarization this results in a broader, slightly more prominent resonance at 600 nm. Due to the isotropy of the lower metasurface the stack displays two resonances in y-polarization. The phase is mainly determined by the collective heights of spacer and cover. Phase jumps at the resonance positions of the single layers combine in the stack [148].

6.3.3 Reflection path analysis

With a suitable SASA model of the fabricated stack we can perform a reflection path analysis to reveal internal interactions that were hidden from measurement. We recalculated the stack with a geometric expansion up to second order, $\Psi = 2$, yielding the transmission up to order $T_{\{\Psi\}}$ and their virtual coefficients T_{Ψ} . Both their amplitude and phase are plotted in fig. 6.5 for x- and y-polarization.

Clearly, the full SASA result is already well approximated at first order. Looking at the respective coefficients shows that the second order amplitude is strongly damped and its contributions are negligible. As expected the metasurfaces' resonances manifest themselves in the amplitude profile of the first order. The phase of $T_{\{\Psi\}}$ seems to be unchanging with the expansion. This is explained by the fact that the phase is largely determined by the propagation lengths of paths in the stack. Any accumulated phase vanishes due to interference, eq. (6.13). Predictably, the set of coefficients contributing to each order T_{Ψ} shows the accumulated phase of the taken paths.

Interestingly, we can observe in the lower row of fig. 6.5 that the ellipticity of light transmitted through the stack is not everywhere zero and, thus, not linear but elliptical. The effect is weak for incident x-polarization with only a small deviation from zero close to the 600 nm resonance. At the 800 nm resonance for y-polarization we can see a clear jump to elliptically polarized light. This is surprising because the combination of the metasurfaces' C_4 and C_2 symmetry forbids non-linear polarization states.

If we take a closer look at the average wire-particles (fig. 6.3.c), we notice a small asymmetry along the x- and y-axis giving the particles a very subtle pear-shape. Revisiting our simulation results and investigating the off-diagonal components of the Jones matrices we find a non-vanishing cross-polarization with a maximum for y-polarization of $|T_{xy}| = |T_{yx}| \approx 0.05$ and $|R_{xy}| = |R_{yx}| \approx 0.08$ at $\lambda \approx 800$ nm. This was unexpected but the question remains how such a small geometrical perturbation can have such a noticeable effect on the ellipticity?

More insight can be found by analyzing the geometric expansion of the ellipticity. Here, the convergence is equally fast at first order. Moreover, higher order contributions enhance the maximum zeroth order ellipticity by about 10% (inset in fig. 6.5.g). This tells us two things. First, the increase (or decrease) in ellipticity is mostly determined by the phase shift of the resonance. Second, higher order paths transport a certain degree of anisotropy. The ellipticity of higher order T_{Ψ} shows a variety of polarization states that are created. Their interpretation needs to be handled carefully. The second order contributions have an amplitude close to zero which makes their phase and ellipticity inconsequential. Even higher orders should be considered noise.

⁶The optical measurement was performed by Matthias Falkner.

Yet, unnoticeable in the full response, the first order produces highly elliptical polarization, which is almost circular at 1000 nm in x-polarization. We identify these as *virtual polarization states*. Their creation is related to the accumulation of phase and larger number of interactions with the symmetry-broken wire-metasurface. This can be understood further by calculating the transmission coefficients of the expansion explicitly. Using the geometric expansion for a four layer stack⁷, eq. (6.15), and renaming the subscripts accordingly, we get

$$\hat{T}_{\text{stack}}^f = \hat{T}_W^f \left(\hat{\mathbb{I}} + \sum_{\alpha=1}^{\Psi} \left(\hat{R}_{I,S}^b \hat{R}_L^f \right)^\alpha \right) \mathcal{P}_S \hat{T}_U^f \left(\hat{\mathbb{I}} + \sum_{\beta=1}^{\Psi} \left(\hat{R}_{I,C}^b \hat{R}_W^f \right)^\beta \right) \mathcal{P}_C \hat{T}_I^f, \quad (6.23)$$

while using the same naming convention for homogeneous layers as in eq. (6.19). With the support of eq. (6.10) to calculate the reflection matrices in (6.23), we can write explicit expressions of the virtual reflection paths in eq. (6.23). The transmission matrices of the first four paths contained up to first order ($\Psi = 1$) read as⁸

$$\hat{T}_0^f = \hat{T}_W^f \mathcal{P}_S T_P \mathcal{P}_C T_I, \quad (6.24)$$

$$\hat{T}_{(1)}^f = \hat{T}_W^f \mathcal{P}_{S_P} T_P R_P R_I \mathcal{P}_C^3 T_I, \quad (6.25)$$

$$\hat{T}_{(2)}^f = \hat{T}_W^f \hat{R}_W^f R_P \mathcal{P}_S^3 T_P \mathcal{P}_C T_I, \quad (6.26)$$

$$\hat{T}_{(3)}^f = \hat{T}_W^f \hat{R}_W^f \mathcal{P}_S^3 T_P^3 R_I \mathcal{P}_C^3 T_I. \quad (6.27)$$

The indices in parentheses refer to paths (1)–(3) illustrated in fig. 6.1. Each contains two reflections that result in a different number of interactions with the anisotropic lower metasurface. Whereas both the leading order term \hat{T}_0^f and $\hat{T}_{(1)}^f$ only transmit once through the bottom layer, $\hat{T}_{(2)}^f$ and $\hat{T}_{(3)}^f$ have twice the number of interactions through additional reflections. We can therefore argue that they add a higher degree of anisotropy to the interferometric part of the stack's transmission. If we account for the geometrical deviation of the nano-wires, we have to add a small asymmetric perturbation $\xi_T := T_{xy}$ and $\xi_R := R_{xy}$ for each polarization, for instance,

$$T_{0,x}^f = (T_{xx}^f + \xi_T) \mathcal{P}_S T_P \mathcal{P}_C T_I \quad (6.28)$$

$$T_{(2),x}^f = (T_{xx}^f + \xi_T) (R_{xx}^f + \xi_R) R_P \mathcal{P}_S^3 T_P \mathcal{P}_C T_I \quad (6.29)$$

$$(6.30)$$

These perturbations propagate with each reflection path and add interferometrically to the polarization of the stack. They exist as an inextricably part of the interaction.

⁷With $N = 5$ S-matrix layers.

⁸All isotropic Jones matrices can be reduced to a scalar, e.g. $\hat{T}_P = T_P \hat{\mathbb{I}}$.

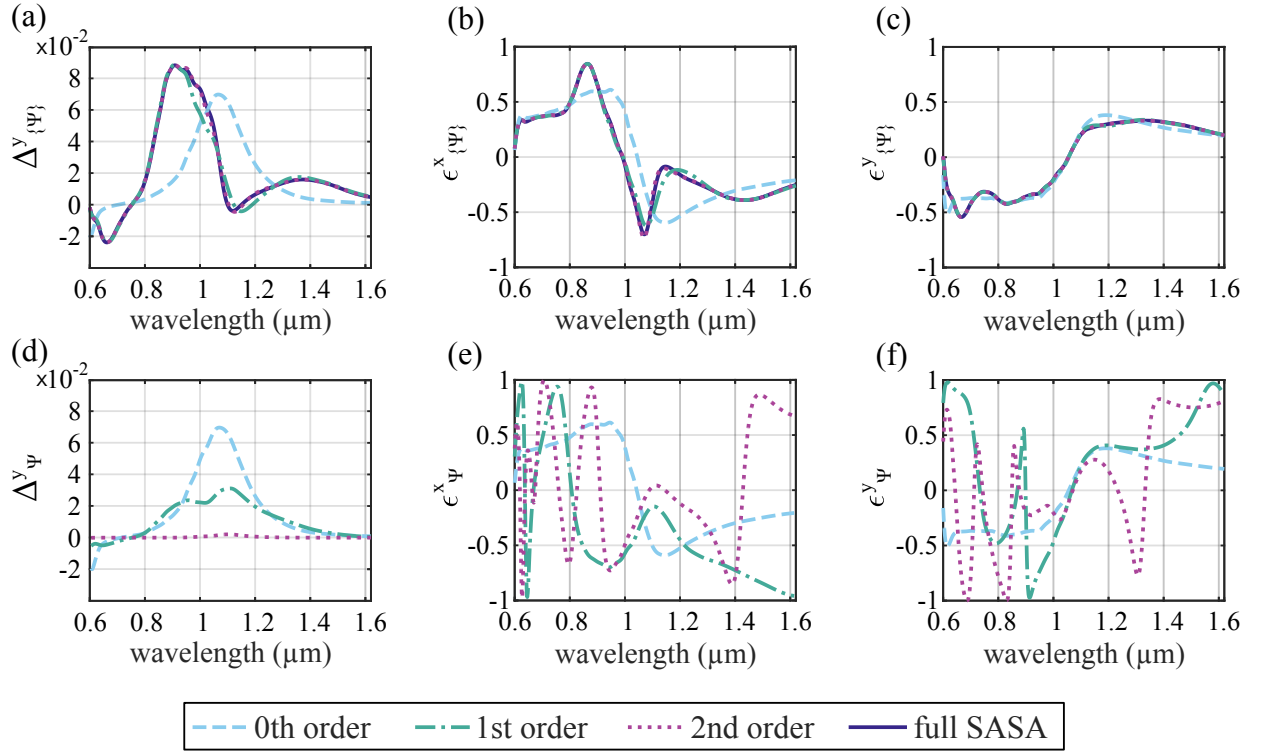


Figure 6.6: Geometric expansion of the asymmetric transmission Δ^y and ellipticity $\epsilon^{x,y}$ up to second order, $\Psi = 2$. The upper row, (a)–(c), shows the series up to order Ψ , and lower row, (d)–(f), the corresponding coefficients. For reference the full SASA result is plotted for each case in the upper row (solid indigo line). Dashed, dashed-dotted, and dotted lines show the zeroth, first, and second order. For convenience they are additionally color coded as shown in the legend.

6.4 Chiral reflection paths

6.4.1 Higher order effects on chirality

To conclude our discussion on reflection paths and their possible interpretation we take another look at the first experimental example in this thesis. In sec. 5.1 we saw that a stack of twisted nano-wires could produce a chiral response in the absence of near-field coupling. We identified the combined symmetry operations of its S-matrices on the incident field as the mechanism creating the necessary asymmetric transmission. Moreover, we observed that Fabry-Pérot resonances played an important role in enhancing the asymmetric transmission while controlling ellipticity.

Based on what we have learned, reflection paths should have some impact on the stack's asymmetric response. With each round trip within the stack they experience symmetry operations imposed by the S-matrices. The broken symmetry of the twisted wires is a much more

complex problem than the previously discussed patch-wire stack. This begs the question how the relative rotation of the wires by an angle α maps onto the reflection paths.

Using the SASA model based on our experimental evaluation of this stack from sec. 5.1 we calculated the geometric expansion of its asymmetric transmission $\Delta_{\{\Psi\}}^y$ and ellipticity $\epsilon_{\{\Psi\}}^{x,y}$. Fig. 6.6 shows both the truncated series and its related coefficients ($\Delta_{\Psi}^y, \epsilon_{\Psi}^{x,y}$) up to second order $\Psi = 2$.⁹ The first thing we observe is that the series converges at second order. Focusing on asymmetric transmission (figs. 6.6.a), there is a noticeable blue-shift between the zeroth order and all higher orders, including the full SASA result. Clearly, the leading order transmission is sufficient to produce asymmetric transmission, as should be expected by our symmetry argument. The blue-shift, however, is a result of higher order paths and, therefore, also of the reflection of each individual layer. Surprisingly, this blue-shift can not be observed in the corresponding coefficients Δ_{Ψ}^y (fig. 6.6.d). This tells us that the interference of all paths is responsible for the shift, in conjunction with the added reflections.

A closer look at the ellipticity (figs. 6.6.b,c) reveals a similar modification of the leading order characteristic, especially in x-polarization. As $\epsilon_{\{\Psi\}}^{x,y}$ informs us about the final shape of the polarization ellipse, the coefficients $\epsilon_{\Psi}^{x,y}$ ascertain the accumulated phase shifts at each order. Figs. 6.6.e) and (f) show increasing fluctuations for higher orders, which are more frequent at smaller wavelengths. We can observe virtual circular polarization, some of which coincides with the extrema of $\epsilon_{\{\Psi\}}^{x,y}$ in figs. 6.6.b) and (c), e.g. $\lambda_x \approx 880$ nm or $\lambda_y \approx 680$ nm.

A case can be made that the Fabry-Pérot resonances observed in fig. 5.4 subtly influence the polarization asymmetry. The virtual polarization, relative phase shifts, and collective interference of the reflection paths within it affect the polarization ellipse and blue-shift the asymmetric transmission. In that regard, the spectral band in which the stack's response can be considered chiral is affected by reflection paths.

6.4.2 Geometric expansion of the asymmetric transmission

The S-matrix formalism in combination with the geometric expansion enables us to find analytical expressions of effects that normally hide from view. Such is the case with the asymmetric transmission of the twisted-wire-stack. Above, we have seen that there are, indeed, observable higher order effects that are inextricable in rigorous simulations and measurements [146, 267]. But even the SASA calculations presented in fig. 6.6 do not show directly how reflection paths produce $\Delta_{\{\Psi\}}^y$.

In the following we will treat this problem analytically by revisiting the wire-S-matrices (5.1) and (5.2). As we proved in sec. 5.1.2 they correctly represent the symmetry of the experimental stack. Even numerically, layer rotation approximates the rotation of wires in their unit cells

⁹Because $\Delta^y = -\Delta^x$ it is sufficient to discuss the asymmetric transmission for only one input polarization.

sufficiently well, as shown in appendix A.3. In order to calculate the expansion of asymmetric transmission we need to first calculate the expanded coefficients of the stack. To reduce our mathematical effort we utilize the associativity of the star product to rewrite eq. (5.5) using eq. (5.3), such that

$$S_{\text{stack}} = (S_{n_1, n_2} * S_{d_C, n_2}) * (S_W^\alpha * (S_{d_S, n_2} * S_W)) = S_{n_1, n_2} * (S_{d_C, n_2} * \bar{S}_{\text{stack}}). \quad (6.31)$$

Deliberately ignoring the cover layer, we can make a statement about the asymmetry of the reflection paths based solely on the reduced stack \bar{S}_{stack} . Paths that include the cover follow the same mathematical three-layer structure like \bar{S}_{stack} , as seen on the right-hand-side above. The higher nesting level increases the combinatorial count of paths while adding multinomials of forward reflection in the cover (see eq. (A.33)). Recalling the sketch in fig. 6.1, reflection events will apply the same but *flipped* symmetry operations as in transmission if we ignore, for a moment, the exact amplitudes and phases. In other words, reduction of the nested star product structure to \bar{S}_{stack} produces a heuristic, analytical model of the asymmetry of reflection paths.

Using the three-layer expansion, eq. (6.7), and replacing the second layer with the actual spacer ($\hat{R}_2 = 0$, $T_2^{ij} = \delta_{ij}\mathcal{P}$, with $\mathcal{P} = \mathcal{P}_{d_S, n}$) the transmission of the stack becomes

$$T_{ij} = \mathcal{P}T_{ik}^3 T_1^{kj} + T_{ik}^3 \sum_{m=1}^{\infty} \mathcal{P}^{2m+1} \left[\left(\hat{R}_1 \hat{R}_3 \right)^m \right]^{kl} T_{lj}^1, \quad (6.32)$$

where the sub- or superscripts 1 and 3 denote variables pertaining to S_W^α and S_W , respectively. For brevity we use the sum convention $\sum_{j=1}^2 a_{ij} b_{jk} = a_{ij} b^{jk}$. Because the power of the matrix product $\hat{R}_1 \hat{R}_3$ leads to nested multinomial products we use the notation $[\cdot]^{kl}$ for the coefficient of its resulting matrix. Inserting eq. (6.32) into the formula for asymmetric transmission (2.40) and using eq. (6.13) for the absolute square of the geometric series we arrive at

$$\begin{aligned} \Delta_{\{\Psi\}}^x &= \sum_{m=0}^{\Psi} \underbrace{|T_{xy, m}|^2 - |T_{yx, m}|^2}_{:=\Delta_m} \\ &+ 2 \sum_{m=1}^{\Psi} \sum_{n=0}^{\Psi-m} \underbrace{\left(|T_{xy, n}| |T_{xy, m+n}| \cos(\delta_{mn}^{xy}) - |T_{yx, n}| |T_{yx, m+n}| \cos(\delta_{mn}^{yx}) \right)}_{:=\Gamma_{mn}}. \end{aligned} \quad (6.33)$$

We will now calculate $\Delta_{\{\Psi\}}^x$ up to first order, which is already close to convergence, as shown in fig. 6.6 for the analogous $\Delta_{\{\Psi\}}^y$. For this, we calculate the leading asymmetries Δ_0 and Δ_1 as well as the first order interferometric term Γ_{10} . Here, we utilize the symmetry properties

$T_1^{12} = T_1^{21}$, $R_1^{12} = R_1^{21}$ and $T_3^{12} = T_3^{21} = R_3^{12} = R_3^{21} = 0$. Then, the *zeroth* order difference reads

$$\begin{aligned}\Delta_0^x &= |T_{xy,0}|^2 - |T_{yx,0}|^2 = |T_1^{xy}|^2 \left(|T_3^{xx}|^2 - |T_3^{yy}|^2 \right) \\ &= (|T_x|^2 - |T_y|^2)(|T_x|^2 + |T_y|^2 - 2|T_x||T_y|\cos(\phi_x - \phi_y)) \cos^2 \alpha \sin^2 \alpha.\end{aligned}\quad (6.34)$$

The first order difference is more complicated, producing upon insertion of the S-matrix components a polynomial of trigonometric functions,

$$\begin{aligned}\Delta_1^x &= |T_{xy,1}|^2 - |T_{yx,1}|^2 \\ &= (A_1 \cos^4 \alpha + A_2 \cos^6 \alpha) \sin^2 \alpha + (A_3 \cos^2 \alpha + A_4 \cos^4 \alpha) \sin^4 \alpha + A_5 \cos^2 \alpha \sin^6 \alpha,\end{aligned}\quad (6.35)$$

where the coefficients $A_i = A_i(|T_x|, |T_y|, |R_x|, |R_y|; \phi_x - \phi_y, \gamma_x - \gamma_y)$ are multinomial functions of amplitudes and phase differences¹⁰ Of course, all reflection paths interfere amongst each other, including the leading order. This is taken care of by the first order correction,

$$\Gamma_{10} = |T_3^{11}| |T_3^{11} R_{1k}^1 R_3^{kl} T_{12}^1| \cos \delta_{10}^{xy} - |T_3^{22}| |T_3^{22} R_{2k}^1 R_3^{kl} T_{11}^1| \cos \delta_{10}^{yx}.\quad (6.36)$$

The mathematical structure is comparable to eq. (6.35) but depends on the phase differences $\delta_{10}^{xy} = \phi_0^{xy} - \phi_1^{xy}$. Their calculation is rather less revealing¹¹. Even a multinomial analysis using the pattern matching capabilities of Mathematica remained inconclusive. In a future work a combinatorial approach based on eq. (A.33) could be used to identify contributions of individual paths as well as interferometric corrections.

Intuitively, with every revolution inside the stack the twist angle α accumulates. Both Δ_0^x and Δ_1^x depend on the rotation angle α and vanish for $\alpha = 0$. The higher powers of the cosine and sine functions in Δ_1^x indicate repeated symmetry operations on the reflection paths, as the rotation of the metasurface is mapped onto the field vector with each interaction. This can be interpreted as the following: a reflection path effectively experiences more than a two-layer stack with just one rotated layer. Rather, in its carried coordinate system it propagates through a stack of multiple layers of rotated wires, depending on its optical path length. We notice that at first order there is a maximum total power of $\cos^m \alpha \cdot \sin^n \alpha$ with $m + n \leq 8$. This translates, in our interpretation, into consecutive rotations of up to six times the initial layer angle α . As discussed by Y. ZHAO et al. (2012) [267] the asymmetric response of a stack broadens with an increased number of layers. This explains, partially, the broadening (and shift) of the asymmetric transmission in fig. 6.6.a).

Even though the paths themselves only experience a virtually expanded stack, the collective result seems to adhere to the same principle. Our calculation of the expanded asymmetric

¹⁰The exact results can be found in appendix A.4.4, eqs. (A.35)–(A.39).

¹¹See appendix A.4.5 for details.

transmission shows quantitatively how the layer or wire rotation influences the asymmetry of the stack. It represents the literal twist that is mixed into the overall response of the stack.

7 | Summary and outlook

In this thesis we set out to find a semi-analytic description of metasurface stacks that supports versatile stack designs and delivers sound physical insights. At first, we asked the subtle question of what differentiated stacked metasurfaces from (bulk) metamaterials. Generally speaking, metamaterials are the overarching category. As we discussed in the introduction (chapter 1), the definition of metamaterials relies on specifically engineered optical functionality and incorporates a vast variety of different nano-photonics designs. Here, we explained how to conceptually transition from a periodic bulk metamaterial to a system of stacked homogeneous metasurface layers (sec. 3.3). We define individual metasurfaces by attributes of the fundamental mode approximation (FMA). It implies subwavelength metasurface periods, zeroth order diffraction, and the absence of evanescent fields. In order to quantify the validity of the FMA, we derived a critical distance at which the far-field conditions are met (sec. 3.3.2). Categorizing the types of coupling a stack can exhibit, we introduced the concept of a coupling phase diagram (CPD). Depending on the wavelength, layer distance, and periods a stack transitions between diffractive, near-field and far-field coupling (sec. 3.4). The latter identifies the FMA-regime and in our definition a proper metasurface stack.

While the definition of stacks via FMA validity is of some academic merit, its applicability emerges in combination with a proper mathematical formalism, describing optical characteristics. We chose scattering matrices (S-matrices) to encode the transmission and reflection of both individual metasurfaces and full stacks. As anisotropy can be an important feature for polarization manipulation, S-matrices can be used to describe both the symmetry of a stack and the involved (polarized) fields. In conjunction with the FMA we developed a semi-analytic stacking algorithm (SASA), which was implemented in MATLAB and Mathematica (sec. 4.1). Meanwhile, SASA has also been transferred to Python and further optimized as a program with open source access [268]. SASA was shown to be computationally efficient and reproduced rigorous FMM and FDTD simulations accurately (sec. 4.2). One of its most advantageous features is the analytical manipulation of S-matrices. Either resulting from numerical simulations or Fresnel equations, S-matrices can be stacked arbitrarily and flipped, rotated, or mirrored as needed. Importantly, these present symmetry operations *relative* to incident *polarized* fields (sec. 4.1.3).

We employed this feature of SASA to analyze the polarization symmetry of a stack of twisted-wire-metasurfaces (sec. 5.1). Characterizing the structure of each layer’s S-matrix and the stack as a whole, we could predict chiral polarization behavior by the presence of asymmetric transmission, without the necessity to simulate any nano-optical effects. Comparing to experimental results we could prove the validity of our SASA model and deduce the emergence of elliptical polarization, and therefore *handedness*. We recall that in the FMA-regime near-field coupling and, hence, bi-anisotropy are prohibited. Consequently, the handed polarization asymmetry was a result of symmetry operations applied by each *achiral* metasurface on the incident field, enhanced by metasurface resonance bands (sec. 5.1.1). Indeed, a stacked configuration was *necessary* to break the symmetry. Here, we could also explain that, based on our validated SASA model, the layer distance had an influence on the asymmetric transmission and ellipticity via Fabry-Pérot modulation (sec. 5.1.2). Thus, metasurface stack polarization asymmetry is spacer dependent.

Continuing our evaluation of SASA’s capability, we demonstrated the experimental realization of a pseudo-incommensurable metasurface stack comprised of two isotropic patch-metasurfaces with differing meta-atom diameters and periods (sec. 5.2). The prefix pseudo relates to ratios that are incommensurable by design, but are limited by fabrication accuracy. In the case of our electron beam lithography machine this was about 1 nm. We achieved a super-period of approximately 68.2 μm , demanding a practically infinite computational domain for rigorous optical simulations. Here, SASA was shown to be capable of accurately predicting and adapting to experimental results (sec. 5.2.2). This suggests that FMA-based models can in fact be used to compute any period ratio. Furthermore, we took the opportunity to test FMA validity conditions. The same pseudo-incommensurable stack was fabricated 23 times with varying spacer thicknesses, transitioning from a near-field regime to far-field coupling. SASA compared well in all cases. Moreover, an analysis of the mean-square-deviation between experimental and simulated data sets satisfied the predicted coupling phase transitions on the basis of the CPD (sec. 5.2.3). If a stack is non-diffractive but the FMA invalid, we can deduce in *argumentum e contrario* the presence of near-field coupling. In short, SASA is highly accurate and our conceptual transition from metamaterial to metasurface stack is in accordance with physical reality.

To summarize, metasurface stacks are clearly distinguishable from bulk metamaterials by the validity of the FMA. This allows for strong simplifications leading to SASA, which accurately models the optical properties of said stacks. This incorporates complex polarization as well as arbitrary period ratios. Moreover, SASA efficiently varies the spacer thickness of stacks in order to identify, analyze, and optimize Fabry-Pérot resonances and their effects.

While semi-analytical modeling is a useful addition to the toolkit of computational nanophotonics, it can also provide deeper physical insights into a stack’s internal field interactions.

Interestingly, the S-matrix multiport-formalism used in nano-optics conceptually overlaps with the treatment of scattering in mesoscopic electron transport. The path an electron takes after scattering at a junction can be represented as a superposition of all possible paths between connected leads. Using the terminology of quantum electrodynamics, these paths represent *Feynman paths*. In metasurface stacks this corresponds to a geometric expansion of internal reflection matrices (sec. 6.1). Then, transmission through a stack can be separated into leading order transmission through consecutive layers and interferometric corrections. The latter constitute equivalents to Feynman paths, which we called *reflection paths*. Individual paths carry virtual amplitudes, phases, and polarization, conglomerating with all other paths to the full response of the stack. Revisiting the incommensurable metasurface stack we applied the reflection path concept to the experimentally validated SASA model (sec. 6.2). A geometric expansion of its transmission showed that its main Fabry-Pérot resonance was composed of mainly first and second order paths. All higher order contributions experienced strong dampening and were negligible. Using a uniform truncation across all partial sums of the expansion we could, furthermore, identify each constituent virtual path.

These results suggested that studying reflection paths could be an addition to the analysis of a stack's optical response. Therefore, we applied the method to a specifically designed anisotropic stack comprising a wire- and a patch-metasurface (sec. 6.3). Because meta-atom dimensions were chosen close to the limits of our fabrication machines, shape deviations occurred. Using reflection paths, we could show that symmetry *perturbations* created nearly circular virtual polarization states, manifesting chirality from on average C_2 -symmetric structures. Although the virtual polarization largely vanished upon interfering there remained an ellipticity well above zero in the nano-wire resonance band. The reflection path analysis showed a noticeable increase of the ellipticity due to first order contributions.

It is now conceivable that reflection path polarization can be significant. Recalling our analysis of the chiral twisted-wire-stack, we asked how its asymmetric transmission and ellipticity were affected by interferometric corrections (sec. 6.4). We already understood, that Fabry-Pérot resonances modulated asymmetric transmission. Reflection paths revealed a significant blue-shift of the asymmetric transmission due to first and second order contributions. This was accompanied by highly elliptical as well as circular, virtual polarization states that maximized and blue-shifted the chiral response. After some calculation we could even find mathematical expressions of the accumulated "twist" at each order, enhancing the asymmetry.

All in all, the results of this thesis demonstrate that SASA produces valid and applicable semi-analytic models of periodic metasurface stacks. Our endeavor into reflection paths even suggests an expanded potential for further analytical understanding of layer interactions. For instance, it is imaginable that more complex, inhomogeneous stacks, like the multi-wavelength meta-lens design by ZHOU et al. [74], could be analyzed by extracting reflection paths from

higher diffraction orders. Surmising that near-fields could be treated as perturbations to the FMA, one could also attempt to investigate interference effects in more closely stacked bilayers [269–271] or metasurfaces of multi-layered particles [272, 273]. In general, all presented concepts and equations can be expanded or adopted to other types of layered media, with or without metasurfaces [274, 275].

Future work will address the inverse design of nano-photonic functionality. Here, one sets a target function or property and searches for nano-structures that perform as desired. This is already prevalent in the research community, where machine learning or data driven algorithms such as neural networks are applied for inverse design [177, 178, 276–279]. Work following this thesis already adapts SASA for that purpose. As we discussed, stacked metasurfaces can provide a simplification of parameter spaces and allow for rapid repetition and modification of simulations. This is ideal for machine learning. Here, one could create a database of metasurfaces that provides training data, e.g. for an evolutionary algorithm [280, 281] that provides an optimized stack configuration based on a user-defined figure of merit. Because the stacking itself and all layer manipulation is done analytically, this would be several orders of magnitude faster than any fully numeric approach.

As a final remark, we should briefly mention related work that was out of the scope of this thesis. As emphasized in the introduction, nano-photonic color filters are one of the many promising applications of metasurfaces. Here, we touched upon a remarkable application case in medicine: contactless sensing of vital parameters based on time-dynamic NIR-color variations of human skin [282–284]. Causally connected, oxygenated and deoxygenated hemoglobin is responsible for changing the absorption spectrum of blood with every breath and heart beat. If we filter two specific wavelengths, say 750 nm and 840 nm, we can produce a signal based on the ratio of time-varying ratios of absorptances, which relates to the oxygen saturation of blood [285]. This can be measured with a camera sensor that monitors (facial) skin in these spectral bands [286]. For the purpose of NIR-filtering we designed and fabricated a pixelized metasurface-filter-array. Although the filters were single layer metasurfaces, SASA was successfully employed to optimize the cladding material for uniformity and filter contrast.¹ The combination of metasurface-filtering and camera-based measurement of dynamic multispectral color changes was filed as a patent [287]. This shows emphatically that metasurfaces and seemingly academic design approaches, like FMA-based semi-analytic modeling, are relevant for future photonic technologies.

¹At the moment of writing this thesis a publication is in preparation.

A | Supplementary material

A.1 Dispersion of gold and glass

The materials used in every experimental example and corresponding FMM-simulation were gold and glass. For nano-structuring, gold was evaporated and thus deposited on fused silica (SiO_2) wafers. Here, we used measured ellipsometric data from in-house¹ produced gold layers and fitted a Drude-Lorentz model based on $\varepsilon(\omega)$ defined in eq. (2.12) [145]. Describing bound and free electrons ($\omega_0 = 0$) the three-term model for gold reads

$$\varepsilon_{\text{DL}}(\omega) = \varepsilon_{\infty} + \frac{f_1}{-\omega^2 - i\gamma_1\omega} + \frac{f_2}{\omega_{0,2}^2 - \omega^2 - i\gamma_2\omega}, \quad (\text{A.1})$$

with normalized parameters $\varepsilon_{\infty} = 5.53$, $f_1 = 2178.43$, $\gamma_1 = 0.30978$, $\omega_{0,1} = 0$, $f_2 = 465.79$, $\gamma_2 = 2.94869$ and $\omega_{0,2}^2 = 228.713$. Here, ε_{∞} comprises arbitrary electronic transitions, with $\varepsilon_{\infty} = 1 + \sum_{j=3} f_j / (\omega_{0,j}^2 - \omega^2 - i\gamma_j\omega)$. In the unit-free normalization the angular frequency becomes $\omega = 2\pi/\lambda$. Fig. A.1 shows $\varepsilon(\omega)$ for frequencies in the NIR. Moreover, by using eq. (2.13) ($n(\omega) = \sqrt{\varepsilon(\omega)}$) and substituting $\omega \rightarrow \lambda$ we can also find the wavelength dependent refractive index of gold, additionally plotted in fig. A.1. Both cases were compared to tabulated data by OLMON et al. [288], showing an overall good agreement with growing deviations towards the SWIR.

In the case of glass we have to differentiate the type of glass and fabrication method. Generally, wafer substrates were comprised of fused silica (SiO_2). If chemical vapor deposition (CVD) is used to produce homogeneous glass layers, amorphous crystalline SiO_2 is the result, which closely resembles fused silica. An alternative method is presented by spin-on glass. Here, we used Futurrex IC1-200², comprising silicon and silanol groups in an n-Butan solution. Depositing a volumetrically precise droplet of IC1-200, the sample is then rotated at high frequencies (50 Hz) so that an even coating is achieved. After baking at various high temperatures (200 °C – 800 °C) the solvent evaporates, polymerization occurs and an amorphous silica layer is left. As shown in fig. A.1, there is a small yet significant difference between fused silica and

¹Institute of Applied Physics of the University of Jena.

²<https://futurrex.com/en/products/spin-on-glass-coatings.html>

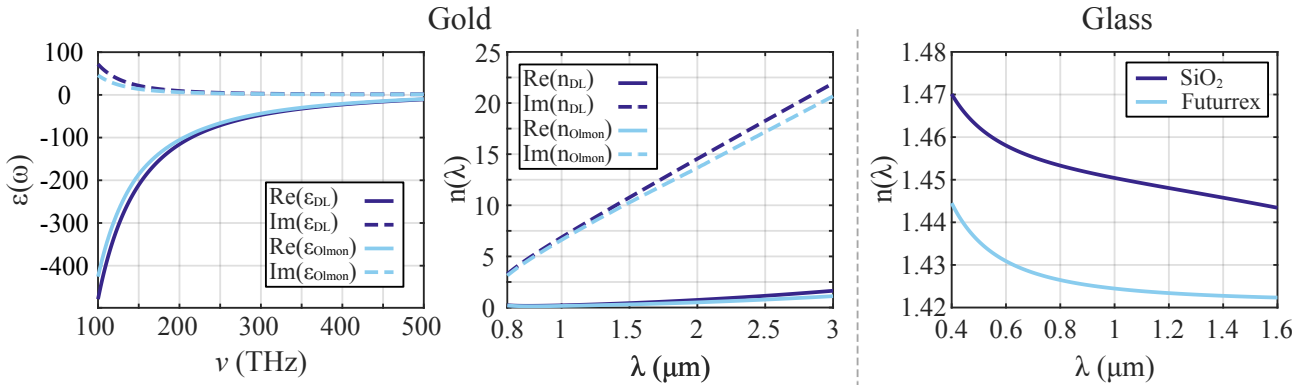


Figure A.1: Left: complex permittivity and refractive index of gold, comparing a Drude-Lorentz model based on in-house measurements and data by OLMON et al. [288]. Right: Refractive index of two kinds of glass: fused silica (SiO_2) and Futurrex IC1-200 spin-on-glass.

IC1-200-based glass.

Here, we describe the refractive index of fused silica using the Sellmeier dispersion equation [289] with parameters attained from MALITSON et al. [290],

$$n^2 - 1 = \frac{0.6961663\lambda^2}{\lambda^2 - 0.0684043^2} + \frac{0.4079426\lambda^2}{\lambda^2 - 0.1162414^2} + \frac{0.8974794\lambda^2}{\lambda^2 - 9.896161^2}. \quad (\text{A.2})$$

Using data provided by Futurrex, we compared eq. (A.2) to IC1-200 in a VIS to NIR wavelength range, fig. A.1. Both types of glass have a real valued refractive index, showing similar gradients but differing by a constant shift of approximately 0.02–0.025.

A.2 Implementation of SASA

The FMA-based S-matrix formalism described in section 4.1 is an analytical framework for calculating stacks of arbitrary layers in all possible combinations. S-matrices of metasurfaces can be simulated numerically and combined with analytical S-matrices with the same options for transformations. Hence, in combination it forms the starting point of a semi-analytic stacking algorithm (SASA). In the following we will describe how SASA can be utilized to automate the process of stacking and significantly reduce the computational effort for simulating metasurface stacks. The following description is tailored towards an implementation in MATLAB but can analogously be transferred to Python as well. All analytical elements of the S-matrix formalism were also implemented in Wolfram Mathematica. To a large part, Mathematica was used to simplify and structure the calculus.

It is important to note that the transmission and reflection coefficients populating the S-matrix should generally be considered wavelength dependent. This is especially true when pertaining to measurements or simulation results, i.e. available data is usually not monochro-

matic.

In that regard, SASA for MATLAB (or Python) is fully vectorized, so that all operations can be performed over the complete discretized wavelength interval as *array*-operations. This includes Redheffer's star product, which was numerically optimized for an efficient calculation of all vectorized block matrix elements. For that, we *analytically* calculated the star product of two arbitrary S-matrices using Mathematica. Then, each element of the resulting 4×4 S-matrix can be calculated by point-wise operations over the wavelength discretization, which is most efficient for MATLAB (i.e. OpenBLAS) vectorization. The efficiency was tested by benchmarking runs of different implementations of the star product using both the system clock time and MATLAB's profiler tool.

There are three main parts to SASA's implementation:

1. Constructing a stack from input data.
2. Performing optional operations on certain layers as demanded.
3. Calculating the star product of the stack.

These will be explain in the necessary detail in following in order to understand how SASA works as a program. A flow chart of the program can be found in figs. A.2–A.4.

A.2.1 Stack construction

As a user of SASA we usually have a mix of pre-calculated metasurface S-matrices S_{MS_p} and homogeneous layers defined by their refractive indices n_p . Ideally, SASA should automatically construct all necessary propagation and interface S-matrices from the given layer distribution of refractive indices and embed the metasurfaces accordingly. For that it is important to properly define how to count and enumerate layers. Lets say we have a simple stack of two arbitrary metasurfaces separated by three homogeneous layers. The top of the stack, which we define as the cladding, there is a half-space of air and the bottom, the substrate, there is glass. The intuitive, physical way of counting layers would give us five in total ($2 + 3$). Yet, the algorithm should consider the interfaces between the layers. This gives us a larger count for internal numbering in SASA,

$$\text{physical: } S = \overbrace{S_1 * S_2 * \cdots * S_{N-1} * S_N}^{N \text{ layers}} \quad (\text{A.3})$$

$$\text{SASA: } S = \underbrace{S_1 * S_{1,2} * S_2 * \cdots * S_{N-1} * S_{N-1,N} * S_N}_{2N-1 \text{ layers}}. \quad (\text{A.4})$$

So, whereas physically there are N layers the algorithm constructs $2N - 1$. Conceptually, a stack is then a structure with four properties:

- a wavelength interval with L entries over which it is defined,
- the layer distribution of media - an $N \times La$ array,
- the height of each layer - N in total,
- the media embedding the stack (short *embedding*), i.e. a set of two refractive indices.

These properties depend on the design of the stack and have to be defined by the user. The discrete wavelength interval $[\lambda_1, \dots, \lambda_L]$ is used by SASA in order to correctly calculate the dispersion and phase propagation of all homogeneous layers. Obviously, all precalculated data, e.g. metasurface simulations, should be defined over the same interval. From the input of N media and N heights SASA constructs the necessary distribution of propagators and interfaces. For instance, a stack of two metasurfaces separated by a glass spacer, with a glass substrate, air cladding and an additional cladding layer of glass on top would read

$$(S_{\text{air,glass}} * S_{d_1,\text{glass}} * S_{\text{glass},MS_1}) * (S_{MS_1}) * (S_{MS_1,\text{glass}} * S_{d_2,\text{glass}} * S_{\text{glass},MS_2}) * (S_{MS_2} * S_{MS_2,\text{glass}}).$$

The parentheses collect the S-matrices related to the physical layers. It is clear that metasurfaces need to be calculated with the correct embedding in order to fulfill the boundary conditions with their local surrounding. Listing A.1 shows a code snippet of the corresponding SASA function call. All properties listed above are collected as parameters in the MATLAB struct `SASA_PARS`. SASA identifies so-called *complex* layers by the keyword `Smatrix` and checks their `embedding` with respect to adjacent layers. All homogeneous layers are calculated using the equations from sec. 4.1.2. Each individual S-matrix is sorted into a list and numbered according to (A.4).

Once the stack is constructed optional operations can be performed. These refer to the symmetry operations from sec. 4.1.3 and are called using the keywords `rotate`, `mirror`, and `flip`. SASA can identify whether layers are isotropic or anisotropic and will perform the options according to sec. 4.1.4.

A.2.2 Array vectorization

As mentioned before all operations should be vectorized for optimal efficiency. The vectorization targets the wavelength dimension of the stack. Looping over λ_p would be inefficient and can be replaced by matrix operations. Each S-matrix of the stack is of size $L \times 4 \times 4$. First, we can flatten the wavelength dimension by linearizing the 3D array along one dimension³. Let \bar{S} be

³In MATLAB this can be done using the `reshape` function.

```

1  % create input struct for SASA
2
3  % the metasurface S-matrix of layer 1 (upper layer)
4  MetaS_1 = struct('Smatrix', SMAT_1, 'embedding', { n_SiO2, n_SiO2 });
5
6  % the metasurface S-matrix of layer 2 (lower layer)
7  MetaS_2 = struct('Smatrix', SMAT_2, 'embedding', { n_SiO2, n_SiO2 });
8
9  % the composition of the stack (read: left to right as top to bottom)
10 stack_medium = {n_SiO2, MetaS_1, n_SiO2 , MetaS_2};
11
12 % height of each layer (0 denotes metasurfaces)
13 stack_height = {H_cladding, 0, H_Spacer, 0};
14
15 % the embedding of the stack
16 n_embed = struct(...
17 'cladding', n_air ,...
18 'substrate', n_SiO2 );
19
20 % create parameter struct for SASA input
21 SASA_PARS = struct(...
22 'Lambda', wavelength_vector ,...
23 'medium', stack_medium ,...
24 'height', stack_height ,...
25 'embedding', n_embed);
26
27 % options: rotate 3rd layer by alpha_ degrees
28 alpha_ = 60;
29 SASA_OPTS = struct('rotate', {3, alpha_});
30
31 % run SASA
32 SMAT_SASA = SASA(SASA_PARS, SASA_OPTS);

```

Listing A.1: MATLAB function call of SASA: example on how to input stack properties.

an $(L \cdot 4) \times 4$ array of S-matrices with

$$\bar{S} = (S_1(\lambda_1), \dots, S_L(\lambda_L))^T \quad (\text{A.5})$$

Similarly, we can define an $L \cdot 4 \times L \cdot 4$ array $\bar{\Omega}^{-1}$ populated by L copies of a 4×4 operator Ω^{-1} . A transformation of the S-matrix array, \bar{S}' , is then written as the product

$$\bar{S}' = \bar{\Omega}^{-1} \bar{S} \Omega, \quad (\text{A.6})$$

applying the transformation Ω to each wavelength element $S_p(\lambda_p)$.

In similar fashion we can formulate an array multiplication for S-matrices. Starting with

the S-matrix array \bar{S} we can put together a block diagonal matrix of S-matrices \mathcal{S} with \bar{S} as its main diagonal,

$$\mathcal{S} = \text{diag}(S_1(\lambda_1), \dots, S_L(\lambda_L)). \quad (\text{A.7})$$

For a high number of wavelengths L or a very fine discretization, \mathcal{S} can be defined as a sparse matrix. Then, any two S-matrix arrays can be multiplied as

$$\bar{S}_{1,2} = \mathcal{S}_1 \cdot \bar{S}_2. \quad (\text{A.8})$$

All the above also maps onto the treatment of Jones matrices. The array multiplication is useful for an efficient implementation of the star product.

A.2.3 Calculating the star product

The star product is at the core of SASA. There are two ways of implementation: iterative and recursive. Depending on the machine the code is run on, one might be more efficient than the other. The user can choose which to use via the SASA input options `SASA_OPTS` (figs. A.2–A.4).

The iterative calculation follows directly from the associativity of the star product [208],

$$S = (((S_1 * S_2) * S_3) * \dots) * S_{2N-1} \implies S_{N_p} = S_{N_{p-1}} * S_p, \quad (\text{A.9})$$

where multi-index $N_p = (1, \dots, p)$ collects all previous star products, with $1 < p \leq 2N - 1$ and N_{2N-1} resulting in the full stack.

The recursive star product is performed pair-wise such that

$$S_{m,n} \quad \text{with} \quad n == m \implies S_m, \quad (\text{A.10})$$

$$\text{if} \quad n == m + 1 \implies S_m * S_n, \quad (\text{A.11})$$

$$\text{otherwise} \implies (S_m * S_{m+1}) * S_{m+2,n}, \quad (\text{A.12})$$

In contrast to the iteration, the recursion calculates the stack beginning with the last S-matrix pair.

The associativity allows another reduction in computational effort [208, 291]. If we need to vary the distance of a homogeneous layer we get a vector of distances $d_p = (d_p^{(1)}, \dots, d_p^{(D)})$ or the set $d_p \in \{d_p^i\}$, we can avoid performing *all* calculations D times and instead split the stack, such that

$$S = (S_1 * \dots * S_{p-1}) * S_{d_p, n_p} * (S_{p+1} * \dots * S_{2N-1}). \quad (\text{A.13})$$

Thus, all other star products only need to be calculated once and the height variation is,

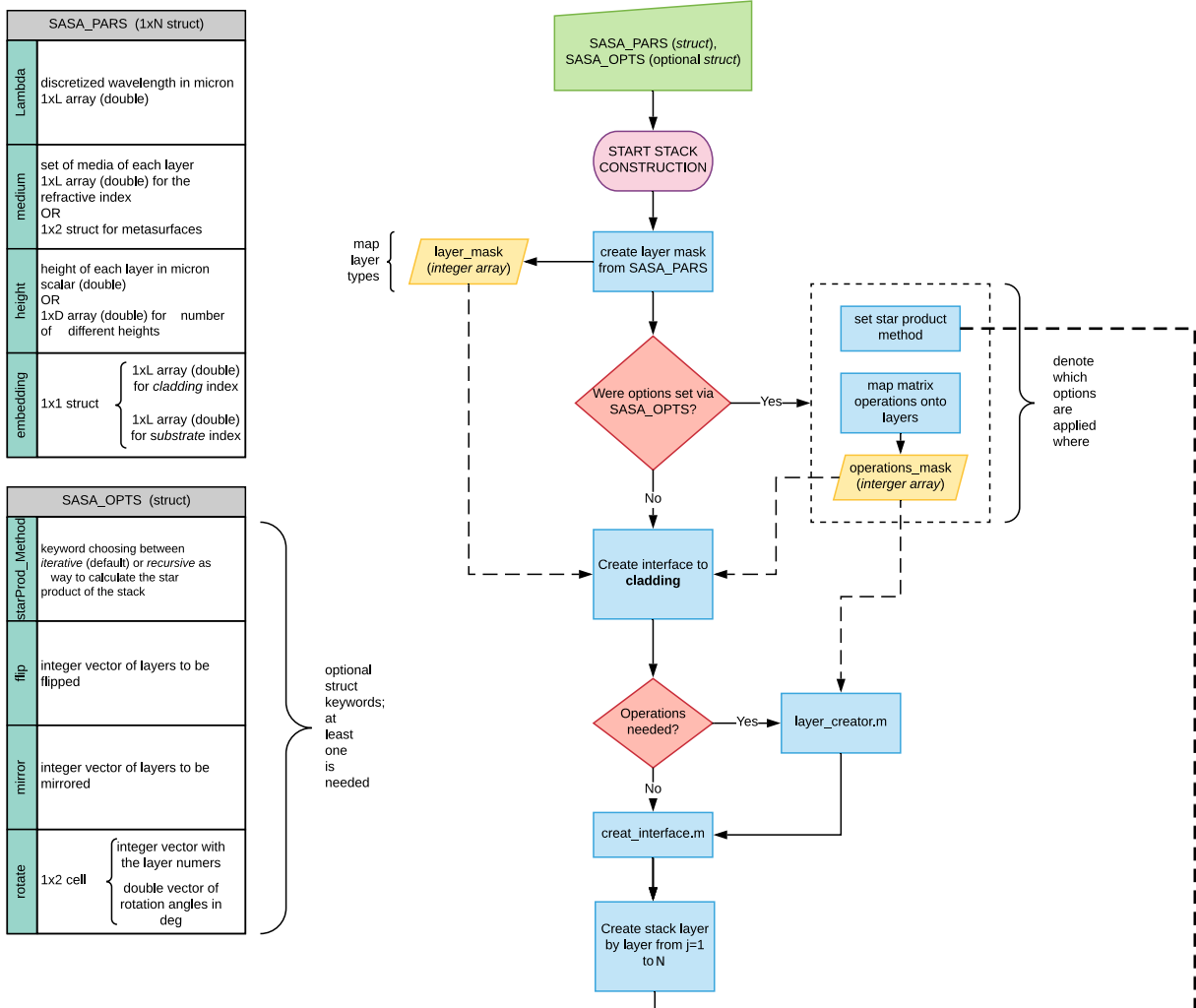


Figure A.2: SASA flow chart part 1 of 3: initialization of the program and recognition of the stack pattern via `create_layer_mask.m`. Using the auxiliary interface function `create_interface.m` the first layer (interface) is created.

mathematically, a star product of three S-matrices. Our implementation of SASA will detect whether one layer of a stack has multiple heights and split the stack accordingly. The benefit of this for scanning layer heights, say to analyze Fabry-Pérot resonances, cannot be overstated. This was used, e.g., for the stack design in sec. 5.1. Explicit numbers on computation times regarding that design can be found in appendix A.2.4.

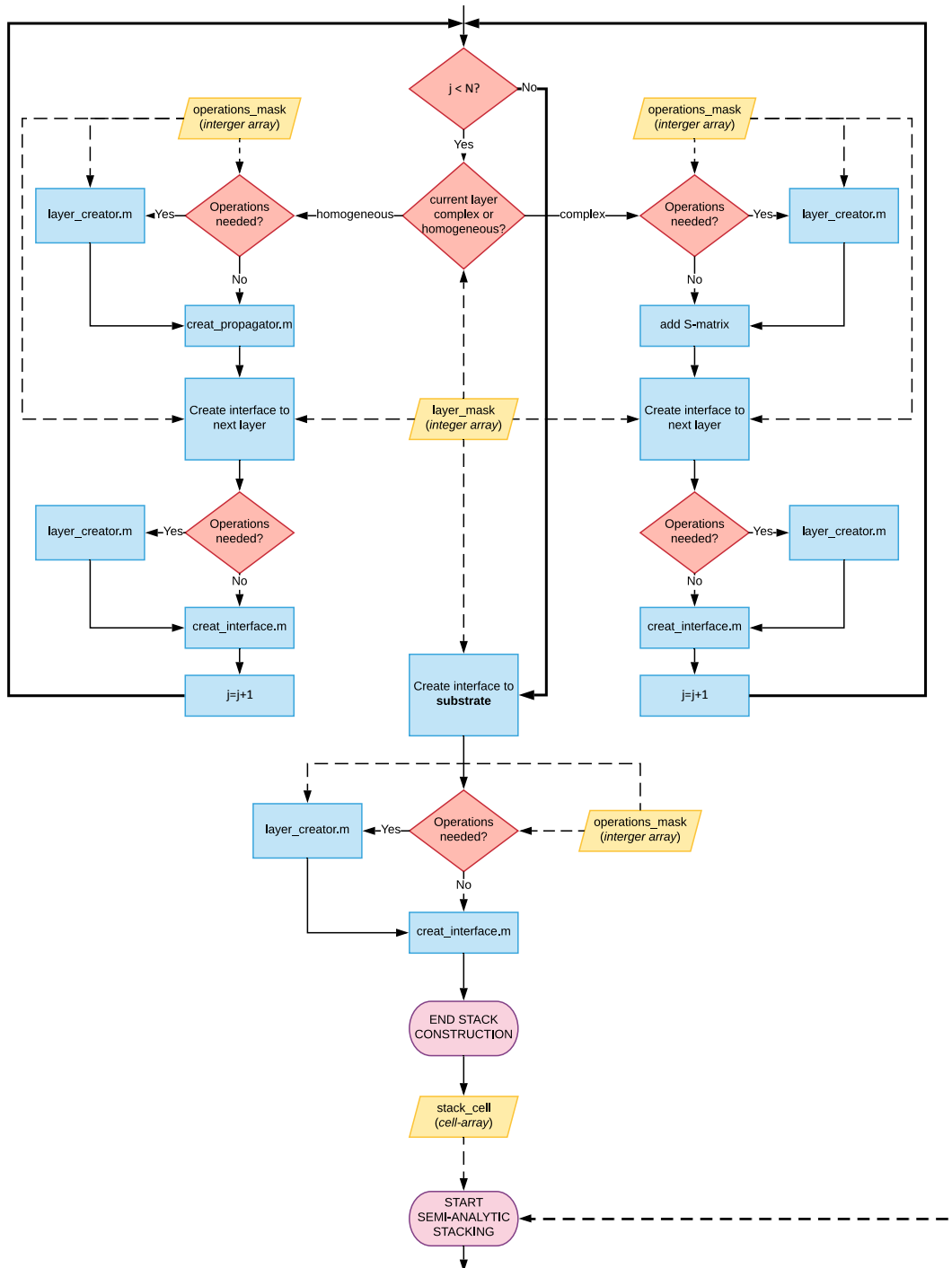


Figure A.3: SASA flow chart part 2 of 3: stack construction based on the previously identified layer pattern. Using the auxiliary functions `create_interface.m` and `create_propagator.m` the stack S-matrices are created iteratively, while applying layer operations where they are demanded by the user. Complex S-matrices (metasurfaces) are taken from pre-simulated results.

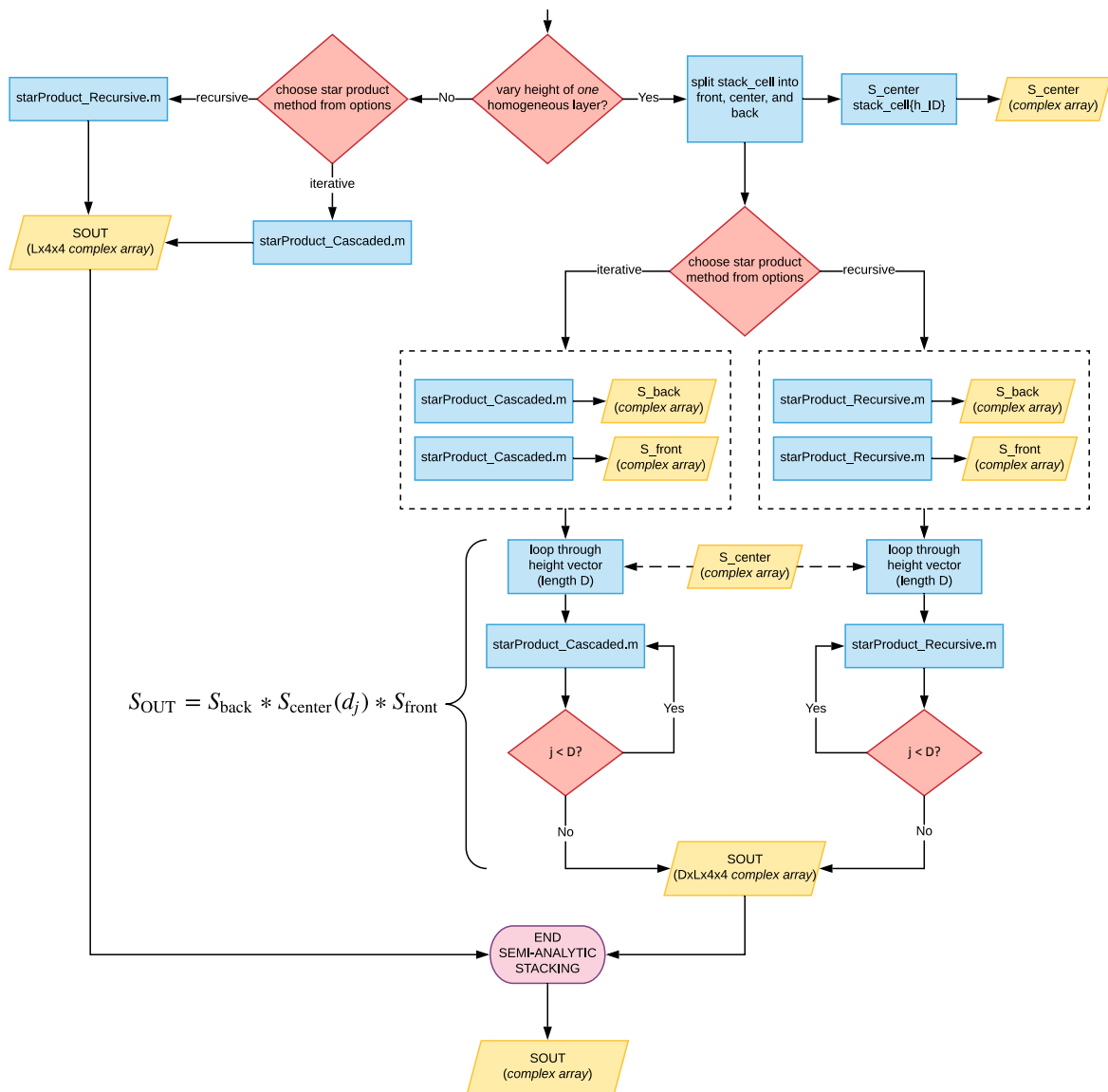


Figure A.4: SASA flow chart part 3 of 3: efficiently perform the Redheffer star product either iteratively (cascaded) or recursively. *One* homogeneous layer can have a vector of heights as a property. The SASA uses the associativity of the star product and precalculate the adjacent parts of stack, before iterating through all heights.

A.2.4 Computation time

Since SASA computes purely algebraic equations, it took only about 8×10^{-5} s to simulate the stack in sec. 5.1 for a single wavelength point on a standard laptop (2.7 GHz Sandy Bridge Intel Core i7 (2620M) and 16 GB 1333 MHz DDR3 memory). Moreover, the FMM for the single layer metasurfaces took about 790 s per wavelength point on a cluster node (using 2 threads on a Harpertown Intel Xeon-L5420 processor and 16 GB DDR memory). On the other hand, the rigorous FMM of the entire stack took about 1.7×10^3 s per wavelength using the same cluster nodes. Adding the time for the algebraic calculations and the single layer FMMs together and taking into account that simulations on a cluster can be run in parallel the semi-analytic approach is twice as fast for a single calculation as the rigorous FMM. When varying stack parameters such as spacer thickness, the order of layers or their orientation, the saved computation time by using SASA increases significantly. Nevertheless, a proper benchmark test would be needed for a thorough comparison of computation times.⁴

A.3 Comparison between layer rotation and unit cell rotation in twisted-wire-stack

As discussed in sec. 5.1.1 there is a difference between rotating an entire layer wire-metasurface or rotating its unit cells. The symmetry of both is the same - a broken C_2 symmetry with equal cross-polarization components. This was proven by comparison to the experimental results in sec. 5.1.2. The question remains, how the two types of rotation actually compare. In fig. A.5 we plotted the full FMM result, which was matched against experiment, and the SASA model using layer rotation. This was accomplished by using the lower wire-metasurface twice and rotating it in the upper layer by 60° . Of course, there is a small difference in the actual length of the wires as they resulted from fabrication. This is an error we should keep in mind when comparing the two results. Nevertheless, as fig. A.5 shows us, they are surprisingly similar. Most strikingly, the cross-polarization components match really well. We can conclude that our analytical models of the stack correctly approximate the real stack, well beyond a mere symmetry argument.

⁴Excerpt of the appendix in [146].

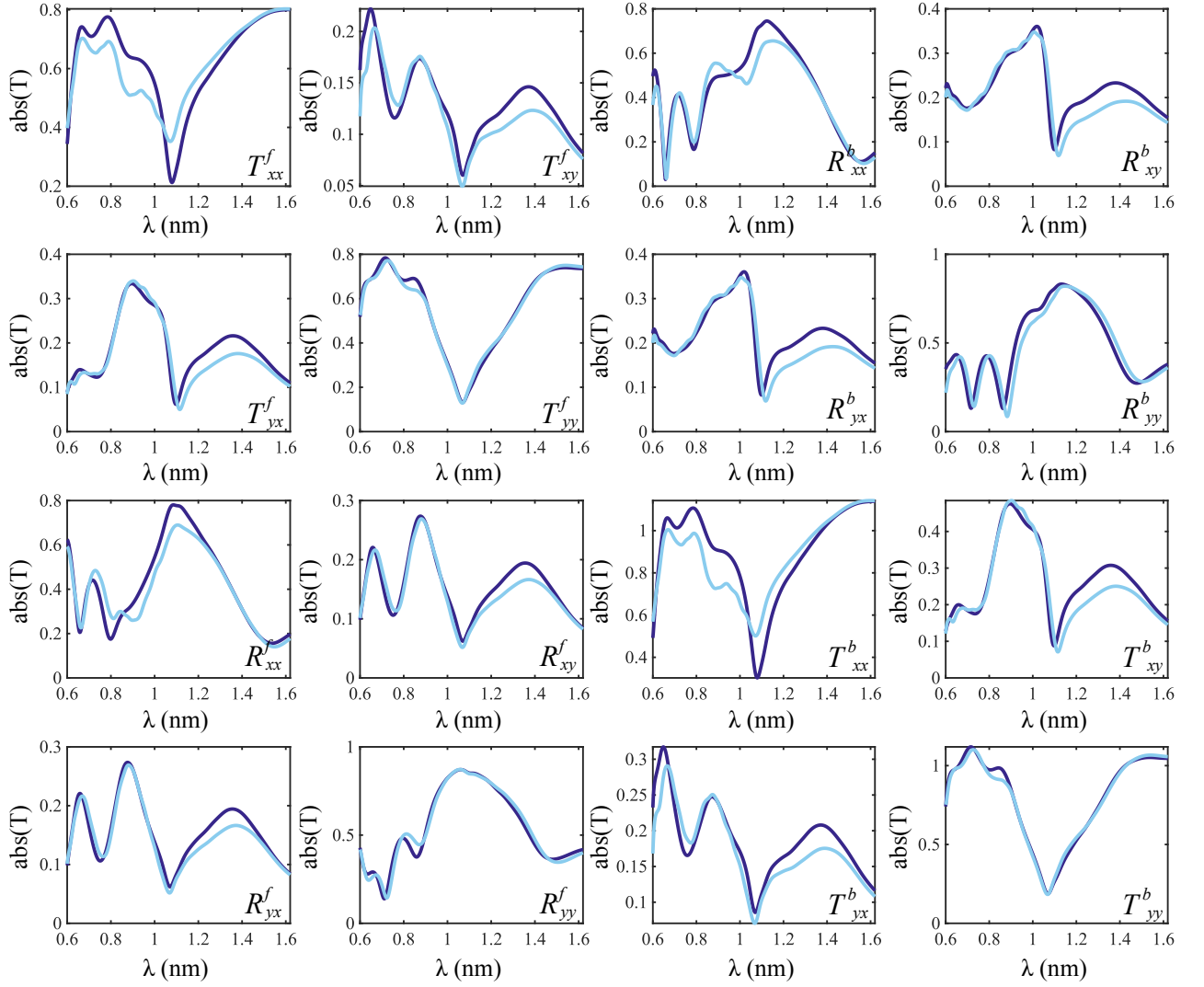


Figure A.5: Full 4×4 S-matrix of the twisted-wire-stack described in sec. 5.1. Each subplot shows the amplitude of the corresponding coefficient annotated in its lower right corner. The indigo blue lines show the result using SASA and layer rotation of the upper layer by 60° . The cyan lines show the full FMM-result.

A.4 Expressions of series coefficients and explicit calculations

A.4.1 Chiral stack S-matrix coefficients

The explicit expressions for the transmission coefficients of equation (5.3) are given by,

$$\bar{T}_{xx} = \frac{\mathcal{P}T_x (\mathcal{P}^2 R_y (R_{xy}^\alpha T_{xy}^\alpha + R_{yy}^\alpha T_{xx}^\alpha) - T_{xx}^\alpha)}{\mathcal{P}^4 R_x R_y (R_{xy}^{\alpha 2} - R_{xx}^\alpha R_{yy}^\alpha) + \mathcal{P}^2 (R_x R_{xx}^\alpha + R_y R_{yy}^\alpha) - 1}, \quad (\text{A.14})$$

$$\bar{T}_{xy} = \frac{\mathcal{P}T_y (\mathcal{P}^2 R_x (R_{xy}^\alpha T_{xx}^\alpha + R_{xx}^\alpha T_{xy}^\alpha) - T_{xy}^\alpha)}{\mathcal{P}^4 R_x R_y (R_{xy}^{\alpha 2} - R_{xx}^\alpha R_{yy}^\alpha) + \mathcal{P}^2 (R_x R_{xx}^\alpha + R_y R_{yy}^\alpha) - 1}, \quad (\text{A.15})$$

$$\bar{T}_{yx} = \frac{\mathcal{P}T_x (\mathcal{P}^2 R_y (R_{xy}^\alpha T_{yy}^\alpha + R_{yy}^\alpha T_{xy}^\alpha) - T_{xy}^\alpha)}{\mathcal{P}^4 R_x R_y (R_{xy}^{\alpha 2} - R_{xx}^\alpha R_{yy}^\alpha) + \mathcal{P}^2 (R_x R_{xx}^\alpha + R_y R_{yy}^\alpha) - 1}, \quad (\text{A.16})$$

$$\bar{T}_{yy} = \frac{\mathcal{P}T_y (\mathcal{P}^2 R_x (R_{xy}^\alpha T_{xy}^\alpha + R_{xx}^\alpha T_{yy}^\alpha) - T_{yy}^\alpha)}{\mathcal{P}^4 R_x R_y (R_{xy}^{\alpha 2} - R_{xx}^\alpha R_{yy}^\alpha) + \mathcal{P}^2 (R_x R_{xx}^\alpha + R_y R_{yy}^\alpha) - 1}. \quad (\text{A.17})$$

Reflection coefficients read

$$\begin{aligned} \bar{R}_{xx}^b = & \left(\mathcal{P}^4 R_x R_y (2R_{xy}^\alpha T_{xx}^\alpha T_{xy}^\alpha - R_{xx}^\alpha T_{xy}^{\alpha 2} - R_{yy}^\alpha T_{xx}^{\alpha 2} - R_{xx}^\alpha (R_{xy}^{\alpha 2} - R_{xx}^\alpha R_{yy}^\alpha)) \right. \\ & \left. + \mathcal{P}^2 (R_x T_{xx}^{\alpha 2} + R_y T_{xy}^{\alpha 2} - R_{xx}^\alpha (R_x R_{xx}^\alpha + R_y R_{yy}^\alpha)) + R_{xx}^\alpha \right) / \\ & (\mathcal{P}^4 R_x R_y (R_{xx}^\alpha R_{yy}^\alpha - R_{xy}^{\alpha 2}) - \mathcal{P}^2 (R_x R_{xx}^\alpha + R_y R_{yy}^\alpha) + 1), \end{aligned} \quad (\text{A.18})$$

$$\begin{aligned} \bar{R}_{xy}^b = & \left(\mathcal{P}^4 R_x R_y (R_{xy}^\alpha (R_{xx}^\alpha R_{yy}^\alpha + T_{xy}^{\alpha 2} - R_{xy}^{\alpha 2} + T_{xx}^\alpha T_{yy}^\alpha) - T_{xy}^\alpha (R_{yy}^\alpha T_{xx}^\alpha + R_{xx}^\alpha T_{yy}^\alpha)) \right. \\ & \left. + \mathcal{P}^2 (R_x T_{xx}^\alpha T_{xy}^\alpha + R_y T_{xy}^\alpha T_{yy}^\alpha - R_{xy}^\alpha (R_x R_{xx}^\alpha + R_y R_{yy}^\alpha)) + R_{xy}^\alpha \right) / \\ & (\mathcal{P}^4 R_x R_y (R_{xx}^\alpha R_{yy}^\alpha - R_{xy}^{\alpha 2}) - \mathcal{P}^2 (R_x R_{xx}^\alpha + R_y R_{yy}^\alpha) + 1), \end{aligned} \quad (\text{A.19})$$

$$\begin{aligned} \bar{R}_{yy}^b = & \left(\mathcal{P}^4 (-R_x) R_y (R_{yy}^\alpha (-R_{xx}^\alpha R_{yy}^\alpha + R_{xy}^{\alpha 2} + T_{xy}^{\alpha 2}) + R_{xx}^\alpha T_{yy}^{\alpha 2} - 2R_{xy}^\alpha T_{xy}^\alpha T_{yy}^\alpha) \right. \\ & \left. + \mathcal{P}^2 (R_x T_{xy}^{\alpha 2} + R_y T_{yy}^{\alpha 2} - R_{yy}^\alpha (R_x R_{xx}^\alpha + R_y R_{yy}^\alpha)) + R_{yy}^\alpha \right) / \\ & (\mathcal{P}^4 R_x R_y (R_{xx}^\alpha R_{yy}^\alpha - R_{xy}^{\alpha 2}) - \mathcal{P}^2 (R_x R_{xx}^\alpha + R_y R_{yy}^\alpha) + 1), \end{aligned} \quad (\text{A.20})$$

$$\begin{aligned} \bar{R}_{xx}^f = & \frac{R_x^2 - T_x^2}{R_x} \\ & + \frac{T_x^2 (1 - \mathcal{P}^2 R_y R_{yy}^\alpha)}{R_x (\mathcal{P}^4 R_x R_y (R_{xx}^\alpha R_{yy}^\alpha - R_{xy}^{\alpha 2}) - \mathcal{P}^2 (R_x R_{xx}^\alpha + R_y R_{yy}^\alpha) + 1)} \end{aligned} \quad (\text{A.21})$$

$$\bar{R}_{xy}^f = - \frac{\mathcal{P}^2 T_x T_y R_{xy}^\alpha}{\mathcal{P}^4 R_x R_y (R_{xy}^{\alpha 2} - R_{xx}^\alpha R_{yy}^\alpha) + \mathcal{P}^2 (R_x R_{xx}^\alpha + R_y R_{yy}^\alpha) - 1}, \quad (\text{A.22})$$

$$\begin{aligned} \bar{R}_{yy}^f = & \frac{R_y^2 - T_y^2}{R_y} \\ & + \frac{T_y^2 (1 - \mathcal{P}^2 R_x R_{xx}^\alpha)}{R_y (\mathcal{P}^4 R_x R_y (R_{xx}^\alpha R_{yy}^\alpha - R_{xy}^{\alpha 2}) - \mathcal{P}^2 (R_x R_{xx}^\alpha + R_y R_{yy}^\alpha) + 1)}. \end{aligned} \quad (\text{A.23})$$

A.4.2 Multi-index backward reflection matrices

Here, we show the explicit calculation of the recursive multi-index backward reflection matrices for $N = 5$ layers from sec. 6.1.4. Importantly, the backward matrices have to be treated in reverse layer order. Occurring forward matrices are then defined in that particular *slice* of the stack, e.g. forward propagating modes between layer $N - 2$ and N for forward reflection *starting* at N and considered until $N - 2$. In other words, the recursion of reflection matrices has to be performed slice-wise, in reverse layer order, and with slice dependent transmission coefficients. Fortunately, because the composition of the five-layer stack entails only two metasurfaces, we can eliminate those reflection matrices that refer to propagators through homogeneous layers (layers 2 and 4). This leads to the following sequence of step by step unfolded recursions, while eliminating propagator-reflections,

$$\hat{R}_{M_1}^b = \hat{R}_{4,3,2,1}^b = \hat{R}_{4,3,2}^b + \hat{T}_{2,3,4}^f \hat{R}_1^b \left(\hat{\mathbb{I}} + \sum_{\gamma=1}^{\Psi} \left(\hat{R}_{2,3,4}^f \hat{R}_1^b \right)^\gamma \right) \hat{T}_{4,3,2}^b, \quad (\text{A.24})$$

$$\hat{R}_{M_2}^b = \hat{R}_{4,3,2}^b = \hat{R}_{4,3}^b + \hat{T}_{4,3}^f \hat{R}_2^b \left(\hat{\mathbb{I}} + \sum_{\gamma=1}^{\Psi} \left(\hat{R}_{3,4}^f \hat{R}_2^b \right)^\gamma \right) \hat{T}_{4,3}^b, \quad (\text{A.25})$$

$$\hat{R}_{M_3}^b = \hat{R}_{4,3}^b = \hat{R}_4^b + \hat{T}_4^f \hat{R}_3^b \left(\hat{\mathbb{I}} + \sum_{\gamma=1}^{\Psi} \left(\hat{R}_4^f \hat{R}_3^b \right)^\gamma \right) \hat{T}_4^b, \quad (\text{A.26})$$

$$\hat{R}_{M_2}^f = \hat{R}_{2,3,4}^b = \hat{R}_{2,3}^f + \hat{T}_{3,2}^b \hat{R}_4^f \left(\hat{\mathbb{I}} + \sum_{\gamma=1}^{\Psi} \left(\hat{R}_{3,2}^b \hat{R}_4^f \right)^\gamma \right) \hat{T}_{2,3}^f, \quad (\text{A.27})$$

$$\hat{R}_{M_3}^f = \hat{R}_{2,3}^b = \hat{R}_2^f + \hat{T}_2^b \hat{R}_3^b \left(\hat{\mathbb{I}} + \sum_{\gamma=1}^{\Psi} \left(\hat{R}_2^b \hat{R}_3^f \right)^\gamma \right) \hat{T}_2^f. \quad (\text{A.28})$$

The respective slice transmission matrices, $\hat{T}_{2,3,4}^f$ and $\hat{T}_{4,3,2}^b$, then follow by using eq. (6.9) and obeying the layer ordering of each slice,

$$\begin{aligned} \hat{T}_{M_2}^f &= \hat{T}_{2,3,4}^f = \hat{T}_4^f \prod_{p=1}^2 \left(\hat{\mathbb{I}} + \sum_{\alpha=1}^{\Psi} \left(\hat{R}_{M_p}^b \hat{R}_{n_{p-1}}^f \right)^\alpha \right) \hat{T}_{n_p}^f \\ &= \hat{T}_4^f \left(\hat{\mathbb{I}} + \sum_{\alpha=1}^{\Psi} \left(\hat{R}_{3,2}^b \hat{R}_4^f \right)^\alpha \right) \hat{T}_3^f \left(\hat{\mathbb{I}} + \sum_{\alpha=1}^{\Psi} \left(\hat{R}_2^b \hat{R}_3^f \right)^\alpha \right) \hat{T}_2^f \end{aligned} \quad (\text{A.29})$$

$$\Rightarrow \hat{T}_{M_2}^b = \hat{T}_{4,3,2}^b = \hat{T}_2^f \hat{T}_3^f \hat{T}_4^f. \quad (\text{A.30})$$

Inserting all above equations into each other as well as rewriting $\hat{T}_2^f \rightarrow \mathcal{P}_2$ and $\hat{T}_4^f \rightarrow \mathcal{P}_4$ yields the explicit reflection series for layers 4 to 1

$$\hat{R}_{M_1}^b = \mathcal{P}_4 \hat{R}_3^b \mathcal{P}_4 + \mathcal{P}_4 \hat{T}_3^f \mathcal{P}_2 \hat{R}_1^b \left(\hat{\mathbb{I}} + \sum_{\gamma=1}^{\Psi} \left(\mathcal{P}_2 \hat{R}_3^f \mathcal{P}_2 \hat{R}_1^b \right)^\gamma \right) \mathcal{P}_2 \hat{T}_3^b \mathcal{P}_4. \quad (\text{A.31})$$

A.4.3 Combinatoric formulation of 5-Layer transmission

We can recognize from the paths in fig. 6.1 that the power of the propagators \mathcal{P} is a counter for the number of revolutions in the stack. Accordingly, we can rewrite eq. (6.18) such that all terms are ordered by powers of \mathcal{P} . Partially resolving all parentheses in eq. (6.18) lets us identify individual terms of (recurring) Feynman paths,

$$\begin{aligned} \hat{T}_{M_0}^f &= \hat{T}_5^f \mathcal{P}_4 \hat{T}_3^f \mathcal{P}_2 \hat{T}_1^f \\ &+ \hat{T}_5^f \sum_{\alpha=1}^{\Psi} \left(\mathcal{P}_4 \hat{R}_3^b \mathcal{P}_4 \hat{R}_5^f + \mathcal{P}_4 \hat{T}_3^f \mathcal{P}_2 \hat{R}_1^b \mathcal{P}_2 \hat{T}_3^b \mathcal{P}_4 \hat{R}_5^f + \mathcal{P}_4 \hat{T}_3^f \mathcal{P}_2 \hat{R}_1^b \sum_{\gamma=1}^{\Psi} \left(\mathcal{P}_2 \hat{R}_3^f \mathcal{P}_2 \hat{R}_1^b \right)^\gamma \mathcal{P}_2 \hat{T}_3^b \mathcal{P}_4 \hat{R}_5^f \right)^\alpha \mathcal{P}_2 \hat{T}_1^f \\ &+ \hat{T}_5^f \mathcal{P}_4 \hat{T}_3^f \sum_{\beta=1}^{\Psi} \left(\mathcal{P}_2 \hat{R}_1^b \mathcal{P}_2 \hat{R}_3^f \right)^\beta \mathcal{P}_2 \hat{T}_1^f \\ &+ \hat{T}_5^f \sum_{\delta=1}^{\Psi} \left(\mathcal{P}_4 \hat{R}_3^b \mathcal{P}_4 \hat{R}_5^f + \mathcal{P}_4 \hat{T}_3^f \mathcal{P}_2 \hat{R}_1^b \mathcal{P}_2 \hat{T}_3^b \mathcal{P}_4 \hat{R}_5^f + \mathcal{P}_4 \hat{T}_3^f \mathcal{P}_2 \hat{R}_1^b \sum_{\nu=1}^{\Psi} \left(\mathcal{P}_2 \hat{R}_3^f \mathcal{P}_2 \hat{R}_1^b \right)^\nu \mathcal{P}_2 \hat{T}_3^b \mathcal{P}_4 \hat{R}_5^f \right)^\delta \\ &\times \mathcal{P}_4 \hat{T}_3^f \sum_{\mu=1}^{\Psi} \left(\mathcal{P}_2 \hat{R}_1^b \mathcal{P}_2 \hat{R}_3^f \right)^\mu \mathcal{P}_2 \hat{T}_1^f. \end{aligned} \quad (\text{A.32})$$

We can clearly recognize elements of paths that recur in each of the three main sums. Using the multinomial theorem, we can sort these by their multinomial factors and the power of propagator pairs $\mathcal{P}_2 \mathcal{P}_4$. Finally, we arrive at

$$\begin{aligned} \hat{T}_{M_0}^f &= \hat{T}_5^f \mathcal{P}_4 \hat{T}_3^f \mathcal{P}_2 \hat{T}_1^f \\ &+ \hat{T}_5^f \sum_{\alpha=1}^{\Psi} \sum_{\alpha_1 + \dots + \alpha_{\Psi+2} = \alpha} \binom{\alpha}{\alpha_1, \dots, \alpha_{\Psi+2}} \prod_{p=1}^{\Psi} \left(\mathcal{P}_2^{\alpha_2 + \alpha_{p+2}(1+p)} \mathcal{P}_4^{\alpha_1 + \alpha_2 + \alpha_{p+2}} \right)^2 \\ &\times \left(\hat{R}_3^b \hat{R}_5^f \right)^{\alpha_1} \left(\hat{T}_3^f \hat{R}_1^b \hat{T}_3^b \hat{R}_5^f \right)^{\alpha_2} \prod_{\gamma=1}^{\Psi} \left(\hat{T}_3^f \hat{R}_1^b \left(\hat{R}_3^f \hat{R}_1^b \right)^\gamma \hat{T}_3^b \hat{R}_5^f \right)^{\alpha_{\gamma+2}} \mathcal{P}_2 \hat{T}_1^f \\ &+ \hat{T}_5^f \mathcal{P}_4 \hat{T}_3^f \sum_{\beta=1}^{\Psi} \left(\mathcal{P}_2 \hat{R}_1^b \mathcal{P}_2 \hat{R}_3^f \right)^\beta \mathcal{P}_2 \hat{T}_1^f \end{aligned}$$

$$\begin{aligned}
& + \hat{T}_5^f \sum_{\delta=1}^{\Psi} \sum_{\delta_1+\dots+\delta_{\Psi+2}=\delta} \binom{\delta}{\delta_1, \dots, \delta_{\Psi+2}} \prod_{p=1}^{\Psi} \left(\mathcal{P}_2^{\delta_2+\delta_{p+2}(1+p)} \mathcal{P}_4^{\delta_1+\delta_2+\delta_{p+2}} \right)^2 \\
& \times \left(\hat{R}_3^b \hat{R}_5^f \right)^{\delta_1} \left(\hat{T}_3^f \hat{R}_1^b \hat{T}_3^b \hat{R}_5^f \right)^{\delta_2} \prod_{\nu=1}^{\Psi} \left(\hat{T}_3^f \hat{R}_1^b \left(\hat{R}_3^f \hat{R}_1^b \right)^{\nu} \hat{T}_3^b \hat{R}_5^f \right)^{\delta_{\nu+2}} \mathcal{P}_2 \hat{T}_1^f \\
& \times \mathcal{P}_4 \hat{T}_3^f \sum_{\mu=1}^{\Psi} \left(\mathcal{P}_2 \hat{R}_1^b \mathcal{P}_2 \hat{R}_3^f \right)^{\mu} \mathcal{P}_2 \hat{T}_1^f. \tag{A.33}
\end{aligned}$$

A.4.4 Coefficients of the first order asymmetric transmission

The asymmetric transmission of the expanded transmission matrix pertaining to the chiral metasurface stack can be calculated using eq. (6.33). An explicit expression of the first order term Δ_1^x , eq. (6.35), follows by inserting the matrix coefficients from eqs. (5.1) and (5.2). Then,

$$\begin{aligned}
\Delta_1^x & = |T_{xy,1}|^2 - |T_{yx,1}|^2 = |T_3^{11} R_{1k}^1 R_3^{kl} T_{l2}^1|^2 - |T_3^{22} R_{2k}^1 R_3^{kl} T_{l1}^1|^2 \\
& = |T_x|^2 \cos^2 \alpha \sin^2 \alpha |R_x(T_y - T_x)(R_x \cos^2 \alpha + R_y \sin^2 \alpha) + R_y(R_y - R_x)(T_y \cos^2 \alpha + T_x \sin^2 \alpha)|^2 \\
& - |T_y|^2 \cos^2 \alpha \sin^2 \alpha |R_y(T_y - T_x)(R_y \cos^2 \alpha + R_x \sin^2 \alpha) + R_x(R_y - R_x)(T_x \cos^2 \alpha + T_y \sin^2 \alpha)|^2 \\
& \stackrel{!}{=} (A_1 \cos^4 \alpha + A_2 \cos^6 \alpha) \sin^2 \alpha + (A_3 \cos^2 \alpha + A_4 \cos^4 \alpha) \sin^4 \alpha + A_5 \cos^2 \alpha \sin^6 \alpha. \tag{A.34}
\end{aligned}$$

The coefficients A_i are the factors of the trigonometric functions that follow from expanding and sorting eq. (A.34). Denoting the amplitude $|T|$ and $|R|$ with t and r , respectively, the coefficients read

$$A_1 = 2t_x t_y r_x r_y (t_y^2 r_y^2 - t_x^2 r_x^2) \cos(\phi_x - \phi_y + \gamma_x - \gamma_y), \tag{A.35}$$

$$\begin{aligned}
A_2 & = 2t_x t_y (\cos(\phi_x - \phi_y) (t_y^2 r_y^4 - t_x^2 r_x^4) + r_x r_y (r_x r_y (t_y^2 - t_x^2) \cos(\phi_x - \phi_y + 2\gamma_x - 2\gamma_y))) \\
& + t_x^4 r_x^4 - t_y^4 r_y^4 - A_1, \tag{A.36}
\end{aligned}$$

$$A_3 = 2t_x t_y r_x r_y ((t_x^2 r_y^2 - t_y^2 r_x^2) \cos(\phi_x - \phi_y - \gamma_x + \gamma_y) + 2r_x r_y (t_y^2 - t_x^2) \cos(\phi_x - \phi_y)), \tag{A.37}$$

$$\begin{aligned}
A_4 & = 2 \left(r_x r_y \left(2 \cos(\gamma_x - \gamma_y) (t_x^4 r_x^2 - t_y^4 r_y^2) + r_x r_y (t_y^4 - t_x^4) \cos(2\gamma_x - 2\gamma_y) \right. \right. \\
& + t_x t_y (t_x^2 - t_y^2) (r_x r_y \cos(\phi_x - \phi_y - 2\gamma_x + 2\gamma_y) - 2(r_x^2 + r_y^2) \cos(\phi_x - \phi_y - \gamma_x + \gamma_y)) \\
& + 2t_x t_y (t_y r_x - t_x r_y) (t_x r_y + t_y r_x) \cos(\phi_x - \phi_y + \gamma_x - \gamma_y) \left. \right) \\
& + t_x t_y \cos(\phi_x - \phi_y) (t_x^2 r_y^4 + 4r_x^2 r_y^2 (t_x - t_y)(t_x + t_y) - t_y^2 r_x^4), \tag{A.38}
\end{aligned}$$

$$A_5 = 4r_x r_y \cos(\gamma_x - \gamma_y) (t_y^4 r_x^2 - t_x^4 r_y^2) + t_x^4 r_y^2 (4r_x^2 + r_y^2) - t_y^4 (4r_x^2 r_y^2 + r_x^4). \tag{A.39}$$

A.4.5 Phase shift of the first order asymmetric transmission

Here, we show the calculation of the phase shifts producing the interferometric corrections of Γ_{10} in eq. (6.36) The phases of zeroth and first order can be calculated for order ψ by

$$\phi_\psi^{ij} = \arctan(\text{Im } T_\psi^{ij} / \text{Re } T_\psi^{ij}) := \arctan(\zeta_\psi^{ij}). \quad (\text{A.40})$$

Using the identities of arcus functions and compositions of arcus functions and trigonometric functions,

$$\arctan x + \arctan y = \arctan\left(\frac{x-y}{1+xy}\right) \quad \text{and} \quad \cos(\arctan x) = \frac{x}{\sqrt{1+x^2}}, \quad (\text{A.41})$$

the phase difference term in eq. (A.34) reads

$$\cos \delta_{10}^{xy} = \cos(\phi_0^{xy} - \phi_1^{xy}) = \frac{\zeta_0^{xy} - \zeta_1^{xy}}{\sqrt{1 + (\zeta_0^{xy})^2 + (\zeta_0^{xy} \zeta_1^{xy})^2 + (\zeta_1^{xy})^2}}. \quad (\text{A.42})$$

The ratios ζ_ψ^{ij} require the imaginary and real parts of eq. (6.32) with the matrix coefficients from eqs. (5.1) and (5.2) inserted. These are very complex expressions that have to be calculated and simplified using Mathematica (or similar software). After some calculation and pattern matching (structurally sorting terms) we arrive at

$$\zeta_0^{xy} = \frac{t_x \sin(2\phi_x + nk_0d) - t_y \sin(\phi_x + \phi_y + nk_0d)}{t_x \cos(2\phi_x + nk_0d) - t_y \cos(\phi_x + \phi_y + nk_0d)} \quad (\text{A.43})$$

$$\zeta_0^{yx} = \frac{t_y \sin(2\phi_y + nk_0d) - t_x \sin(\phi_x + \phi_y + nk_0d)}{t_y \cos(2\phi_y + nk_0d) - t_x \cos(\phi_x + \phi_y + nk_0d)}. \quad (\text{A.44})$$

The first order ratios include reflection phases, $\tilde{\phi}$ of the metasurfaces and read

$$\begin{aligned} \zeta_1^{xy} = & 4 \sin(2\alpha) \left(\cos^2(\alpha) \left(r_x^2 (t_y \sin(\phi_x + \phi_y + 2\tilde{\phi}_x + 3nk_0r_y) - t_x \sin(2(\phi_x + \tilde{\phi}_x) + 3nk_0d)) \right. \right. \\ & + r_y^2 t_y \sin(\phi_x + \phi_y + 2\tilde{\phi}_y + 3nk_0d) \left. \right) - r_x r_y t_y \cos(2\alpha) \sin(\phi_x + \phi_y + \tilde{\phi}_x + \tilde{\phi}_y + 3nk_0d) \\ & + r_y t_x \sin^2(\alpha) (r_y \sin(2(\phi_x + \tilde{\phi}_y) + 3nk_0d) - 2r_x \sin(2\phi_x + \tilde{\phi}_x + \tilde{\phi}_y + 3nk_0d)) \left. \right) \\ & / 8 \sin(\alpha) \cos^3(\alpha) \left(r_x^2 (t_y \cos(\phi_x + \phi_y + 2\tilde{\phi}_x + 3nk_0d) - t_x \cos(2(\phi_x + \tilde{\phi}_x) + 3nk_0d)) \right. \\ & + r_y^2 t_y \cos(\phi_x + \phi_y + 2\tilde{\phi}_y + 3nk_0d) \left. \right) - r_y \sin(4\alpha) (2r_x t_y \cos(\phi_x + \phi_y + \tilde{\phi}_x + \tilde{\phi}_y + 3nk_0d) \\ & + r_y t_x \cos(2(\phi_x + \tilde{\phi}_y) + 3nk_0d)) - 16r_x r_y t_x \sin^3(\alpha) \cos(\alpha) \cos(2\phi_x + \tilde{\phi}_x + \tilde{\phi}_y + 3nk_0d) \\ & + 2r_y^2 t_x \sin(2\alpha) \cos(2(\phi_x + \tilde{\phi}_y) + 3nk_0d), \end{aligned} \quad (\text{A.45})$$

$$\begin{aligned}
\zeta_1^{yx} = & 4 \sin(2\alpha) \left(\cos^2(\alpha) \left(r_x^2 t_x \sin\left(\phi_x + \phi_y + 2\tilde{\phi}_x + 3nk_0d\right) + r_y^2 (t_x \sin\left(\phi_x + \phi_y + 2\tilde{\phi}_y + 3nk_0d\right) \right. \right. \\
& \left. \left. - t_y \sin\left(2(\phi_y + \tilde{\phi}_y) + 3nk_0d\right)\right) - r_x r_y t_x \cos(2\alpha) \sin\left(\phi_x + \phi_y + \tilde{\phi}_x + \tilde{\phi}_y + 3nk_0d\right) \right. \\
& \left. + r_x t_y \sin^2(\alpha) (r_x \sin\left(2(\phi_y + \tilde{\phi}_x) + 3nk_0d\right) - 2r_y \sin\left(2\phi_y + \tilde{\phi}_x + \tilde{\phi}_y + 3nk_0d\right)) \right. \\
& \left. / 8 t_x \sin(\alpha) \cos^3(\alpha) \left(r_x^2 \cos\left(\phi_x + \phi_y + 2\tilde{\phi}_x + 3nk_0d\right) + r_y^2 \cos\left(\phi_x + \phi_y + 2\tilde{\phi}_y + 3nk_0d\right) \right) \right. \\
& \left. - r_y \sin(4\alpha) (2r_x t_x \cos\left(\phi_x + \phi_y + \tilde{\phi}_x + \tilde{\phi}_y + 3nk_0d\right) + r_y t_y \cos\left(2(\phi_y + \tilde{\phi}_y) + 3nk_0d\right)) \right. \\
& \left. + 8 r_x t_y \sin^3(\alpha) \cos(\alpha) (r_x \cos\left(2(\phi_y + \tilde{\phi}_x) + 3nk_0d\right) - 2r_y \cos\left(2\phi_y + \tilde{\phi}_x + \tilde{\phi}_y + 3nk_0d\right)) \right. \\
& \left. - 2r_y^2 t_y \sin(2\alpha) \cos\left(2(\phi_y + \tilde{\phi}_y) + 3nk_0d\right) \right). \tag{A.46}
\end{aligned}$$

The different sums of phases in the arguments of the trigonometric functions visibly represent an individual virtual path and its interactions with the metasurfaces. The factor 3 of the spacer phase nk_0d clearly denotes the first order with three passes through the spacer: one revolution and one pass through.

B | Bibliography

- [1] M. Born and E. Wolf, *Principles of Optics*. Cambridge University Press, New York, 1999.
- [2] F.-T. Lentes, M. K. T. Clement, N. Neuroth, H.-J. Hoffmann, Y. T. Hayden, J. S. Hayden, U. Kolberg, and S. Wolff, “The Properties of Optical Glass,” Schott Series on Glass and Glass Ceramics, pp. 19–164. 1998.
- [3] B. E. A. Saleh and M. C. Teich, *Fundamentals of Photonics*. Wiley Series in Pure and Applied Optics. 2018.
- [4] M. Fox, *Optical Properties of Solids*. Oxford University Press, New York, second ed., 2010.
- [5] H. A. Lorentz, S. Boltzmann, and W. S. Laws, “On the scattering of molecules,” *KNAW Proceedings of the section of sciences* **13** 1 (1910) 92–107.
- [6] C. R. Simovski, “Material parameters of metamaterials (a Review),” *Optics and Spectroscopy* (2009) .
- [7] S. Hunklinger, *Festkörperphysik*. De Gruyter Oldenbourg, Oldenbourg, 2014.
- [8] K. W. Böer and U. W. Pohl, *Semiconductor Physics*. 2018.
- [9] A. Sihvola, *Electromagnetic Mixing Formulas and Applications*. The Institution of Engineering and Technology, London, 2nd ed., 2008.
- [10] A. Sihvola, “Metamaterials in electromagnetics,” *Metamaterials* no. 1, mar2–11.
- [11] D. Werdehausen, X. G. Santiago, S. Burger, I. Staude, T. Pertsch, C. Rockstuhl, and M. Decker, “Modeling Optical Materials at the Single Scatterer Level: The Transition from Homogeneous to Heterogeneous Materials,” *Advanced Theory and Simulations* **3** no. 11, (2020) 2000192.
- [12] A. Piel, *Plasma Physics, An Introduction to Laboratory, Space, and Fusion Plasmas*. Graduate Texts in Physics. 2017.

- [13] G. K. Parks, *Characterizing Space Plasmas, A Data Driven Approach*. Astronomy and Astrophysics Library. 2018.
- [14] B. A. Munk, *Frequency Selective Surfaces*. John Wiley & Sons, Inc., Hoboken, NJ, USA, apr.
- [15] H. A. Lorentz, “Ergebnisse und Probleme der Elektronentheorie,” in *Ergebnisse und Probleme der Elektronentheorie*, pp. 5–62. Springer, Berlin, Heidelberg, 1905.
- [16] T. W. Kornbau, *ANALYSIS OF PERIODIC ARRAYS OF ROTATED LINEAR DIPOLES, ROTATED CROSSED DIPOLES, AND OF BIPLANAR DIPOLE ARRAYS IN DIELECTRIC (SPATIAL FILTER, DICHROIC REFLECTOR, FREQUENCY SELECTIVE SURFACE)*. PhD thesis. Last updated - 2021-05-25.
- [17] R. Kiebertz and A. Ishimaru, “Scattering by a periodically apertured conducting screen,” *IRE Transactions on Antennas and Propagation* **9** no. 6, (1961) 506–514.
- [18] R. Mittra, C. Chan, and T. Cwik, “Techniques for analyzing frequency selective surfaces-a review,” *Proceedings of the IEEE* (1988) , *Proceedings of the IEEE*.
- [19] D. F. Sievenpiper, M. E. Sickmiller, and E. Yablonovitch, “3D Wire Mesh Photonic Crystals,” *Physical Review Letters* (1996) , *Physical Review Letters*.
- [20] D. Sievenpiper, L. Zhang, R. Broas, N. Alexopolous, and E. Yablonovitch, “High-impedance electromagnetic surfaces with a forbidden frequency band,” *IEEE Transactions on Microwave Theory and Techniques* (1999) , *IEEE Transactions on Microwave Theory and Techniques*.
- [21] R. Quarfoth and D. Sievenpiper, “Surface Wave Scattering Reduction Using Beam Shifters,” *IEEE Antennas and Wireless Propagation Letters* **13** (2014) 963–966.
- [22] F. Gao, F. Zhang, H. Wakatsuchi, and D. F. Sievenpiper, “Synthesis and Design of Programmable Subwavelength Coil Array for Near-Field Manipulation,” *IEEE Transactions on Microwave Theory and Techniques* **63** no. 9, (2015) 2971–2982.
- [23] D. J. Bisharat and D. F. Sievenpiper, “Electromagnetic-Dual Metasurfaces for Topological States along a 1D Interface,” *Laser & Photonics Reviews* **13** no. 10, (2019) 1900126, 1907.06684.
- [24] S. Wu, V. V. Yachin, V. I. Shcherbinin, and V. R. Tuz, “Chiral metasurface formed by 3D-printed square helices: A flexible tool to manipulate wave polarization,” *arXiv* (2019) , 1906.05690.

- [25] A. Li, S. Singh, and D. Sievenpiper, “Metasurfaces and their applications,” *Nanophotonics* (2018) , *Nanophotonics*.
- [26] A. Alù, “Metamaterials: Prime time,” *Nature Materials* no. 12, nov1229–1231.
- [27] Q. Chen, X. Hu, L. Wen, Y. Yu, and D. R. S. Cumming, “Nanophotonic Image Sensors,” *Small* **12** no. 36, (2016) 4922–4935.
- [28] F. Capasso, F. Aieta, M. Khorasaninejad, P. Genevet, and R. Devlin, “Recent advances in planar optics: from plasmonic to dielectric metasurfaces,” *Optica* **4** no. 1, (2017) 139–152.
- [29] S. Boroviks, R. A. Deshpande, N. A. Mortensen, and S. I. Bozhevolnyi, “Multifunctional Metamirror: Polarization Splitting and Focusing,” *ACS Photonics* **5** no. 5, (2018) 1648–1653, 1709.04257.
- [30] I. Staude, T. Pertsch, and Y. S. Kivshar, “All-Dielectric Resonant Meta-Optics Lightens up,” *ACS Photonics* **6** no. 4, (2019) 802–814.
- [31] J. B. Pendry, “Extremely Low Frequency Plasmons in Metallic Mesostructures,” *Physical Review Letters* **76** no. 25, (1996) 4773–4776.
- [32] J. B. Pendry, A. J. Holden, D. J. Robbins, and W. J. Stewart, “Low frequency plasmons in thin-wire structures,” *Journal of Physics: Condensed Matter* (1998) , *Journal of Physics: Condensed Matter*.
- [33] V. G. Veselago, “THE ELECTRODYNAMICS OF SUBSTANCES WITH SIMULTANEOUSLY NEGATIVE VALUES OF EPSILON AND MU,” *Soviet Physics Uspekhi* no. 4, 509.
- [34] J. B. Pendry, “Negative refraction makes a perfect lens,” *Physical Review Letters* no. 18, 3966–3969.
- [35] S. A. Maier, *Plasmonics: Fundamentals and Applications*. Springer Science, New York, 2007.
- [36] A. Sihvola, “Metamaterials in electromagnetics,” *Metamaterials* **1** no. 1, (2007) 2–11.
- [37] D. F. Sievenpiper, M. E. Sickmiller, and E. Yablonovitch, “3D Wire Mesh Photonic Crystals,” *Physical Review Letters* no. 14, apr2480–2483.
- [38] S. Tretyakov, *Analytical Modeling in Applied Electrodynamics*. Artech House, Inc.

- [39] J. Petschulat, A. Chipouline, A. Tünnermann, T. Pertsch, C. Menzel, C. Rockstuhl, T. Paul, and F. Lederer, “Simple and versatile analytical approach for planar metamaterials,” *Physical Review B* **82** no. 7, (2010) 075102, 0909.0778.
- [40] C. Menzel, E. Hebestreit, R. Alaee, M. Albooyeh, S. Mühlig, S. Burger, C. Rockstuhl, C. Simovski, S. Tretyakov, F. Lederer, and T. Pertsch, “Extreme coupling: A route towards local magnetic metamaterials,” *Physical Review B* **89** no. 15, (2014) 155125.
- [41] A. Rahimzadegan, D. Arslan, D. Dams, A. Groner, X. Garcia-Santiago, R. Alaee, I. Fernandez-Corbaton, T. Pertsch, I. Staude, and C. Rockstuhl, “Beyond dipolar Huygens’ metasurfaces for full-phase coverage and unity transmittance,” *Nanophotonics* **9** no. 1, (2019) 75–82.
- [42] N. Perdana, C. Rockstuhl, and A. A. Iskandar, “Induced higher order multipolar resonances from interacting scatterers,” *Journal of the Optical Society of America B* **38** no. 1, (2020) 241.
- [43] A. Monti, A. Alu, A. Toscano, and F. Bilotti, “Design of High-Q Passband Filters Implemented through Multipolar All-Dielectric Metasurfaces,” *IEEE Transactions on Antennas and Propagation* **PP** no. 99, (2020) 1–1.
- [44] V. A. Zenin, C. E. Garcia-Ortiz, A. B. Evlyukhin, Y. Yang, R. Malureanu, S. M. Novikov, V. Coello, B. N. Chichkov, S. I. Bozhevolnyi, A. V. Lavrinenko, and N. A. Mortensen, “Engineering Nanoparticles with Pure High-Order Multipole Scattering,” *ACS Photonics* **7** no. 4, (2020) 1067–1075, 2001.03489.
- [45] C. Rockstuhl and T. Scharf, *Amorphous Nanophotonics*. Nano-Optics and Nanophotonics. Springer-Verlag, Berlin, 2013.
- [46] C. L. Holloway, A. Dienstfrey, E. F. Kuester, J. F. O’Hara, A. K. Azad, and A. J. Taylor, “A discussion on the interpretation and characterization of metafilms/metasurfaces: The two-dimensional equivalent of metamaterials,” *Metamaterials* **3** no. 2, (2009) 100–112.
- [47] C. L. Holloway, E. F. Kuester, J. A. Gordon, J. O’Hara, J. Booth, and D. R. Smith, “An Overview of the Theory and Applications of Metasurfaces: The Two-Dimensional Equivalents of Metamaterials,” *IEEE Antennas and Propagation Magazine* (2012) .
- [48] N. Yu and F. Capasso, “Flat optics with designer metasurfaces,” *Nature Materials* **13** no. 2, (2014) 139–150.

- [49] I. Staude and J. Schilling, “Metamaterial-inspired silicon nanophotonics,” *Nature Photonics* **11** no. 5, (2017) 274–284.
- [50] W. T. Chen, A. Y. Zhu, and F. Capasso, “Flat optics with dispersion-engineered metasurfaces,” *Nature Reviews Materials* (2020) , **Nature Reviews Materials**.
- [51] S. A. Tretyakov, “A personal view on the origins and developments of the metamaterial concept,” *Journal of Optics* **19** no. 1, (2016) 013002.
- [52] D. R. Smith, W. J. Padilla, D. C. Vier, S. C. Nemat-Nasser, and S. Schultz, “Composite Medium with Simultaneously Negative Permeability and Permittivity,” *Physical Review Letters* no. 18, may4184–4187, [arXiv:1006.4109](#).
- [53] D. R. Smith, S. Schultz, P. Markoš, and C. M. Soukoulis, “Determination of effective permittivity and permeability of metamaterials from reflection and transmission coefficients,” *Physical Review B* **65** no. 19, (2002) 195104.
- [54] D. R. Smith, “Metamaterials and Negative Refractive Index,” *Science* no. 5685, aug788–792.
- [55] M. Kafesaki, I. Tsiapa, N. Katsarakis, T. Koschny, C. M. Soukoulis, and E. N. Economou, “Left-handed metamaterials: The fishnet structure and its variations,” *Physical Review B - Condensed Matter and Materials Physics* **75** no. 23, (2007) .
- [56] C. R. Simovski and S. A. Tretyakov, “Local constitutive parameters of metamaterials from an effective-medium perspective,” *Physical Review B* **75** no. 19, (2006) 195111.
- [57] C. R. Simovski, “Bloch material parameters of magneto-dielectric metamaterials and the concept of Bloch lattices,” *Metamaterials* **1** no. 2, (2007) 62–80.
- [58] A. Andryieuski, S. Ha, A. A. Sukhorukov, Y. S. Kivshar, and A. V. Lavrinenko, “Bloch-mode analysis for retrieving effective parameters of metamaterials,” *Physical Review B* **86** no. 3, (2010) 035127, [1011.2669](#).
- [59] A. Andryieuski, C. Menzel, C. Rockstuhl, R. Malureanu, F. Lederer, and A. Lavrinenko, “Homogenization of resonant chiral metamaterials,” *Physical Review B* **82** no. 23, (2010) 235107, [1008.4295](#).
- [60] A. Andryieuski, A. V. Lavrinenko, and S. V. Zhukovsky, “Anomalous effective medium approximation breakdown in deeply subwavelength all-dielectric photonic multilayers,” *Nanotechnology* (2015) , **Nanotechnology**.

- [61] I. I. Sobel'man, "On the theory of light scattering in gases," *Physics-Uspokhi* **45** no. 1, (2002) 75–80.
- [62] M. Planck, "Zur elektronischen Theorie der Dispersion in isotropen Nichtleitern," *Sitzungsber. Konig. Preuss Acad* **24** (1902) 470–494.
- [63] L. I. Mandelstam, "Zur Theorie der Dispersion," *Physikalische Zeitschrift* 641–642.
- [64] P. Genevet, F. Capasso, F. Aieta, M. Khorasaninejad, and R. Devlin, "Recent advances in planar optics: from plasmonic to dielectric metasurfaces," *Optica* no. 1, jan139.
- [65] I. Staude, T. Pertsch, and Y. S. Kivshar, "All-Dielectric Resonant Meta-Optics Lightens up," *ACS Photonics* no. 4, apr802–814.
- [66] N. I. Zheludev and Y. S. Kivshar, "From metamaterials to metadevices," *Nature Materials* **11** no. 11, (2012) 917–924.
- [67] S. S. Kruk, A. N. Poddubny, D. A. Powell, C. Helgert, M. Decker, T. Pertsch, D. N. Neshev, and Y. S. Kivshar, "Polarization properties of optical metasurfaces of different symmetries," *Physical Review B* **91** no. 19, (2015) 195401.
- [68] S. Fasold, S. Linß, T. Kawde, M. Falkner, M. Decker, T. Pertsch, and I. Staude, "Disorder-Enabled Pure Chirality in Bilayer Plasmonic Metasurfaces," *ACS Photonics* **5** no. 5, (2018) 1773–1778.
- [69] A. Rahimzadegan, D. Arslan, R. N. S. Suryadharma, S. Fasold, M. Falkner, T. Pertsch, I. Staude, and C. Rockstuhl, "Disorder-Induced Phase Transitions in the Transmission of Dielectric Metasurfaces," *Physical Review Letters* **122** no. 1, (2019) 015702.
- [70] S. a. Kuznetsov, M. a. Astafev, M. Beruete, and M. Navarro-Cía, "Planar Holographic Metasurfaces for Terahertz Focusing," *Scientific Reports* jan7738.
- [71] A. Forouzmmand and H. Mosallaei, "Composite Multilayer Shared-Aperture Nanostructures: A Functional Multispectral Control," *ACS Photonics* no. 4, apr1427–1439.
- [72] L. Jin, Z. Dong, S. Mei, Y. F. Yu, Z. Wei, Z. Pan, S. D. Rezaei, X. Li, A. I. Kuznetsov, Y. S. Kivshar, J. K. W. Yang, and C.-w. Qiu, "Noninterleaved Metasurface for (2 6 -1) Spin- and Wavelength-Encoded Holograms," *Nano Letters* no. 12, dec8016–8024.
- [73] X. Li, L. Chen, Y. Li, X. Zhang, M. Pu, Z. Zhao, X. Ma, Y. Wang, M. Hong, and X. Luo, "Multicolor 3D meta-holography by broadband plasmonic modulation," *Science Advances* no. 11, nove1601102–e1601102.

- [74] Y. Zhou, I. I. Kravchenko, H. Wang, J. R. Nolen, G. Gu, and J. Valentine, “Multilayer Noninteracting Dielectric Metasurfaces for Multiwavelength Metaoptics,” *Nano Letters* no. 12, dec7529–7537.
- [75] A. Arbabi, E. Arbabi, S. M. Kamali, Y. Horie, S. Han, and A. Faraon, “Miniature optical planar camera based on a wide-angle metasurface doublet corrected for monochromatic aberrations,” *Nature Communications* nov13682, arXiv:arXiv:1604.06160v2.
- [76] L. Rayleigh, “LVI. On the influence of obstacles arranged in rectangular order upon the properties of a medium,” *The London, Edinburgh, and Dublin Philosophical Magazine and Journal of Science* no. 211, dec481–502.
- [77] C. R. Simovski, “Material parameters of metamaterials (a Review),” *Optics and Spectroscopy* no. 5, nov726–753.
- [78] S. Arslanagic, T. V. Hansen, N. A. Mortensen, A. H. Gregersen, O. Sigmund, R. W. Ziolkowski, and O. Breinbjerg, “A Review of the Scattering-Parameter Extraction Method with Clarification of Ambiguity Issues in Relation to Metamaterial Homogenization,” *IEEE Antennas and Propagation Magazine* **55** no. 2, (2013) 91–106, 1206.4801.
- [79] K. Mnasri, A. Khrabustovskyi, M. Plum, and C. Rockstuhl, “Retrieving effective material parameters of metamaterials characterized by nonlocal constitutive relations,” *Physical Review B* **99** no. 3, (2019) 035442, 1808.00748.
- [80] C. R. Simovski, “Bloch material parameters of magneto-dielectric metamaterials and the concept of Bloch lattices,” *Metamaterials* **1** no. 2, (2007) 62–80.
- [81] N. A. Rubin, G. D’Aversa, P. Chevalier, Z. Shi, W. T. Chen, and F. Capasso, “Matrix Fourier optics enables a compact full-Stokes polarization camera,” *Science* no. 6448, juleaax1839.
- [82] A. Karalis and J. D. Joannopoulos, “Plasmonic Metasurface “Bullets” and other “Moving Objects”: Spatiotemporal Dispersion Cancellation for Linear Passive Subwavelength Slow Light,” *Physical Review Letters* no. 6, aug067403.
- [83] S. Colburn, A. Zhan, and A. Majumdar, “Metasurface optics for full-color computational imaging,” *Science Advances* no. 2, febeaar2114.
- [84] X. Zhu, W. Yan, U. Levy, N. A. Mortensen, and A. Kristensen, “Resonant laser printing of structural colors on high-index dielectric metasurfaces,” *Science Advances* no. 5, maye1602487.

- [85] M. Hentschel, M. Schäferling, X. Duan, H. Giessen, and N. Liu, “Chiral plasmonics,” *Science Advances* no. 5, maye1602735.
- [86] F. Aieta, M. A. Kats, P. Genevet, and F. Capasso, “Multiwavelength achromatic metasurfaces by dispersive phase compensation,” *Science* no. 6228, mar1342–1345, [arXiv:1411.3966](#).
- [87] D. Lin, P. Fan, E. Hasman, and M. L. Brongersma, “Dielectric gradient metasurface optical elements,” *Science* no. 6194, jul298–302.
- [88] R. A. Aoni, M. Rahmani, L. Xu, K. Z. Kamali, A. Komar, J. Yan, D. Neshev, and A. E. Miroshnichenko, “High-Efficiency Visible Light Manipulation Using Dielectric Metasurfaces,” *Scientific Reports* **9** no. 1, (2019) 6510.
- [89] G. Kenanakis, A. Xomalis, A. Selimis, M. Vamvakaki, M. Farsari, M. Kafesaki, C. M. Soukoulis, and E. N. Economou, “Three-Dimensional Infrared Metamaterial with Asymmetric Transmission,” *ACS Photonics* no. 2, feb287–294.
- [90] H. Liu and P. Lalanne, “Comprehensive microscopic model of the extraordinary optical transmission,” *Journal of the Optical Society of America A* no. 12, dec2542.
- [91] K. Andrei, R. Ahmmed, Aoni, X. Lei, R. Mohsen, A. E., Miroshnichenko, and D. N., Neshev, “Edge Detection with Mie-Resonant Dielectric Metasurfaces,” *ACS Photonics* **8** no. 3, (2021) 864–871, *ACS Photonics*.
- [92] A. N. Poddubny, I. V. Iorsh, and A. A. Sukhorukov, “Generation of Photon-Plasmon Quantum States in Nonlinear Hyperbolic Metamaterials,” *Physical Review Letters* no. 12, sep123901.
- [93] M. F. Limonov, M. V. Rybin, A. N. Poddubny, and Y. S. Kivshar, “Fano resonances in photonics,” *Nature Photonics* no. 9, 543–554.
- [94] K. Wang, J. G. Titchener, S. S. Kruk, L. Xu, H.-p. Chung, M. Parry, I. I. Kravchenko, Y.-h. Chen, A. S. Solntsev, Y. S. Kivshar, D. N. Neshev, and A. A. Sukhorukov, “Quantum metasurface for multiphoton interference and state reconstruction,” *Science* no. 6407, sep1104–1108.
- [95] K. Wang, S. V. Suchkov, J. G. Titchener, A. Szameit, and A. A. Sukhorukov, “Inline detection and reconstruction of multiphoton quantum states,” *Optica* no. 1, jan41.
- [96] F. Yesilkoy, E. R. Arvelo, Y. Jahani, M. Liu, A. Tittl, V. Cevher, Y. Kivshar, and H. Altug, “Ultrasensitive hyperspectral imaging and biodetection enabled by dielectric metasurfaces,” *Nature Photonics* no. 6, jun390–396.

- [97] Y. S. Do, J. H. Park, B. Y. Hwang, S.-M. Lee, B.-K. Ju, and K. C. Choi, “Color Filters: Plasmonic Color Filter and its Fabrication for Large-Area Applications,” *Advanced Optical Materials* no. 2, feb109–109.
- [98] S. Junger, N. Verwaal, W. Tschekalinskij, and N. Weber, “Multispectral CMOS sensors with on-chip nanostructures for wavelength monitoring of LED devices,” *Light-Emitting Diodes: Materials, Devices, and Applications for Solid State Lighting XVII* (2013) 86411B–86411B–6.
- [99] C. Williams, G. S. D. Gordon, S. Gruber, T. D. Wilkinson, and S. E. Bohndiek, “Grayscale-to-Color: Scalable Fabrication of Custom Multispectral Filter Arrays,” *ACS Photonics* **6** no. 12, (2019) 3132–3141, 1901.10949.
- [100] S. P. Burgos, S. Yokogawa, and H. A. Atwater, “Color Imaging via Nearest Neighbor Hole Coupling in Plasmonic Color Filters Integrated onto a Complementary Metal-Oxide Semiconductor Image Sensor,” *ACS Nano* **7** no. 11, (2013) 10038–10047.
- [101] J. Berzinš, S. Fasold, T. Pertsch, S. M. B. Bäumer, and F. Setzpfandt, “Submicrometer Nanostructure-Based RGB Filters for CMOS Image Sensors,” *ACS Photonics* no. 4, apr1018–1025, arXiv:1812.01652.
- [102] J. Billuart, S. Héron, B. Loiseaux, C. Amra, and M. Lequime, “Towards a metasurface adapted to hyperspectral imaging applications: from subwavelength design to definition of optical properties,” *Optics Express* **29** no. 21, (2021) 32764.
- [103] X. Chen, L. Huang, H. Mühlenbernd, G. Li, B. Bai, Q. Tan, G. Jin, C.-W. Qiu, S. Zhang, and T. Zentgraf, “Dual-polarity plasmonic metalens for visible light,” *Nature Communications* (2012) , *Nature communications*.
- [104] P. Lalanne and P. Chavel, “Metalenses at visible wavelengths: past, present, perspectives,” *Laser & Photonics Reviews* **11** no. 3, (2017) 1600295, 1610.02507.
- [105] T. Sun, J. Hu, S. Ma, F. Xu, and C. Wang, “Polarization-insensitive achromatic metalens based on computational wavefront coding,” *Optics Express* **29** no. 20, (2021) 31902.
- [106] C. W. Hsu, B. Zhen, J. Lee, S.-l. Chua, S. G. Johnson, J. D. Joannopoulos, and M. Soljačić, “Observation of trapped light within the radiation continuum,” *Nature* no. 7457, jul188–191.
- [107] F. Monticone and A. Alù, “Embedded Photonic Eigenvalues in 3D Nanostructures,” *Physical Review Letters* no. 21, may213903.

- [108] C. W. Hsu, B. Zhen, A. D. Stone, J. D. Joannopoulos, and M. Soljačić, “Bound states in the continuum,” *Nature Reviews Materials* jul16048.
- [109] A. Cerjan, C. W. Hsu, and M. C. Rechtsman, “Bound States in the Continuum through Environmental Design,” *Physical Review Letters* no. 2, jul023902.
- [110] S.-G. Lee, S.-H. Kim, and C.-S. Kee, “Metasurfaces with Bound States in the Continuum Enabled by Eliminating First Fourier Harmonic Component in Lattice Parameters,” *Physical Review Letters* **126** no. 1, (2021) 013601, 2007.00352.
- [111] R. Geiss, S. Diziain, R. Iliw, C. Etrich, H. Hartung, N. Janunts, F. Schrepel, F. Lederer, T. Pertsch, and E.-B. Kley, “Light propagation in a free-standing lithium niobate photonic crystal waveguide,” *Applied Physics Letters* **97** no. 13, (2010) 131109.
- [112] R. Geiss, S. Saravi, A. Sergeev, S. Diziain, F. Setzpfandt, F. Schrepel, R. Grange, E.-B. Kley, A. Tünnermann, and T. Pertsch, “Fabrication of nanoscale lithium niobate waveguides for second-harmonic generation,” *Optics Letters* **40** no. 12, (2015) 2715.
- [113] C. Menzel, C. Helgert, C. Rockstuhl, E.-B. Kley, A. Tünnermann, T. Pertsch, and F. Lederer, “Asymmetric Transmission of Linearly Polarized Light at Optical Metamaterials,” *Physical Review Letters* **104** no. 25, (2010) 253902, 1005.1970.
- [114] E. Plum, V. A. Fedotov, and N. I. Zheludev, “Asymmetric transmission: A generic property of two-dimensional periodic patterns,” *Journal of Optics* **13** no. 2, (2011) , arXiv:1007.2620.
- [115] S. Fang, K. Luan, H. F. Ma, W. Lv, Y. Li, Z. Zhu, C. Guan, J. Shi, and T. J. Cui, “Asymmetric transmission of linearly polarized waves in terahertz chiral metamaterials,” *Journal of Applied Physics* no. 3, jan033103.
- [116] K. Dietrich, D. Lehr, C. Helgert, A. Tünnermann, and E.-B. Kley, “Circular Dichroism from Chiral Nanomaterial Fabricated by On-Edge Lithography,” *Advanced Materials* no. 44, novOP321–OP325.
- [117] Z. Wang, B. H. Teh, Y. Wang, G. Adamo, J. Teng, and H. Sun, “Enhancing circular dichroism by super chiral hot spots from a chiral metasurface with apexes,” *Applied Physics Letters* no. 22, may221108.
- [118] E. Plum, V. A. Fedotov, and N. I. Zheludev, “Optical activity in extrinsically chiral metamaterial,” *Applied Physics Letters* **93** no. 19, (2008) 1–4, arXiv:arXiv:0807.0523v1.

- [119] M. V. Gorkunov, a. a. Ezhov, V. V. Artemov, O. Y. Rogov, and S. G. Yudin, “Extreme optical activity and circular dichroism of chiral metal hole arrays,” *Applied Physics Letters* **104** no. 22, (2014) 8–12, [arXiv:1404.7615](#).
- [120] C. Caloz and A. Sihvola, “Electromagnetic Chirality, Part 1: The Microscopic Perspective,” *IEEE Antennas and Propagation Magazine* **62** no. 1, (2020) 58–71.
- [121] M. Thiel, M. Decker, M. Deubel, M. Wegener, S. Linden, and G. von Freymann, “Polarization Stop Bands in Chiral Polymeric Three-Dimensional Photonic Crystals,” *Advanced Materials* no. 2, jan207–210.
- [122] C. Helgert, E. Pshenay-Severin, M. Falkner, C. Menzel, C. Rockstuhl, E.-B. Kley, A. Tünnermann, F. Lederer, and T. Pertsch, “Chiral Metamaterial Composed of Three-Dimensional Plasmonic Nanostructures,” *Nano Letters* no. 10, oct4400–4404.
- [123] J. Kaschke, J. K. Gansel, and M. Wegener, “On metamaterial circular polarizers based on metal N-helices,” *Optics express* no. 23, 26012–20.
- [124] M. Schäferling, D. Dregely, M. Hentschel, and H. Giessen, “Tailoring Enhanced Optical Chirality: Design Principles for Chiral Plasmonic Nanostructures,” *Physical Review X* no. 3, aug031010.
- [125] E. Plum, *Chirality and Metamaterials*. PhD thesis, 2010.
- [126] J. Kaschke and M. Wegener, “Gold triple-helix mid-infrared metamaterial by STED-inspired laser lithography,” *Optics Letters* no. 17, sep3986.
- [127] K. Konishi, B. Bai, Y. Toya, J. Turunen, Y. P. Svirko, and M. Kuwata-Gonokami, “Surface-plasmon enhanced optical activity in two-dimensional metal chiral networks,” *Optics Letters* **37** no. 21, (2012) 4446.
- [128] I. Sersic, M. Frimmer, E. Verhagen, and a. F. Koenderink, “Electric and Magnetic Dipole Coupling in Near-Infrared Split-Ring Metamaterial Arrays,” *Physical Review Letters* no. 21, nov213902, [arXiv:arXiv:0907.3026v2](#).
- [129] A. V. Novitsky, V. M. Galynsky, and S. V. Zhukovsky, “Asymmetric transmission in planar chiral split-ring metamaterials: Microscopic Lorentz-theory approach,” *Physical Review B - Condensed Matter and Materials Physics* **86** no. 7, (2012) 1–12, [arXiv:1012.5119](#).
- [130] E. Plum, V. A. Fedotov, and N. I. Zheludev, “Planar metamaterial with transmission and reflection that depend on the direction of incidence,” *Applied Physics Letters* **94** no. 13, (2009) 131901, [0812.0696](#).

- [131] L. Cong, N. Xu, W. Zhang, and R. Singh, “Polarization Control in Terahertz Metasurfaces with the Lowest Order Rotational Symmetry,” *Advanced Optical Materials* no. 9, sep1176–1183.
- [132] E. Plum and N. I. Zheludev, “Chiral mirrors,” *Applied Physics Letters* no. 22, 221901.
- [133] C. Chen, S. Gao, W. Song, H. Li, S.-N. Zhu, and T. Li, “Metasurfaces with Planar Chiral Meta-Atoms for Spin Light Manipulation,” *Nano Letters* **21** no. 4, (2021) 1815–1821.
- [134] G. Kenanakis, R. Zhao, A. Stavrinidis, G. Konstantinidis, N. Katsarakis, M. Kafesaki, C. M. Soukoulis, and E. N. Economou, “Flexible chiral metamaterials in the terahertz regime: a comparative study of various designs,” *Optical Materials Express* no. 12, 1702.
- [135] C. Pfeiffer, C. Zhang, V. Ray, L. J. Guo, and A. Grbic, “High performance bianisotropic metasurfaces: Asymmetric transmission of light,” *Physical Review Letters* **113** no. 2, (2014) 1–5.
- [136] J. H. Shi, H. F. Ma, C. Y. Guan, Z. P. Wang, and T. J. Cui, “Broadband chirality and asymmetric transmission in ultrathin 90°-twisted Babinet-inverted metasurfaces,” *Physical Review B* no. 16, apr165128.
- [137] J.-G. Yun, S.-J. Kim, H. Yun, K. Lee, J. Sung, J. Kim, Y. Lee, and B. Lee, “Broadband ultrathin circular polarizer at visible and near-infrared wavelengths using a non-resonant characteristic in helically stacked nano-gratings,” *Optics Express* no. 13, jun14260.
- [138] M. Decker, M. Ruther, C. E. Kriegler, J. Zhou, C. M. Soukoulis, S. Linden, and M. Wegener, “Strong optical activity from twisted-cross photonic metamaterials.,” *Optics letters* **34** no. 16, (2009) 2501–2503.
- [139] K. Hannam, D. a. Powell, I. V. Shadrivov, and Y. S. Kivshar, “Broadband chiral metamaterials with large optical activity,” *Physical Review B - Condensed Matter and Materials Physics* **89** no. 12, (2014) 1–6, [arXiv:arXiv:1401.8032v1](https://arxiv.org/abs/1401.8032v1).
- [140] Z. Wu and Y. Zheng, “Moiré Chiral Metamaterials,” *Advanced Optical Materials* apr1700034.
- [141] G. Kenanakis, E. N. Economou, C. M. Soukoulis, and M. Kafesaki, “Controlling THz and far-IR waves with chiral and bianisotropic metamaterials,” *EPJ Applied Metamaterials* feb15.
- [142] Y. Zhao, M. Belkin, and A. Alù, “Twisted optical metamaterials for planarized ultrathin broadband circular polarizers,” *Nature Communications* **3** no. May, (2012) 870.

- [143] Y. Zhao, J. Shi, L. Sun, X. Li, and A. Alù, “Alignment-free three-dimensional optical metamaterials,” *Advanced Materials* **26** no. 9, (2014) 1439–1445.
- [144] C. Pfeiffer and A. Grbic, “Cascaded metasurfaces for complete phase and polarization control,” *Applied Physics Letters* **102** no. 23, (2013) 231116.
- [145] C. Menzel, J. Sperrhake, and T. Pertsch, “Efficient treatment of stacked metasurfaces for optimizing and enhancing the range of accessible optical functionalities,” *Physical Review A* **93** no. 6, (2016) 063832, [arXiv:1511.09239](#).
- [146] S. Jan, D. Manuel, F. Matthias, F. Stefan, K. Thomas, S. Isabelle, and P. Thomas, “Analyzing the polarization response of a chiral metasurface stack by semi-analytic modeling,” *Optics Express* (2019) .
- [147] S. Chen, Y. Zhang, Z. Li, H. Cheng, and J. Tian, “Empowered Layer Effects and Prominent Properties in Few-Layer Metasurfaces,” *Advanced Optical Materials* no. 14, [jul1801477](#).
- [148] J. Sperrhake, M. Falkner, S. Fasold, T. Kaiser, and T. Pertsch, “Equivalence of reflection paths of light and Feynman paths in stacked metasurfaces,” *Physical Review B* **102** no. 24, (2020) 245108, [1909.11541](#).
- [149] A. Berkhout and A. F. Koenderink, “Perfect Absorption and Phase Singularities in Plasmon Antenna Array Etalons,” *ACS Photonics* **6** no. 11, (2019) 2917–2925.
- [150] A. Berkhout and A. F. Koenderink, “A simple transfer-matrix model for metasurface multilayer systems,” *Nanophotonics* no. 12, [jul3985–4007](#).
- [151] J. Sperrhake, M. Falkner, M. Steinert, S. Fasold, and T. Pertsch, “Experimental validation of the fundamental mode approximation for stacked metasurfaces and its application to the treatment of arbitrary period ratios,” *APL Photonics* **6** no. 9, (2021) 096109.
- [152] P. Yeh, *Optical Waves in Layered Media*. John Wiley & Sons, Inc., New Jersey, 2005.
- [153] L. Pjotr Stoevelaar, J. Berzinš, F. Silvestri, S. Fasold, K. Zangeneh Kamali, H. Knopf, F. Eilenberger, F. Setzpfandt, T. Pertsch, S. M. B. Bäumer, and G. Gerini, “Nanostructure-modulated planar high spectral resolution spectro-polarimeter,” *Optics Express* no. 14, [jul19818](#), [arXiv:2003.04403](#).
- [154] R. Alaei, B. Gurlek, M. Albooyeh, D. Martín-Cano, and V. Sandoghdar, “Quantum Metamaterials with Magnetic Response at Optical Frequencies,” *Physical Review Letters* **125** no. 6, (2020) 063601, [2002.03385](#).

- [155] L. Novotny and B. Hecht, *Principles of Nano-Optics*. Cambridge University Press, Cambridge.
- [156] T. Paul, C. Menzel, W. Śmigaj, C. Rockstuhl, P. Lalanne, and F. Lederer, “Reflection and transmission of light at periodic layered metamaterial films,” *Physical Review B* **84** no. 11, (2011) 115142.
- [157] C. R. Simovski, S. A. Tretyakov, and ., “Local constitutive parameters of metamaterials from an effective-medium perspective,” *Physical Review B* **75** no. 19, (2007) 195111.
- [158] C. R. Simovski, “Bloch material parameters of magneto-dielectric metamaterials and the concept of Bloch lattices,” *Metamaterials* **1** no. 2, (2007) 62–80.
- [159] W. Śmigaj and B. Gralak, “Validity of the effective-medium approximation of photonic crystals,” *Physical Review B* **77** no. 23, (2008) 235445.
- [160] Z. Lu and D. W. Prather, “Calculation of effective permittivity, permeability, and surface impedance of negative-refraction photonic crystals,” *Optics Express* **15** no. 13, (2007) 8340.
- [161] T. Kaiser, S. B. Hasan, T. Paul, T. Pertsch, and C. Rockstuhl, “Impedance generalization for plasmonic waveguides beyond the lumped circuit model,” *Physical Review B* **88** no. 3, (2013) 035117, 1305.3125.
- [162] C. Wolff, K. Busch, and N. A. Mortensen, “Modal expansions in periodic photonic systems with material loss and dispersion,” *Physical Review B* **97** no. 10, (2018) 104203, 1801.01791.
- [163] M. M. R. Elsayy, S. Lanteri, R. Duvigneau, G. Brière, M. S. Mohamed, and P. Genevet, “Global optimization of metasurface designs using statistical learning methods,” *Scientific Reports* no. 1, dec17918.
- [164] M. M. Elsayy, S. Lanteri, R. Duvigneau, J. A. Fan, and P. Genevet, “Numerical Optimization Methods for Metasurfaces,” *Laser and Photonics Reviews* **14** no. 10, (2020) 1–17.
- [165] P. I. Schneider, X. Garcia Santiago, V. Soltwisch, M. Hammerschmidt, S. Burger, and C. Rockstuhl, “Benchmarking Five Global Optimization Approaches for Nano-optical Shape Optimization and Parameter Reconstruction,” *ACS Photonics* **6** no. 11, (2019) 2726–2733, arXiv:1809.06674.
- [166] H. T. Chen, A. J. Taylor, and N. Yu, “A review of metasurfaces: Physics and applications,” *Reports on Progress in Physics* **79** no. 7, (2016) , arXiv:1605.07672.

- [167] D. G. Baranov, D. A. Zuev, S. I. Lepeshov, O. V. Kotov, A. E. Krasnok, A. B. Evlyukhin, and B. N. Chichkov, “All-dielectric nanophotonics: the quest for better materials and fabrication techniques,” *Optica* no. 7, jul814, [arXiv:1702.00677](#).
- [168] F. F. Qin, Z. Z. Liu, Q. Zhang, H. Zhang, and J. J. Xiao, “Mantle Cloaks Based on the Frequency Selective Metasurfaces Designed by Bayesian Optimization,” *Scientific Reports* **8** no. 1, (2018) 14033.
- [169] W. T. Chen, A. Y. Zhu, and F. Capasso, “Flat optics with dispersion-engineered metasurfaces,” *Nature Reviews Materials* no. 8, 604–620.
- [170] A. Tamang, R. Parsons, U. Palanchoke, H. Stiebig, V. Wagner, A. Salleo, and D. Knipp, “Color Sensing by Optical Antennas: Approaching the Quantum Efficiency Limit,” *ACS Photonics* julacsphotonics.9b00490.
- [171] A. Basiri, X. Chen, J. Bai, P. Amrollahi, J. Carpenter, Z. Holman, C. Wang, and Y. Yao, “Nature-inspired chiral metasurfaces for circular polarization detection and full-Stokes polarimetric measurements,” *Light: Science and Applications* no. 1, .
- [172] W. Mai, D. Zhu, Z. Gong, X. Lin, Y. Chen, J. Hu, and D. H. Werner, “Broadband transparent chiral mirrors: Design methodology and bandwidth analysis,” *AIP Advances* no. 4, .
- [173] C. Wang, S. Yu, W. Chen, and C. Sun, “Highly Efficient Light-Trapping Structure Design Inspired By Natural Evolution,” *Scientific Reports* no. 1, dec1025.
- [174] S. Jafar-Zanjani, S. Inampudi, and H. Mosallaei, “Adaptive Genetic Algorithm for Optical Metasurfaces Design,” *Scientific Reports* **8** no. 1, (2018) 1–16.
- [175] W. Ma, F. Cheng, and Y. Liu, “Deep-Learning-Enabled On-Demand Design of Chiral Metamaterials,” *ACS Nano* **12** no. 6, (2018) 6326–6334.
- [176] P. R. Wiecha and O. L. Muskens, “Deep Learning Meets Nanophotonics: A Generalized Accurate Predictor for near Fields and Far Fields of Arbitrary 3D Nanostructures,” *Nano Letters* **20** no. 1, (2020) 329–338, [arXiv:1909.12056](#).
- [177] X. Xu, M. Tan, B. Corcoran, J. Wu, A. Boes, T. G. Nguyen, S. T. Chu, B. E. Little, D. G. Hicks, R. Morandotti, A. Mitchell, and D. J. Moss, “11 TOPS photonic convolutional accelerator for optical neural networks,” *Nature* **589** no. 7840, (2021) 44–51, [2011.07393](#).

- [178] T. Beucler, M. Pritchard, S. Rasp, J. Ott, P. Baldi, and P. Gentine, “Enforcing Analytic Constraints in Neural Networks Emulating Physical Systems,” *Physical Review Letters* **126** no. 9, (2021) 098302, 1909.00912.
- [179] G. Hu, M. Wang, Y. Mazor, C. W. Qiu, and A. Alù, “Tailoring Light with Layered and Moiré Metasurfaces,” *Trends in Chemistry* no. 5, 342–358.
- [180] G. Marino, D. Rocco, C. Gigli, G. Beaudoin, K. Pantzas, S. Suffit, P. Filloux, I. Sagnes, G. Leo, and C. De Angelis, “Harmonic generation with multi-layer dielectric metasurfaces,” *Nanophotonics* apr1–7.
- [181] S. Zhao, L. Shao, J. Wang, H.-Q. Lin, and W. Zhang, “Chirality-selective transparency induced by lattice resonance in bilayer metasurfaces,” *Photonics Research* **9** no. 4, (2021) 484.
- [182] L. Li, “Formulation and comparison of two recursive matrix algorithms for modeling layered diffraction gratings,” *Journal of the Optical Society of America A* **13** no. 5, (1996) 1024.
- [183] Changhua Wan and J. Encinar, “Efficient computation of generalized scattering matrix for analyzing multilayered periodic structures,” *IEEE Transactions on Antennas and Propagation* no. 11, 1233–1242.
- [184] S. Stallinga, “Berreman 4 x 4 matrix method for reflective liquid crystal displays,” *Journal of Applied Physics* no. 6, 3023–3031.
- [185] D. Whittaker and I. Culshaw, “Scattering-matrix treatment of patterned multilayer photonic structures,” *Physical Review B* **60** no. 4, (1999) 2610–2618.
- [186] I. M. Fradkin, S. A. Dyakov, and N. A. Gippius, “Fourier modal method for the description of nanoparticle lattices in the dipole approximation,” *Physical Review B* no. 7, feb075310, arXiv:2524299 [arXiv:submit].
- [187] R. C. Jones, “A New Calculus for the Treatment of Optical SystemsI Description and Discussion of the Calculus,” *Journal of the Optical Society of America* (1941) , **Journal of the Optical Society of America**.
- [188] C. Menzel, C. Rockstuhl, and F. Lederer, “Advanced Jones calculus for the classification of periodic metamaterials,” *Physical Review A - Atomic, Molecular, and Optical Physics* **82** no. 5, (2010) 1–9, arXiv:1008.4117.

- [189] X. Romain, F. Baida, and P. Boyer, “Extended Malus law with terahertz metallic metamaterials for sensitive detection with giant tunable quality factor,” *Physical Review B* **94** no. 4, (2016) 045407, 1601.07022.
- [190] X. Romain, F. I. Baida, and P. Boyer, “Spectrally tunable linear polarization rotation using stacked metallic metamaterials,” *Journal of Optics* **19** no. 8, (2017) 085102, 1702.08769.
- [191] C. Kilchoer, N. Abdollahi, U. Steiner, I. Gunkel, and B. D. Wilts, “Determining the complex Jones matrix elements of a chiral 3D optical metamaterial,” *APL Photonics* **4** no. 12, (2019) 126107.
- [192] X. Romain, *Study of polarization of light through a stack of metallic metamaterials*. PhD thesis, 2019.
- [193] J. C. Maxwell, “VIII. A dynamical theory of the electromagnetic field,” *Philosophical Transactions of the Royal Society of London* **155** no. 155, (1865) 459–512.
- [194] J. C. Maxwell, *A Treatise on Electricity and Magnetism*. Clarendon Press, Oxford, 1873.
- [195] L. Landau and E. Lifshitz, *Electrodynamics of Continuous Media*. Pergamon, 1984.
- [196] R. A. DeCrescent, R. M. Kennard, M. L. Chabinye, and J. A. Schuller, “Optical-Frequency Magnetic Polarizability in a Layered Semiconductor,” *Physical Review Letters* **127** no. 17, (2021) 173604.
- [197] P. Drude, “Zur Elektronentheorie der Metalle,” *Annalen der Physik* **306** no. 3, (1900) 566–613.
- [198] W. Nolting, *Theoretical Physics 3, Electrodynamics*. Springer International Publishing, Switzerland, 2016.
- [199] E. Collet, *Polarized Light: Fundamentals and Applications*. Marcel Dekker, Inc., New York, 1993.
- [200] C. Menzel, C. Rockstuhl, and F. Lederer, “Advanced Jones calculus for the classification of periodic metamaterials,” *Physical Review A* **82** no. 5, (2010) 053811, 1008.4117.
- [201] R. J. Potton, “Reciprocity in optics,” *Reports on Progress in Physics* **67** no. 5, (2004) 717–754.
- [202] P. Ben-Abdallah and B. Ni, “Single-defect Bragg stacks for high-power narrow-band thermal emission,” *Journal of Applied Physics* **97** no. 10, (2005) 104910.

- [203] H. H. Sheinfux, I. Kaminer, Y. Plotnik, G. Bartal, and M. Segev, “Subwavelength Multilayer Dielectrics: Ultrasensitive Transmission and Breakdown of Effective-Medium Theory,” *Physical Review Letters* **113** no. 24, (2014) 243901.
- [204] I. Staude, A. E. Miroshnichenko, M. Decker, N. T. Fofang, S. Liu, E. Gonzales, J. Dominguez, T. S. Luk, D. N. Neshev, I. Brener, and Y. Kivshar, “Tailoring Directional Scattering through Magnetic and Electric Resonances in Subwavelength Silicon Nanodisks,” *ACS Nano* **7** no. 9, (2013) 7824–7832.
- [205] J. S. Clausen, E. Højlund-Nielsen, A. B. Christiansen, S. Yazdi, M. Grajower, H. Taha, U. Levy, A. Kristensen, and N. A. Mortensen, “Plasmonic Metasurfaces for Coloration of Plastic Consumer Products,” *Nano Letters* **14** no. 8, (2014) 4499–4504.
- [206] M. Keil, A. E. Wetzal, K. Wu, E. Khomtchenko, J. Urbankova, A. Boisen, T. Rindzevicius, A.-I. Bunea, and R. J. Taboryski, “Large plasmonic color metasurfaces fabricated by super resolution deep UV lithography,” *Nanoscale Advances* **3** no. 8, (2021) 2236–2244.
- [207] L. Li, “Bremmer series, R-matrix propagation algorithm, and numerical modeling of diffraction gratings,” *Journal of the Optical Society of America A* **11** no. 11, (1994) 2829.
- [208] L. Li, “Use of Fourier series in the analysis of discontinuous periodic structures,” *Journal of the Optical Society of America A* **13** no. 9, (1996) 1870.
- [209] L. Li, “New formulation of the Fourier modal method for crossed surface-relief gratings,” *JOSA A* (1997), *Journal of the Optical Society of America A*.
- [210] L. Li, “Note on the S-matrix propagation algorithm,” *Journal of the Optical Society of America A* no. 4, 655.
- [211] P. Lalanne and G. M. Morris, “Highly improved convergence of the coupled-wave method for TM polarization,” *Journal of the Optical Society of America A* **13** no. 4, (1996) 779.
- [212] E. Popov and M. Nevière, “Differential theory for diffraction gratings: a new formulation for TM polarization with rapid convergence,” *Optics Letters* **25** no. 9, (2000) 598.
- [213] E. Popov and M. Nevière, “Grating theory: new equations in Fourier space leading to fast converging results for TM polarization,” *Journal of the Optical Society of America A* **17** no. 10, (2000) 1773.

- [214] T. Weiss, G. Granet, N. A. Gippius, S. G. Tikhodeev, and H. Giessen, “Matched coordinates and adaptive spatial resolution in the Fourier modal method,” *Optics Express* **17** no. 10, (2009) 8051.
- [215] T. Weiss, N. A. Gippius, S. G. Tikhodeev, G. Granet, and H. Giessen, “Derivation of plasmonic resonances in the Fourier modal method with adaptive spatial resolution and matched coordinates,” *Journal of the Optical Society of America A* **28** no. 2, (2011) 238.
- [216] T. Paul, C. Rockstuhl, and F. Lederer, “A numerical approach for analyzing higher harmonic generation in multilayer nanostructures,” *Journal of the Optical Society of America B* **27** no. 5, (2010) 1118.
- [217] T. Paul, C. Rockstuhl, and F. Lederer, “Integrating cold plasma equations into the Fourier modal method to analyze second harmonic generation at metallic nanostructures,” *Journal of Modern Optics* **58** no. 5-6, (2011) 438–448.
- [218] E. Noponen and J. Turunen, “Eigenmode method for electromagnetic synthesis of diffractive elements with three-dimensional profiles,” *Journal of the Optical Society of America A* **11** no. 9, (1994) 2494.
- [219] H. Kim, J. Park, and B. Lee, *Fourier Modal Method and Its Applications in Computational Nanophotonics*. CRC Press, Boca Raton, 2012.
- [220] J. W. Strutt, “On the dynamical theory of gratings,” *Proceedings of the Royal Society of London. Series A, Containing Papers of a Mathematical and Physical Character* (1907) .
- [221] F. Bloch, “Über die Quantenmechanik der Elektronen in Kristallgittern,” *Zeitschrift für Physik* **52** no. 7-8, (1929) 555–600, *Zeitschrift für Physik*.
- [222] T. Paul, C. Menzel, W. Śmigaj, C. Rockstuhl, P. Lalanne, and F. Lederer, “Reflection and transmission of light at periodic layered metamaterial films,” *Physical Review B* **84** no. 11, (2011) 115142.
- [223] R. M. Redheffer, “On a Certain Linear Fractional Transformation,” *Journal of Mathematics and Physics* **39** no. 1-4, (1960) 269–286.
- [224] J. C. M. Garnett, “XII. Colours in metal glasses and in metallic films,” *Philosophical Transactions of the Royal Society of London. Series A, Containing Papers of a Mathematical or Physical Character* no. 359-371, jan385–420.
- [225] Z. Chen, R. Maik, B. Andreas, and N. Gunther, “A novel 3D multispectral vision system based on filter wheel cameras,” 2016.

- [226] D. Werdehausen, X. G. Santiago, S. Burger, I. Staude, T. Pertsch, C. Rockstuhl, and M. Decker, “Modeling Optical Materials at the Single Scatterer Level: The Transition from Homogeneous to Heterogeneous Materials,” *Advanced Theory and Simulations* **3** no. 11, (2020) 2000192.
- [227] A. Alù, “Restoring the physical meaning of metamaterial constitutive parameters,” *Physical Review B* no. 8, feb081102, arXiv:1012.1353.
- [228] E. Noponen and J. Turunen, “Eigenmode method for electromagnetic synthesis of diffractive elements with three-dimensional profiles,” *Journal of the Optical Society of America A* **11** no. 9, (1994) 2494.
- [229] J. Yang, C. Sauvan, T. Paul, C. Rockstuhl, F. Lederer, and P. Lalanne, “Retrieving the effective parameters of metamaterials from the single interface scattering problem,” *Applied Physics Letters* **97** no. 6, (2010) 061102.
- [230] C. Rockstuhl, C. Menzel, T. Paul, T. Pertsch, and F. Lederer, “Light propagation in a fishnet metamaterial,” *Physical Review B* **78** no. 15, (2008) 155102.
- [231] X. Zhang, M. Davanço, Y. Urzhumov, G. Shvets, and S. R. Forrest, “From Scattering Parameters to Snell’s Law: A Subwavelength Near-Infrared Negative-Index Metamaterial,” *Physical Review Letters* **101** no. 26, (2008) 267401.
- [232] P. Y. Chen, R. C. McPhedran, C. M. d. Sterke, C. G. Poulton, A. A. Asatryan, L. C. Botten, and M. J. Steel, “Group velocity in lossy periodic structured media,” *Physical Review A* **82** no. 5, (2010) 053825.
- [233] G. Lecamp, J. P. Hugonin, and P. Lalanne, “Theoretical and computational concepts for periodic optical waveguides,” *Optics Express* **15** no. 18, (2007) 11042.
- [234] R. Wood, “XLII. On a remarkable case of uneven distribution of light in a diffraction grating spectrum,” *Philosophical Magazine Series 6* **4** no. 21, (1902) 396–402.
- [235] A. Hessel and A. A. Oliner, “A New Theory of Wood’s Anomalies on Optical Gratings,” *Applied Optics* **4** no. 10, (1965) 1275.
- [236] L. Li, “Formulation and comparison of two recursive matrix algorithms for modeling layered diffraction gratings,” *Journal of the Optical Society of America A* no. 5, may1024 – 1035.
- [237] A. F. Oskooi, D. Roundy, M. Ibanescu, P. Bermel, J. Joannopoulos, and S. G. Johnson, “Meep: A flexible free-software package for electromagnetic simulations by the FDTD method,” *Computer Physics Communications* **181** no. 3, (2010) 687–702.

- [238] J. Sperrhake, M. Decker, M. Falkner, S. Fasold, T. Kaiser, I. Staude, and T. Pertsch, “Analyzing the polarization response of a chiral metasurface stack by semi-analytic modeling,” *Optics Express* no. 2, jan1236.
- [239] C. Menzel, C. Helgert, C. Rockstuhl, E. B. Kley, A. Tünnermann, T. Pertsch, and F. Lederer, “Asymmetric transmission of linearly polarized light at optical metamaterials,” *Physical Review Letters* **104** no. 25, (2010) 1–4, arXiv:1005.1970.
- [240] N. A. Gippius, S. G. Tikhodeev, and T. Ishihara, “Optical properties of photonic crystal slabs with an asymmetrical unit cell,” *Physical Review B* no. 4, jul045138.
- [241] Y. Zhao, N. Engheta, and A. Alù, “Homogenization of plasmonic metasurfaces modeled as transmission-line loads,” *Metamaterials* no. 2-3, jun90–96.
- [242] A. Andrei, M. Christoph, R. Carsten, M. Radu, L. Falk, and L. Andrei, “Homogenization of resonant chiral metamaterials,” *Physical Review B* (2010) , *Physical Review B*.
- [243] C. Pfeiffer and A. Grbic, “Emulating Nonreciprocity with Spatially Dispersive Metasurfaces Excited at Oblique Incidence,” *Physical Review Letters* **117** no. 7, (2016) 077401.
- [244] C. Pfeiffer, C. Zhang, V. Ray, L. J. Guo, and A. Grbic, “High Performance Bianisotropic Metasurfaces: Asymmetric Transmission of Light,” *Physical Review Letters* **113** no. 2, (2014) 023902, *Physical Review Letters*.
- [245] R. Alaee, M. Albooyeh, A. Rahimzadegan, M. S. Mirmoosa, Y. S. Kivshar, and C. Rockstuhl, “All-dielectric reciprocal bianisotropic nanoparticles,” *Physical Review B* **92** no. 24, (2015) 245130.
- [246] A. B. Evlyukhin, V. R. Tuz, V. S. Volkov, and B. N. Chichkov, “Bianisotropy for light trapping in all-dielectric metasurfaces,” *Physical Review B* **101** no. 20, (2020) 205415.
- [247] E. Pshenay-Severin, M. Falkner, C. Helgert, and T. Pertsch, “Ultra broadband phase measurements on nanostructured metasurfaces,” *Applied Physics Letters* no. 22, jun221906.
- [248] L. Li, “New formulation of the Fourier modal method for crossed surface-relief gratings,” *Journal of the Optical Society of America A* no. 10, oct2758.
- [249] D. Lehr, R. Alaee, R. Filter, K. Dietrich, T. Siefke, C. Rockstuhl, F. Lederer, E. B. Kley, and A. Tünnermann, “Plasmonic nanoring fabrication tuned to pitch: Efficient,

- deterministic, and large scale realization of ultra-small gaps for next generation plasmonic devices,” *Applied Physics Letters* **105** no. 14, (2014) .
- [250] A. Andryieuski, S. Ha, A. a. Sukhorukov, Y. S. Kivshar, and A. V. Lavrinenko, “Bloch-mode analysis for retrieving effective parameters of metamaterials,” *Physical Review B* no. 3, jul035127, [arXiv:1011.2669](#).
- [251] S. S. Kruk, A. N. Poddubny, D. a. Powell, C. Helgert, M. Decker, T. Pertsch, D. N. Neshev, and Y. S. Kivshar, “Polarization properties of optical metasurfaces of different symmetries,” *Physical Review B* no. 19, 1–9.
- [252] I. H. Malitson, “Interspecimen Comparison of the Refractive Index of Fused Silica*,†,” *Journal of the Optical Society of America* no. 10, oct1205.
- [253] S. Datta, *Electronic transport in mesoscopic systems*. Cambridge University Press, 1 ed., 1995.
- [254] S. J. Robinson and M. Jeffery, “Conductance fluctuations in mesoscopic three-dimensional multiply connected normal-wire networks,” *Physical Review B* no. 23, jun16807–16816.
- [255] M. Büttiker, “Four-Terminal Phase-Coherent Conductance,” *Physical Review Letters* no. 14, oct1761–1764.
- [256] Y. V. Nazarov, “Block-determinant formalism for an action of a multi-terminal scatterer,” *Physica E: Low-dimensional Systems and Nanostructures* nov561–569.
- [257] G. Shavit and Y. Oreg, “Fractional Conductance in Strongly Interacting 1D Systems,” *Physical Review Letters* no. 3, jul036803.
- [258] C. Texier and G. Montambaux, “Reprint of: Four-terminal resistances in mesoscopic networks of metallic wires: Weak localisation and correlations,” *Physica E: Low-dimensional Systems and Nanostructures* aug272–285.
- [259] N. A. Mortensen, K. Flensberg, and A.-P. Jauho, “Angle dependence of Andreev scattering at semiconductor–superconductor interfaces,” *Physical Review B* **59** no. 15, (1998) 10176–10182, [cond-mat/9807049](#).
- [260] M. Buttiker, “Symmetry of electrical conduction,” *IBM Journal of Research and Development* no. 3, may317–334.

- [261] M. Büttiker, Y. Imry, R. Landauer, and S. Pinhas, “Generalized many-channel conductance formula with application to small rings,” *Physical Review B* no. 10, may6207–6215.
- [262] R. P. Feynman, “Space-Time Approach to Quantum Electrodynamics,” *Physical Review* **76** no. 6, (1949) 769–789.
- [263] R. Feynman, *QED: The Strange Theory of Light and Matter*. 1985.
- [264] H. Bremmer, “The W.K.B. approximation as the first term of a geometric-optical series,” *Communications on Pure and Applied Mathematics* no. 1, jun105–115.
- [265] L. Li, “Bremmer series, R-matrix propagation algorithm, and numerical modeling of diffraction gratings,” *Journal of the Optical Society of America A* no. 11, nov2829.
- [266] J. Sperrhake, M. Falkner, S. Fasold, T. Kaiser, and T. Pertsch, “Equivalence of reflection paths of light and Feynman paths in stacked metasurfaces,” *Physical Review B* no. 24, dec245108.
- [267] Y. Zhao, M. Belkin, and A. Alù, “Twisted optical metamaterials for planarized ultrathin broadband circular polarizers,” *Nature Communications* **3** no. 1, (2012) 870.
- [268] T. L. Turan and J. Sperrhake, “sasa_phys,” 2019.
- [269] S. Zhao, L. Shao, J. Wang, H.-Q. Lin, and W. Zhang, “Chirality-selective transparency induced by lattice resonance in bilayer metasurfaces,” *Photonics Research* **9** no. 4, (2021) 484.
- [270] C. Zhang, X. Zhang, P. Xie, H. Hou, K. Liu, J. Lou, H. Bai, J. Zhang, Z. Li, W. Zhu, and G. Wang, “Filter-Assisted Metasurface for Full-Space Wavefront Manipulation and Energy Allocation,” *ACS Applied Electronic Materials* (2021) .
- [271] B. Lou, N. Zhao, M. Minkov, C. Guo, M. Orenstein, and S. Fan, “Theory for Twisted Bilayer Photonic Crystal Slabs,” *Physical Review Letters* **126** no. 13, (2021) 136101.
- [272] P. Manley, M. Segantini, D. Ahiboz, M. Hammerschmidt, G. Arnaoutakis, R. W. MacQueen, S. Burger, and C. Becker, “Double-layer metasurface for enhanced photon up-conversion,” *APL Photonics* (2021) , 2012.03587.
- [273] G. Marino, D. Rocco, C. Gigli, G. Beaudoin, K. Pantzas, S. Suffit, P. Filloux, I. Sagnes, G. Leo, and C. D. Angelis, “Harmonic generation with multi-layer dielectric metasurfaces,” *Nanophotonics* **10** no. 7, (2021) 1837–1843.

- [274] K. Tanaka, D. Arslan, S. Fasold, M. Steinert, J. Sautter, M. Falkner, T. Pertsch, M. Decker, and I. Staude, “Chiral Bilayer All-Dielectric Metasurfaces,” *ACS Nano* **14** no. 11, (2020) 15926–15935.
- [275] G. Hu, M. Wang, Y. Mazor, C.-W. Qiu, and A. Alù, “Tailoring Light with Layered and Moiré Metasurfaces,” *Trends in Chemistry* (2021) , **Trends in Chemistry**.
- [276] D. Liu, Y. Tan, E. Khoram, and Z. Yu, “Training Deep Neural Networks for the Inverse Design of Nanophotonic Structures,” *ACS Photonics* **5** no. 4, (2018) 1365–1369, 1710.04724.
- [277] W. Ma, F. Cheng, and Y. Liu, “Deep-Learning-Enabled On-Demand Design of Chiral Metamaterials,” *ACS Nano* **12** no. 6, (2018) 6326–6334.
- [278] J. A. Fan, “Generating high performance, topologically-complex metasurfaces with neural networks,” *2019 Conference on Lasers and Electro-Optics (CLEO)* (2019) 1–2.
- [279] P. R. Wiecha and O. L. Muskens, “Deep Learning Meets Nanophotonics: A Generalized Accurate Predictor for Near Fields and Far Fields of Arbitrary 3D Nanostructures,” *Nano Letters* **20** no. 1, (2020) 329–338, 1909.12056.
- [280] C. Wang, S. Yu, W. Chen, and C. Sun, “Highly Efficient Light-Trapping Structure Design Inspired By Natural Evolution,” *Scientific Reports* **3** no. 1, (2013) 1025.
- [281] M. Najiminaini, F. Vasefi, B. Kaminska, and J. J. L. Carson, “Adaptive Genetic Algorithm for Optical Metasurfaces Design,” *Scientific Reports* (2018) , **Scientific Reports**.
- [282] D. J. McDuff, J. R. Estep, A. M. Piasecki, and E. B. Blackford, “A Survey of Remote Optical Photoplethysmographic Imaging Methods,” *2015 37th Annual International Conference of the IEEE Engineering in Medicine and Biology Society (EMBC)* (2015) .
- [283] J.-C. Cobos-Torres, M. Abderrahim, and J. Martínez-Orgado, “Non-Contact, Simple Neonatal Monitoring by Photoplethysmography,” *Sensors* (2018) , **Sensors**.
- [284] Khanam, Al-Naji, and Chahl, “Remote Monitoring of Vital Signs in Diverse Non-Clinical and Clinical Scenarios Using Computer Vision Systems: A Review,” *Applied Sciences* (2019) , **Applied Sciences**.
- [285] L. Kong, Y. Zhao, L. Dong, Y. Jian, X. Jin, B. Li, Y. Feng, M. Liu, X. Liu, and H. Wu, “Non-contact detection of oxygen saturation based on visible light imaging device using ambient light,” *Optics Express* **21** no. 15, (2013) 17464.

- [286] S. Heist, J. Sperrhake, and A. Thoss, “Fast 3D imaging for industrial and healthcare applications,” *Laser Focus World* (2019) .
- [287] J. Sperrhake, T. Pertsch, M. Nisser, M. Rapczynski, A. Al-Hamadi, C. Zhang, and G. Notni, “Method and device for the non-contact determination of color and intensity variations over time in objects,” 2021. International application WO2021110531A1.
- [288] R. L. Olmon, B. Slovick, T. W. Johnson, D. Shelton, S.-H. Oh, G. D. Boreman, and M. B. Raschke, “Optical dielectric function of gold,” *Physical Review B* **86** no. 23, (2012) 235147.
- [289] W. Sellmeier, “Ueber die durch die Aetherschwingungen erregten Mitschwingungen der Körpertheilchen und deren Rückwirkung auf die ersteren, besonders zur Erklärung der Dispersion und ihrer Anomalien,” *Annalen der Physik* **223** no. 11, (1872) 386–403.
- [290] I. H. Malitson, “Interspecimen Comparison of the Refractive Index of Fused Silica,” *Journal of the Optical Society of America* **55** no. 10, (1965) 1205.
- [291] T. Weiss, N. A. Gippius, S. G. Tikhodeev, G. Granet, and H. Giessen, “Efficient calculation of the optical properties of stacked metamaterials with a Fourier modal method,” *Journal of Optics A: Pure and Applied Optics* no. 11, nov114019.

C | Acknowledgments

Every journey has its heros. If there is one thing I have learned during my personal journey through the course of my PhD, it is that science is a highly social process. Some people provide opportunities and the right environment for personal as well as scientific development. Others are team members that support with their unique set of skills. It is my pleasure to have worked with so many talented people, without which I would not have gotten far. Each and everyone has my heartfelt gratitude. There are some that I am especially thankful to and would like to briefly acknowledge their contributions.

I am deeply thankful to Prof. Thomas Pertsch who took me into his group when I was a stray student freshly out of a master in theoretical physics with no knowledge of nano-optics, at all. During the job interview he delicately identified my weaknesses and remarked that "optics is a highly competitive field". This, of course, held true. Thomas' honesty and guidance helped shape my career over the years. He also gave me many degrees of freedom that allowed me to pursue my interests in medical photonics and forge interdisciplinary collaborations. I believe this is an opportunity that not many PhD students have and I am grateful for the trust invested in me.

I would like to thank Dr. Christoph Menzel, who was my supervisor for the first couple of years. He helped me to get into computational nano-photonics and metamaterials. After Christoph left I had to define my own path. I am, therefore, very grateful to my friend and colleague Dr. Thomas Kaiser, who was always eager to discuss science. Any thoughts and questions I had I could run by him and get honest and detailed answers. Besides, there were not many others in the group, apart from Thomas Pertsch maybe, who really got why stacked metasurfaces and all that Feynman stuff were fun.

Most of my work was theoretical or computational. While I designed the samples and defined experimental goals, I could not realize any of the surprisingly good results without the help of my more experimentally inclined colleagues. Fabrication of all samples presented in this thesis was managed by Stefan Fasold and supported by the technical staff of the IAP as well as the micro structure technology group of Prof. Uwe Zeitner. Optical characterization was performed by Matthias Falkner, using his magical interferometere called *CES*. Of course, it was often difficult for me to fully grasp the physics of nano-fabrication, as I had no experience with

it. Here, my friend and colleague Michael Steinert was always there to give me stern and clear advice. I firmly believe that he saved some of my projects by preventing vaguely unphysical mishaps.

An important turning point in my personal development as a scientist was an interdisciplinary conference on the sociology of science, which started as an enthusiastic idea by the sociology professor Tilman Reiz and myself. It was inspiring to gather scientist of many different disciplines, both social and natural. I am very grateful to Tilman for his openness, which motivated me to look for more opportunities for interdisciplinary collaboration. Indeed, this led me to collaborate on a medical project together with my close friend and colleague (almost Dr.) Maria Nisser, who is a sports scientist. As I started my journey I never would have thought that anything like this would happen. Luckily, this even motivated me to more applied research in nano-photonics. In that regard, I have to mention Dr. Jonas Berzinš, who was a brother in arms during my endeavor into nano-photonics color filters. I shall never forget his brutally direct way of handling internship students; always a neat possibility to learn from a safe distance.

Last but certainly not least, I would like to thank all my friends and family. Your support has meant the world to me.

D | Zusammenfassung

Ziel dieser Arbeit war die Entwicklung eines semi-analytischen Modells mehrschichtiger nanostrukturierter Oberflächen. Einzelne Schichten werden hierbei in Forschungsgemeinschaft als “Metasurface” bezeichnet. In Folge nennt man Schichtsysteme aus Metasurfaces “Metasurface Stacks” oder “Stacked Metasurfaces”. Das besondere an Metasurfaces liegt an einer speziellen Art der Licht-Materie-Wechselwirkung. Im Gegensatz zu herkömmlichen, natürlich vorkommenden optischen Materialien, welche im Wesentlichen durch ihre atom- und molekularphysikalischen Eigenschaften Wechselwirken, besitzen Metasurfaces mesoskopische Strukturen. Diese haben Größen, die der von Lichtwellen entsprechen. Dadurch entstehen zum einen Streuphänomene die komplexe Feldwechselwirkungen erzeugen. Darüberhinaus sorgen evaneszente Felder, die auf der Oberfläche der Nano-Strukturen angeregt werden können, für ein geändertes Resonanzverhalten, welches sich durch verschiedene Reflektions- und Absorptionseigenschaften auszeichnet. Beispielsweise wird im Falle von Metallen wie Gold das durch Licht in Schwingung versetzte Elektronengas durch die begrenzte Ausdehnung einzelner Strukturen lokalisiert. Dies führt zu einem optischen Verhalten, welches stark von dem homogen ausgedehnten Metalle abweicht. Insgesamt bedeutet dies, dass die Beschreibung solcher Metasurfaces mit mathematischen Modellen so komplex wird, dass charakteristische Größen wie der Brechungsindex oder die Permittivität ihre Bedeutung verlieren können. Diese bleibt nur erhalten, wenn die Metasurface als Ganzes als effektives Medium beschrieben werden kann. Hierbei muss man zu klassischen Mischmaterialien differenzieren. Aufgrund der mesoskopischen Größe ist die optische Antwort des Materials mehr als nur die Summe aller darin befindlichen Materialeigenschaften. Das Verhalten der Felder muss abgewogen werden. Im Kern gilt es zu untersuchen, unter welchen Bedingungen die Feldwechselwirkung einer Metasurface als homogen und damit als effektives Medium behandelt werden kann.

Sind die Strukturen einer Metasurface periodisch angeordnet lassen sich die dort angeregten Felder durch sogenannte Bloch-Moden beschreiben. Diese sind periodische Feldlösungen der Maxwell-Gleichungen. Betrachtet man nun die Gesamtheit aller Bloch-Moden der Metasurface, kann man eine dominante Mode mit, im Vergleich zu allen anderen, maximalem Energietransport in das Fernfeld identifizieren. Diese nennt man in der Literatur Fundamentalmode. Ist die Metasurface so beschaffen, dass bei Wechselwirkung mit Licht einer bestimmten Wellenlänge

diese Fundamentalmode signifikant alle anderen Moden dominiert und letztere stark dämpfen, das heißt evaneszent abfallen, so kann das betreffende Medium als homogen gedeutet werden. In der vorliegenden Arbeit wurden solche homogenen Metasurfaces in Form von Mehrschichtern untersucht. Die bereits benannten Metasurface Stacks können durch die Fundamentalmoden der jeweiligen Schichten im Fernfeld wechselwirken. Daraus ergeben sich viele Anwendungen theoretischer und experimenteller Natur. Um dies zu erreichen, wurde ein semi-analytisches Modell entwickelt, welches einen Metasurface Stack in Gänze effizient beschreibt. In Konkurrenz dazu stehen rigorose numerische Simulationen. Diese können mit einem gewissen Rechenaufwand nahezu beliebige nano-strukturierte Systeme simulieren. Durch das semi-analytische Modell spart man jedoch mehrere Größenordnungen an Rechenzeit und -aufwand. Hierbei werden einzelne Schichten durch Streumatrizen beschrieben. Streumatrizen homogener Schichten wie Glas können analytisch aus Fresnel-Gleichungen berechnet werden. Streumatrizen von Metasurfaces werden einzeln numerisch simuliert. Da es sich um periodische Metasurfaces handelte wurde die sogenannte Fourier Modal Method (FMM) verwendet. Die Tatsache, dass so Metasurfaces nur je einmal simuliert werden müssen, bedeutet einen enormen Vorteil bei der Berechnung.

Ein weiterer Vorteil liegt in der mathematischen Struktur der Streumatrizen. Diese lassen sich algebraisch behandeln und können mit einfachen Transformationsmatrizen manipuliert werden. Dies beinhaltet beispielsweise Rotationsoperationen aber auch Basistransformationen. Das Besondere daran: Jede Transformation einer Streumatrix entspricht einer äquivalenten Transformation einer Metasurface. Somit können diese analytisch manipuliert werden und viele Varianten eines Metasurface Stacks in kurzer Zeit simuliert werden.

All dies ist jedoch nur möglich, wenn nach wie vor die Fundamentalmoden dominieren. Dies kann durch einen Sicherheitsabstand der Schichten gewährleistet werden. An der Schwelle, dem kritischen Abstand, fallen die evaneszenten Felder benachbarter Schichten gerade stark genug ab, um ein gültiges homogenes Medium zu repräsentieren. Die Herleitung und das numerische und experimentelle Testen des kritischen Abstands war wesentlicher Bestandteil der vorliegenden Arbeit. Es konnte gezeigt werden, dass das semi-analytische Modell bei einem kritischen Abstand stabil bleibt und physikalische Phänomene korrekt vorhersagt. Des Weiteren konnte die Theorie der approximativen Fundamentalmodendominanz experimentell nachgewiesen werden. An verschiedenen Stacks wurden auch die analytischen Stärken der Streumatrixtheorie gezeigt. So konnten Aussagen über die Anisotropie eines Metasurface Stacks aus verdrehten Nano-Drähten getroffen werden, die rein numerisch schwer abzuleiten sind. Dabei wurde auch erklärt, wie Chiralität aus nicht-chiralen Bestandteilen entstehen kann. Die Antwort: Einzelne Metasurfaces bilden Symmetrie-Operationen auf die Felder ab, die diese dann mit sich tragen und so ihre Gesamtsymmetrie chiral brechen.

In Anlehnung an Konzepte zum Elektronentransport in mesoskopischen Systemen wurde das semi-analytische Modell erweitert. Aufgrund vergleichbarer mathematischer Strukturen konnten

sogenannte Feynman-Pfade identifiziert werden. Diese beschreiben jeden möglich Pfad den ein Teilchen oder eine Welle bei Streuprozessen zwischen mehreren beteiligten Streuern nehmen kann. In der Beschreibung von Metasurface Stacks erlaubt dies ein detailliertes Verständnis von Zwischenschichtwechselwirkungen. Damit konnten Resonanzen der Fundamentalmoden im Fernfeld aufgedeckt werden, die maßgeblich zur optischen Antwort des Gesamtsystems beitragen. Als Beispiel ist hier wieder der bereits benannte anisotrope Metasurface Stack zu nennen. Eine Feynman-Pfad-Analyse ergab, dass Resonanzeffekte erster und zweiter Ordnung ein zusätzliches Verdrehen des Feldvektors erzeugen. Dies verursacht eine verstärkte chirale Asymmetrie der Felder und erklärt die Stärke der experimentell gemessenen Effekte.

Insgesamt wurde in der vorliegenden Arbeit ein semi-analytisches Model von Stacked Metasurfaces entwickelt, welches verschiedenen experimentellen Tests stand hielt. Dabei konnten auch vielseitige deskriptive Fähigkeiten gezeigt werden. Ein besonderer Erfolg liegt in der Erweiterung des Modells zur Untersuchung von Feynman-Pfaden in Mehrschichtsystemen.

E | Ehrenwörtliche Erklärung

Ich erkläre hiermit ehrenwörtlich, dass ich die vorliegende Arbeit selbständig, ohne unzulässige Hilfe Dritter und ohne Benutzung anderer als der angegebenen Hilfsmittel und Literatur angefertigt habe. Die aus anderen Quellen direkt oder indirekt übernommenen Daten und Konzepte sind unter Angabe der Quelle gekennzeichnet.

Bei der Auswahl und Auswertung folgenden Materials haben mir die nachstehend aufgeführten Personen in der jeweils beschriebenen Weise unentgeltlich geholfen:

1. Der in dieser Dissertation zur Simulation nano-optischer Phänomene verwendete FMM-Kernel wurde aus der ursprünglichen Implementierung von Dr. Thomas Paul, ehemals am Institut für Festkörperphysik und Optik (FSU Jena), jetzt Fraunhofer Institut für Angewandte Optik und Feinmechanik, adaptiert.
2. Die in Kapitel 4 ausgewerteten FDTD-Simulationen wurde durchgeführt von Dr. Christoph Menzel, ehemals Institut für Angewandte Physik (IAP).
3. Die Herstellung aller nano-strukturierten Proben wurde durch Stefan Fasold, ehemals Institut für Angewandte Physik (FSU Jena), durchgeführt.
4. Die optische Charakterisierung nano-strukturierter Proben mittels Weißlicht-Interferometrie wurde durch Matthias Falkner am Institut für Angewandte Physik (FSU Jena) durchgeführt.
5. Strukturelle Charakterisierungen mittels Rasterelektronenmikroskopie wurden von Stefan Fasold und Michael Steinert am Institut für Angewandte Physik (FSU Jena) durchgeführt.

Weitere Personen waren an der inhaltlich-materiellen Erstellung der vorliegenden Arbeit nicht beteiligt. Insbesondere habe ich hierfür nicht die entgeltliche Hilfe von Vermittlungs- bzw. Beratungsdiensten (Promotionsberater oder andere Personen) in Anspruch genommen. Niemand hat von mir unmittelbar oder mittelbar geldwerte Leistungen für Arbeiten erhalten, die im Zusammenhang mit dem Inhalt der vorgelegten Dissertation stehen.

Die Arbeit wurde bisher weder im In- noch im Ausland in gleicher oder ähnlicher Form einer anderen Prüfungsbehörde vorgelegt.

Die geltende Promotionsordnung der Physikalisch-Astronomischen Fakultät ist mir bekannt.

Ich versichere ehrenwörtlich, dass ich nach bestem Wissen die reine Wahrheit gesagt und nichts verschwiegen habe.

Ort, Datum

Unterschrift d. Verfassers